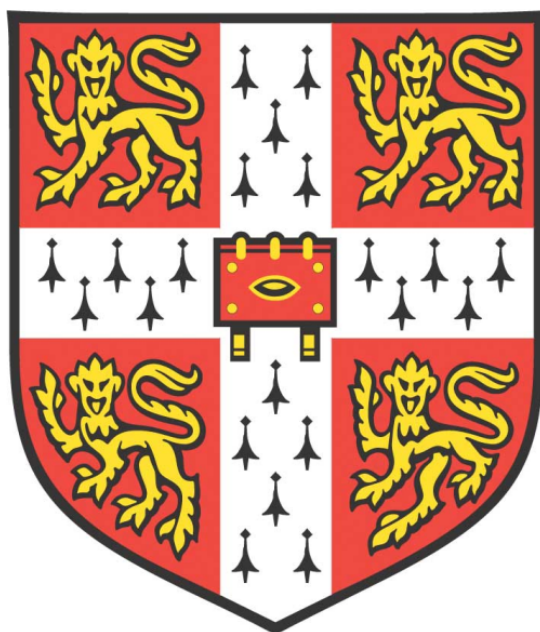


OPTIMIZING ELECTROGENIC ACTIVITY FROM  
PHOTOSYNTHETIC BACTERIA IN  
BIOELECTROCHEMICAL SYSTEMS



**Toby Primo Call**

**Department of Biochemistry**

**University of Cambridge**

**This dissertation is submitted for the degree of Doctor of Philosophy**

**December 2017**

## DECLARATION

This dissertation is the result of my own work and includes nothing which is the outcome of work done in collaboration except as declared in the Preface and specified in the text. It is not substantially the same as any that I have submitted, or, is being concurrently submitted for a degree or diploma or other qualification at the University of Cambridge or any other University or similar institution except as declared in the Preface and specified in the text. I further state that no substantial part of my dissertation has already been submitted, or, is being concurrently submitted for any such degree, diploma or other qualification at the University of Cambridge or any other University or similar institution except as declared in the Preface and specified in the text. This dissertation does not exceed the prescribed word limit of 60,000 words specified by the Biology Degree Committee.

Toby Primo Call

The experiments outlined in Chapter 7 were published in the following article:

Call, T.P. et al., 2017. Platinum-free, graphene based anodes and air cathodes for single chamber microbial fuel cells. *Journal of Materials Chemistry A*, 5, pp.23872–23886.

Available at: <http://pubs.rsc.org/en/content/articlelanding/2017/ta/c7ta06895f#!divAbstract>

*“Ex libro ad sapientiam vocari.”*

# CONTENTS

<b>DECLARATION</b>	<b>16</b>
<b>ACKNOWLEDGEMENTS</b>	<b>17</b>
<b>ABSTRACT</b>	<b>18</b>

## **1. INTRODUCTION**

---

<b>1.1. Bioelectrochemical systems in a global energy context</b>	<b>19</b>
<b>1.2. Key principles of bioelectrochemical systems</b>	<b>20</b>
1.2.1. Microbial fuel cells	20
1.2.2. Biophotovoltaic fuel cells	23
1.2.3. Applications of MFC and BPV systems	24
<b>1.3. Cyanobacteria as model organisms for BPV devices</b>	<b>24</b>
1.3.1. <i>Synechocystis</i> sp. PCC6803	25
1.3.2. Light capture by phycobilisomes and photosystem II in <i>Synechocystis</i> :	26
1.3.3. Photosynthetic electron transport in <i>Synechocystis</i>	29
1.3.4. Flavodiirons protect photosystems from overreduction	29
1.3.5. Respiratory terminal oxidases overlap with and protect the electron transport chain from excess reduction	30
1.3.6. Extracellular reducing power originates from the thylakoid membrane bound electron transport chain	30
<b>1.4. Purple non-sulphur bacteria</b>	<b>30</b>
1.4.1. <i>Rhodospseudomonas palustris</i> CGA009 as a model organism	31
1.4.2. Photosynthesis and respiratory electron transport in <i>R. palustris</i>	34
1.4.3. Structure and characteristics of chlorophyll, bacteriochlorophyll, and phycocyanobilin in <i>Synechocystis</i> and <i>R. palustris</i> :	35
<b>1.5. Physiology of electron export</b>	<b>37</b>
1.5.1. Cell contact – outer membrane cytochromes	37
1.5.2. Electrically conductive pili	38
1.5.3. The importance of biofilms	39
<b>1.6. MFC and BPV system design considerations</b>	<b>39</b>
1.6.1. Electrode materials	40
1.6.2. Proton exchange membrane	40
1.6.3. Direct or indirect EET	41
1.6.4. Light utilization in BPV devices	42
1.6.5. Cellular electron sinks	42
<b>1.7. Outline of PhD project</b>	<b>43</b>

## **2. MATERIALS AND METHODS**

---

<b>2.1. Microbiology</b>	<b>45</b>
2.1.1. Growth media preparation	45
2.1.2. Cell culture	47
2.1.2.1. Antibiotics	48
2.1.2.2. Glycerol stock storage	48

<b>2.2. Molecular biology</b>	<b>48</b>
2.2.1. Plasmids	48
2.2.2. Primers	48
2.2.3. Genomic DNA extraction from <i>Synechocystis</i> and <i>R. palustris</i>	49
2.2.4. Cloning	50
2.2.4.1. PCR protocol	50
2.2.4.2. Gel electrophoresis	51
2.2.4.3. Gel extraction	51
2.2.4.4. Restriction digest	51
2.2.4.5. Ligation	52
2.2.4.6. <i>E. coli</i> competent cell preparation	53
2.2.4.7. <i>E. coli</i> transformation	53
2.2.4.8. Plasmid extraction	53
2.2.4.9. Plasmid sequencing	54
2.2.5. Transformation of <i>Synechocystis</i>	54
2.2.6. Transformation of <i>R. palustris</i>	54
2.2.7. Colony PCR of transformants	55
<b>2.3. Characterization of strains</b>	<b>56</b>
2.3.1. Cell density adjustments	56
2.3.2. Light penetration	56
2.3.3. Ferricyanide reduction assay	57
2.3.4. Bioelectrochemical system design and construction	59
2.3.4.1. Initial biophotovoltaic device design	59
2.3.4.2. Revised bioelectrochemical system design	60
2.3.4.3. Bioelectrochemical system set up as a biophotovoltaic device	62
2.3.4.5. Biophotovoltaic device adapted for fluorescence measurements	63
2.3.4.6. Bioelectrochemical system set up as a microbial fuel cell	64
2.3.5. Graphene based electrodes	65
2.3.5.1. Preparation of graphene based electrode materials	65
2.3.5.2. Dry mass change of graphene coated carbon foam with <i>R. palustris</i>	66
2.3.6. Electrochemical characterization techniques	66
2.3.7. Glycerol concentration assay	67
2.3.8. Scanning electron microscopy	68
2.3.9. Pulse amplitude modulation (PAM) fluorescence measurements	68

### **3. OPTIMIZING BIOPHOTOVOLTAIC DEVICE DESIGN AND INVESTIGATING LIGHT ABSORPTION LIMITATIONS ON BIOPHOTOVOLTAIC CURRENT OUTPUT IN *SYNECHOCYSTIS***

<b>3.1. Introduction</b>	<b>70</b>
3.1.1. Transduction of light energy to electrical current: Optimizing biophotovoltaic devices	70
3.1.2. Characterizing biofilm based BPVs	71

3.1.3. Light harvesting attenuation as a means to improve productivity and photosynthetic efficiency	72
3.1.4. PBS antenna truncation mutants	75
3.2. Results	77
3.2.1. Biophotovoltaic activity from <i>Synechocystis</i> sp. PCC 6803	77
3.2.1.1. Initial biophotovoltaic current results	77
3.2.1.2. Biophotovoltaic current from revised device design	78
3.2.3.3. Effect of biofilm vs suspended culture in anodic chamber on BPV output	79
3.2.1.4. Fast biofilm – biophotovoltaic polarization light responses	82
3.2.1.5. Cyclic voltammetry of electroactive <i>Synechocystis</i> biofilms	85
3.2.2. Imaging of <i>Synechocystis</i> pili in biofilms on ITO with SEM	87
3.2.3. Effect of light absorbance by <i>Synechocystis</i> on extracellular electron transport	92
3.2.3.1. Increase in red light penetration through PBS truncated biofilms	92
3.2.3.2. Antenna truncation increases the sensitivity to cell density of ferricyanide reduction rate	93
3.2.3.3. PBS truncation enhances the rate of photo-induced ferricyanide reduction at medium light intensity	96
3.2.3.4. Biophotovoltaic output from biofilms of PBS truncated mutants	98
3.3. Discussion	105
3.3.1. Cells in a biofilm exhibit faster BPV kinetics	105
3.3.2. The role of type IV pili as conductive nanowires in <i>Synechocystis</i>	107
3.3.4. Tuning light absorbance to optimize BPV light use efficiency	108
3.4. Conclusions	110

## **4. COMBINING SIMULTANEOUS FLUORESCENCE AND ELECTROCHEMICAL MEASUREMENTS TO MONITOR BIOPHOTOVOLTAIC EFFICIENCY AND NON-PHOTOCHEMICAL QUENCHING IN *SYNECHOCYSTIS***

---

4.1. Introduction	111
4.1.1. Coupling photosynthetic electron generation to extracellular electron transfer	111
4.1.2. Quantifying intracellular photosynthetic electron flux to EET	112
4.1.3. Effect of phycocyanin removal on non-photochemical quenching	112
4.2. Results	114
4.2.1. Effects of bias potential on basal fluorescence of anodic biofilms	114
4.2.2. Coupling fluorescence to chronoamperometry	118
4.2.3. Using PAM fluorescence and chronoamperometry to probe BPV efficiency	119
4.2.4. Pulse amplitude modulation fluorescence analysis of PBS truncated mutants in custom PAM/BPV devices	124

4.2.4.1. PBS truncated mutants have reduced fluorescence changes under actinic light	124
4.2.4.2. PBS antenna mutants confound derivation of photosynthetic parameters	126
4.2.4.5. Relative NPQ changes within strain	130
4.2.4.6. Effect of bias potential on NPQ	131
4.3. Discussion	133
4.3.1. Simultaneous PAM fluorescence and chronoamperometry as a technique to probe BPV efficiency	133
4.3.2. PBS truncation may reduce NPQ in <i>Synechocystis</i>	134
4.4. Conclusions	136

## **5. ENHANCED BIOPHOTOVOLTAIC PHOTOCURRENT FROM KNOCKOUTS OF COMPETING ELECTRON SINKS IN *SYNECHOCYSTIS***

---

5.1 Introduction	137
5.1.1. Electron sinks in the electron transport chains of <i>Synechocystis</i>	137
5.1.2. Metabolic electron sinks downstream of the thylakoid electron transport chain	138
5.2. Results	140
5.2.1. Generation of unmarked electron sink knockouts in <i>Synechocystis</i>	140
5.2.2. <i>Synechocystis</i> knockout vector construction	140
5.2.3. Generation of unmarked gene knockouts in <i>Synechocystis</i> sp. PCC6803	145
5.2.4. Growth assay of electron sink knockout strains	151
5.2.5. Electron sink knockouts enhance extracellular electron transfer	156
5.2.5.1. How does the rate of ferricyanide reduction by <i>Synechocystis</i> change over time?	156
5.2.5.2. Initial, 'slow', BPV experiments	160
5.2.5.3. Revised 'Fast' BPV protocol	161
5.2.5.4. Cyclic voltammetry confirmed electrochemical interaction in fast BPV protocol	165
5.2.5.5. Chronoamperometry revealed increasing biophotovoltaic response from electron sink knockouts	165
5.3. Discussion	172
5.3.1. Cumulative electron sink knockout in <i>Synechocystis</i> enhances biophotovoltaic output	174
5.3.2. Nitrate assimilation knockout impedes redox balancing regulation	174
5.3.3. Ferricyanide reduction rates and biophotovoltaic output may not be equivalent	172
5.3. Conclusions	175

## **6. EFFECT OF DELETION OF GLYCOGEN AND POLY- $\beta$ -HYDROXYBUTYRATE SYNTHESIS IN *RHODOPSEUDOMONAS***

## ***PALUSTRIS* ON BIOELECTROCHEMICAL OUTPUT IN A MICROBIAL FUEL CELL**

---

<b>6.1. Introduction</b>	<b>176</b>
6.1.1. <i>R. palustris</i> in microbial fuel cells	176
6.1.2. Extracellular electron transport from <i>Rhodopseudomonas palustris</i>	177
6.1.3. Glycerol as a proxy substrate to waste crude glycerol	177
6.1.4. Removing key storage compounds may divert electron flux to the anode	178
<b>6.2. Results</b>	<b>160</b>
6.2.1. Generation of glycogen and PHB synthesis knockouts in <i>R. palustris</i>	160
6.2.2. <i>R. palustris</i> pK18mobsacB knockout vector construction	182
6.2.3. Generation of unmarked knockouts in <i>R. palustris</i>	183
6.2.4. Effects on growth and glycerol consumption by storage molecule gene knockouts	187
6.2.5. Cyclic voltammetry confirmed bioelectrochemical output from <i>R. palustris</i> in a single chamber microbial fuel cell	188
6.2.6. Maturation of bioelectrochemical interaction and glycerol consumption over initial three days was similar between wild type, $\Delta$ glgAC, $\Delta$ phaAB, and $\Delta$ glgAC $\Delta$ phaAB	189
6.2.7. Electrochemical interaction and glycerol consumption from established MFC biofilms	193
6.2.8. Chronoamperometric responses to glycerol spiking in depleted MFCs	195
<b>6.3. Discussion</b>	<b>202</b>
6.3.1. Deletion of storage molecule synthesis had little effect on EET	202
6.3.2. MFC conditions may not have been optimized	203
6.3.3. Glycerol concentration quantification	204
<b>6.4. Conclusions</b>	<b>206</b>

## **7. EFFECT OF CELL TO ELECTRODE INTERACTIONS IN *R. PALUSTRIS* MFC OPERATION**

---

<b>7.1. Introduction</b>	<b>207</b>
7.1.1. Optimizing electrode properties for applied use of MFCs	207
7.1.2. Surface area of MFC electrodes is an important factor contributing to power output	207
7.1.3. Graphene based MFC electrodes	208
7.1.4. Use of graphene oxide in MFC electrodes	208
7.1.5. Use of pristine graphene in MFC electrodes	209
7.1.6. Conductive polymers in aerogels	209
7.1.7. Graphene as a cathodic catalyst	210
7.1.8. Aims	211
<b>7.2. Results</b>	<b>212</b>
7.2.1. Alternative electrode material fabrication and characterization	212
7.2.2. Raman spectroscopy	213

7.2.3. Specific surface area and morphological characteristics from mercury porosimetry and SEM	215
7.2.4 Electrochemical impedance spectroscopy (EIS)	220
7.2.5. Loading of MFC devices	228
7.2.6. Cyclic voltammetry of operational microbial fuel cells	229
7.2.7. Effect of graphene on cell to anode material adherence	230
7.2.8. Power output enhancement by anode extension materials	232
7.2.9. An MFC powered digital clock	236
7.2.10. Volumetric power scaling in millilitre scale MFCs	237
7.2.11. Graphene as an MFC cathodic catalyst	238
7.2.12. Graphene – graphene catalysed MFC	238
7.3. Discussion	239
7.3.1. Effect of graphene flakes inclusion in MFC aerogel anodes on power output	239
7.3.2. Effect of PEDOT:PSS inclusion in MFC aerogel anodes on power output	240
7.3.3. Effect of anode surface area on power output	241
7.3.4. Effect of anode material on biofilm formation	243
7.3.5. Potential applications of graphene/PEDOT:PSS aerogel electrodes	244
7.4. Conclusions	245
<b>8. GENERAL DISCUSSION</b>	
8.1. Achievement of aims	246
8.1.1. Light absorption and dissimilation by <i>Synechocystis</i> affect BPV output	246
8.1.2. Metabolic electron sink knockouts in <i>Synechocystis</i> increase BPV output	247
8.1.3. Storage molecule outputs in <i>R. palustris</i> did not increase MFC output	247
8.1.4. EET to materials – interesting findings, surface area and conductivity important	248
8.2. Technical challenges and shortcomings of lab based ‘DIY’ devices	249
8.2.1. Importance of developing modular, standardized, and high throughput BES equipment	249
8.2.2. Inclusion of a reference electrode proved problematic	250
8.3. Notable phenomena for future study	250
8.3.1. Understanding mechanisms of EET is key to designing more efficient BESs	250
8.3.2. Electrogenic activity of <i>Synechocystis</i> biofilms emerges only after initial light exposure	251
8.3.3. Initial photocurrent fluctuation	252
8.4. Technical developments	252
8.4.1. Multifaceted BPV analysis by combining PAM fluorescence with a BPV device	252
8.4.2. Graphene based anodes and cathodes	253
8.3. Alternative project aims and next steps	254
8.3.1. Engineering <i>R. palustris</i> for biofuel production	254

8.3.2. Towards a combined waste remediation and bioelectrosynthetic system	254
8.4. Conclusions	255
<b>BIBLIOGRAPHY</b>	<b>257</b>

## LIST OF TABLES

<b>Table 2.1:</b> Reagents mix for cloning PCR	<b>50</b>
<b>Table 2.2:</b> Temperature protocol for cloning PCR	<b>50</b>
<b>Table 2.3:</b> Reagents mix for restriction digest reactions	<b>52</b>
<b>Table 2.4:</b> Reagents mix for DNA ligation reactions	<b>52</b>
<b>Table 2.5:</b> Reagents mix for colony PCR reactions	<b>55</b>
<b>Table 2.6:</b> Temperature protocol for colony PCR reactions	<b>55</b>
<b>Table 3.1:</b> Examples of light harvesting attenuation for productivity gains	<b>74</b>
<b>Table 5.1</b> Primers used for vector construction and knockout diagnosis	<b>142</b>
<b>Table 5.2:</b> List of gene knockout combinations generated in <i>Synechocystis</i>	<b>151</b>
<b>Table 6.1.</b> Primers used for vector construction and knockout diagnosis	<b>181</b>
<b>Table 7.1:</b> Electrode materials used in this study	<b>213</b>
<b>Table 7.2:</b> Summary of electrochemical and surface area measurements from electrode materials tested here	<b>234</b>

## LIST OF FIGURES

<b>Fig. 1.1:</b> Diagram illustrating principles of bioelectrochemical systems	<b>21</b>
<b>Fig. 1.2:</b> Diagram of electron transport in <i>Synechocystis</i>	<b>27</b>
<b>Fig. 1.3:</b> Diagram of electron transport in <i>R. palustris</i>	<b>33</b>
<b>Fig. 1.4:</b> Diagram of chlorophyll and bacteriochlorophyll biosynthesis	<b>35</b>
<b>Fig. 1.5:</b> Diagram of phycocyanobilin synthesis	<b>36</b>
<b>Fig. 1.6:</b> Diagram illustrating key limitations in energy transduction in bioelectricity production	<b>43</b>
<b>Fig. 2.1</b> Fast calibration of ferricyanide concentration	<b>58</b>
<b>Fig. 2.2:</b> Calibration of ferricyanide concentration	<b>59</b>
<b>Fig. 2.3:</b> Early BPV devices	<b>60</b>
<b>Fig. 2.4:</b> Diagram of the single chamber bioelectrochemical system used for microbial fuel cell and biophotovoltaics experiments	<b>61</b>
<b>Fig. 2.5:</b> Diagram of the BPV device with a stirrer or a biofilm	<b>62</b>
<b>Fig. 2.6:</b> Diagram of a BPV device adapted for simultaneous PAM fluorimetry measurements	<b>63</b>
<b>Fig. 2.7:</b> Diagram of the MFC device	<b>64</b>
<b>Fig. 3.1:</b> Diagram showing the principle of increased light penetration (yellow arrow) through a biofilm increasing the overall production of electricity	<b>76</b>
<b>Fig. 3.2:</b> Chronoamperometric output from wild type <i>Synechocystis</i>	<b>78</b>
<b>Fig. 3.3:</b> Diagram of cell distribution and electron transfer in BPV devices	<b>79</b>
<b>Fig. 3.4:</b> Direct vs indirect extracellular electron transfer in from <i>Synechocystis</i>	<b>81</b>
<b>Fig. 3.5:</b> Chronoamperometric traces BPV photoeffect from <i>Synechocystis</i> biofilms	<b>83</b>
<b>Fig. 3.6:</b> Alternative representation of chronoamperometric BPV photoeffect	<b>85</b>
<b>Fig. 3.7:</b> Representative cyclic voltammogram from an electroactive photosynthetic biofilm of <i>Synechocystis</i>	<b>87</b>
<b>Fig. 3.8:</b> SEM of wild type <i>Synechocystis</i>	<b>89</b>
<b>Fig. 3.9:</b> SEM of AGW wild type <i>Synechocystis</i> and the $\Delta hfq$ knockout	<b>91</b>
<b>Fig. 3.10:</b> The percentage of light absorbed through biofilms of PBS truncated mutants	<b>93</b>
<b>Fig. 3.11</b> Graph showing the reduction in concentration of ferricyanide	<b>94</b>
<b>Fig. 3.12:</b> Rates of reduction of ferricyanide over 24 hours	<b>96</b>
<b>Fig. 3.13:</b> Rate of reduction of ferricyanide in the light and the dark	<b>98</b>
<b>Fig. 3.14:</b> Dark current prior to BPV light sequence	<b>99</b>
<b>Fig. 3.15:</b> Diagram illustrating analysis of chronoamperometry	<b>100</b>
<b>Fig. 3.16:</b> BPV charge density and maximum biophotovoltaic current increase over the dark current over the full range of light intensities	<b>102</b>
<b>Fig. 3.17:</b> Comparison of the charge density up to 2000 $\mu\text{mol photons m}^{-2} \text{s}^{-1}$	<b>104</b>
<b>Fig. 4.1:</b> Diagram illustrating photoprotection of the photosynthetic electron transport chain of <i>Synechocystis</i>	<b>113</b>
<b>Fig. 4.2:</b> Basal fluorescence ( $F_1$ ) from a wild type <i>Synechocystis</i> anodic biofilm	<b>113</b>

in the dark during step change voltammetry	116
<b>Fig. 4.3:</b> PAM fluorescence from a wild type <i>Synechocystis</i> anodic biofilm during step change voltammetry in dark versus vs high light	117
<b>Fig. 4.4:</b> Simultaneous PAM fluorescence and chronoamperometry	119
<b>Fig. 4.5:</b> Relative electron transport rate from actinic light PAR and stabilized photocurrent from a wild type <i>Synechocystis</i> anodic biofilm	121
<b>Fig. 4.6:</b> Relative electron transport rate and photocurrent from saturating pulse illumination	122
<b>Fig. 4.7:</b> Percentage estimates of electrons produced from photosynthetic light capture	124
<b>Fig. 4.8:</b> Fluorescence profiles of samples from induction curves	126
<b>Fig. 4.9:</b> The relative coefficients of quantum efficiency from wild type and PBS truncated mutants	128
<b>Fig. 4.10:</b> NPQ values for the wild type and PBS truncated mutants	130
<b>Fig. 4.11:</b> Within strain comparison of NPQ values from induction curves from wild type and PBS truncated	131
<b>Fig. 4.12:</b> NPQ values for the wild type and olive strains subjected to positive and negative bias potentials	133
<b>Fig. 5.1:</b> Circular plasmid maps for the first stage knockout vectors in <i>Synechocystis</i>	143
<b>Fig. 5.2:</b> Circular plasmid maps for the second stage knockout vectors in <i>Synechocystis</i>	145
<b>Fig. 5.3:</b> Gel electrophoresis of PCR products from the wild type and unmarked terminal oxidase knockouts	146
<b>Fig. 5.4:</b> Diagrams of gene knockout strategy in <i>Synechocystis</i>	148
<b>Fig. 5.5:</b> Gel electrophoresis of PCR products from the wild type and unmarked knockouts of <i>nirA</i> , <i>narB</i> , <i>hoxH</i> , and, <i>norB</i>	150
<b>Fig. 5.6:</b> Chlorophyll concentration measured throughout the growth assay	152
<b>Fig. 5.7:</b> The rate of change in OD <sub>750</sub> and chlorophyll concentration over 9 days	154
<b>Fig. 5.8:</b> Comparison of absorbance at 750 nm and concentration of chlorophyll at day 9	155
<b>Fig. 5.9:</b> Rates of ferricyanide reduction over eight hours between the wild type and electron sink mutants	158
<b>Fig. 5.10:</b> BPV Charge density from ‘slow’ protocol over ten minute periods from wild type and mutant <i>Synechocystis</i>	161
<b>Fig. 5.11:</b> Illustration of the revised ‘fast’ BPV method	163
<b>Fig. 5.12:</b> Cyclic voltammograms of the wild type and key electron sink knockouts	164
<b>Fig. 5.13:</b> Overview of charge accumulation with the ‘fast’ BPV protocol	166
<b>Fig. 5.14:</b> Plots of the stabilized ‘dark current’ and charge density at each light intensity	170
<b>Fig. 5.15:</b> Charge accumulation enhancement over the wild type at 1000 $\mu\text{mol photons m}^{-2} \text{s}^{-1}$ for key strains	172
<b>Fig. 6.1:</b> Plasmid diagrams of two stage assembly of knockout vectors for <i>R. palustris</i>	182
<b>Fig. 6.2:</b> Diagram illustrating gene knockout strategy	185
<b>Fig. 6.3:</b> Growth assay and glycerol consumption of <i>R. palustris</i> strains	187
<b>Fig. 6.4:</b> Cyclic voltammograms of an MFC device with carbon fibre anode containing <i>R. palustris</i>	188
<b>Fig. 6.5:</b> Bioelectrochemical parameters of MFC assay over 74 hours	191

<b>Fig. 6.6:</b> Concentration of glycerol over 74 hours from MFC assay	<b>192</b>
<b>Fig. 6.7:</b> Cyclic voltammograms at day six from wild type <i>R. palustris</i> , $\Delta glgAC$ , $\Delta phaAB$ , and $\Delta glgAC\Delta phaAB$	<b>194</b>
<b>Fig. 6.8:</b> Bioelectrochemical parameters of MFC assay at day six from wild type <i>R. palustris</i> , $\Delta glgAC$ , $\Delta phaAB$ , and $\Delta glgAC\Delta phaAB$	<b>195</b>
<b>Fig. 6.9:</b> Chronoamperometry at day six from wild type <i>R. palustris</i> , $\Delta glgAC$ , $\Delta phaAB$ , and $\Delta glgAC\Delta phaAB$	<b>197</b>
<b>Fig. 6.10:</b> Plots of the projected dark current	<b>198</b>
<b>Fig. 6.11:</b> Normalised current output due to glycerol	<b>199</b>
<b>Fig. 6.12:</b> a) Total summed charge over time	<b>201</b>
<b>Fig. 7.1:</b> Illustration of the structures of graphene and PEDOT:PSS	<b>210</b>
<b>Fig. 7.2:</b> Raman spectroscopy of the anode materials	<b>214</b>
<b>Fig. 7.3:</b> SEM images of conventional anode materials	<b>217</b>
<b>Fig. 7.4:</b> SEM images show aerogels A-CMC, A-CMC-PD, A-CMC-Gr, and A-CMC-Gr-PD	<b>219</b>
<b>Fig. 7.5:</b> SEM images of marine grade stainless steel mesh after use in the MFC with <i>R. palustris</i>	<b>222</b>
<b>Fig. 7.6:</b> SEM images of carbon foam with and without graphene after use in the MFC	<b>224</b>
<b>Fig. 7.7:</b> SEM images of the A-CMC aerogel after use in the MFC	<b>224</b>
<b>Fig. 7.8:</b> SEM images of the A-CMC-PD (10%) aerogel after use in the MFC	<b>225</b>
<b>Fig. 7.9:</b> SEM images of the A-CMC-Gr aerogel after use in the MFC	<b>226</b>
<b>Fig. 7.10:</b> SEM images of the A-CMC-Gr-PD aerogel after use in the MFC	<b>227</b>
<b>Fig. 7.11:</b> Cyclic voltammograms for each aerogel	<b>229</b>
<b>Fig. 7.12:</b> Dry weight changes of biomass between carbon foam and carbon foam with graphene coating	<b>231</b>
<b>Fig. 7.13:</b> Analysis of linear sweep voltammetry from the aerogels	<b>235</b>
<b>Fig. 7.14:</b> Bioelectrochemical parameters of 10 MFC devices connected to the digital clock	<b>236</b>
<b>Fig. 7.15:</b> Power output from low and medium volume carbon fibre anodes	<b>237</b>
<b>Fig. 7.16:</b> Polarization and power curves from MFC devices with graphene cathodes	<b>238</b>

## LIST OF ABBREVIATIONS AND ACRONYMS

(DCMU)	3-(3,4-dichlorophenyl)-1,1-dimethylurea	Im(Z)	Imaginary impedance
(PABA)	4-aminobenzoic acid	(IEET)	Indirect extracellular electron transfer
(ATP)	Adenosine triphosphate	(ITO)	Indium tin oxide
(APC)	Allophycocyanin	(ISA)	Isopropyl alcohol
(AC)	Alternating current	(LED)	Light emitting diode
(ARTO)	Alternative respiratory terminal oxidase	(LHC-1)	Light harvesting complex 1
(Ft)	Basal fluorescence	(LHC-2)	Light harvesting complex 2
(Cyd)	Bd-quinol oxidase	(LSV)	Linear sweep voltammetry
(BESs)	Bioelectrochemical systems	(LPE)	Liquid phase exfoliation
(BPV)	Biophotovoltaics	(LB)	Lysogeny broth
(BSA)	Bovine serum albumin	(I <sub>D</sub> )	Maximum current density
(NADPH)	B-nicotinamide adenine dinucleotide phosphate	(P <sub>r</sub> )	Maximum volumetric power
(Cyt- <i>c</i> )	C-type cytochrome	(Mtr)	Metal reducing pathway
(CGC)	Cambridge Graphene Centre	(MFC)	Microbial fuel cell
(CNS)	Cambridge Nanosystems	(NDH-1)	NADPH-dehydrogenase 1
(CFi)	Carbon fibre	(NDH-2)	NADPH-dehydrogenase 2
(CF)	Carbon foam	(NarB)	Nitrate reductase
(CMC)	Carboxymethylcellulose	(NorB)	Nitric oxide reductase
( <i>R<sub>ct</sub></i> )	Charge transfer resistance	(NirA)	Nitrite reductase
(CVD)	Chemical vapour deposition	(NPQ)	Non-photochemical quenching
(CV)	Cyclic voltammetry	(OCP)	Open circuit potential
(Cyt- <i>b6f</i> )	Cytochrome b6f complex	(OD)	Optical density
(Cyt- <i>bc<sub>1</sub></i> )	Cytochrome-bc1	(OCP <sup>OR</sup> )	Orange carotenoid protein
(COX)	Cytochrome-c oxidase	(OEC)	Oxygen evolving complex
(COX- <i>aa<sub>3</sub></i> )	Cytochrome-c oxidase aa3	(OEC)	Oxygen evolving complex
(COX- <i>cbb<sub>3</sub></i> )	Cytochrome-c oxidase cbb3	(ORR)	Oxygen reduction reaction
(DNA)	Deoxyribonucleic acid	(PETC)	Photosynthetic electron transport chain
(dNTP)	Deoxyribonucleotide triphosphate	(PAR)	Photosynthetically active radiation
(DMSO)	Dimethyl sulfoxide	(PSI)	Photosystem I
(DEET)	Direct extracellular electron transfer	(PSII)	Photosystem II
(EDTA)	Ethylenediaminetetraacetic acid	(Pio)	Phototrophic iron oxidation pathway
(EET)	Extracellular electron transfer	(PBS)	Phycobilisomes
(Fd)	Ferredoxin	(PC)	Phycocyanin
(FNR)	Ferredoxin NADP <sup>+</sup> reductase	(Cpca)	Phycocyanin- $\alpha$
(Flv1/3)	Flavodiiron 1/3	(Cpcb)	Phycocyanin- $\beta$
(Flv2/4)	Flavodiiron 2/4	(pmfcs)	Plant microbial fuel cells
(GO)	Graphene oxide	(Pc)	Plastocyanin

(HOX)	Hox bi-directional hydrogenase	(PQH2)	Plastoquinol
(PQ)	Plastoquinone	(RGO)	Reduced graphene oxide
(PHB)	Poly-β-hydroxybutyrate	(RETR)	Relative electron transport rate
(PEDOT:PSS)	Poly(3,4-ethylenedioxythiophene)-poly(styrenesulfonate)	(RNA)	Ribonucleic acid
(PAm)	Polyacrylamide	(rubisco)	Ribulose-1,5-bisphosphate carboxylase
(PANI)	Polyalanine	(SEM)	Scanning electron microscopy
(PET)	Polyethylene terephthalate	(RS)	Sheet resistance
(PCR)	Polymerase chain reaction	(SS)	Stainless steel
(Pcc)	Porin-cytochrome pathway	(SDH)	Succinate dehydrogenase
(PEM)	Proton exchange membrane	(TEM)	Terminal emitter
(PAM)	Pulse amplitude modulated	(TCA)	Tricarboxylic acid
(PNSB)	Purple non-sulphur bacteria	(TBE)	Tris-borate-EDTA
Y(II)	Quantum efficiency	(TE)	Tris-EDTA
(RC)	Reaction centre	(Tris)	Tris(hydroxymethyl)aminomethane
(ROS)	Reactive oxygen species	(UQ)	Ubiquinone
Re(Z)	Real impedance		

## ACKNOWLEDGEMENTS

I am extremely grateful to Prof. Chris Howe for having welcomed me into his laboratory for my PhD, his guidance and counsel throughout this project have been invaluable, and his deep knowledge of vast tracts of biochemistry never ceases to impress. The past four years have been as formative as they were enjoyable. I am especially thankful to Dr. David Lea-Smith for guidance and mentorship and for wielding his impressive molecular biology skills to generate the majority of the cyanobacterial mutants used in this project. And to Dr. Paolo Bombelli, for equally thorough induction and instruction into the science of bioelectrochemistry and the art of coaxing electrons from bacteria.

The Howe lab has evolved over the four years but each and every member has proved as kind and supportive as the last, from tea room respite to lab meeting grillings. It was as much a privilege to have known Dr. Derek Bendall in his final years, as it was a pleasure to work with talented undergrads such as Liat and Pavel. And many a late night working in the lab was enlivened by the company of Anthony, Clayton, and Paolo's parental updates.

I extend my thanks to the Biotechnology and Biological Sciences Research Council for having the vision to fund this area of research and support my PhD, and to the Doctoral Training Partnership staff in Cambridge for allowing me to bend the rules and elope to the ISU/NASA for my PIPS.

Finally, I must also thank my Fair Street flatmates Aran, Ruth, Adam, and Brittany, as well as my family for always being there and encouraging me through, Cambridge University Polo Club for lifelong friendships and memories, and Dr. Olivia Macleod for maintaining my sanity to the very end.

## ABSTRACT

The aims of this project were to investigate a range of limitations affecting the electrical performance of bioelectrochemical systems (BES) and their use as analytical tools. The model cyanobacterium *Synechocystis* sp. PCC6803 was used to characterize light-driven BESs, or biophotovoltaic (BPV) devices. The phycobilisome (PBS) antenna size was altered to modify light absorption. At low to medium light intensities the optimum PBS antenna size was found to consist of one phycocyanin (PC) disc. Incorporating pulsed amplitude fluorescence (PAM) measurements into the BPV characterization allowed simultaneous comparison of photosynthetic efficiency to EET in *Synechocystis*. Non-photochemical quenching (NPQ) was investigated as a limiting factor in biophotovoltaic efficiency and was found to be reduced in the PBS antenna-truncated mutants. Fluorescence and electrochemical data were combined to develop a framework for quantifying the efficiency of light to bioelectricity conversion. This approach is a first step towards a more comprehensive and detailed set of analytical tools to monitor EET in direct relation to the underlying photosynthetic biology. A set of metabolic electron sinks were deleted to remove a selection of pathways that might compete with extracellular electron transfer (EET). The combined deletion of a bi-directional hydrogenase – HoxH, nitric oxide reductase – NorB, cytochrome-c oxidase – COX, bd-quinol oxidase – cyd, and the respiratory terminal oxidase – ARTO, roughly doubled light driven electron flux to EET. Deletion of nitrate reductase – NarB, and nitrite reductase – NirA, increased EET to a similar degree, but combination with the other knockouts compromised cell viability and did not increase output further. In addition to *Synechocystis*, the purple non-sulphur  $\alpha$ -proteobacterium *Rhodospseudomonas palustris* CGA009 was used to test the effect of storage molecule synthesis knockout in a more industrially relevant organic carbon source driven BES, or microbial fuel cell (MFC). However, the removal of glycogen and poly- $\beta$ -hydroxybutyrate

(PHB) did not have a significant effect on electrical output. Finally, the importance of electrode material and design for cell to anode connections in an MFC was investigated. EET from *R. palustris* was greatly enhanced using custom designed graphene and poly(3,4-ethylenedioxythiophene)-poly(styrenesulfonate) (PEDOT:PSS) aerogels. Pristine graphene is also shown for the first time to be a viable, low cost alternative to platinum as a cathodic catalyst. Together, these results present a holistic view of major limitations on electrical output from BESs that may contribute to enhancing EET for power generation from MFCs in the long term, and optimization of BPV devices as reliable analytical tools in the short term.

# 1. INTRODUCTION:

## 1.1. Bioelectrochemical systems in a global energy context:

In the 21<sup>st</sup> century global energy consumption is predicted to double from 13.5 terawatts (TW) in 2001 to 27 TW by 2050 (Tsao et al. 2006). In 2001 86% of energy came from fossil fuels, and whilst socioeconomic momentum has since then begun to shift in favour of renewable energy sources, the continued rate of production of greenhouse gases still has us hurtling towards potentially catastrophic climate change (Arutyunov & Lisichkin 2017). Avoiding drastic increases in greenhouse gases will mean deriving a significant proportion of our energy from carbon neutral means by employing a diverse array of renewable energy solutions (Hansen et al. 2013). Accompanying the drive for low carbon emissions is a growing recognition of the importance of recycling and energy recovery from waste streams. Despite the rapid advancement of solar and electrical technology there is still interest in biologically derived energy, with liquid hydrocarbons still unparalleled for energy density and safe storage. Additional applications such as waste remediation and the production of higher value compounds diversify the options for bioengineered production platforms (Standards et al. 2012). Bioelectrochemical systems (BESs) offer an alternative means of directly generating electrical energy from biomass. BESs generate electrical current from the potential difference of oxidation and reduction reactions taking place on spatially separated electrodes, with at least one of the anodic or cathodic reactions being catalyzed by a biological component. First described by Potter (1911), BESs have gained increasing attention over the past few decades, as their potential for renewable energy generation, waste water treatment, and electrosynthesis is being recognized (Bajracharya et al. 2016). The use of photosynthetic bacteria as bio-solar catalysts adds a new dimension with the possibility of a self propagating solar energy capture platform (McCormick et al. 2015).

## **1.2. Key principles of bioelectrochemical systems:**

The underlying driving force behind a BES is the flow of charge between the two spatially separated halves of a redox reaction (Logan et al. 2006), illustrated in Fig. 1.1. The anodic reaction oxidizes a substrate, accepting electrons to the working electrode, or anode. The anodic chamber is connected to a second chamber by a selectively permeable membrane allowing only positive ions to flow through. The second chamber contains the counter electrode, or cathode, to which electrons flow from the anode *via* an external circuit. There, the cathode is in turn oxidized, either by the oxygen reduction reaction (ORR) or by a chemical or biological agent. The flow of electrons from anode to cathode can be measured precisely using a potentiostat or harnessed as electrical current to perform work (Zhao et al. 2009). Different classes of BESs have emerged depending on whether a biological component is reducing the anode, oxidizing the cathode, or both, and what the energy inputs are. Here, discussion is limited to devices containing electrogenic microorganisms in the anodic chamber, bacteria in particular; however, systems have been described using sub-cellular components – isolated enzymes, photosystems and thylakoid membranes – and energy transduction from whole plants (Zhang et al. 2017; Bombelli et al. 2016).

### **1.2.1. Microbial fuel cells:**

A microbial fuel cell (MFC) is the most common form of BES, and generally describes a device harnessing electrons generated by electrogenic microorganisms in the anodic chamber oxidizing an organic substrate (Logan et al. 2006). Many species found to have high rates of extracellular electron transfer (EET) are found in mixed anaerobic environments such as soil, mud, and decomposing organic matter, and are metabolically versatile and robust enough to break down a range of low cost waste products (Gude 2016; Aelterman et al. 2006). Species

that donate electrons to an external electron acceptor when deprived of oxygen in an MFC are said to be ‘anode respiring’. The cathode of an MFC most often contains an inorganic catalyst to make reduction of the anode more favourable; however, the use of biological cathode catalysts is being increasingly reported and reflects the prevalence of evolved mechanisms of electron uptake as well as export in many species (Cao et al. 2009; Rengasamy et al. 2017). The efficiency of substrate conversion to electricity with some anode respiring bacteria has been reported in some cases to be from 50-100% depending on the species and substrate (Xing et al. 2008; Reguera et al. 2006).

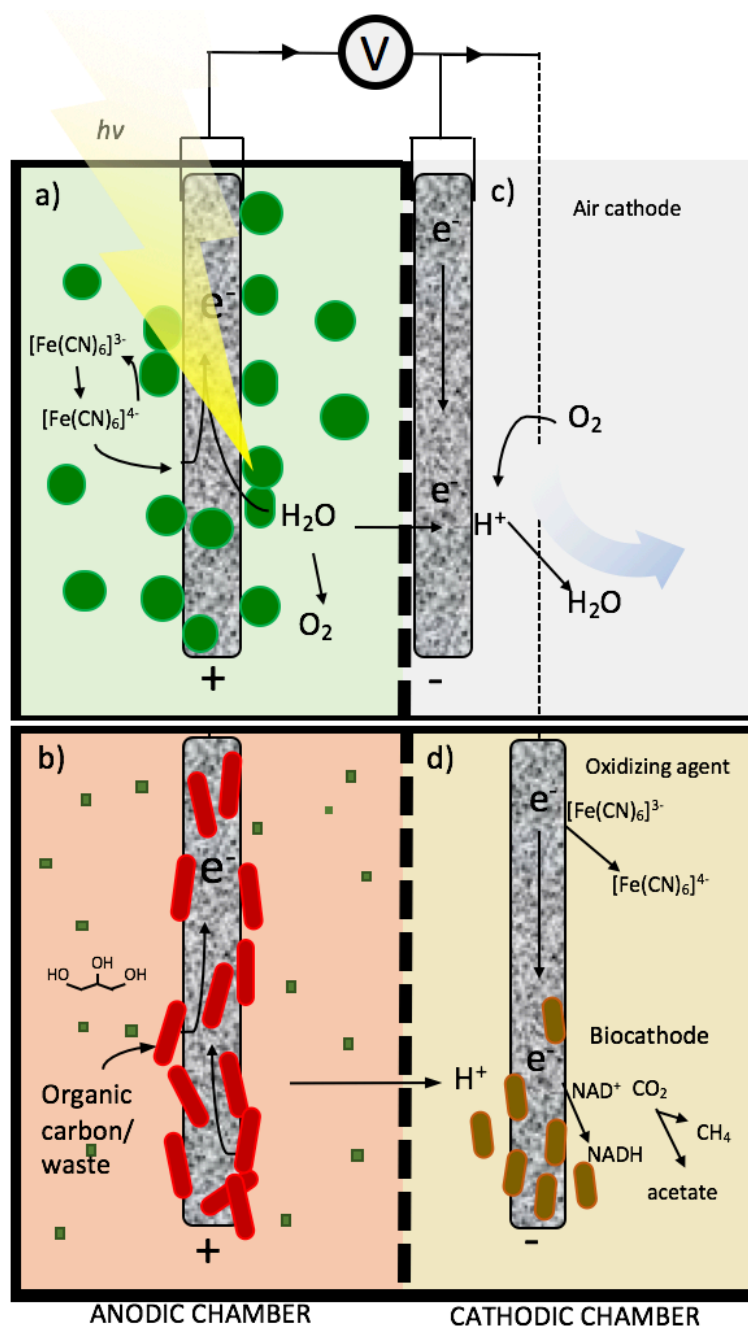


**Fig. 1.1:** Diagram illustrating principles of bioelectrochemical systems set up with the anodic chamber containing a) oxygenic photosynthetic microorganisms reducing either the anode directly or a soluble electron carrier with light as the only energy input, or b) anode respiring bacteria oxidizing a defined or mixed waste organic carbon source. As electrons are conducted around an external circuit to the cathode, protons travel through a proton permeable membrane to the cathodic chamber, where c) electrons and protons reduce atmospheric oxygen to water on an air cathode in a single chamber setup, or d) the cathode is oxidized by an electron accepting molecule or by metal oxidizing bacteria to convert carbon dioxide to methane or acetate or reducing equivalents in the form of NADH. Anodic and cathodic chamber setups are interchangeable provided the potential difference to drive a current and requirements such as anoxia can be maintained if necessary.

### **1.2.2. Biophotovoltaic fuel cells:**

Some MFCs are designed to harness electrons generated by bacteria in the rhizosphere of bacteria supported by plants, metabolizing sugars and other fixed organic carbon excreted from the roots. Plant microbial fuel cells (PMFCs) derive energy from photosynthesis in the plant's leaves, although functionally they still behave as an MFC. Biophotovoltaics (BPV) is rapidly emerging as a form of BES employing only photosynthetic microorganisms including green algae and cyanobacteria in the anodic chamber. These microorganisms are grown without addition of external carbon sources, and in the BPV devices they can directly reduce the anode to produce a defined 'photocurrent' over and above the current produced in the dark (McCormick et al. 2015). The key aspect of a BPV device is the near direct conversion of light absorption by photosynthesis to electrical current *via* EET, resulting in some cases to a near-instantaneous electrical response to light. The efficiency of energy transduction of light to electricity in a BPV is generally one or two orders of magnitude lower than that of an organic substrate to electricity in a MFC. BPV devices are inherently less efficient than MFCs, with

light to electron conversion measured at 0.5% for the cyanobacterium *Porphyridium* sp., but theoretically up to 2.9% (McCormick et al. 2015). Light absorption limitations and photoprotective mechanisms are part of the reason behind this discrepancy, as well as the inherent reduced requirement of oxygenic photosynthetic microorganisms have inherently less need for highly evolved pathways to transfer respiratory electrons to an external terminal acceptor than many anaerobic soil bacteria used in MFCs.

### **1.2.3. Applications of MFC and BPV systems:**

MFCs offer several advantages for applications in industrial biotechnology and renewable energy: the bio-catalyst is self-propagating and in theory scalable at minimal cost, and versatile microorganisms can break down multiple, complex substrates with minimal energy input. Energy recovery during wastewater treatment is developing as the flagship application for MFC systems, with MFCs providing biofiltration by metabolizing organic carbon and producing electrical power that can be recycled into the process (Abourached et al. 2016; Oh et al. 2010). As a source of renewable electricity, MFCs can already be applied to a growing area of low power consumption microwatt technology, such as wearable technology and low power mobile phones (Kwong 2012; Kellogg et al. 2017). Sensors are prime examples of low power technology, which require just a few microwatts to power remote data acquisition from implantable medical sensors or MFCs off-grid environmental sensors (Han et al. 2010; Dong et al. 2013; Yang et al. 2015). Light delivery and stability of an anodic chamber culture are limiting factors for application of BPV devices. However, novel methods of depositing cyanobacterial cells in membranes or paper substrates could provide power to an emerging field of disposable point of care paper-based medical diagnostic technologies (Fraiwan et al. 2013; Sawa et al. 2017). Aside from powered applications, the development of more sensitive electrochemical fuel cell setups opens the door to electrophysiological characterization of

bacterial metabolism, with enough accuracy to track differential breakdown of specific compounds to detect, for example, antibiotic resistance (Schneider et al. 2015).

### **1.3. Cyanobacteria as model organisms for BPV devices:**

Cyanobacteria are a diverse phylum of bacteria found in nearly all habitats and environments on Earth. Having evolved oxygenic photosynthesis over 2.4 billion years ago, they were responsible for raising oxygen levels in the atmosphere and, *via* endosymbiosis, were the progenitors of chloroplasts in plants and algae. Today, cyanobacteria perform vital processes in maintaining balance and driving fundamental nutrient cycles including carbon fixation, nitrogen fixation, and hydrocarbon generation (Hohmann-Marriott & Blankenship 2011; Nelson 2011). Cyanobacteria can cause large algal blooms and some species are responsible for a significant proportion of the total photosynthesis in the oceans (Ting et al. 2002). Cyanobacteria can be used in biomass generation for the production of chemicals in important areas including cosmetics, food colouring, bioplastics and fertilizers (Abed et al. 2009). With the development of genetic engineering tools, cyanobacteria have gained increasing interest as a photosynthetic production chassis for biosynthetic compounds including low value, high volume biofuels and higher value pharmaceuticals (Wang et al. 2012).

#### **1.3.1. *Synechocystis* sp. PCC6803:**

One of the best studied cyanobacteria and models for oxygenic photosynthesis is *Synechocystis* sp. PCC6803 (hereafter *Synechocystis*). *Synechocystis* is a spherical, gram-negative, freshwater species, roughly two microns in diameter, capable of photoautotrophic growth as well as heterotrophic growth in the dark using external carbon sources. Cell structure consists of an inner plasma membrane, peptidoglycan layer, and outer membrane surrounded by a proteinaceous S-layer. Within the cell, separated thylakoid membranes form distinct, layered

compartments, converging at numerous thylakoid centres around the cytoplasmic membrane, into which the photosynthetic machinery creates a proton gradient to drive the metabolism of the cell (Liberton et al. 2006). Structures within the cytoplasm include carboxysomes that concentrate carbon dioxide for carbon fixation by ribulose-1,5-bisphosphate carboxylase (RuBisCo), granules of glycogen, cyanophycin, and polyhydroxybutyrate (PHB) that store carbon, nitrogen, and reducing equivalents, lipid bodies around the periphery of the inner cell membrane, and ribosomes distributed primarily in centre of the cell (Van De Meene et al. 2006). The *Synechocystis* genome was sequenced in 1996: it has 3,725 open reading frames predicted in 3.9 Mb of deoxyribonucleic acid (DNA) in chromosomes ranging in copy number from four to fifty three depending on phosphate availability (Kaneko & Tabata 1997; Nakao et al. 2009; Tajima et al. 2011; Zerulla et al. 2016). *Synechocystis* can be transformed by taking up plasmids and is amenable to genetic manipulation by homologous recombination and CRISPR-Cas9 derived systems (Smart et al. 1994; Kufryk et al. 2002; Lea-Smith et al. 2014; Ungerer & Pakrasi 2016).

### **1.3.2. Light capture by phycobilisomes and photosystem II in *Synechocystis*:**

Photosynthetic light capture in *Synechocystis* begins at the phycobilisomes (PBSs), thylakoid membrane bound protein pigment complexes that play a vital role in cyanobacterial photosynthesis by associating with photosystem I (PSI) and photosystem II (PSII) to increase the cross-sectional area and spectral range of light absorption (Kwon et al. 2013). In *Synechocystis* the PBS core consists of tricylindrical allophycocyanin (APC) ( $\lambda_{\max} = 652$  nm) with six cylindrical antenna rods radiating perpendicularly from the APC core, each composed of a stack of three phycocyanin (PC) discs, ( $\lambda_{\max} = 620$  nm) (Cooley & Vermaas 2001; Arteni et al. 2009). Each PC disc is composed of six hetero-dimers of phycocyanin- $\alpha$  (CpcA) and phycocyanin- $\beta$  (CpcB), and connected via linker proteins CpcC1 and CpcC2 (Kirst et al. 2014). Light absorbed by the PBS is transmitted through PC to APC *via* the linker proteins, and though

a terminal emitter (TEM) at the base of the APC core to PSII. PSII is a multisubunit protein complex bound in the thylakoid membrane that catalyzes the splitting of water and the reduction of plastoquinone PQ in the photosynthetic electron transport chain (PETC). Each monomer of the functional PSII dimer has a structure consisting of 20 protein subunits that carefully incorporate 35 chlorophyll molecules, amongst other components, during biosynthesis in the thylakoid membrane. Exciton energy from absorbed photons is transduced to the P680 reaction centre, a specific pair of chlorophyll molecules that induce charge separation, and subsequent reduction by electrons from the oxidation of water at the catalytic  $Mn_4O_5Ca$  centre of the oxygen evolving complex (OEC) (Heinz et al. 2016). After a series of oxidation/reduction steps *via* pheophytin and a bound plastoquinone (PQ)  $Q_A$ , the PQ pool accepts two electrons from the plastoquinone  $Q_B$  binding pocket on PSII, and combined with two protons from the lumen side of the thylakoid, becomes reduced to plastoquinol ( $PQH_2$ ) (Müh et al. 2012; Lea-Smith et al. 2015). The ratio of PSI to PSII in cyanobacteria is about 5:1, compared to higher plants where it is about 1:1 (Vermaas 2001), which might be a consequence of having to maintain the relatively abundant shared PQ pool oxidized to minimize photodamage under high light.



### **1.3.3. Photosynthetic electron transport in *Synechocystis*:**

As summarized in Fig. 1.2, the PQ pool can alternatively be reduced to PQH<sub>2</sub> by bi-directional electron flow from membrane bound succinate dehydrogenase (SDH) or by a number of types of NAD(P)H dehydrogenases (NDH-1, NDH-2) in the overlapping respiratory electron transport chain that oxidize β-nicotinamide adenine dinucleotide phosphate (NADPH) for variously defined functions, including contributing to proton gradient generation (Cooley & Vermaas 2001; Lea-Smith et al. 2015). PQH<sub>2</sub> diffuses through the thylakoid membrane to reduce the cytochrome b<sub>6</sub>f complex (Cyt b<sub>6</sub>f), which in turn reduces the soluble electron carrier cytochrome c<sub>6</sub> (Cyt c<sub>6</sub>) or plastocyanin (Pc). For every two PQH<sub>2</sub>, four protons and two PQ are produced in the lumen, and one PQH<sub>2</sub> is regenerated on the cytoplasmic side; the resulting proton gradient is used to drive adenosine triphosphate (ATP) synthase. Pc and Cyt c<sub>6</sub> diffuse to reduce the lumenal side of PSI, which consists of 12 protein subunit monomers with numerous cofactors arranged in a trimer in the thylakoid membrane. Light energy is transduced to the P700 PSI reaction centre, also using two central chlorophyll molecules, where the electron is excited to a higher energy state in order to reduce ferredoxin (Fd) in the cytoplasm and ferredoxin NADP<sup>+</sup> reductase (FNR), reducing NADP<sup>+</sup> to NADPH (Pisciotta et al. 2011; Grotjohann & Fromme 2005; Vermaas 2001). Fd and NADPH serve as reducing factors for many metabolic pathways, or electron sinks, including carbon fixation *via* the Calvin cycle.

### **1.3.4. Flavodiirons protect photosystems from overreduction:**

The electron transport chain has mechanisms to prevent the build up of high-energy electrons that could cause damage and photoinhibition, especially in high light. PSII and PSI are protected by the flavodiiron (Flv) proteins from damage and photoinhibition, which are caused by reactive oxygen species (ROS) formed by excess production of high energy electrons (Allahverdiyeva et al. 2015). Flv2/4 can oxidize PSII instead of PQ, regulating energy transfer

from the PBS to PSII *via* the TE, and possibly donating electrons to oxygen or to an unknown electron acceptor (Zhang et al. 2012; L. Bersanini et al. 2014). Flv1/3 oxidizes NADPH to reduce oxygen, preventing excess build up of reducing power in PSI and providing essential protection during fluctuating light conditions (Mustila et al. 2016; Allahverdiyeva et al. 2013).

### **1.3.5. Respiratory terminal oxidases overlap with and protect the electron transport chain from excess reduction:**

In the thylakoid membrane (Fig. 1.2), *Synechocystis* has two terminal oxidases that reduce oxygen to water in the cytoplasm: the *bd*-quinol oxidase (Cyd) can directly oxidize an over-reduced PQ pool, and cytochrome-*c* oxidase (COX) oxidizes Pc or Cyt *c*<sub>6</sub> to reduce oxygen as the terminal respiratory electron acceptor. The electron transport chain in the plasma membrane, less well characterized but thought to be involved only in respiration, is also buffered by Cyd, and by the alternative respiratory terminal oxidase (ARTO) (Lea-Smith et al. 2015). Due to the overlap of the respiratory and photosynthetic electron transport chains, terminal oxidases also provide a key role in buffering the redox state of thylakoid membrane, albeit with a slower timescale and reduced capacity to the flavodiiron proteins (Ermakova et al. 2016).

### **1.3.6. Extracellular reducing power originates from the thylakoid membrane bound electron transport chain:**

One or more of the routes for electron flux leads to EET across the cell membrane, cell wall, and S-layer, to reduce an external electron acceptor, however the mechanism for EET in *Synechocystis* has yet to be elucidated. Given that the ‘dark’ current measured in absence of light is supplemented by a ‘photocurrent’, the process must be linked to photosynthetic energy production at the PETC (Pisciotta et al. 2011). BPV output is completely eliminated by addition

of methyl viologen, which preferentially accepts electrons from the reductive side of PSI; this demonstrates PSI to be the exit point for BPV power from the PETC. Inhibition of PQ reduction by PSII with the inhibitor 3-(3,4-dichlorophenyl)-1,1-dimethylurea (DCMU) and loss of function of a key PSII protein PsbB lead to a reduction in BPV output by 65% and 81-84% respectively, suggesting that a greater proportion of photosynthetic than respiratory electrons reach the anode from the overlapping photosynthetic and respiratory electron transport chains (Bombelli et al. 2011; Cereda et al. 2014). The relative proportion of photosynthetic versus respiratory electrons contributing to EET likely depends on growth and light conditions before and during measurements, as does the relative importance of metabolic electron sinks that oxidize Fd or NADPH.

#### **1.4. Purple non-sulphur bacteria:**

Purple non-sulphur bacteria (PNSB) are part of the Rhodospirillaceae in the alphaproteobacteria that have evolved a simpler form of photosynthesis than cyanobacteria. Light harvesting complexes surround a reaction centre containing bacteriochlorophyll (BChl). Light catalyzed charge separation is used to drive a cyclic electron flow that produces ATP, but not NADPH or any other form of reducing power. As the name suggests, PNSB do not source photosynthetic electrons from sulphides, but instead use organic electron donors, hydrogen, or even external metal donors. Their robust nature, coupled with phototrophic growth, diverse metabolism, electron export and import capability, in conjunction with a growing suite of genetic modification tools, make PNSBs an attractive platform for industrial applications. They are often found in anaerobic environments, commonly the dominant group in bacterial mats, and have gained attention for industrial hydrogen production, bioremediation,

and even supplementing plant fertilizers and animal feed (McKinlay et al. 2014; Wang et al. 2015; Wong et al. 2014; Xu et al. 2014).

#### **1.4.1. *Rhodopseudomonas palustris* CGA009 as a model organism:**

The best characterized PNSB is *Rhodopseudomonas palustris* CGA009, a gram negative rod shaped cell around 2µm long that reproduces by budding motile swarmer cells from terminally differentiated mother cells (Westmacott & Primrose 1976). It is widely distributed in nature, and has been isolated from anaerobic light exposed environments including industrial waste lagoons, a wide variety of pond water, lake bed mud deposits, animal faeces, soils, and coastal sediments. *R. palustris* thrives under anaerobic photoheterotrophic metabolism, using organic compounds and light energy (Inglesby et al. 2012a). However, under different environmental conditions it has the ability to switch to chemoautotrophy: using energy from organic compounds and carbon from CO<sub>2</sub>, and chemoheterotrophy: using organic compounds for energy and carbon. Some authors have claimed that *R. palustris* can grow photoautotrophically as well (Novak et al. 2004; Larimer et al. 2004). *R. palustris* is able to break down an unusually wide range of electron donors, including inorganic minerals, and contains pathways to metabolize many carbon sources considered to be environmental pollutants (Xing et al. 2008; Bose & Newman 2011). Lignin, the second most common polymer on Earth, is made up of a variety of aromatic monomers that *R. palustris* can actively import from its environment via high affinity periplasmic binding proteins linked to an ABC transporter system (Salmon et al. 2013). *R. palustris* can degrade a wide variety of aromatic compounds through two main anaerobic reductive ring dissimilation pathways for benzoate and hydroxybenzoate (Dutton & Evans 1969). Harwood & Gibson (1988) found several compounds that could only be metabolized by *R. palustris* out of many strains tested, for example cinnamate can be used to select for it from environmental samples. *R. palustris* also has pathways to degrade toxic

pollutants such as halocarboxylic acids and 3-chlorobenzoate highlighting its potential for processing industrial waste (McGrath & Harfoot 1997; Oda et al. 2003). It's genome consists of a 5.46Mb circular chromosome and an 8.4kb circular plasmid, containing 4,836 protein encoding genes, a large proportion of which are involved in energy metabolism (Larimer et al. 2004).

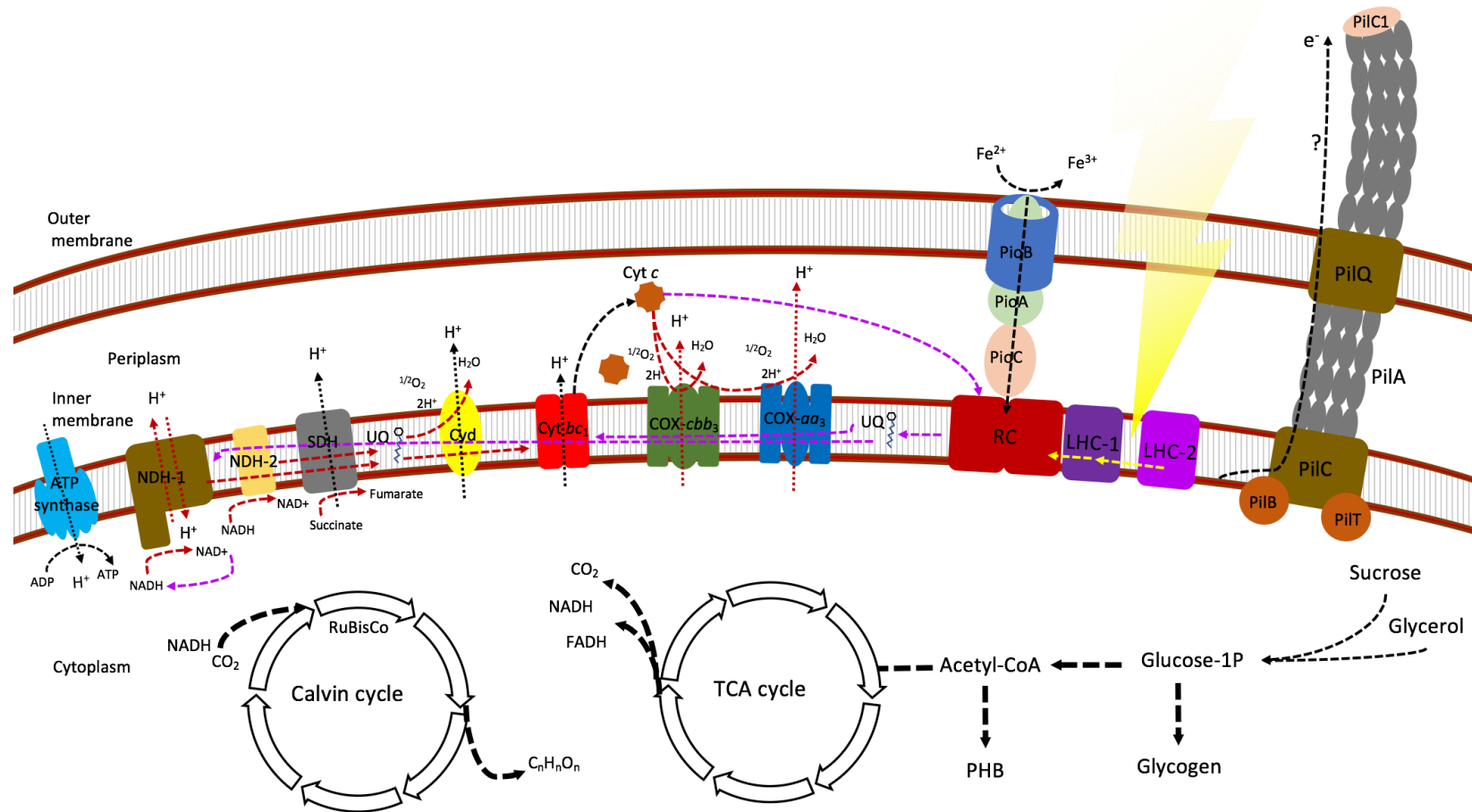


**Fig. 1.3:** Diagram of electron transport in flow in *R. palustris* showing respiratory (red arrows) and photosynthetic (purple arrows) electron transport chains including: ATP synthase, NADH-dehydrogenases 1 (NDH-1) and 2 (NDH-2), succinate dehydrogenase (SDH), ubiquinone (UQ), cytochrome-*bc*<sub>1</sub> (Cyt- *bc*<sub>1</sub>), a *c*-type cytochrome (Cyt-*c*), cytochrome-*c* oxidase *cbb*<sub>3</sub> (COX-*cbb*<sub>3</sub>), and cytochrome-*c* oxidase *aa*<sub>3</sub> (COX-*aa*<sub>3</sub>), ;light harvesting complex 1 (LHC-1), light harvesting complex 2 (LHC-2), the reaction centre (RC). The phototrophic iron oxidation pathway (PioB, PioA, PioC), putative type IV pili assembled from the PilA. In the cytoplasm the TCA cycle is powered by imported organic carbon substrates, and the Calvin cycle fixes CO<sub>2</sub> using reducing equivalents.

#### 1.4.2. Photosynthesis and respiratory electron transport in *R. palustris*:

In *R. palustris* respiratory electron flow (Fig. 1.3) from NADH and succinate oxidation at NDH-1 and 2 and SDH respectively reduces lipid soluble ubiquinone (UQ), that diffuses to terminal oxidases including Cyt<sub>d</sub> and to Cyt-*bc*<sub>1</sub>, where electrons are transferred onto a water soluble iron-sulfur cytochrome-*c* type protein (Cyt-*c*), which in turn reduces cytochrome-*c*-oxidase *cbb*<sub>3</sub> (COX- *cbb*<sub>3</sub>) and cytochrome-*c*-oxidase *aa*<sub>3</sub> (COX- *aa*<sub>3</sub>) that drive a proton gradient into the periplasm (Imam et al. 2011). Light energy is channeled from the peripheral light harvesting antenna (LH2), including BChl and carotenoids, through the core complex (LH1), to the RC, where Cyt-*c* is oxidized to reduce a lipid soluble electron carriers in the membrane including UQ. Five different pairs of peripheral LH2 complex subunits are arranged in concentric rings around each RC, and, unlike other observed PNSB, *R. palustris* is able to regulate the expression level and complex type in response to changes in light intensity and wavelengths (Brotosudarmo et al. 2011). Two photons are used to reduce two UQ, that in turn reduce membrane bound cytochrome-*bc*<sub>1</sub> to pump protons into the periplasm; electrons are returned to the RC *via* periplasmic Cyt-*c* in cyclic electron transfer. The proton gradient produced is used to generate ATP *via* F<sub>0</sub>F<sub>1</sub> H<sup>+</sup> ATP synthase (Scheuring et al. 2006). Light absorption by *R. palustris* is strong throughout the near ultra-violet, visible (up to 650 nm), and near infra-red spectrum (Ritchie 2013). As in cyanobacteria, high light conditions can lead to the generation of ROS such as superoxide (O<sub>2</sub><sup>-</sup>) and hydroxyl (\*OH) free radicals from molecular oxygen. *R. palustris* possesses RuBisCo with which it can fix atmospheric carbon, supporting autotrophic growth, and can also fix nitrogen in anaerobic conditions (Mekjinda & Ritchie 2015; Carlozzi et al. 2006). Carbon dioxide fixation is a significant electron sink for *R. palustris*, which has multiple forms of RuBisCo (Mckinlay & Harwood 2010). Reducing equivalents for the Calvin cycle can come from the TCA cycle, or by phototrophic oxidation

of iron by the PioBAC pathway, which can transfer new electrons to the RC to reduce UQ, in turn drive the reduction of  $\text{NAD}^+$  to NADH by reverse action of NDH-1 (Bird et al. 2011).

### 1.4.3. Structure and characteristics of chlorophyll, bacteriochlorophyll, and phycocyanobilin in *Synechocystis* and *R. palustris*:

Central to the ability of *Synechocystis* to catalyse light to electricity production in a BPV device is light capture by the pigments chlorophyll and phycocyanobilin. Cyanobacteria contain chlorophyll-*a*. Chlorophyll-*a* structure is defined by a tetrapyrrole ring with four nitrogen atoms holding a central magnesium atom and a hydrophobic phytol chain tail that serves to anchor it with light harvesting complexes. It absorbs light with peaks at 430 and 680 nm. 35 chlorophylls are arranged in the PSII, amongst other pigments, to channel captured light energy to a central Chl pair in the reaction centre (Mirkovic et al. 2016).

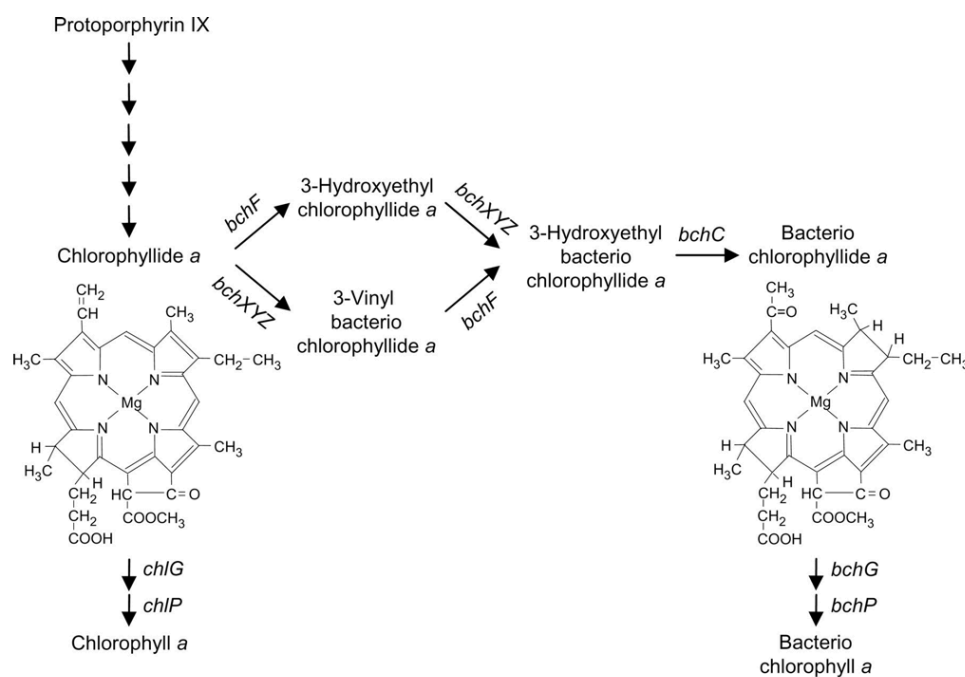


**Fig. 1.4:** Reproduced from Kim & Lee (2010). The shared biosynthetic pathways of chlorophyll-*a* and bacteriochlorophyll-*a* and when they bifurcate to produce chlorophyllide-*a* and bacteriochlorophyllide-*a*. Chlorophyllide-*a* is further modified to bacteriochlorophyllide-

*a* by chlorophyllide-*a* reductase, whose three subunits are encoded by *bchXYZ*, 3-vinyl bacteriochlorophyllide hydratase, encoded by *bchF*, and 3-hydroxyethyl bacteriochlorophyllide dehydrogenase, encoded by *bchC*. The final steps for bacteriochlorophyll-*a* synthesis are catalysed by bacteriochlorophyll synthase, encoded for by *bchG*, and bacteriochlorophyll reductase, encoded for by *bchP*. The final steps for chlorophyll-*a* synthesis are catalyzed by chlorophyll synthase, encoded for by *chlG*, and chlorophyll reductase, encoded for by *chlP*.

BChl, found in purple bacteria including *R. palustris* is, related in structure to cyanobacterial chlorophyll. They absorb light in the near infra-red range of 800 to 1040 nm. BChl differs from chlorophyll by having more reduced groups around the outside of the porphyrin ring, this and varying phytol chain lengths give it its different absorbance properties. There is debate as to which evolved first, and while Chl takes fewer steps to synthesize, there is some evidence that BChl evolved first (Lockhart et al. 2006). In purple bacteria, BChl is located in rings of light harvesting complexes surrounding a reaction centre.

Another principle pigment family in cyanobacteria are the bilins. Phycocyanobilin (PCB), for example is incorporated in PC as the chromophore, each PC contains 3 PCBs, absorbing light around 610 nm (Mirkovic et al. 2016).

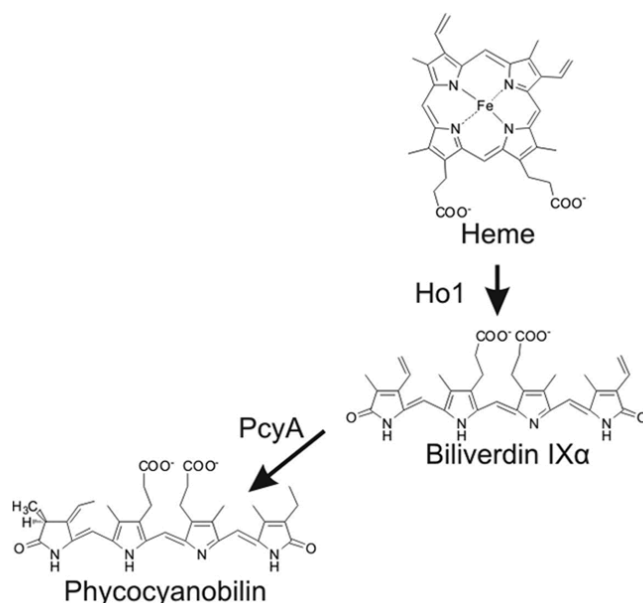


**Fig. 1.5:** Adapted from Alvey et al. (2011). Overview of phycocyanobilin biosynthesis in cyanobacteria from linearization of heme by heme oxidase, Ho1, to biliverdin, and reduction to phycocyanobilin by phycocyanobilin:ferredoxin oxidoreductase, PcyA.

## 1.5. Physiology of electron export:

### 1.5.1. Cell contact – outer membrane cytochromes:

Many species of microorganisms have evolved mechanisms of electron transfer that allow them to bypass the non-conductive cell envelope and reduce minerals in their environment. This permits reduction of terminal external acceptors for respiration or oxidation as a source of electrons for photosynthetic growth. Interspecies electron transfer has been reported, with minerals acting as a charge store or as direct conductors between cells (Shi et al. 2016). Two well characterized mechanisms of EET are the metal reducing (Mtr) pathway from *Shewanella oneidensis* MR-1 and the porin-cytochrome (Pcc) pathways from *Geobacter sulfurreducens*; however, equivalent pathways for electron export have not been identified in *Synechocystis* or *R. palustris*. These are protein complexes that redox couple quinols in the inner cytoplasmic

membrane to electron transfer with minerals across the outer membrane. They have been principally characterized as mediating electron export, but are also capable of electron import. Homologues of MtrA in *R. palustris* only bear 18% sequence identity to *S. oneidensis* MtrA, and so have likely evolved independently with no horizontal gene transfer (Venkidusamy et al. 2015). The Pio pathway in *R. palustris* is well characterized for oxidizing Fe(II) as a source of electrons for carbon fixation. The pathway consists of two Mtr pathway homologues, an outer membrane cytochrome, PioA, passing through an outer membrane porin, PioB, and a *R. palustris* specific high redox potential iron sulphur protein, PioC. The Pio pathway is upregulated in anoxic conditions and is essential for photoautotrophic growth (Bose & Newman 2011; Bose et al. 2014). Given the bi-directionality of the Mtr pathway in *S. oneidensis* (Shi et al. 2016), it may be possible that in the right conditions the Pio pathway could conduct electrons out of the cells as well as in.

### **1.5.2. Electrically conductive pili:**

Recently, pili have been the subject of many reports regarding their role in mediating EET. In particular, conductive type IV pili, previously known for motility, have been putatively described in *Synechocystis* and well characterized in *R. palustris* (Gorby et al. 2009; Venkidusamy et al. 2015). Pili in *Synechocystis*, or fimbriae as they were first termed, have been shown to facilitate phototaxis by growth and retraction in the direction of blue light (Nakane & Nishizaka 2017). They are assembled by the *pil* operon with PilA1 as the principal subunit (Bhaya et al. 2000). PilA1 has been implicated in reducing external acceptors both to allow respiration in the absence of oxygen, and for iron acquisition by reducing insoluble ferric ( $\text{Fe}^{3+}$ ) iron to ferrous ( $\text{Fe}^{2+}$ ) iron (Lamb et al. 2014). In *R. palustris*, nanowires have been characterized as electrically conductive, although their structure remains a mystery (Venkidusamy et al. 2015). Pili from the *G. sulfurreducens* and *Pseudomonas aeruginosa*

contain cytochromes, although the conductivity of pili is thought to come primarily from the proteon structure of the pili subunits (Sure et al. 2016). *Synechocystis* PilA1 was found to have metallic conductivity along backbone chains of aromatic amino acids (Sure et al. 2015).

### **1.5.3. The importance of biofilms:**

Both *Synechocystis* and *R. palustris* form biofilms, although with different degrees of adhesion strength and complexity, which are key to mediating direct electron transfer to the anode. Type IV pili in *Synechocystis* have also been shown to vary in phenotype from promoting motility to a surface adherence morphotype promoting biofilm formation (Chandra et al. 2017). Secreted extracellular polysaccharides also play a vital role in binding cells in a matrix and importantly, trapping nutrients and minerals to optimize the biofilm microenvironment (Jittawuttipoka et al. 2013). Light limitation may be less of an issue for *R. palustris*, which forms very strongly attached biofilms and can survive for a long time without dividing at a relatively high metabolic rate (Kernan et al. 2015; Pechter et al. 2017). The recognition of the importance in biofilms and cell to material connection has been behind the general rise in power densities reported over the past few years (Babauta et al. 2012).

### **1.6. MFC and BPV system design considerations:**

The design and configuration of MFC or BPV devices are flexible depending on the requirements of the microorganism. But, bottlenecks for energy flow appear at all stages from biological and physical limitations. Overcoming them will require both bioengineering and materials design approaches.

### **1.6.1. Electrode materials:**

The choice of electrode material is central to EET from cell to anode. Important considerations are the biocompatibility, conductivity, porosity, specific surface area, and chemical interaction with electrogenic bacteria (Schneider et al. 2016). Indium tin oxide (ITO) is a versatile and conductive material that has been deposited on plastic or glass substrates to make transparent electrodes, ideal for BPV devices (Zhang et al. 2017; Okamoto et al. 2014; Ng et al. 2014). ITO has also been assembled into 3D porous structures to attempt to increase surface area without compromising light delivery for photosynthetic microorganisms (Wenzel et al. 2018). Metals such as copper, steel, nickel, silver, and gold have been used for electrodes. These metals are durable and highly conductive; however, they have low specific surface area and can be subject to corrosion unless meeting the standards of marine grade stainless steel. Diverse carbon-based materials have been used as anodes including carbon foam, carbon paper, carbon fibre, graphite, and more recently carbon nanotubes and graphene (Bajracharya et al. 2016). Carbon materials offer high conductivity and high specific surface area, and carbon nanomaterials in particular are very promising for the engineering of high performance electrodes for BPV and MFC devices (Mustakeem 2015). At the catalytic cathode, if a biocathode or chemical oxidant is not present, a platinum coating is often used in single chamber devices on an air cathode to catalyze the ORR; however, platinum is expensive and a severe limitation on scale-up for commercial use (Chaturvedi & Verma 2016).

### **1.6.2. Proton exchange membrane:**

The separated redox reaction imposes a fundamental limitation on BES design: the requirement for protons to flow directly, yet selectively, from anodic to cathodic chamber, as they cannot be conducted like electrons. To facilitate this, a salt bridge filled with positive ions can be constructed between the two chambers, physically separating cells and most metabolites in

each, but allowing protons to travel unimpeded from chamber to chamber. The salt bridge can be composed of filter or carbon paper, which is sufficient to physically separate cells and prevent a short circuit. Alternatively, a nonporous proton permeable membrane or proton exchange membrane (PEM) can be used to separate the two chambers. Nafion® is one of the best known and most widely used examples, as it is durable enough for industrial fuel cell use, and functions well in BESs. While the surface area of electrodes is often optimized using novel materials and designs, the PEM design is usually limited to a planar separation (Rahimnejad et al. 2014).

### **1.6.3. Direct or indirect EET:**

If the cell culture is kept in suspension by stirring, an exogenous electron mediator can be added to shuttle electrons from the cell to the anode. Potassium ferricyanide is commonly used, as it can be reduced to potassium ferrocyanide at the cell membrane (Zhao et al. 2009). Other mediators can be naturally excreted, such as phenazine and pyocyanin, that facilitate extracellular redox reactions for metabolism, or reduce an anode (Chen et al. 2013). Use of a mediator is justifiable by trying to normalize light exposure of every cell in a photosynthetic BPV device anode chamber. However, as described previously, many mechanisms of EET can directly reduce an electrode, and so benefit from being in direct contact. As such, MFCs and increasingly BPV devices are designed to exploit an electrogenic biofilm. In BPV devices, photosynthetic biofilms display more rapid EET responses to light stimulation, and in MFCs biofilms can be more robust and sequester resources (Flemming et al. 2016). A well-established biofilm could be essential for devices designed with a flow through of material such as wastewater, as opposed to being set up in batches (Lepage et al. 2012).

#### **1.6.4. Light utilization in BPV devices:**

In BPV devices light delivery and absorption is a primary concern (Ooms et al. 2016). For the purposes of quantifying output, a smaller device down to microchannel scale ensures light gradients are minimal (Bombelli et al. 2015), but in any larger device light attenuation must be taken into account. Photosynthetic microorganisms have evolved to use light as efficiently as possible and to protect themselves from damaging high light irradiance. Non-photochemical quenching (NPQ) and other photoprotective adaptations limit the individual light absorption and affect the overall path length of light through the culture or biofilm. Altering cellular light absorption by reducing the size of light harvesting antenna has been shown to increase productivity by reducing light energy dissipation and shading of lower layers (Kirst et al. 2014). Removing or tuning other photoprotective mechanisms may increase vulnerability to light, but optimize BPV output by diverting more electrons to the anode. If EET is in fact a form of photoprotection, it will be important to identify the underlying mechanism and promote that route of electron flux over others.

#### **1.6.5. Cellular electron sinks:**

Competition of EET pathways with other metabolic electron sinks may be less of a limitation in specialized anode respiring bacteria, especially MFC conditions promoting a stable biofilm rather than exponential growth. However, biomass accumulation in the form of storage molecules may still be enough of a sink to divert significant reducing power away from the anode (Yilmaz et al. 2010; Freguia & Rabaey 2007). In BPV devices, photosynthetic microorganisms have less natural reliance on EET, and are highly efficient at distributing captured photosynthetic energy. Carbon fixation, nitrate uptake, hydrogen formation and many other electron sinks are tightly regulated to compensate for fluctuating light levels and to maintain the redox balance in the cell. Removing electron sinks such as the terminal oxidases

or nitrate uptake may divert reducing power to EET (Gutthann et al. 2007; Bradley et al. 2013a).

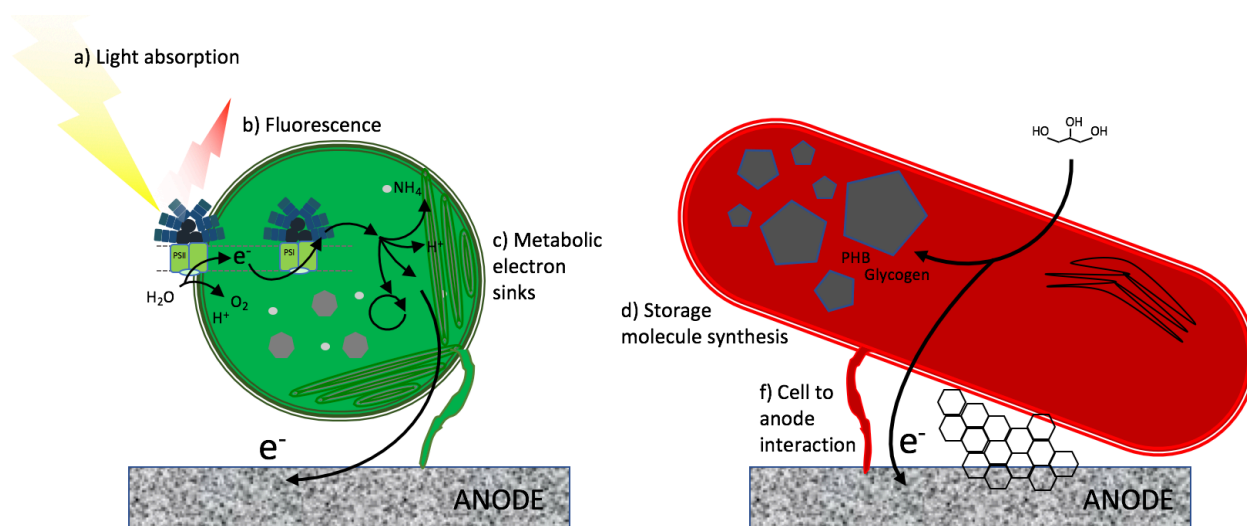


**Fig. 1.6:** Diagram illustrating key limitations in energy transduction in bioelectricity production that will be the focus of this project in *Synechocystis* sp. PCC6803 (green) and *Rhodospseudomonas palustris* CGA009 (red). a) Light absorption limitations, b) energy dissipation by fluorescence, c) competition from metabolic electron sinks, d) competition from storage molecule electron sinks, and e) the cell to electrode material interface.

### 1.7. Outline of PhD project:

Using *Synechocystis* and *R. palustris* as model organisms, we explored a range of strategies to address limitations in electron flux from light capture or substrate oxidation to reduction of the anode (Fig. 1.6). In Chapter 3, we characterized the electrogenic behavior of *Synechocystis* in the BPV device, demonstrated the advantages of anodic biofilms over soluble electron mediators, and identified pili as key biofilm structures. We then investigated the effect of altering photosynthetic light harvesting on BPV output. Truncating PBS antenna in *Synechocystis* was found to increase photosynthetic charge accumulation by EET at low to

medium light intensities. Chapter 4 introduces a combined pulse amplitude modulated (PAM) fluorescence and BPV device in which anode bias potential was seen to directly affect fluorescence and therefore photosynthetic efficiency, and a methodology to compare quantum efficiency and electron transport rate to BPV current output is outlined. NPQ was found qualitatively to be lower in mutants lacking PC on the PBS; however, many difficulties in quantifying NPQ from mutants with inherently different absorption profiles were highlighted. In Chapter 5 we explored the relative importance of metabolic electron sinks in competing with EET for reducing power. Removal of a bi-directional hydrogenase – HoxH, nitric oxide reductase – NorB, cytochrome-c oxidase – COX, bd-quinol oxidase – cyd, and the respiratory terminal oxidase – ARTO, roughly doubled light driven electron flux to EET. Deletion of nitrate reductase – NarB, and nitrite reductase – NirA, increased EET to a similar degree, but proved unstable in combination with other knockouts and did not increase output further. In Chapter 6 we investigated the effect of removing storage molecule synthesis on MFC output from *R. palustris*. Deletion of glycogen and poly- $\beta$ -hydroxybutyrate (PHB) synthesis did not have a significant effect on electrical output. Finally, in Chapter 7 we investigated the importance of surface area and conductivity for anode materials, and demonstrate the effectiveness of pristine graphene at catalyzing both the anodic and cathodic reaction. Together these results inform future design considerations and bioengineering strategies to optimize the efficiency of BPV and MFC devices.

## 2. MATERIALS AND METHODS

### 2.1. Microbiology:

#### 2.1.1. Growth media preparation:

Unless otherwise stated all chemicals and components were sourced from Sigma Aldrich.

BG11: Standard BG11 medium was prepared for culture of *Synechocystis* sp. PCC6803 from several sub-components: i) 100X BG11 was made up with di H<sub>2</sub>O to 1 l with 149.6 g NaNO<sub>3</sub>, 7.49 g MgSO<sub>4</sub>·7H<sub>2</sub>O, 3.60 g CaCl<sub>2</sub>, 0.60 g citric acid, 1.12 ml Na<sub>2</sub>EDTA (0.25 M sol. pH 8.0). ii) 100 ml of trace elements solution was made up with di H<sub>2</sub>O to 100 ml with 0.286 g H<sub>3</sub>BO<sub>3</sub>, 0.181 g MnCl<sub>2</sub>·4H<sub>2</sub>O, 0.022 g ZnSO<sub>4</sub>·7H<sub>2</sub>O, 0.039 g Na<sub>2</sub>MoO<sub>4</sub>·5H<sub>2</sub>O, 0.008 g CuSO<sub>4</sub>·5H<sub>2</sub>O, 0.005 g Co(NO<sub>3</sub>)<sub>2</sub>·6H<sub>2</sub>O. iii) Iron stock was made up with di H<sub>2</sub>O to 100 ml with 1.11 g ferric ammonium citrate, iv) phosphate stock was made up with di H<sub>2</sub>O to 100 ml with 3.05 g K<sub>2</sub>HPO<sub>4</sub>, v) sodium carbonate stock was made up with di H<sub>2</sub>O to 100 ml with 2.0 g Na<sub>2</sub>CO<sub>3</sub>, vi) sodium bicarbonate stock was made up with di H<sub>2</sub>O to 100 ml with 8.4 g NaHCO<sub>3</sub>, and vii) optional ammonium stock was made up with di H<sub>2</sub>O to 200 ml with 10.69 g NH<sub>4</sub>Cl for 1 M. All stocks were pre-autoclaved except for sodium bicarbonate stock which was filter sterilized. For 1 l BG11 10 ml of 100X BG11, 1 ml of trace elements, and 1 ml iron stock were added to 976 ml di H<sub>2</sub>O and autoclaved. After autoclaving, 1 ml of phosphate stock, 1 ml of sodium carbonate stock and 10 ml of sodium bicarbonate stock were added. If an ammonium source was required, 5 ml ammonia stock was added.

For BG11 agar plates 5 ml 100X BG11, 0.5 ml of trace elements stock, 0.5 ml of iron stock, and 3 g of sodium thiosulphate were added to 500 ml di H<sub>2</sub>O with 7.5 g of bacto-agar (Becton,

Dickinson, & Co.). After autoclaving, 0.5 ml of phosphate stock, 0.5 ml of carbonate stock, 0.5 ml of bicarbonate stock, and 5 ml of filter sterilized 1 M TES buffer at pH 8.2 were added. For sucrose selection on BG11 sucrose plates 50 ml of filter sterilized 1 M sucrose was added, and the bicarbonate stock omitted.

Yeast-peptone (YP) medium: Standard yeast-peptone (YP) medium was prepared for the culture of *R. palustris*. 2.5 g of yeast extract and 2.5 g of peptone (Becton, Dickinson, & Co.) were added to 1 l of di H<sub>2</sub>O before autoclaving. YP agar plates were prepared by autoclaving 1.25 g of yeast extract, 1.25 g of peptone, and 7.5 g of bacto-agar (Becton, Dickinson, & Co.) with 500 ml of di H<sub>2</sub>O. YP-sucrose plates were as for YP agar plates, except that 450 ml of di H<sub>2</sub>O was used, and 50 ml of filter sterilized 50% v/v sucrose was added after autoclaving.

‘Gosse’ defined minimal medium: A defined minimal medium was prepared for the culture of *R. palustris* based on the formulation described by Gosse et al. (2007). Stock solutions were prepared and autoclaved separately: i) Trace elements stock was prepared with 0.007 g ZnCl<sub>2</sub>, 0.1 g MnCl<sub>2</sub>·4H<sub>2</sub>O, 0.06 g H<sub>3</sub>BO<sub>3</sub>, 0.2 g CoCl<sub>2</sub>·6H<sub>2</sub>O, 0.02 g CuCl<sub>2</sub>·2H<sub>2</sub>O, 0.02 g NiCl<sub>2</sub>·6H<sub>2</sub>O, 0.04 g NaMoO<sub>4</sub>·2H<sub>2</sub>O, dissolved in 100 ml di H<sub>2</sub>O; ii) 0.2g of 4-aminobenzoic acid (PABA) was prepared in 100ml di H<sub>2</sub>O; iii) iron citrate stock was prepared with 0.5 g in 100 ml di H<sub>2</sub>O; iv) 1 M urea stock was prepared with 6 g in 100 di H<sub>2</sub>O; v) 4 M glycerol stock was prepared with 92.5 ml of glycerol and 157.5 ml di H<sub>2</sub>O. 1 l of ‘Gosse’ defined minimal medium was prepared with 1.7 g KH<sub>2</sub>PO<sub>4</sub>, 0.4 g NaCl, 0.2 g MgSO<sub>4</sub>, and 0.05 g CaCl<sub>2</sub> with 872 ml di H<sub>2</sub>O. 1.7 g of K<sub>2</sub>HPO<sub>4</sub> was autoclaved separately before adding to the bulk solution along with 1 ml of trace elements stock, 1 ml of PABA stock, 1ml of iron citrate stock, 5 ml of urea stock, and 10 ml of glycerol stock.

Lysogeny broth (also known as Luria broth, LB) medium: LB medium for growing *Escherichia coli* was made using LB standard pre-mix (Becton, Dickinson, & Co.).

### **2.1.2 Cell culture:**

*E. coli* DH5 $\alpha$  was inoculated from stocks in LB medium and incubated at 37°C on agar plates or with shaking at 150 rpm for liquid cultures.

*Synechocystis* sp. PCC6803 wild type strain was obtained from lab stocks and grown in BG11 medium at 30°C in an Infors shaker incubator in aerated 40 ml NUNC flasks at 120 rpm under c. 30  $\mu\text{mol photons m}^{-2} \text{ s}^{-1}$  light intensity from Sylvania GroLux F15W fluorescent bulbs with strong emission peaks at 410, 440, 550, 615, and 660 nm. Ammonium citrate was added at to a final concentration of 5 mM to BG11 to make BG11/N, supporting growth of the nitrate uptake pathway deletion strains.

*Rhodospseudomonas palustris* CGA009 wild type was obtained from lab stocks and grown in defined minimal media as described by Gosse et al. (2007). Strains were inoculated in 50 ml sealed Falcon tubes and incubated at 30°C in an Infors shaker incubator at 120 rpm under c. 30  $\mu\text{mol photons m}^{-2} \text{ s}^{-1}$  light intensity from Sylvania GroLux F15W fluorescent bulbs. Once optical density reached around OD 1.0, as measured on a ThermoSpectronic Helios- $\gamma$  spectrophotometer, the cultures were used to inoculate 500 ml Schott bottles of minimal medium with 50 mM glycerol. These were incubated at room temperature with a magnetic stirrer, over defined LED lights optimized by Ruth Laing for photosynthesis with *R. palustris* with emission peaks at 380, 490, 590, 800, and 860 nm.

### **2.1.2.1. Antibiotics:**

Stocks of kanamycin were made at 10 mg/ml and ampicillin at 50 mg/ml with di water, stored in aliquots of 2 ml at -20°C, and added where required to culture media to final concentrations of 100 µg/ml and 500 µg/ml respectively.

### **2.1.2.2. Glycerol stock storage:**

Freezer stocks were made by growing up a pure axenic culture to mid-log phase, collecting cells from 50 ml of culture by centrifugation and resuspending them in 2 ml of freshly autoclaved BG11, repeating the centrifugation and resuspension steps twice to wash cells three times in total. The cells were split into a 16% glycerol stock (800 µl cell culture + 200 µl of 80% filter sterilized glycerol) and 7% dimethyl sulfoxide (DMSO) stock (930 µl of cell culture + 70 µl DMSO) and stored at -80°C in 2 ml screw cap Eppendorf microcentrifuge tubes. Prior to experiments, a sterile, autoclaved splint was used to take a small portion of glycerol stock to streak on BG11 agar plates (*Synechocystis*) and YP plates (*R. palustris*) using sterile techniques. Streaked plates were incubated in an Infors incubator at 30°C under light.

## **2.2. Molecular biology:**

### **2.2.1. Plasmids:**

Plasmids pUC19 (Yanisch-Perron et al. 1985) and pK18mobsacB (Schafer et al. 1994) were obtained from current lab stocks.

### **2.2.2. Primers:**

Primers to construct vectors for generation of marked knockouts by recombination, and for diagnosis of knockout strains, were ordered from Sigma and are listed in Table 1. They were

designed using Primer3 (<http://frodo.wi.mit.edu/>) with reference to the sequenced genome of *Synechocystis* (Kaneko et al. 1996) via Cyanobase (<http://genome.microbedb.jp/cyanobase/>). The genome sequence of *R. palustris* CGA009 for primer design was accessed via JCVI (<http://cmr.jcvi.org/tigr-scripts/CMR>).

### **2.2.3. Genomic DNA extraction from *Synechocystis* and *R. palustris*:**

Cultures of *Synechocystis* and *R. palustris* were grown to mid-log phase in BG11 and Gosse media respectively, before 10-20 ml was centrifuged at 1400 g for 10 minutes and the cells resuspended in 1-2 ml of media. 100 ml of Tris-EDTA (TE) buffer was prepared with 1 ml of 1 M Tris-Cl, 200  $\mu$ l of 0.5 M, pH 8.0 EDTA, and 98.8 ml of autoclaved di water. Samples were centrifuged a second time and resuspended in 600  $\mu$ l of TE buffer (pH8.0). 600  $\mu$ l of water and 100-200  $\mu$ g of acid washed 400-625  $\mu$ m glass beads (Sigma) were added and samples were lysed in a Retsch MM400 bead beater for 1 minute at a frequency of 30 Hz. After bead beating the samples were centrifuged at 8,000 g for 3 minutes and the supernatant was extracted and transferred to a fresh tube. An equal volume of phenol-chloroform-isopropyl alcohol (ISA) (25:24:1) was added and samples were vortexed for 1 minute, before centrifuging at 8,000 g. The supernatant was transferred to a fresh tube and a second volume of phenol-chloroform-ISA added, prior to vortexing and centrifugation. The supernatant was transferred to a sterile crew cap tube and 0.1 vol. of 3M NaAc (pH 5.2) and 2.5 vol. of ice-cold EtOH were added before placing at -80°C for 1 hour. Samples were centrifuged at 11,000 g for 30 minutes at 4°C. The pellet was washed with 70% EtOH, left to air dry, and washed again with 100% EtOH and air dried. Finally, samples were resuspended in 100  $\mu$ l H<sub>2</sub>O and DNA concentrations were measured using the 260:280 ratio on a Nanodrop spectrophotometer (Thermo Scientific).

## 2.2.4. Cloning:

### 2.2.4.1. PCR protocol:

For genomic DNA amplification during cloning and for checking of segregation in transformed strains, Phusion High Fidelity DNA polymerase was used in 50  $\mu$ l reactions with the following reaction mix and temperature cycle. All primers were ordered from Sigma Aldrich and diluted to 100  $\mu$ M stocks.

**Table 2.1:** Reagents mix for cloning PCR:

Reagent	Volume ( $\mu$ l)
GC Buffer (100% DMSO, 50 mM MgCl <sub>2</sub> )	10
10mM dNTP's	1
Primer FW (to 1 $\mu$ M)	1
Primer RV (to 1 $\mu$ M)	1
Template (c. 250ng)	1
DMSO	1.5
Phusion DNA pol	0.5 (1.0 units/50 $\mu$ l of PCR)
H <sub>2</sub> O	34

**Table 2.2:** Temperature protocol for cloning PCR:

Step ( $\times$ 35cycles)	Temperature ( $^{\circ}$ C)	Time (seconds)
Initial denaturation	98	30
Denaturation	98	10
Annealing	65	30
Extension	72	33
Final extension	72	10
Soak	4	On hold

#### **2.2.4.2. Gel electrophoresis:**

To fractionate DNA digestion products for subsequent extraction or to analyse the results of colony PCR amplifications, 100 ml agarose gels were cast by dissolving 1% agarose in Tris-borate-EDTA (TBE) buffer (90 mM Tris-borate/ 1mM EDTA at pH 8.3) using a microwave at 800 Watts for 1.5 minutes. Prior to pouring, 5 µl of ethidium bromide at a concentration of 10 mg/ml or 2 µl of GelRed™ (Biotium) at a concentration of 10,000X in H<sub>2</sub>O were added. Samples were loaded into the gel with TBE loading buffer just covering the gel and subject to electrophoresis at 100 V. After electrophoresis, the positions of DNA bands were identified by illumination at 302 nm UV light by a U-Genius<sup>3</sup> trans-illuminator. A 1 kb DNA ladder (NEB) was loaded in the first channel and used to identify fragment sizes.

#### **2.2.4.3. Gel extraction:**

Gel extraction of digestion products was performed as per the manufacturer's instructions using a Mo Bio Laboratories Gel Extraction Kit.

#### **2.2.4.4. Restriction digest:**

Restriction digest reactions were performed in 30 µl reactions.

**Table 2.3:** Reagents mix for restriction digest reactions:

Reagent	Volume ( $\mu$ l)
Plasmid/fragment	8 (c.1 $\mu$ g)
10X NEB buffer 4	3
BSA	0.5
Restriction enzyme(s)	1 (c.10 units)
H <sub>2</sub> O	17.5
In 37°C bath for 1hr	

**2.2.4.5. Ligation:**

Ligation reactions were performed in 20  $\mu$ l reactions. Vectors were prepared by miniprep from an *E. coli* plasmid stock strain with a QIAGEN miniprep kit before restriction digestion using the above protocol with restriction enzymes from NEB. Inserts were prepared by either a PCR from genomic DNA or restriction digestion of a plasmid before gel extraction using a Mo Bio Gel Extraction kit.

**Table 2.4:** Reagents mix for DNA ligation reactions:

Reagent	Volume ( $\mu$ l)
Buffer (50 mM Tris-HCl, 10 mM MgCl <sub>2</sub> , 1 mM ATP, 10 mM DTT, pH 7.5)	2
T4 ligase	1 (1 unit)
Insert	12
Vector	5
1hr @ room temp.	

#### **2.2.4.6. *E. coli* competent cell preparation:**

*E. coli* cells were grown in 5 ml of LB medium overnight. 5 ml was added to 20 ml pre-warmed LB containing 20 mM MgCl<sub>2</sub> and incubated for one hour at 37°C. The culture was chilled on ice and centrifuged at 4000 rpm in a benchtop centrifuge for 10 minutes at 4°C. The supernatant was poured off and the pellet resuspended in ice cold sterile 75 mM CaCl<sub>2</sub> plus 15% glycerol up to 2.5 ml total. 200 µl aliquots were stored at -80°C.

#### **2.2.4.7. *E. coli* transformation:**

Competent *E. coli* cells were thawed on ice before adding 1 µl (c. 200 ng) of plasmid. After 1 hour on ice samples were subjected to heat shock at 42°C for 1.5 minutes, returned to ice for 2 minutes, and allowed to recover in 1 ml LB medium for 1 hour in a shaker incubator (Infors) at 37°C. Cells were collected by centrifugation at 4000 rpm in a benchtop centrifuge for 5 minutes, resuspended in 250 µl of LB, and 10, 40, and 200 µl samples were plated on LB agar plates with relevant selection antibiotics (kanamycin: 100 µg/ml, ampicillin: 500 µg/ml). Where blue/white screening was used during plasmid construction, 40 µl of IPTG and 40 µl of Xgal were spread over LB agar plates.

#### **2.2.4.8. Plasmid extraction:**

Plasmids were extracted and purified from 5 ml of overnight *E. coli* cultures in LB medium with relevant selection antibiotics (kanamycin: 100 µg/ml or ampicillin: 500 µg/ml), by following the standard protocol from the Qiagen Miniprep Kit as per the manufacturer's instructions.

#### **2.2.4.9. Plasmid sequencing:**

Plasmids were sequenced by Sanger sequencing on an Applied Biosystems 3730xl DNA Analyser in the Department of Biochemistry.

#### **2.2.5. Transformation of *Synechocystis*:**

For each transformation 2 ml of log phase *Synechocystis* culture was spun down at 3000 rpm and the cells resuspended in 100  $\mu$ l of BG11 medium that had been freshly autoclaved to minimize risk of contamination. 2  $\mu$ g of knockout vector plasmid was added to the cells at the base of a 20 ml tube sealed with cotton wool. The mix was incubated under 10  $\mu$ mol photons  $m^{-2} s^{-1}$  for 6 hours at 30°C, with mixing every 2 hours. 20 and 80  $\mu$ l aliquots were then plated on BG11 agar plates. After 24 hours 3 ml of 0.6% agar plus kanamycin (0.5 mg/ml), cooled to 42°C, was poured evenly over each plate (Lea-Smith et al. 2014).

#### **2.2.6. Transformation of *R. palustris*:**

The protocol for *R. palustris* transformation was developed by David Lea-Smith. Cells were grown to early log phase before centrifugation of 50 ml of culture at 2500 g, washed twice by resuspension in ice cold 10% glycerol and centrifugation, followed by resuspension in a final volume of 100  $\mu$ l of 10% glycerol and transfer to a pre-cooled BioRad® Gene Pulser 0.2 cm electroporation cuvette. 1  $\mu$ g of plasmid was added to the cuvette and electroporation was triggered at 600  $\Omega$ , 1.75 kV, and 25  $\mu$ F, followed by recovery in 900  $\mu$ l of freshly autoclaved YP medium and incubation at 30°C for 3 hours before plating onto YP agar with relevant selection antibiotics.

### 2.2.7. Colony PCR of transformants:

Transformants were checked by colony PCR in 50  $\mu$ l reactions using GoTaq DNA Polymerase. Single colonies or a small amount of cells were picked off plates using autoclaved wooden splints and added to 50  $\mu$ l of water with 20  $\mu$ g of acid washed glass beads. The cells were vortexed with glass beads for 1 minute and centrifuged at 10,000 rpm for 1 minute. 5  $\mu$ l of the supernatant was used as template DNA.

**Table 2.5:** Reagents mix for colony PCR reactions:

Reagent	Volume ( $\mu$ l)
GoTaq Green Buffer	10
MgCl <sub>2</sub>	2
10 mM dNTPs	1
Template	5
Primer FW (to 1 $\mu$ M)	1
Primer RV (to 1 $\mu$ M)	1
GoTaq	0.25 (1.25 units)
H <sub>2</sub> O	29.75

**Table 2.6:** Temperature protocol for colony PCR reactions:

Step ( $\times$ 35cycles)	Temp ( $^{\circ}$ C)	Time (minutes)
Initial denaturation	95	2
Denaturation	95	1
Annealing	60	1
Extension	72	1
Final extension	72	5
Soak	4	On hold

## 2.3. Characterization of strains:

### 2.3.1. Cell density adjustments:

*Synechocystis* cultures were adjusted to cell densities corresponding to the concentration of chlorophyll (Chl). Chl concentration was measured spectrophotometrically on a Thermo Spectronic Helios- $\gamma$  spectrophotometer from a) 81, b) 41, and c) 27.666 –fold dilutions (25, 50, and 75  $\mu$ l of culture + 2ml di water) in 2 ml plastic cuvettes, and quantified by the following equation (Porra et al. 1989):

$$Chl(nM\ ml^{-1}) = \frac{10.584 \times [81(OD_{680}^a - OD_{750}^a) + 41(OD_{680}^b - OD_{750}^b) + 27.666(OD_{680}^c - OD_{750}^c)]}{3}$$

*R. palustris* cell density was adjusted measuring OD at 660 nm.

### 2.3.2. Light penetration:

To measure the light absorption of biofilms of *Synechocystis* strains, each strain was adjusted to OD<sub>750</sub> 3.0 in 5 ml well transparent plates and allowed to settle onto the surface, with similar cell density to an established biofilm. A light meter (Skye Instruments®) was used to measure the difference in light intensity in  $\mu$ mol photons  $m^{-2}\ s^{-1}$  at a fixed distance from red (630 nm), blue (458 nm), and warm white LEDs through just BG11 medium and when obstructed by each *Synechocystis* biofilm, and the percentage absorption at each wavelength was calculated by:

$$\% Abs = \frac{Light\ intensity(cells)}{Light\ intensity(no\ cells)} \times 100$$

### 2.3.3. Ferricyanide reduction assay:

Potassium hexacyanoferrate (Sigma) (referred to hereafter as ferricyanide) reduction assays were performed in multiple sealed, transparent 24 well plates with each well containing 5ml of mid-log phase *Synechocystis* cultures in an Infors shaker incubator at 120 rpm at 30°C with a light diffuser panel (Bradley et al. 2013b). Depending on test conditions, the total amount of cells in each well had a Chl content from 5 to 25 nmoles, with constant light delivered from an array above.

The assay was run at i) low and at ii) medium light intensity with a faster and a slower protocol depending on the size of the assay and time sensitivity of measurements. i) An array of 9 red LEDs (peak 635 nm) gave a low irradiance of  $60 \mu\text{mol photons m}^{-2} \text{s}^{-1}$ . Red LEDs were chosen initially to avoid the potential formation of Prussian blue pigment by coupling of ferricyanide to the reduced form ferrocyanide, catalysed by blue light, however this was not found to be a significant problem and warm white LEDs were used in later assays. Ferricyanide was added to each well to a concentration of 55 mM, and samples were extracted for analysis at 0, 24, 48, and 72 hours. 1 ml from each well was extracted under sterile conditions, passed through a 0.2  $\mu\text{m}$  syringe filter and diluted 1:50 in di water in a 2 ml cuvette. The absorption at 420 nm and 680 nm was measured rapidly in a Shimadzu UV-1800 spectrophotometer. Ferricyanide concentration was calculated from a fitted standard curve of mM of ferricyanide in BG11 and the result of  $\text{Abs}_{420\text{nm}} - \text{Abs}_{680\text{nm}}$ , fitted by:

$$\text{ferricyanide (mM)} = 48.928x - 2.282$$

Where

$$x = \text{Abs}_{420\text{nm}} - \text{Abs}_{680\text{nm}}$$

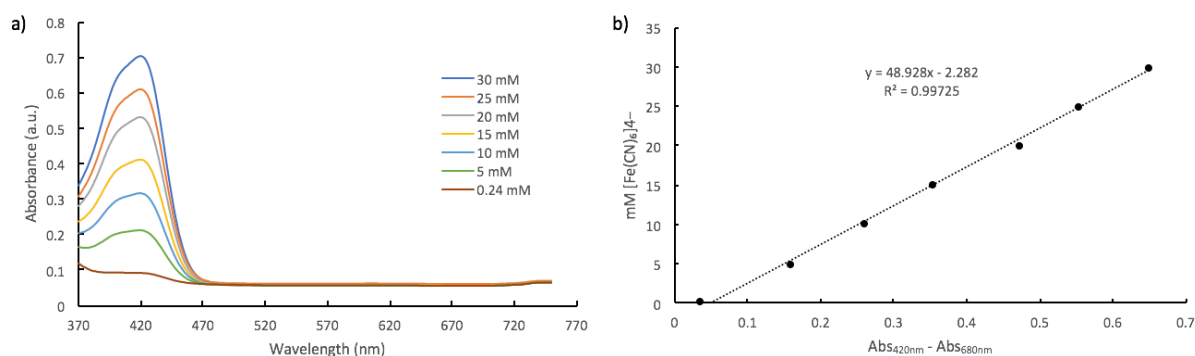


**Fig. 2.1:** Fast calibration of ferricyanide concentration a) Absorbance spectra from BG11 between 370<sub>nm</sub> and 750<sub>nm</sub> with varying concentration of potassium ferricyanide (0.24 – 30 mM). b) Calibration curve of ferricyanide concentration to peak absorbance at 420<sub>nm</sub> with absorbance at 680<sub>nm</sub> subtracted.

ii) For assays at a higher light intensity, an array of 9 warm white halogen bulbs was used to increase the light intensity to a ‘medium level’ irradiance of 180  $\mu\text{mol photons m}^{-2} \text{s}^{-1}$ . Ferricyanide was added to each well to a final concentration of 10 mM. Samples were taken at the start and after 20 hours, centrifuged at 115 g, and diluted 16.7 fold by adding 60  $\mu\text{l}$  of supernatant to 1 ml of BG11. This time the spectrum from 280 to 750 nm was taken for each sample on a Shimadzu UV-1800 spectrophotometer in order to take into account both the peak at 420 nm and a peak at 263 nm related to the concentration of ferricyanide (Fig. 2.2a). This took about 3-5 minutes per sample, limiting the size of assay quantifiable with this method. The concentration of ferricyanide was calculated using the ratio of the peak heights ( $\text{Abs}_{420\text{nm}} - \text{Abs}_{680\text{nm}}$ ) / ( $\text{Abs}_{263\text{nm}} - \text{Abs}_{680\text{nm}}$ ) and a polynomial curve derived from the standards (Fig. 2.2b), before multiplying by the dilution factor:

$$\text{ferricyanide (mM)} = (-4.4702x^2 + 11.948x + 1.8997) \times 150$$

Where

$$x = \frac{(\text{Abs}_{420\text{nm}} - \text{Abs}_{680\text{nm}})}{(\text{Abs}_{263\text{nm}} - \text{Abs}_{680\text{nm}})}$$

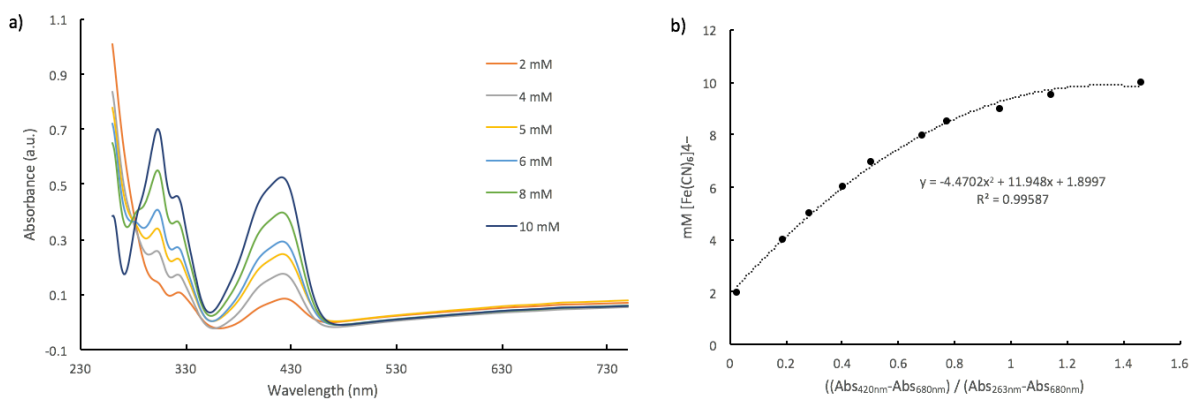


**Fig. 2.2:** Calibration of ferricyanide concentration a) Absorbance spectra from BG11 between 230<sub>nm</sub> and 750<sub>nm</sub> with varying concentrations of potassium ferricyanide (2 – 10 mM). b) Calibration curve of ferricyanide concentration to the ratio of peak absorbance at 420<sub>nm</sub> to 263<sub>nm</sub> with absorbance at 680<sub>nm</sub> subtracted from each.

### 2.3.4. Bioelectrochemical system design and construction:

#### 2.3.4.1. Initial biophotovoltaic device design:

Early BPV experiments were performed in devices consisting of a 25 ml cylindrical acrylic pot with a magnetic stirrer keeping cells in suspension and aiding diffusion of potassium ferri- and ferrocyanide to and from the anode. The anode was transparent ITO coated non-porous polyethylene terephthalate (PET) (Sigma Aldrich) at one end of the cylinder, with the incident LED light shining through the same end. The air cathode at the opposite end was platinum coated carbon paper (Hydrogen electrode/reformate cathode, Alfa Aesar®) with a layer of dialysis membrane (Medicell International Ltd) of pore size 200 nm preventing passage of cells but allowing diffusion of protons to the cathode (Bombelli et al. 2011).

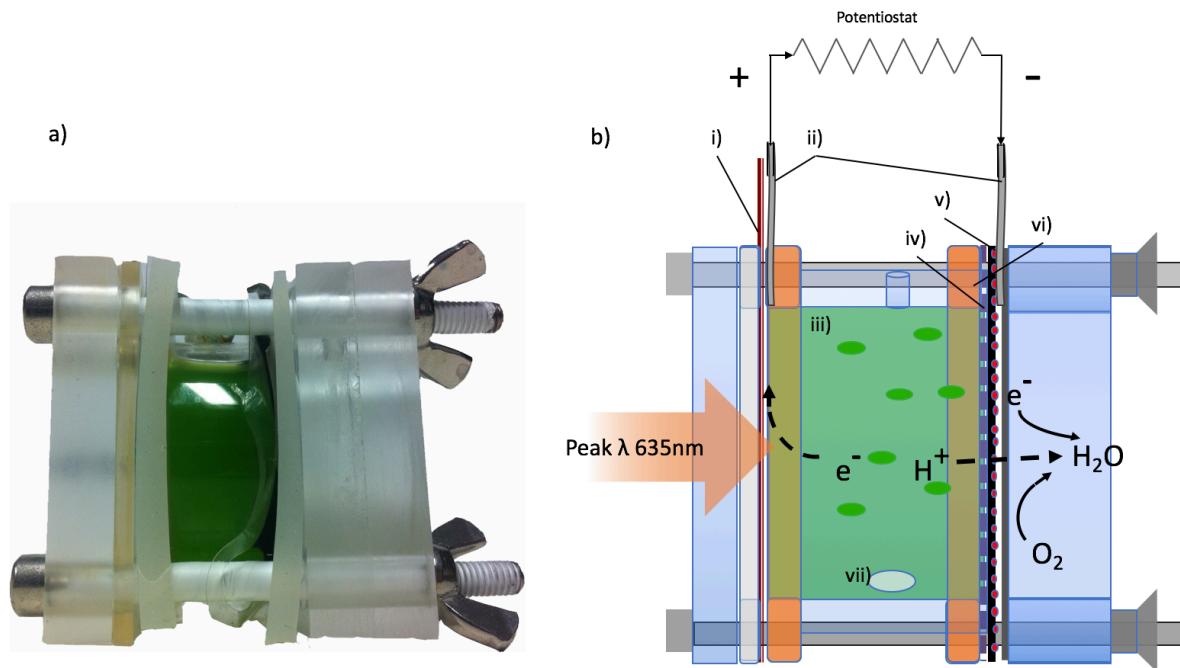


**Fig. 2.3:** Early BPV devices a) Photograph of an early BPV configuration and b) diagram of components and BPV circuit with electrons being transferred to the anode, passing through a circuit and potentiostat to the cathode, where they recombine with protons and atmospheric oxygen at the catalytic surface to form water. i) Stainless steel mesh anode connector, ii) stainless steel electrode connectors, iii) 25 ml culture chamber, iv) porous dialysis membrane, v) platinum coated carbon paper, vi) rubber gasket seal, and vii) a magnetic stirrer.

#### 2.3.4.2. Revised bioelectrochemical system design:

The revised BES design provided a robust and adaptable platform for further BPV and MFC experiments. A 3.5 ml anodic culture chamber was machined from a  $3 \times 3 \times 7.5$  cm Teflon® block in the workshop of the Department of Plant Sciences, University of Cambridge (see Fig. 2.4). The electrode assembly at the base of the chamber was clamped using stainless steel bolts between the chamber block and a base plate with a rubber gasket seal. The anode was marine grade stainless steel mesh, followed by a double dielectric layer of dialysis membrane (Medicell International Ltd) with pore size 200 nm containing the platinum wire pseudo-

reference electrode. Below the dialysis membrane was a Nafion® membrane with the air chamber facing catalytic carbon/platinum coating, and a marine grade stainless steel mesh cathode contact.

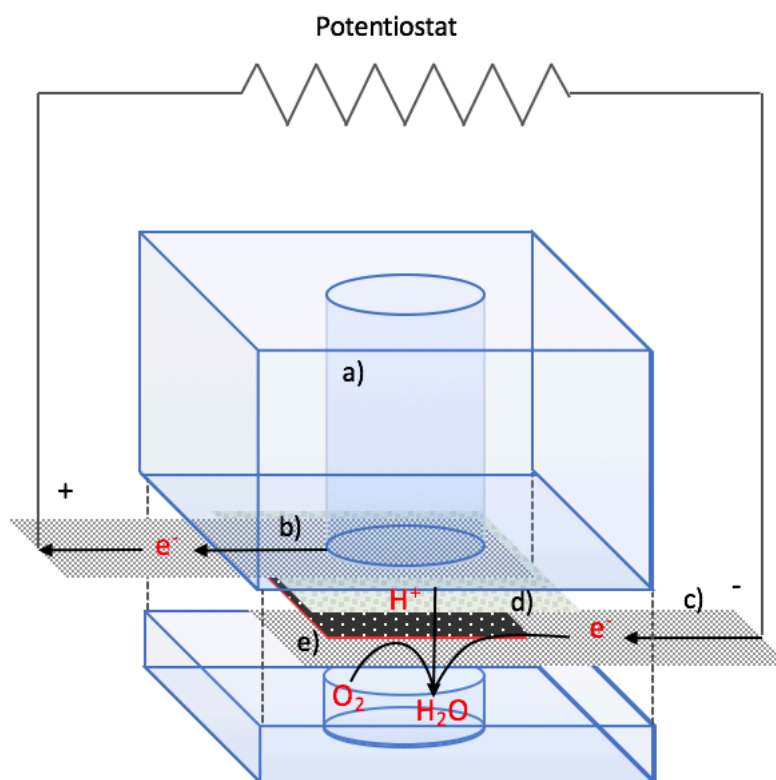


**Fig. 2.4:** Diagram of the single chamber bioelectrochemical system used for microbial fuel cell and biophotovoltaics experiments. In the anodic chamber (a), the anode (b) is reduced, and electrons pass through a potentiostat to the stainless steel cathode connector (c). Protons pass through (d) a dialysis membrane and (e) Nafion® proton exchange membrane with a conductive and catalytic carbon/platinum coating facing the air cathode chamber, on which oxygen is reduced to water.

### 2.3.4.3. Bioelectrochemical system set up as a biophotovoltaic device:

Light from white LEDs illuminated the biofilm from a fixed distance above the culture chamber. Light intensity was controlled externally by a programmable power box (Hantek/AimTTI). Device control software was written in Labview® by Dr. Jordan Baglo (personal communication). A MultiEmstat 4-channel potentiostat was connected to the stainless-steel anode and cathode contacts *via* crocodile clamps. This device could be configured to be operated with either cells in suspension, using a magnetic stirrer and a soluble electron carrier such as potassium ferricyanide, or with cells settled and allowed to form a biofilm on the anodic substrate.

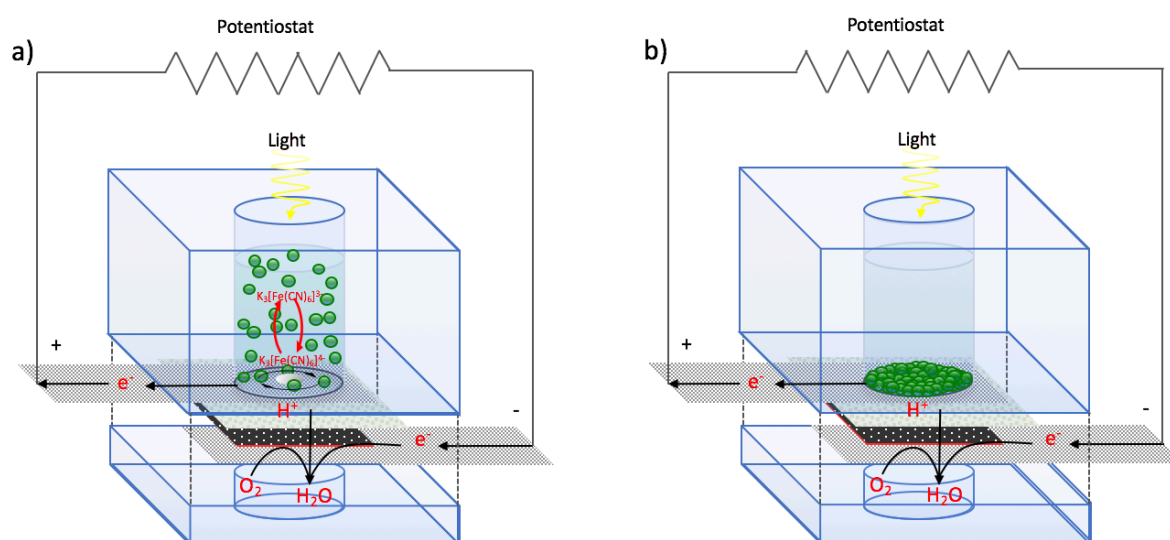


**Fig. 2.5:** Diagram of the BPV device with a stirrer or a biofilm. a) cells in suspension, stirred by a magnetic bar with potassium ferricyanide as an electron carrier diffusing between cells and the stainless steel mesh anode. b) The same device operated without a magnetic stirrer or soluble electron carrier to allow cells to settle as a biofilm on the anodic substrate.

#### 2.3.4.5. Biophotovoltaic device adapted for fluorescence measurements:

The modified electrodes for the PAM measurements used a transparent ITO covered PET anode and a smaller cathode that did not obstruct the fibre optic probe inserted from underneath (Fig. 2.6). The tip of the Walz Mini PAM device fibre optic was flush with the biofilm covered ITO surface.

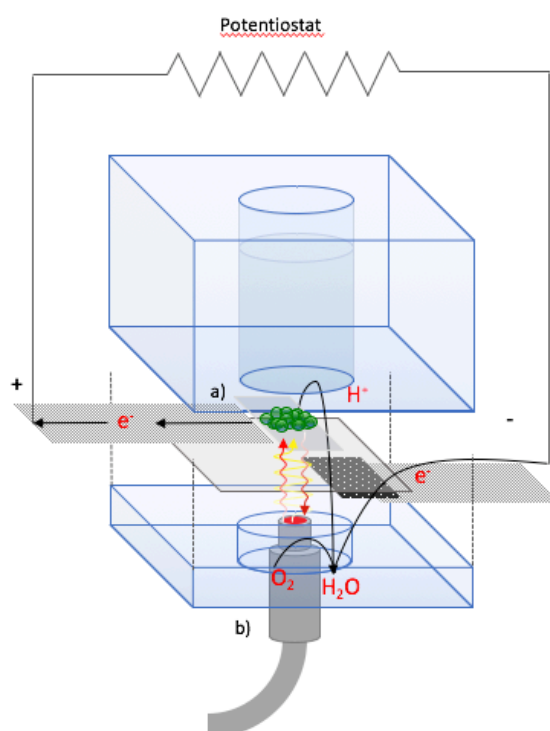


**Fig. 2.6:** Diagram of a BPV device adapted for simultaneous PAM fluorimetry measurements.

a) Cells form a biofilm on a transparent but impermeable ITO/PET anode covering only part of the anodic chamber base, with electrons transferred to the stainless steel mesh anode connector in contact with the conductive ITO surface. Protons pass over the side of the ITO/PET anode, through a dialysis membrane and Nafion® proton permeable membrane to the cathodic carbon-platinum side. b) The fibre optic cable of a Walz Mini PAM device sits in the cathodic chamber, against the underside of the transparent ITO/PET anode. Light can be delivered from above or below from the PAM device itself.

#### 2.3.4.6. Bioelectrochemical system set up as a microbial fuel cell:

The same Teflon® block design was used for MFC experiments using *R. palustris* without illumination and with the top anodic chamber sealed by adhesive assay plate covers to maintain as far as possible an anaerobic microenvironment at the biofilm (Fig. 2.7). 50 mM glycerol was provided as the carbon source for MFC experiments with *R. palustris*. Anode extension materials were placed on top of the marine grade stainless steel mesh anode connector and clamped in place. Each MFC device was inoculated with 4 ml of OD<sub>660</sub> 3.0 *R. palustris* culture and left for a period of time at room temperature for the cells to form an electroactive biofilm on the substrate.

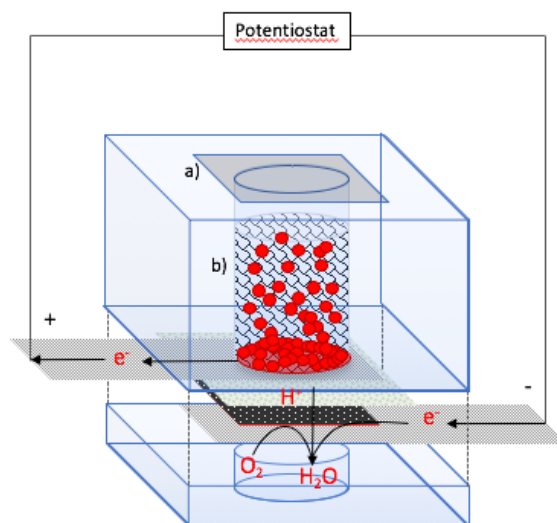


**Fig. 2.7:** Diagram of the MFC device based on the same basic design as the BPV device, but a) sealed and without light delivery, and b) with alternative anode materials inserted into the anodic chamber in electrical contact with the stainless steel mesh anode connector.

### **2.3.5. Graphene based electrodes:**

#### **2.3.5.1. Preparation of graphene based electrode materials:**

Graphene coated carbon foam, graphene based aerogels, and graphene coated stainless steel mesh were fabricated by Tian Carey and Dr. Felice Torrisi at the Cambridge Graphene Centre. To coat existing electrode materials a graphene ink was prepared, with graphene flakes produced by ultrasonication and centrifugation of graphite in IPA. 1% (v/v) of conductive polymer poly(3,4-ethylenedioxythiophene)-poly(styrenesulfonate) (PEDOT:PSS) (Sigma Aldrich) as a stabilization agent. Graphene coated carbon foam was created by drop-casting the ink onto carbon foam where the low surface tension of IPA helped infiltrate ink into the pores. Graphene coated stainless steel was created by vacuum filtering the IPA based ink through stainless steel mesh to deposit a layer of graphene flakes.

Graphene based aerogels were made from a second, water based, ink with 5  $\text{gl}^{-1}$  of the scaffold polymer carboxymethylcellulose (CMC). Graphene flakes from Cambridge Nanosystems (CNS), with average thickness of 5 nm and average width 1  $\mu\text{m}$ , were added at 10  $\text{gl}^{-1}$ , as well as PEDOT:PSS at 10 or 20% (v/v). To compare the effect of including graphene flakes and PEDOT:PSS with the CMC scaffold, inks were prepared containing CMC only, CMC + CNS graphene flakes, CMC + 10% (v/v) PEDOT:PSS, CMC + 20% (v/v) PEDOT:PSS, and CMC + 10% (v/v) PEDOT:PSS + CNS graphene flakes. Each water based ink was cast in molds, left overnight at  $-20^{\circ}\text{C}$  to freeze, and then placed in a vacuum freeze dryer. The crystallization and subsequent sublimation of water ice crystals resulted in the highly porous high surface area internal structure of the aerogels.

### 2.3.5.2. Dry mass change of graphene coated carbon foam with *R. palustris*:

Small sections of carbon foam and graphene coated carbon foam (c. 20 mg) were weighed on a Mettler A30 precision balance. Each sample was incubated with *R. palustris* OD<sub>660</sub> 3.0 for 4 days at 30°C, before extraction and gentle washing in de-ionized water to remove non-attached cells in suspension. Each sample was left 24 hours to dry in a 40°C cabinet, and dry weights were recorded.

### 2.3.6. Electrochemical characterization techniques:

Initial electrochemical characterization of bioelectrochemical systems was performed using a Metrohm® Autolab potentiostat. However, subsequent measurements beginning with the redesign of the Teflon® based BESs were done on more versatile MultiEmstat 4, 8, and 12 channel potentiostats. Data processing and analysis were done in Microsoft Excel. Biophotovoltaic devices were characterized by chronoamperometry, measuring changes in current due to illumination. When appropriate, the potential at the anode was set to a positive value to promote electron transfer to the anode and establishment of electrogenic biofilms (Wagner et al. 2010). The chronoamperometric light effect was quantified by integrating the area under the chronoamperometry trace during illumination, subtracting the area under the projected dark current trace during the same period, and normalizing to the light exposed surface area of the anode. As electrical current is the rate of flow of charge (coulombs):

$$I = Cs^{-1}$$

The total flow of charge per unit footprint area of electrode was quantified as charge density:

$$\frac{Cs^{-1} \times s}{m^2} = Cm^{-2}$$

Microbial fuel cell configurations containing *R. palustris* were characterized primarily using linear voltage sweeps and full cyclic voltammetry cycles. Linear sweep voltammetry recorded

current as the anode potential was altered from the negative open circuit potential of the device up to 0V. The plot of current (x-axis) vs voltage (y-axis) is the polarization curve, the slope of which gives an approximate measure of resistance *via* Ohm's Law:

$$V = IR$$

Subsequently a power curve is plotted with power (x-axis) normalized to anode area vs potential (y-axis) according to:

$$P = IV$$

where the apex of the curve maximum is the power per unit area or volume (Logan et al. 2006).

### **2.3.7. Glycerol concentration assay:**

To measure the changing concentration of glycerol due to consumption by *R. palustris* in microbial fuel cells, a colorimetric assay adapted from Pott et al. (2013). 50 µl of culture was extracted from each MFC by syringe for minimal biofilm disturbance and subjected to centrifugation at 10,000 rpm. The supernatant was removed and diluted 1:150 (13 µl of supernatant and 1.987 ml of minimal medium without glycerol) and 1.2 ml was added to 0.6 ml 10 mM sodium meta-periodate (Sigma-Aldrich), prepared in 1.6 M acetic acid and 4.0 M ammonium acetate. After 30 seconds shaking 0.6 ml of 0.2 M acetylacetone was added, also prepared in 1.6 M acetic acid and 4.0 M ammonium acetate, and incubated at 70°C for 1 minute before immediate cooling in room temperature water to quench further reaction. Absorbance was recorded at 410 nm on a Shimadzu UV-VIS1800 spectrophotometer and converted to concentration of glycerol based on a standard curve recorded alongside and in the same conditions as each assay.

### **2.3.8. Scanning electron microscopy:**

Anodic materials were prepared for scanning electron microscopy (SEM) with the help of Dr. James MacMillan, after extraction from the MFC by dab drying to remove excess medium and sticking to the SEM sample mount with double sided tape. After fixing in liquid ethane, and mounting on a liquid nitrogen cooled brass plate the samples were left for overnight to freeze dry in a vacuum pump dryer before coating with 16 nm layer of iridium in a sputter coater. Coated samples were stored in silica dried sealed containers. Imaging of samples was done using an FEI Verios 460 scanning electron microscope at the Cambridge Advanced Imaging Centre in the Department of Physiology, Development and Neuroscience.

### **2.3.9. Pulse amplitude modulation (PAM) fluorescence measurements:**

PAM measurements to determine fluorescent kinetic patterns were performed using a Walz Mini PAM© Portable Chlorophyll Fluorometer. Fluorescence was measured by excitation with a pulse modulated red LED with pulse-width of 3  $\mu\text{s}$  and pulse frequency of 20 kHz. A cut-off filter (Balzers DT Cyan, special) gave an excitation band peaking at 650 nm and fluorescence was detected by a PIN-photodiode at 700 nm and longer. Samples were subject to 'induction' curves with varying actinic light components, consisting of an initial saturating pulse after dark adaptation, followed by 2 minutes recovery period in the dark, then 13 minutes exposure to a fixed actinic light level with further saturating pulses every minute. Saturating pulses were set to 4450  $\mu\text{mol photons m}^{-2} \text{s}^{-1}$  and actinic light intensities equivalent to 54, 208, and 714  $\mu\text{mol photons m}^{-2} \text{s}^{-1}$  were used. 'Light' curves followed a similar pattern with an initial saturating pulse followed by actinic light with a series of further saturating pulses, except the actinic light intensity increased between each saturating pulse.

$F_0$  is defined as the minimal dark adapted fluorescence level when all PSII reaction centres are open, i.e. the primary quinone  $Q_A$  is in its oxidised state,  $F_M$  is the maximum fluorescence recorded during a saturating pulse on a dark adapted sample,  $F$  is the light adapted steady state fluorescence, dependent on the fraction of reduced  $Q_A$ , and  $F_M'$  is the maximum fluorescence from a saturating pulse on a light adapted sample (Campbell et al. 1998). The quantum efficiency  $Y(II)$  can be calculated as the variable fluorescence  $F_V$  ( $F_M - F_0$ ) divided by  $F_M$ :

$$Y(II) = \frac{F_V}{F_M} = \frac{F_M - F_0}{F_M}$$

The fractions of absorbed energy dissipated *via* unregulated heat and fluorescence,  $Y(NO)$ , or by regulated non-photochemical quenching mechanisms,  $Y(NPQ)$ , can be estimated by:

$$Y(NO) = \frac{F_0}{F_M}$$

$$Y(NPQ) = 1 - Y(NO) - Y(II)$$

An objective quantification in arbitrary units of non-photochemical quenching of PSII during actinic light exposure can be estimated by:

$$NPQ = \frac{F_M - F_M'}{F_M'}$$

### **3. OPTIMIZING BIOPHOTOVOLTAIC DEVICE DESIGN AND INVESTIGATING LIGHT ABSORPTION LIMITATIONS ON BIOPHOTOVOLTAIC CURRENT OUTPUT IN *SYNECHOCYSTIS***

#### **3.1. Introduction:**

##### **3.1.1. Transduction of light energy to electrical current: Optimizing biophotovoltaic devices:**

Like MFCs, BPV devices exploit microorganisms capable of EET to generate power from the difference in potential between electrons donated to the working electrode in the anodic compartment and the redox potential of the counter electrode in the cathodic compartment (McCormick et al. 2015). Unlike MFCs, BPV devices require no external carbon source as all electrons ultimately derive from photosynthetic splitting of water (Bombelli et al. 2011). Various forms of microbial conversion of light energy to electricity have been demonstrated over the years, from consumption of photosynthetically grown cyanobacterial biomass by electrogenic purple non-sulphur bacteria (Inglesby et al. 2012b), to products of carbon fixation by plants being metabolised by soil bacteria in the vicinity of a buried anode (Bombelli et al. 2016; Strik et al. 2011), to isolated photosystems located directly on an anode (Mershin et al. 2012). Whole cell devices using cultures of photosynthetic microorganisms have proved reliable and easily tractable systems for understanding biophotovoltaic devices (Tsujimura et al. 2001). The photosynthetic microorganisms in the BPV produce a current in the dark from fixed carbon stores derived from photosynthesis. However, when illuminated, some photosynthetic microorganisms produce an additional light dependent ‘photocurrent’ (Pisciotta et al. 2010). The magnitude of the photocurrent depends on the redox state of the cell and the intrinsic need to export electrons to support metabolism or reduce oxidative stress in response

to light, on the mechanisms for transmembrane electron transport, design and illumination configuration of the BPV device itself, and the cell to anode material interaction. Cells suspended in liquid culture can reduce the anode via indirect extracellular electron transfer (IEET), mediated by an externally added soluble electron carrier such as potassium hexacyanoferrate(III) ( $K_3[Fe(CN)_6]$ , hereafter ferricyanide) and potassium hexacyanoferrate(II) ( $K_4[Fe(CN)_6]$ , hereafter ferrocyanide) (Bombelli et al. 2011), or a naturally produced mediator such as phenazine (Rasmussen & Minteer 2014). Use of an externally added soluble electron carrier makes scaling up unfavourable, so recently more attention has been given to biofilms of photosynthetic microorganisms generating photocurrent by directly reducing the anode *via* direct extracellular electron transfer (DEET) (McCormick et al. 2011; Ng et al. 2014).

### **3.1.2. Characterizing biofilm based BPVs:**

Biofilms have proved key to increasing power densities from microbial fuel cells (Reguera et al. 2006), and higher BPV power densities have been obtained from DEET, circumventing the mass transport limitations of electron carrier diffusion (McCormick et al. 2011; Pisciotta et al. 2010). Mechanisms for DEET from most photosynthetic microorganisms remain elusive, although a number of pathways may be involved, potentially mediated by membrane bound multi heme *c*-type cytochromes and conductive type IV pili, or nanofilaments, commonly found in anaerobic iron and sulfur reducing bacteria (Alves et al. 2015; Venkidusamy et al. 2015). Amongst photosynthetic organisms, electrically conductive nanowires between 10-20 nm in width have been observed in biofilms of the cyanobacterium *Synechocystis* sp. PCC6803 when cells were cultured under CO<sub>2</sub> limited (100 ppm) conditions (Gorby et al. 2009). However, neither the composition of the nanowires nor their possible role in electron export was investigated, so the precise DEET mechanism in *Synechocystis* remains elusive. However,

PilA, a major subunit of type IV pili in *Synechocystis*, has been suggested to have a role in reduction of extracellular iron oxide compounds. With electrons transferred directly from the cell to the anode, electrochemical techniques such as cyclic voltammetry can investigate the relationship of photocurrent to the oxidation potential of DEET mechanisms. Another important question is the relationship of current to photosynthetic efficiency of BPV biofilms, especially under high light stress (Ciniciato et al. 2016; Touloupakis et al. 2015). Combining fluorescence and bioelectrochemical measurements may provide new insights and more comprehensive characterization of the relationship between photosynthetic biology and electrical output.

### **3.1.3. Light harvesting attenuation as a means to improve productivity and photosynthetic efficiency:**

The maximum potential efficiency of a BPV device is ultimately limited by its ability to absorb light energy, a key factor which is crucial to device and organism design and engineering that does not apply in MFCs. Cells in a biofilm experience steep gradients in light intensity and resulting photosynthetic efficiency throughout the layer (Al-najjar 2014). The topmost layers of cells in a biofilm can rapidly become light saturated, leading to photoinhibition of photosystem II (PSII), and production of reactive oxygen species (ROS) that cause lipid peroxidation and damage to nucleic acids and proteins (Blokhina 2003; Mussgnug et al. 2007; Beckmann et al. 2009). ROS production due to excess light absorption may affect BPV output not just by damage, but as a potent cellular signal of light levels that is likely to be closely tied with regulation of non-photochemical quenching (NPQ) mechanisms (Foyer et al. 2017). The light penetration path length into a culture or biofilm is thus closely tied to the total photosynthetic efficiency (Al-Najjar et al. 2012; Ritchie & Larkum 2012), which is optimal where photochemistry is maximised and fluorescence and NPQ are minimal (Blankenship et

al. 2011). In cyanobacterial dominated microbial mats the photosynthetic efficiency is almost fully attenuated by a depth of 1 mm (Al-najjar 2014), and in an industrial context excessive light harvesting and dissipation at the surface and excessive shading of cells at lower depths may reduce overall productivity in photobioreactors (Scott et al. 2010; Melis 2009; Ritchie & Larkum 2012). A potential strategy to increase overall efficiency from photosynthetic microorganisms, and therefore productivity or BPV output, is to reduce the light absorbance of individual cells by truncating the light harvesting antenna (Fig. 1). In theory this should limit photoinhibition and energy dissipation in the upper layers and facilitate deeper light penetration (Melis 2009). Table 3.1 summarizes previous work demonstrating that light attenuation of cyanobacteria and microalgae can improve productivity and photosynthetic efficiency, although in practice this may only happen under certain conditions, such as carbon limitation (Lea-Smith et al. 2014).

**Table 3.1: Examples of light harvesting attenuation for productivity gains:**

Species	Modified strain	Intervention	Effect on productivity	Authors
<i>Chlorella vulgaris</i>	E5	Random mutant generation for reduced LHC size and Chlorophyll content	44.5% improvement in biomass productivity at 200 $\mu\text{E}$ , higher light saturation intensity, and lower NPQ.	Shin <i>et al.</i> , 2016
<i>Chlamydomonas reinhardtii</i>	Stm3LR3	RNAi downregulation of LHC I and II proteins	Increased photosynthetic quantum yield and productivity at 1000 $\mu\text{E}$ and reduced photoinhibition at 1400 $\mu\text{E}$	Mussgnug <i>et al.</i> , 2007
“	Stm6Glc4T7	Constitutive expression of LHC translation repressor NAB1	~50% improved mid log growth phase at 700 $\mu\text{E}$ and increased quantum yield at 850 $\mu\text{E}$	Beckmann <i>et al.</i> , 2009
“	TLA3	Disruption of LHC assembly and thylakoid integration	Two-fold increase in photosynthetic productivity and increase in half saturation intensity from 200 to 600 $\mu\text{E}$ .	Kirst <i>et al.</i> , 2012
<i>Synechocystis</i> sp. PCC6803	$\Delta cpc$ (olive)	Deletion of gene encoding phycocyanin synthesis	Increased rate of $\text{O}_2$ evolution at 400 $\mu\text{E}$ and higher growth rates at 100 $\mu\text{E}$	Kwon <i>et al.</i> , 2013
“	$\Delta apcE$ mutant	Deletion of gene encoding phycobilisome anchor protein	1.6-fold increase in biomass production and 2.2-fold increase in glycogen accumulation at 50 to 200 $\mu\text{E}$	Joseph <i>et al.</i> , 2014
“	$\Delta cpcC1C2:p_{cpc}T \rightarrow C$ and olive	Removal of two, and all three phycocyanin discs	Increased cell densities and rates of oxygen evolution under carbon limitation at 1000 $\mu\text{E}$	Lea-Smith <i>et al.</i> , 2014
“	$\Delta cpc$ (olive)	Deletion of gene encoding phycocyanin synthesis	Increased productivity at low to medium light intensities and 1.57-fold increase in biomass accumulation under high density at 2000 $\mu\text{E}$	Kirst <i>et al.</i> , 2014
“	CB, CK (olive), and PAL	Removal of two and all three phycocyanin discs, and whole phycobilisome	Reduction in growth rate at 150 $\mu\text{E}$	Page <i>et al.</i> , 2012

### 3.1.4. PBS antenna truncation mutants:

PBSs play a key role in cyanobacterial photosynthesis (Kwon et al. 2013), associating with PSI and PSII to increase the cross-sectional area and spectral range of light absorption. In *Synechocystis* the PBS consists of a tricylindrical allophycocyanin (APC) core ( $\lambda_{\max} = 652$  nm) with six cylindrical antenna rods radiating perpendicularly from the APC core, each rod being composed of a stack of three phycocyanin (PC) discs, ( $\lambda_{\max} = 620$  nm) (Cooley & Vermaas 2001; Arteni et al. 2009). Each PC disc is composed of six heterodimers of phycocyanin- $\alpha$  (CpcA) and phycocyanin- $\beta$  (CpcB). The core-proximal disc is connected to the middle disk by linker protein CpcC1, and the middle disk to the distal disk by linker protein CpcC2 (Kirst et al. 2014). A series of mutant strains were made by Lea-Smith et al. (2014):  $p_{cpc}T \rightarrow C$ ,  $\Delta CpcC1C2:p_{cpc}T \rightarrow C$ , and  $\Delta Cpc$  (olive), which lack one, two and all three PC discs, respectively (Fig. 3.1).  $p_{cpc}T \rightarrow C$  has a T  $\rightarrow$  C substitution in the *cpc* operon promoter that has been shown to downregulate activity and remove free PC (when linkers are also missing) as well as on average one PC disk from the PBS antennae.  $\Delta CpcC1C2:p_{cpc}T \rightarrow C$  contains the downregulated *cpc* promoter as well as having the CpcC1 and CpcC2 PC disk linker proteins removed, so that only one PC disk remains attached to the AC core. The  $\Delta Cpc$  mutant, hereafter the ‘olive’ mutant due to its colour phenotype, contains a deletion of the Cpc operon, and expresses no PC at all, leaving the PBS as just the bare AC core. These mutants have not previously been tested in a BPV device; we might predict that reduced light absorbance leads to increased power output, although removal of PC also has more complex knock on effects on cell physiology (Liberton et al. 2017).

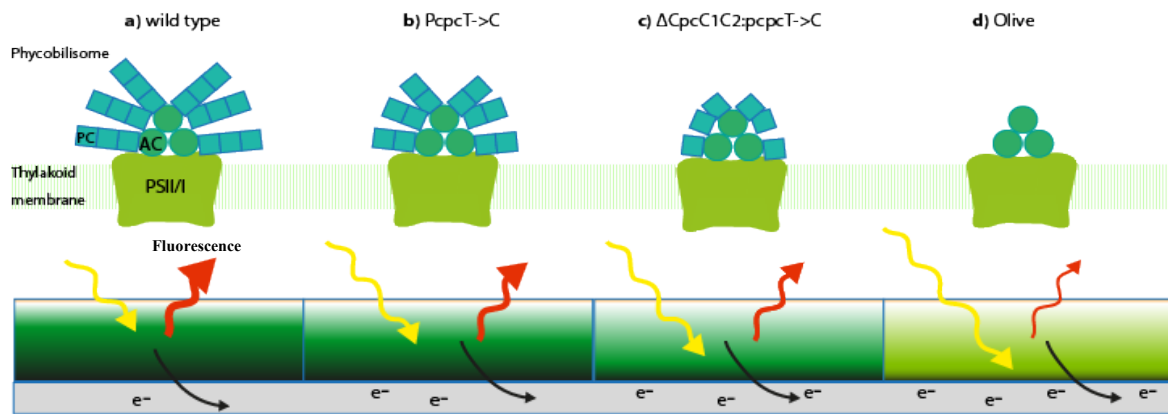


**Fig. 3.1:** Diagram showing the principle of increased light penetration (yellow arrow) through a biofilm increasing the overall production of electricity. a) The phycobilisome (PBS) of *Synechocystis* consists of an allophycocyanin core (AC) with six radial phycocyanin (PC) antennae that capture light energy and channel it to PSII or PSI. b-d) Reduction of PBS antennae is expected to reduce shading and energy dissipation from excess absorbance (red arrow), increasing depth of light penetration and the overall excitation of the biofilm.

In this chapter we aim to characterize improvements in the BPV device design, comparing the use of suspended cell culture with an electron carrier in the anodic chamber to a biofilm in direct contact with the anode, and the effect of altering cellular light absorption by truncating the PBS. The role of pili in electrogenic biofilms of *Synechocystis* is explored with SEM imaging and a pili deficient strain. A series of mutant stains deficient in varying numbers of PC discs in the PBS antennae are characterised in the BPV device with the optimized biofilm protocol. PBS truncation is found to increase BPV output at low to medium light intensities relative to the wild type.

## **3.2. Results:**

### **3.2.1. Biophotovoltaic activity from *Synechocystis* sp. PCC 6803:**

Using the model cyanobacterium *Synechocystis* sp. PCC6803 we began by comparing the performance of mediator-free anodic biofilms with planktonic cultures containing an electron carrier. Several BPV device configurations were designed and constructed with the aim of measuring differences in bioelectrochemical output from a range of *Synechocystis* mutants.

#### **3.2.1.1. Initial biophotovoltaic current results:**

The initial design (Methods Fig. 2.3) used a 25 ml acrylic pot as the anode chamber, with cells suspended IN BG11 MEDIA by mixing with a magnetic stirrer, and ferricyanide supplemented as an electron carrier between planktonic cells and the transparent ITO/PET anode, sourced from Sigma Aldrich. Fig 3.2 shows the current from wild type *Synechocystis* at 2.5 nmol Chl ml<sup>-1</sup> density, and the effect on the current of illumination at 200 μmol photons m<sup>-2</sup> s<sup>-1</sup> in the yellow shaded area. The initial rapid increase is likely to be due to the electron carrier pool consisting entirely of the oxidised form, ferricyanide, rapidly becoming reduced to ferrocyanide by cells as the BPV anode chamber is stirred, and diffusing to the anode to be oxidised back to ferricyanide. After the maximum rate of reduction at the anode, the diffusion of ferricyanide back to cells and ferrocyanide to the anode slowly tends towards an equilibrium, reached when the current stabilizes at a constant level. This discharge effect may also be contributed to by built up charge in cells being lost. The cylindrical pot design took a long time for current to stabilise before a light effect could be reliably measured, severely limiting the throughput of experiments possible.

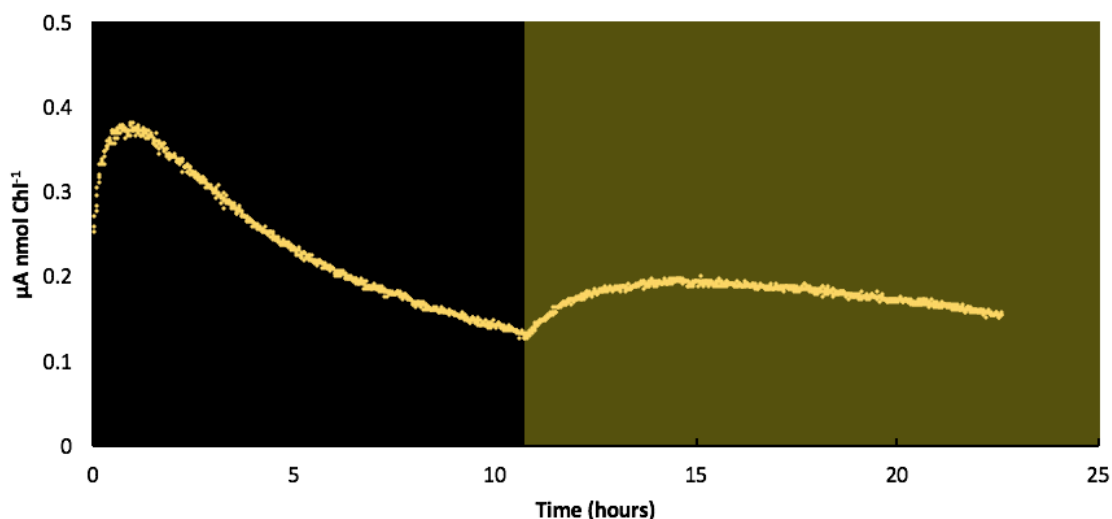


**Fig. 3.2:** Chronoamperometric output from wild type *Synechocystis* in the early configuration cylindrical pot BPV design with ferricyanide as an electron carrier and illumination at 200  $\mu\text{mol photons m}^{-2} \text{s}^{-1}$ . The trace is an average of 3 biological replicates.

### 3.2.1.2. Biophotovoltaic current from revised device design:

This initial design was satisfactory for single BPV experiments, but problems with leaking and the fragility of the platinum coated carbon paper cathodic catalyst meant a redesign was needed to improve robustness and reliability. Light delivery was also limited by the design to around 200  $\mu\text{mol photons m}^{-2} \text{s}^{-1}$ , which although cited as sufficient to saturate photosynthesis for this organism (McCormick et al. 2013), is far below the intensity of full sunlight and the maximum intensity for a BPV device. A significant step forward in designing a robust device for reliable and frequent reuse was taken by using Teflon® blocks as the main body of design (Methods figure 2.4), with a smaller 4 ml chamber machined into the centre. Instead of having the electrodes diametrically opposite each other, as in the previous design, a layered ‘sandwich’ approach was used, stacking all the electrode elements in one plane at the base of the chamber that could be clamped between two of the blocks. The stacked electrode materials were quicker to assemble and resulted in less wear and tear, proving more economical on material use and

more reliable. Using 4 mm bolts to clamp the electrode stack tightly together between two of the blocks prevented leaking, an improvement over the finer screws used to seal the Perspex pot, which were liable to stripping the thread. Aside from construction advantages the redesign allowed higher light intensities up to  $2000 \mu\text{mol photons m}^{-2} \text{s}^{-1}$  to be tested. Current stabilisation was slightly faster, although the mode of operation was essentially the same as the initial pot design, mounted on a stirring block with a small stirrer to keep cells in suspension and aid diffusion of ferricyanide as an electron carrier. BPV response, i.e. the rate of current increase in response to light, was still slow, and even with light exposure periods of 2-3.5 hours a stable plateau was not reached. At higher light intensities long exposure risked damaging cells and affecting subsequent tests. This meant the device was still severely limited in terms of the throughput required measure multiple replicates of different strains.

### 3.2.3.3. Effect of biofilm vs suspended culture in anodic chamber on BPV output:

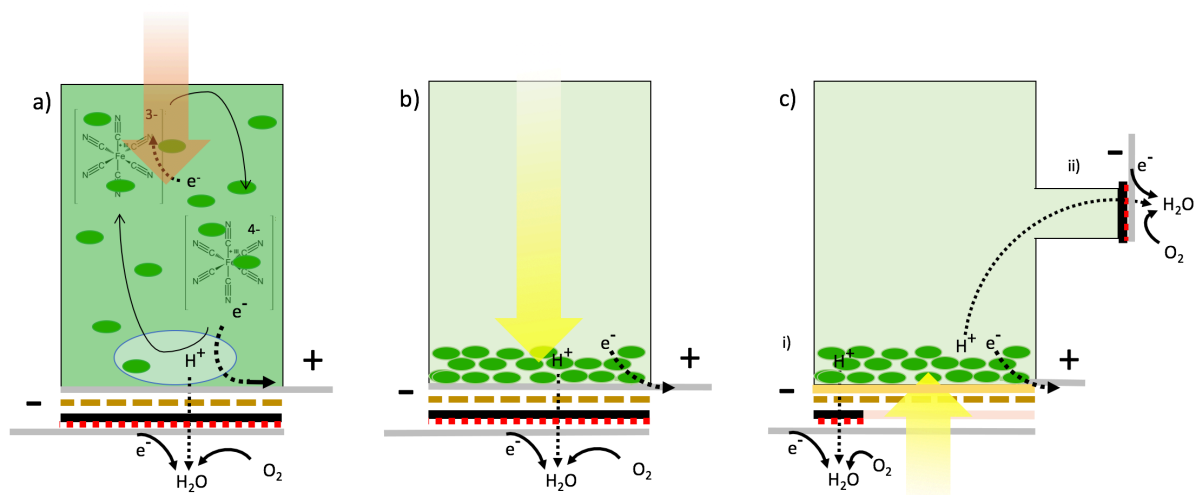


**Fig. 3.3:** Diagram of cell distribution and electron transfer in BPV devices with a) cells in suspension with the soluble electron shuttle ferricyanide, b) cells in a biofilm with light delivered from above, and c) a third option with light delivered from below and the opaque carbon/platinum air cathode either i) reduced in size to allow light through the transparent electrode stack, or ii) in a separate port to one side.

The revised BPV device design with the electrodes stacked at the base of the vertical anode chamber allowed operation of devices without stirring and without a soluble electron carrier (Fig. 3.3). The performance of a device with cells in suspension was compared with one with cells that had been allowed to settle form a biofilm attached to the anode (Methods figure 2.5b). A dramatic difference in BPV response characteristics was seen (Fig. 3.4). The rate of increase of current during illumination was up to 100-fold greater than for a suspended culture (Fig. 3.4c), reaching a plateau of photocurrent within seconds or minutes. In the example comparison from Fig. 3.4a, b this allowed eight light intensities to be tested within a period of 2.8 hours with a biofilm, compared to 4 light intensities over 28 hours for a suspended culture. The shorter, ten minute, illumination period also reduced the risk of photodamage at high light intensity. More than one hour illumination of biofilms of *Synechocystis* was observed to cause bleaching of the cells. The overall current was lower when cells were allowed to settle as a biofilm on the anode compared to cells in suspension with ferricyanide, even though the anode chamber was inoculated with the same total cell concentration. The lower current may be due to a smaller proportion of cells being able to contribute to direct extracellular electron transfer to the anode. By contrast, ferricyanide as a soluble electron carrier would theoretically be able to diffuse to the membrane of every cell in the anodic chamber. In addition, although light penetration would be attenuated in liquid culture (Lea-Smith et al. 2014), scattering between cells should homogenise light distribution to an extent. In a biofilm, by contrast, nearly all light would be absorbed, meaning the deeper layers would not be receiving light.

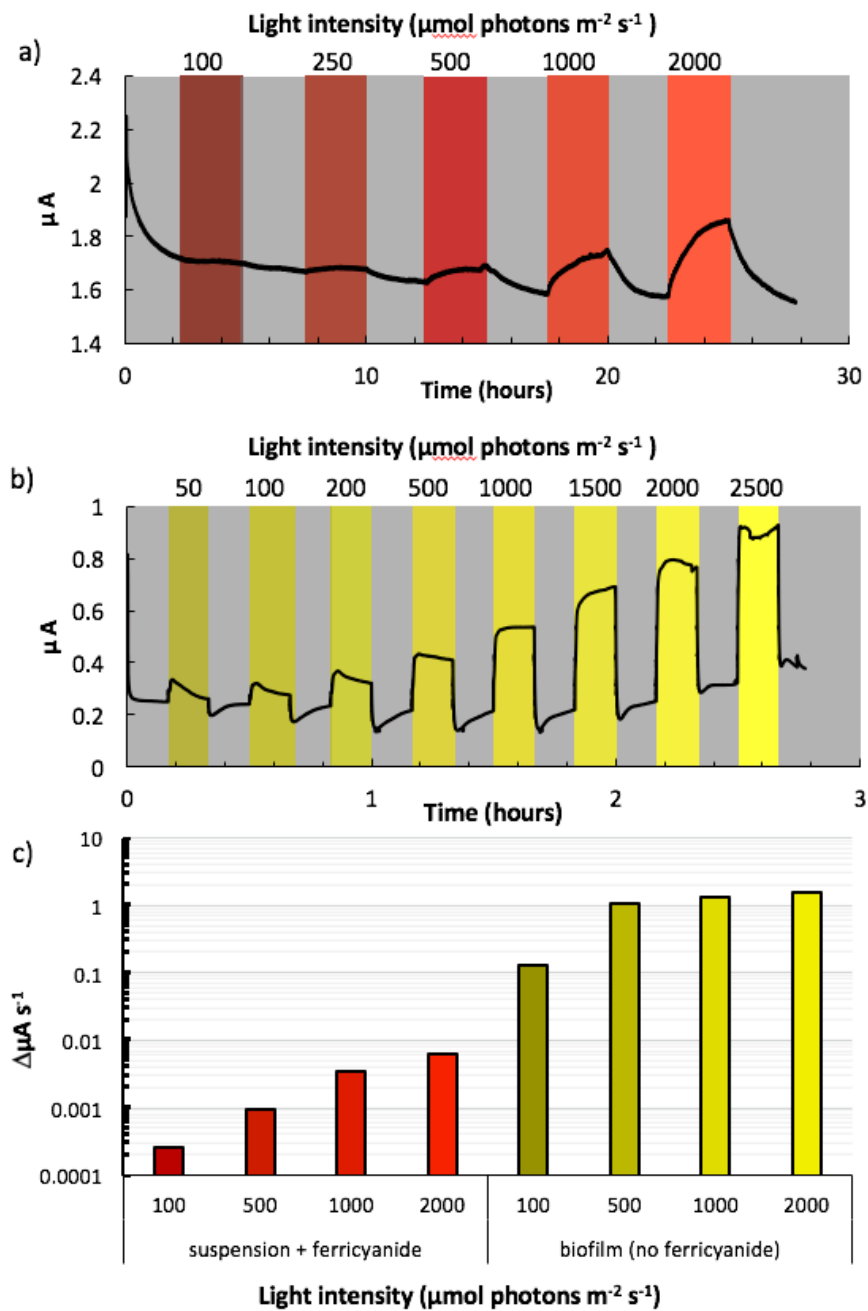


**Fig. 3.4:** Direct vs indirect extracellular electron transfer in from *Synechocystis*. a) Chronoamperometric trace of wild type *Synechocystis* in suspension with ferricyanide showing 5 cycles of current response to illumination under red light (635 nm) and recovery in the dark over 28 hours. b) Chronoamperometric trace of wild type *Synechocystis* in a biofilm with no electron carrier, showing 8 cycles of current response to illumination under warm white LED light over 2.8 hours. c) A semi-logarithmic plot of the rate of change of current during the

initial linear spike light response comparing the reaction to four light intensities from suspended cells and cells in a biofilm.

Using carbon/platinum coated Nafion® as an air cathode provided a reliable proton exchange membrane that could withstand repeated dismantling and reassembling of the BPV device, However, the carbon/platinum catalytic coating on the side facing the cathodic chamber was opaque so light could only be delivered from the top. To circumvent the problem of light attenuation by absorption in the upper layer of the biofilm, a transparent ITO/PET anode could be used with either an air cathode channel drilled laterally into the Teflon® block or a section of Nafion® only partially coated with catalyst could be used. This configuration also allowed the insertion of the fibre optic cable from a PAM fluorimeter directly adjacent to the *Synechocystis* biofilm on the anode (Methods figure 2.6).

#### **3.2.1.4. Fast biofilm – biophotovoltaic polarization light responses:**

To test the dynamics of the photocurrent response to light we exposed biofilms in BPV devices to a series of periods of illumination at a range of light intensities. Fig. 3.5a,b) shows example chronoamperometry traces from two BPV devices set up using the same protocol with wild type *Synechocystis*. The first device (Fig. 3.5a) displayed a simple, rapid increase in the current in response to light, which stabilised at a new level (similar to Fig. 3.4b), reaching a stable plateau in under 1 minute. The photocurrent from a separate device set up in the same way with the same cells shown in Fig. 3.5b was more complex, with different elements apparent at different light intensities. Fig. 3.5c shows the first few minutes, or initial light response, of Fig. 3.5b in more detail. There was an initial peak in the first 5 seconds after lights were turned on that increased in height at higher light, followed by a dip at 10-20 seconds that was apparent even at the lowest light intensity, and a second peak around 30-60 seconds that increased in

height with higher light, before return to a stable current output that was only higher than the dark current under at  $2350 \mu\text{mol photons m}^{-2} \text{s}^{-1}$  and above. Turning the lights off resulted in a rapid decrease in current before it recovered slowly to pre-illumination levels. These results confirm the photocurrent dynamics in response to illumination from cells in a biofilm were not only far faster than for cells in suspension, but also suggests that in some cases the current shape may reflect factors such as the mechanisms of electron export from the cell and redox state as influenced by the metabolic state of the cell at the time of the experiment.

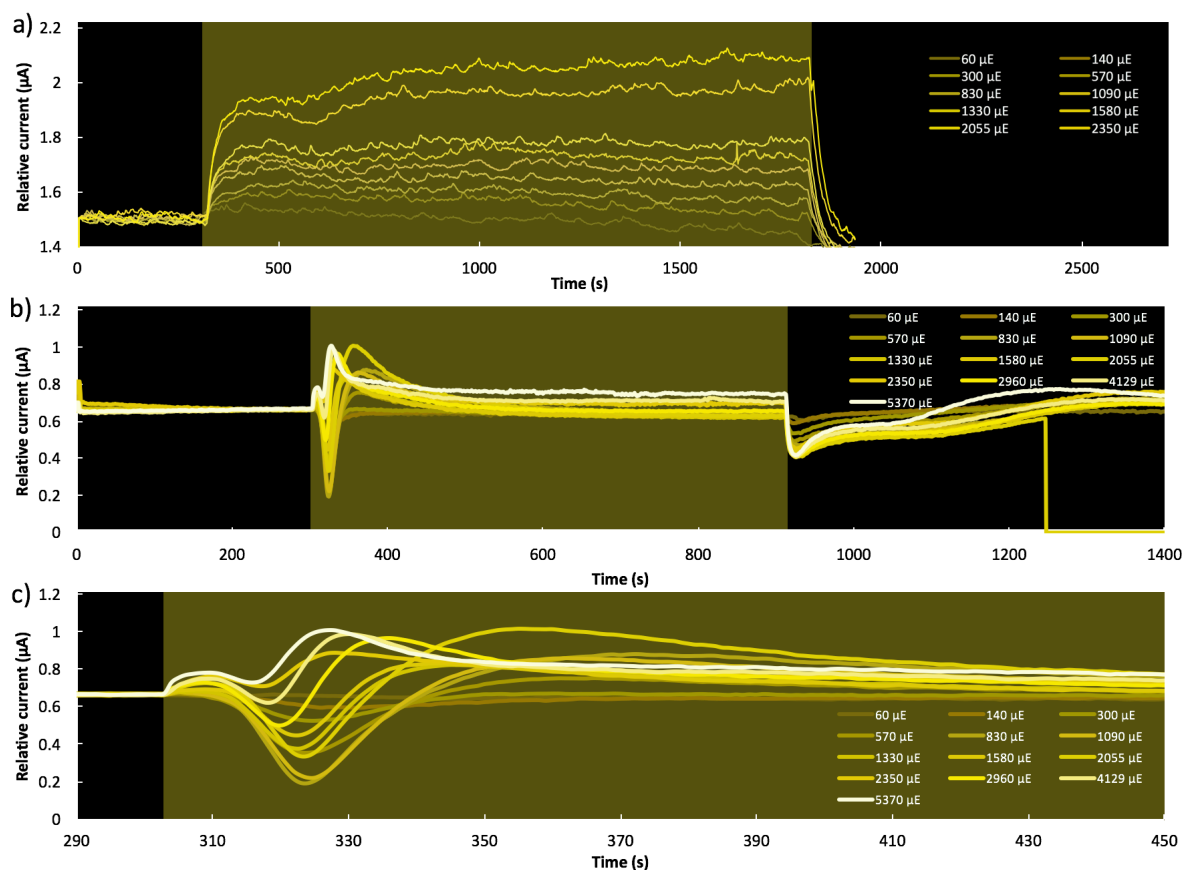


**Fig. 3.5:** Chronoamperometric traces BPV photoeffect from *Synechocystis* biofilms. Traces are normalized to show the current relative to just before illumination, from wild type *Synechocystis* in biofilms with light delivered from above normalised to the current just before illumination, showing a) a consistent increase in current with increasing light intensities, and

b) a more complex photocurrent response. Panel c) shows the initial illumination response magnified from b).

Fig. 3.6 shows the chronoamperometry profile at each light intensity from Figure 3.5c independently. The light response can be broken down into several elements, as described for Figure 3.5c. The initial spike, whose magnitude depended on light intensity, appeared in the first 5 to 10 seconds. This was followed by a significant dip in current to below pre-illumination dark current levels that was apparent even at the lowest light intensity of  $60 \mu\text{mol photons m}^{-2} \text{ s}^{-1}$ , with the biggest decrease at medium light intensity of  $570 \mu\text{mol photons m}^{-2} \text{ s}^{-1}$ . The effect of this drop was cancelled out by a secondary light dependent spike between 15 and 40 seconds after the lights were turned on. The second spike in current increased in magnitude with light intensity. After this peak current decreased to a stable output level. The latter level did not exceed the pre-illumination dark current level until extreme high light intensities were reached at 4130 and 5370  $\mu\text{mol photons m}^{-2} \text{ s}^{-1}$ . When the light was switched off the current rapidly decreased for around 10 seconds, even at after illumination at just  $60 \mu\text{mol photons m}^{-2} \text{ s}^{-1}$ , reaching a lower value the higher the light intensity. After lower light intensities the dark current recovered in a linear fashion, however after light intensities above 1000  $\mu\text{mol photons m}^{-2} \text{ s}^{-1}$  the dark current reached a brief plateau that was lower than the pre-illumination dark current before increasing again to reach a pre-illumination levels. In subsequent BPV testing of mutant strains there were distinct chronoamperometric light response shapes including the two above. There was no obvious correlation between photocurrent shape and strain of *Synechocystis*, although further work to deconstruct the different elements and the conditions that make them appear could increase the scope of BPV systems as tools to probe the underlying cell biology. These kinds of chronoamperometric responses suggest that there are factors involved in the behaviour of an electroactive biofilm of *Synechocystis* that are at present

poorly understood, and have not been widely discussed in the literature. Cereda et al. (2014) showed a similar current profile in their biophotovoltaic characterization of *Synechocystis*, but did not discuss the origin of the initial current spikes, and Zhang et al. (2017) suggest the spikes may be caused by an action potential like effect.

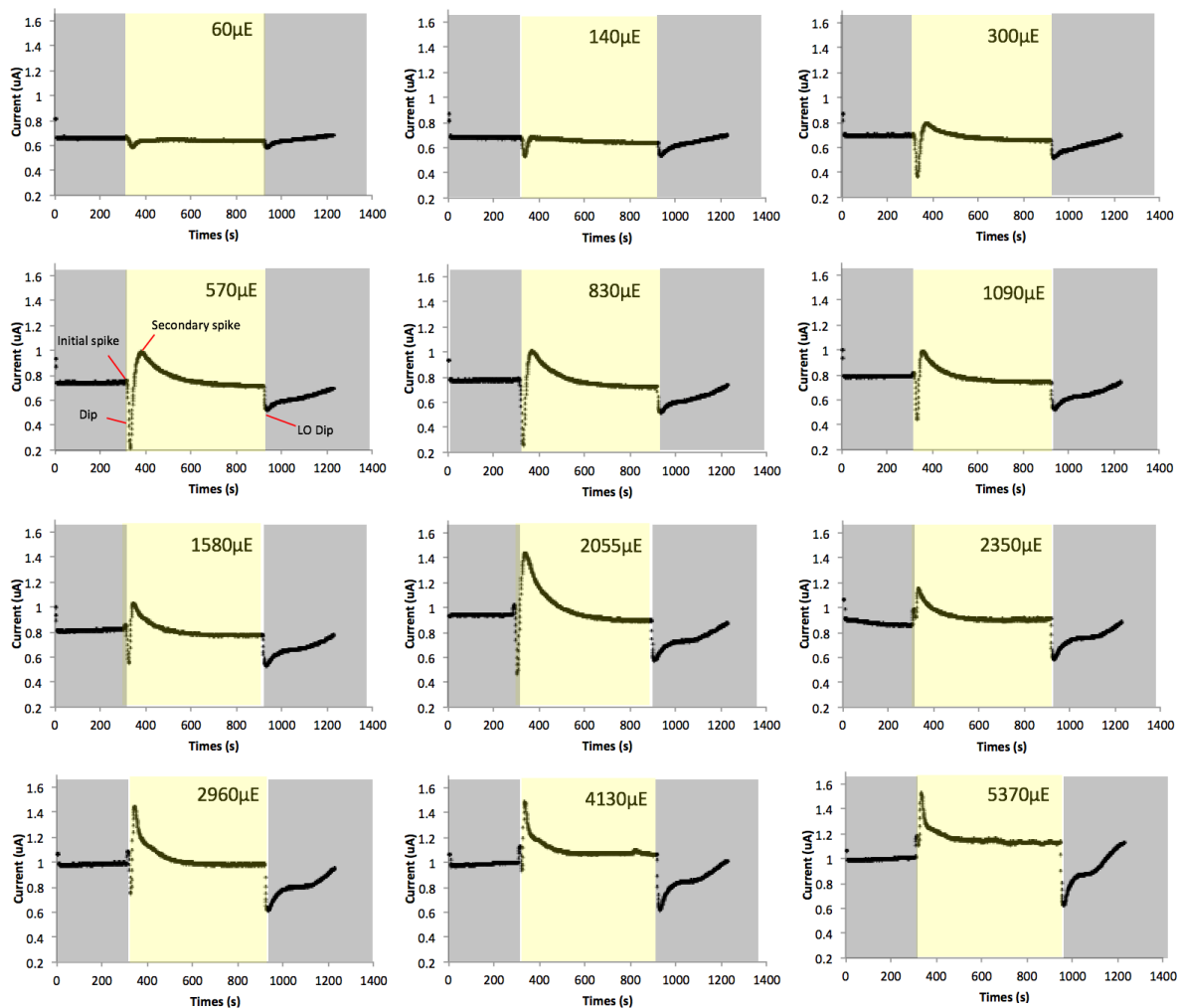


**Fig. 3.6:** Alternative representation of chronoamperometric BPV photoeffect from wild type *Synechocystis* from Figure 3.5b displaying each light intensity separately. Light intensity is displayed in  $\mu\text{mol photons m}^{-2} \text{s}^{-1}$ , abbreviated to  $\mu\text{E}$ . The panel showing the response to 570  $\mu\text{E}$  has the initial spike, current dip, secondary spike and lights off dip (LO Dip) labelled with arrows.

### 3.2.1.5. Cyclic voltammetry of electroactive *Synechocystis* biofilms:

To test the bioelectrochemical interaction of the *Synechocystis* biofilms with the anode, cyclic voltammetry (CV) was performed. In the complex cellular environment there could be multiple pathways involved in electron transfer including electrically conductive pili, outer membrane cytochromes, and soluble electron carriers (McCormick et al. 2015). By sweeping the anode potential back and forth between two potentials, peaks in current can be observed when electron transfer is being facilitated. Depending on the direction of potential change, i.e. negative to positive or positive to negative, CV peaks can reveal the oxidation and reduction potentials of mechanisms involved in EET (Fricke et al. 2008). CV was performed as a secondary measurement to chronoamperometric experiments, revealing striking peaks. However these served mainly to verify occurrence of bioelectrochemical interaction, and were not quantified for comparison. Fig. 3.7 shows a representative CV trace from *Synechocystis* taken at a scan rate of  $1 \text{ mV s}^{-1}$ . Although there was significant variability, the strong oxidation peak clearly visible at 0.2 V was observed in nearly all CV traces of *Synechocystis*. Two small reduction peaks are also visible at -0.03 V and 0.11 V, one of which may be the reduction pair of the 0.2 V peak, and the presence of the other revealing another EET mechanism is potentially masked by the 0.2 V oxidation peak. The EET pathway in *Synechocystis* remains unknown, but the 0.2 V peak is in the oxidation potential range for many types of cytochrome, and so would be a prime target for future studies aimed at uncovering the mechanisms of electron transfer (Kracke et al. 2015).

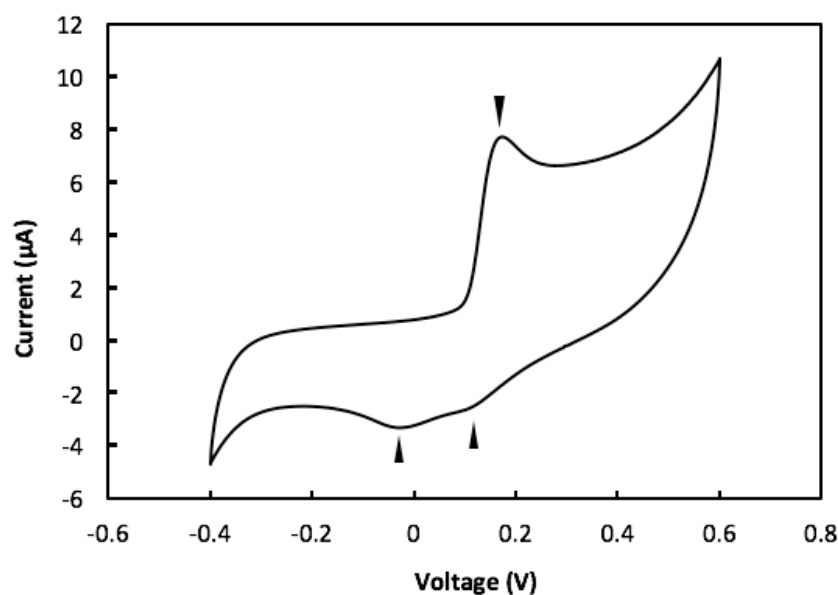


**Fig. 3.7:** Representative cyclic voltammogram from an electroactive photosynthetic biofilm of *Synechocystis* on an ITO anode substrate between -0.4 V and 0.6 V. Arrows show oxidation and reduction peaks, the potential sweep speed was  $1 \text{ mV s}^{-1}$ .

### 3.2.2. Imaging of *Synechocystis* pili in biofilms on ITO with SEM:

To visualize the structure of the biofilm and investigate the presence of structures that might be able to mediate EET, such as pili, the flat ITO/PET anodes were extracted from a BPV device and prepared for SEM imaging. Before extraction of the anode for SEM the biofilm was lit from below with  $200 \text{ } \mu\text{mol photons m}^{-2} \text{ s}^{-1}$  in the configuration illustrated in Fig. 3.3c, i), with the electrode bias potential set to 0.2 V for 48 hours. SEM of *Synechocystis* biofilms on ITO/PET anodes revealed structures resembling pili (Fig. 3.8) as described in the literature with the function of adhesion and phototaxis (Nakane & Nishizaka 2017). Pili (or fimbriae) like appendages could also be seen connecting cells to other cells, and were particularly abundant connecting cells to the ITO surface. *Synechocystis* performs phototaxis by synthesis and retraction of pili in the incident light direction, and blue light in particular has been shown to stimulate phototaxis. In the BPV lit from below, pili synthesis might be induced towards the

anode, with retraction pulling cells into closer contact. The unstirred environment of the BPV anode chamber may also become carbon limiting, another criterion for conductive type IV pili formation reported by Gorby et al. (2009). The smaller, more abundant structures are between 5 and 10 nm in diameter when allowing for the 16 nm thick iridium coating, corresponding to reported sizes for pili (Bhaya et al. 2000). Thicker structures emerging from cells might be bundles of smaller type IV pili, as reported by Yoshihara et al. (2001) and Nakasugi et al. (2006), and can be seen in Fig 3.8c,d branching into smaller units before connecting to the electrode surface. Larger, highway-like structures 100-200 nm in diameter can be seen in Fig 3.8a and highlighted in 3.8b traversing between cells, connecting regions of the biofilm to each other. In places these seem contiguous with regions resembling secreted extracellular polysaccharide (EPS) material, and may be an artefact of sample preparation. Such structures resembling larger connective elements have not been reported in the literature, but it is possible that they arose here from the collapse and aggregation of EPS material during dehydration of the samples prior to SEM (Dohnalkova et al. 2011).

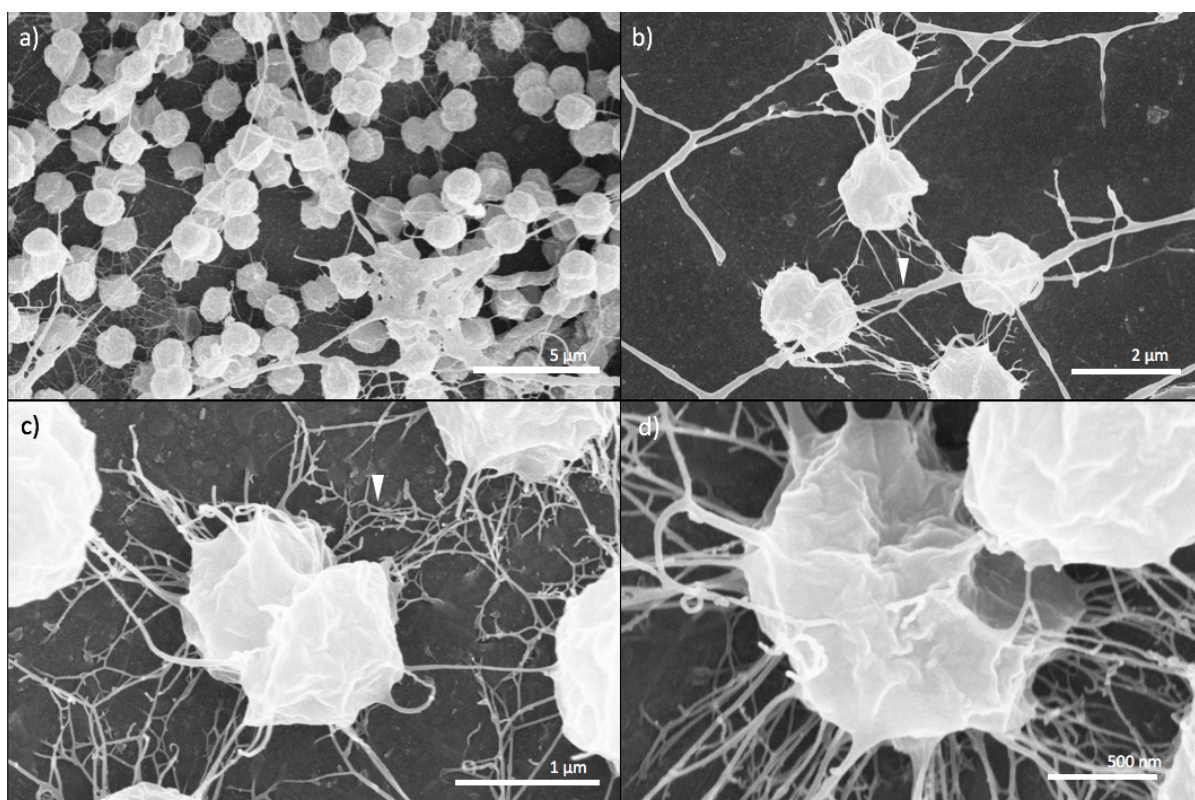


**Fig. 3.8:** SEM of wild type *Synechocystis*, a-d) wild type *Synechocystis* in biofilms over an ITO/PET anode taken from a BPV device illuminated with  $200 \mu\text{mol photons m}^{-2} \text{s}^{-1}$  from below, and withdrawing current with a 0.2V bias potential. The arrow in b highlights a larger connective structure, and the arrow in c highlights a smaller structure likely to be a type IV pilus.

To investigate the role of pili in BPV current generation from *Synechocystis*, anodic biofilms of a pili deficient strain were compared to the wild type. The pili-less strain lacked a gene encoding an RNA chaperone *hfq*, reported to be essential in type IV pili formation, transformation competence, and motility by Dienst et al. (2008) and was originally obtained from the laboratory of Dr. Annegret Wilde. Insufficient BPV experiments comparing  $\Delta hfq$  to the parent wild type were performed, with inconclusive results. However, SEM images were taken of wild type and mutant biofilms to see if pili were indeed absent from the knockout strain. In contrast to the *Synechocystis* biofilm imaged in Fig. 3.8, we did not see the same

abundance of thin pili structures for the wild type cells in Fig. 3.9, although there were structures similar to the larger 100-200 nm connective structures, as well as abundant secreted extracellular material (Fig. 3.9a, b). Potential pili agglomerates can be seen connecting cells to the anodic substrate and bridging cell to cell (Fig. 3.9c, d) but, as estimated by eye, in lower abundance than from the previous SEM of a BPV anode with wild type cells. The  $\Delta hfq$  strain (Fig. 3.9 e, f, g, h) also displayed a lack of obvious type IV pili, except for a sole instance in Fig. 3.9h, where two potentially pilin like structures connect a cell to the surface. No conclusions can be made about the expression of pili as the wild type strain did not provide a clear positive control. The main difference was that no extracellular secreted material could be seen around  $\Delta hfq$  cells, with all visible cells in contact with the surface as in Fig. 3.9a,b,d, as opposed to stacked in a thicker biofilm. Limited conclusions can be drawn from these images, but when expressed, pili, as seen in Fig. 3.8 are likely to be an important physiological component of a *Synechocystis* biofilm, that may directly - by being conductive - or indirectly – by phototaxis – play a role in electrogenic activity. Further work is needed to elucidate factors regulating their expression in a BPV device.

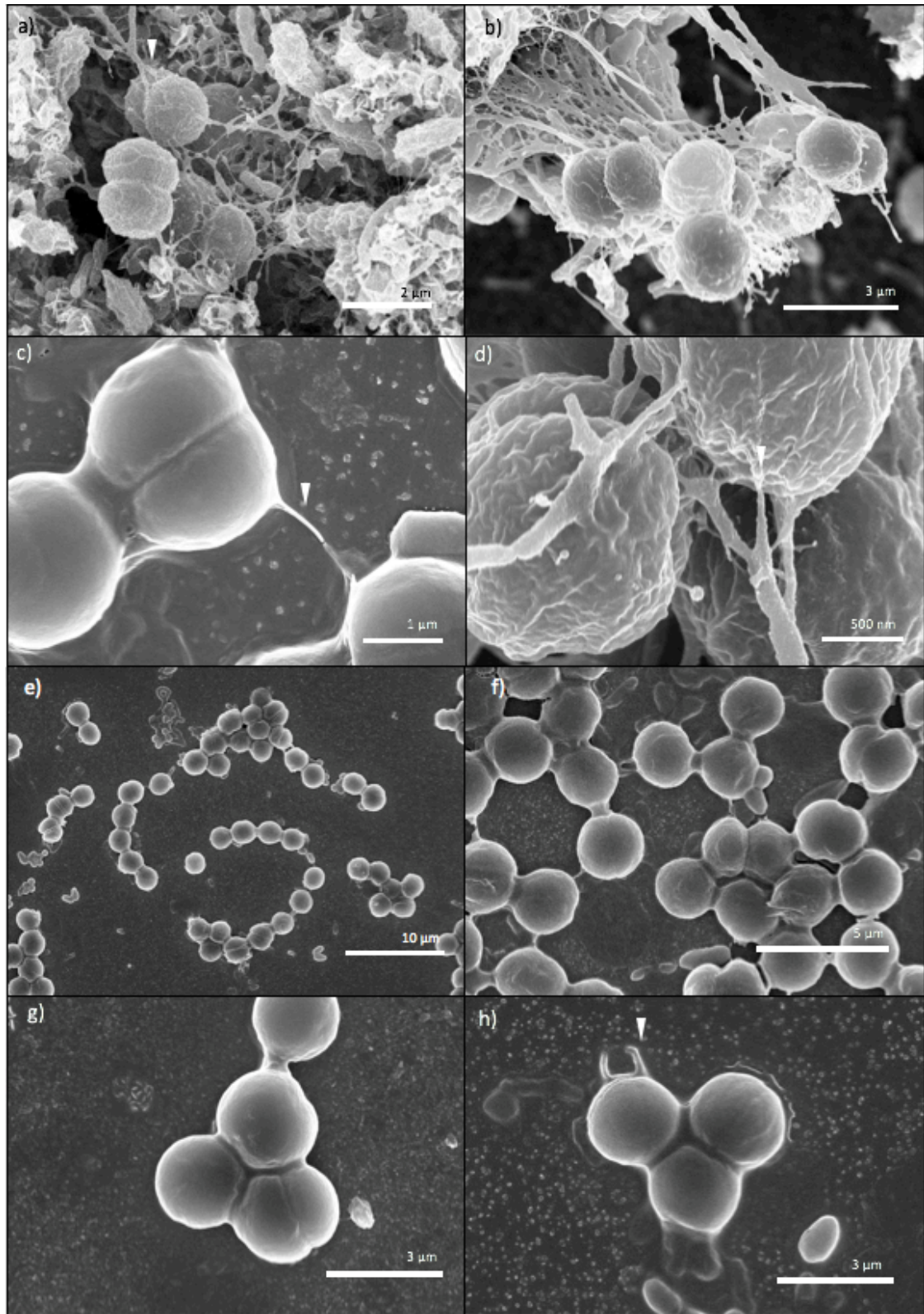


**Fig. 3.9:** SEM of a-d) wild type *Synechocystis* and e-h) the  $\Delta hfq$  knockout cells in biofilms over an ITO/PET anode taken from a BPV device illuminated with  $200 \mu\text{mol photons m}^{-2} \text{s}^{-1}$  from below, and withdrawing current with a 0.2V bias potential.

### **3.2.3. Effect of light absorbance by *Synechocystis* on extracellular electron transport:**

After optimizing the BPV device design and operation, the effect of altering cellular light absorbance on BPV output was investigated. In order to test how light absorption by *Synechocystis* affects BPV current output we characterised three mutant strains deficient in the key light absorbing pigment, phycocyanin (PC), truncating the PBS antennae to differing degrees. The  $p_{cpc}T \rightarrow C$  (one PC disk removed),  $\Delta CpcC1C2:p_{cpc}T \rightarrow C$  (two PC disks removed), and olive (no PC) strains were generated by Lea-Smith et al. (2014) and cultured from lab stocks for these experiments.

#### **3.2.3.1. Increase in red light penetration through PBS truncated biofilms:**

Light penetration through cultures of the PBS truncation mutants was measured by Lea-Smith et al. (2014) in suspended cell cultures. A reduction in PBS size increased light path length through the cultures, particularly for red light. In order to measure the effect of PC removal on light absorption by cells in a biofilm, each strain was adjusted to  $5 \text{ nmol Chl ml}^{-1}$  and allowed to settle on the bottom of 5 ml transparent well plates over 48 hours. Each well containing a biofilm was placed between an LED lamp and a light meter at a set distance and illuminated from above by low intensity red ( $20 \text{ } \mu\text{mol photons m}^{-2} \text{ s}^{-1}$ , peak emission 630 nm), blue ( $11 \text{ } \mu\text{mol photons m}^{-2} \text{ s}^{-1}$ , peak emission 458 nm), and high intensity white LED light ( $3150 \text{ } \mu\text{mol photons m}^{-2} \text{ s}^{-1}$ ) - as would be used in later BPV experiments. The difference in measured light intensity between the samples and controls containing only BG11 medium was recorded and used to calculate the percentage light absorption (Fig. 3.10). The wild type and  $p_{cpc}T \rightarrow C$  strains showed very similar light absorption, absorbing 90-94% of low intensity blue and red light. The  $\Delta CpcC1C2:p_{cpc}T \rightarrow C$  and olive strains showed little difference from the wild type in blue light absorption from either  $p_{cpc}T \rightarrow C$ ,  $\Delta CpcC1C2:p_{cpc}T \rightarrow C$ , or the olive strains. Absorption of red light appeared to reduce in a stepwise manner from 92% in  $p_{cpc}T \rightarrow C$  (94% in wild type)

to 84% in  $\Delta CpcC1C2:p_{cpc}T \rightarrow C$  and 75% in the olive. This shows that PC accounts for a significant proportion of red light absorption in *Synechocystis*. At the unsaturated, low light intensity as used here, absorption of red light by PC is limiting, allowing us to differentiate between different strains. At saturating high white light there was no difference between wild type,  $p_{cpc}T \rightarrow C$ ,  $\Delta CpcC1C2:p_{cpc}T \rightarrow C$  strains with 3, 2, and 1 PC disks respectively (87-88%); only complete removal of PC in the olive reduced absorption of high intensity white LED light to 74%.

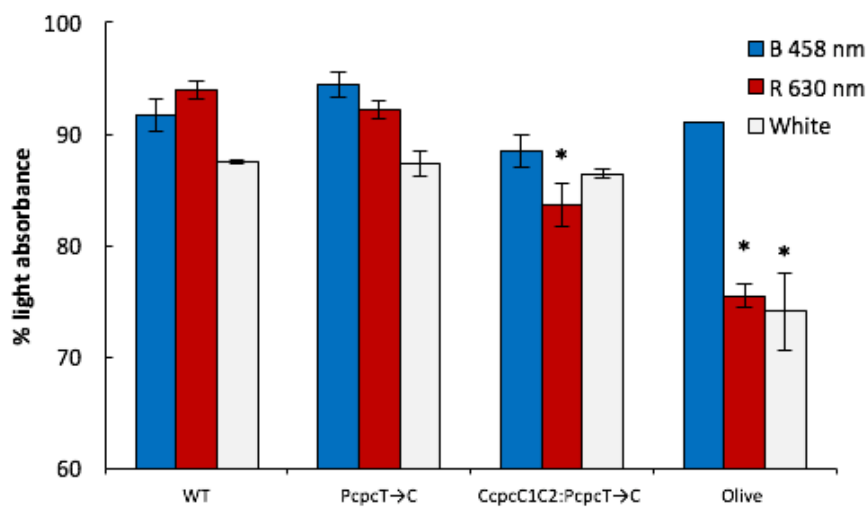


**Fig. 3.10:** The percentage of light absorbed through biofilms of PBS truncated mutants, with blue (458nm peak), red (630nm peak), and saturating ( $3150 \mu\text{mol photons m}^{-2} \text{s}^{-1}$ ) LEDs. Results show the average of three replicates, error bars show the standard deviation about the mean, and asterisks indicate significant difference from the wild type control for each wavelength ( $p < 0.05$ ).

### 3.2.3.2. Antenna truncation increases the sensitivity to cell density of ferricyanide reduction rate:

To test for differences in EET between the wild type and antenna truncated mutants we compared the rate of reduction of potassium ferricyanide to ferrocyanide. Fig. 3.11 shows the

concentration of ferricyanide declining from wild type and antenna truncated strains and controls. The rate of reduction of ferricyanide to ferrocyanide was calculated from a standard curve (see Methods) for each strain at each cell density from samples extracted and filter sterilized at 0, 24, and 52 hours. The assay was illuminated by red light (peak 635 nm) at  $60 \mu\text{mol photons m}^{-2} \text{ s}^{-1}$  in 12 well plates containing 5 ml of culture normalized to  $2 \text{ nmol Chl ml}^{-1}$  in a shaker incubator operated at  $30^\circ\text{C}$  and 120 rpm. This confirmed that in this assay setup *Synechocystis* reduced ferricyanide in a quantifiable manner. After 52 hours, ferricyanide had been almost completely reduced (Fig. 3.11a), meaning the window for calculating the rate of reduction should lie within the first 24 hours. The controls showed there was a very small degree of ferricyanide reduction in BG11 medium alone, and there was no difference when adding ammonium. The control with cells but no ferricyanide showed that there was nothing being secreted by the cells into the medium with an absorbance that could interfere with the quantification of ferricyanide. Taking measurements from the wild type every hour (Fig 3.11b) revealed the concentration of ferricyanide to decline in a relatively linear fashion in the first 8 hours.

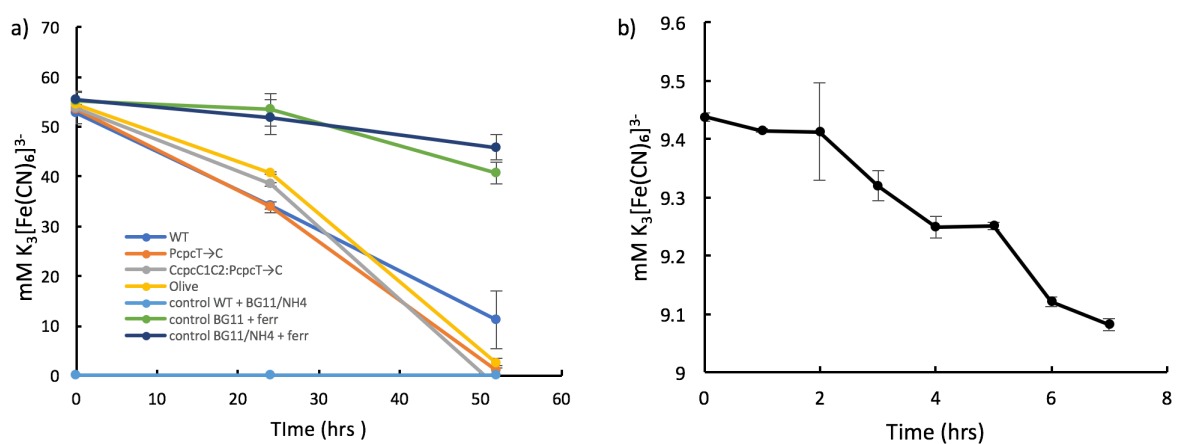


**Fig. 3.11a)** Graph showing the concentration of ferricyanide measured every hour between 0 and 7 hours for wild type *Synechocystis*, and b) measured at 0h, 24h, and 52h, for the wild type, pcpCT→C, ΔCpcC1C2:pcpCT→C, and olive mutants at  $2 \text{ nmol Chl ml}^{-1}$ , and controls with

(cyan) wild type cells in BG11 medium with no added ferricyanide, and ferricyanide in BG11 (orange) and BG11 plus ammonia (dark blue). Results are an average of three replicates and error bars show the standard deviation about the mean.

The difference in ferricyanide concentration in Fig. 3.11a after 24 hours suggested that the olive and  $\Delta\text{CpcC1C2}:\text{p}_{\text{cpcT}\rightarrow\text{C}}$  strains reduced ferricyanide slightly faster than the wild type and  $\text{p}_{\text{cpcT}\rightarrow\text{C}}$ . Lea-Smith et al. (2014) showed the path length of light through cultures to increase with the removal of PC, so changes in ferricyanide reduction rate in the antenna truncated mutants would be likely to follow a different relationship to culture density from the wild type. To test this the assay was conducted at three different cell densities: 2, 5, and 10 nmol Chl ml<sup>-1</sup>, normalising each sample to Chl content using a spectrophotometer (Lea-Smith et al. 2013). At the lowest cell density of 2 nmol Chl ml<sup>-1</sup> the olive mutant had lower rates of ferricyanide reduction at  $0.566 \pm 0.0153 \text{ mM K}_4[\text{Fe}(\text{CN})_6] \text{ hr}^{-1}$  compared to the wild type at  $0.777 \pm 0.00602 \text{ mM K}_4[\text{Fe}(\text{CN})_6]^{4-} \text{ hr}^{-1}$  (Fig. 3.12).  $\Delta\text{CpcC1C2}:\text{p}_{\text{cpcT}\rightarrow\text{C}}$  was slightly lower and  $\text{p}_{\text{cpcT}\rightarrow\text{C}}$  very similar to the wild type at  $0.640 \pm 0.0247$  and  $0.822 \pm 0.0194 \text{ mM K}_4[\text{Fe}(\text{CN})_6]^{4-} \text{ hr}^{-1}$  respectively. At 5 nmol Chl ml<sup>-1</sup> cell density the  $\text{p}_{\text{cpcT}\rightarrow\text{C}}$ ,  $\Delta\text{CpcC1C2}:\text{p}_{\text{cpcT}\rightarrow\text{C}}$ , and olive showed very similar rates of ferricyanide reduction:  $0.976 \pm 0.0212$ ,  $0.962 \pm 0.0429$ , and  $0.991 \pm 0.0597 \text{ mM K}_4[\text{Fe}(\text{CN})_6]^{4-} \text{ hr}^{-1}$  respectively, all greater than the wild type at  $0.809 \pm 0.0368 \text{ mM K}_4[\text{Fe}(\text{CN})_6]^{4-} \text{ hr}^{-1}$ . At 10 nmol Chl ml<sup>-1</sup> cell density the pattern of ferricyanide reduction from 0.4 nmol Chl ml<sup>-1</sup> was reversed, with the wild type producing  $0.980 \pm 0.0932 \text{ mM K}_4[\text{Fe}(\text{CN})_6]^{4-} \text{ hr}^{-1}$ ,  $\text{p}_{\text{cpcT}\rightarrow\text{C}}$  and  $\Delta\text{CpcC1C2}:\text{p}_{\text{cpcT}\rightarrow\text{C}}$   $1.16 \pm 0.130$  and  $1.15 \pm 0.0377 \text{ } \mu\text{mol K}_4[\text{Fe}(\text{CN})_6]^{4-} \text{ hr}^{-1}$  respectively, and the olive the highest at  $1.31 \pm 0.0520 \text{ } \mu\text{mol K}_4[\text{Fe}(\text{CN})_6]^{4-} \text{ hr}^{-1}$ . These results show that at  $60 \text{ } \mu\text{mol photons m}^{-2} \text{ s}^{-1}$  the rate of ferricyanide reduction was clearly dependent on the cell density of the culture, and that removing PC increased the sensitivity of changes in the rate of reduction to cell density.

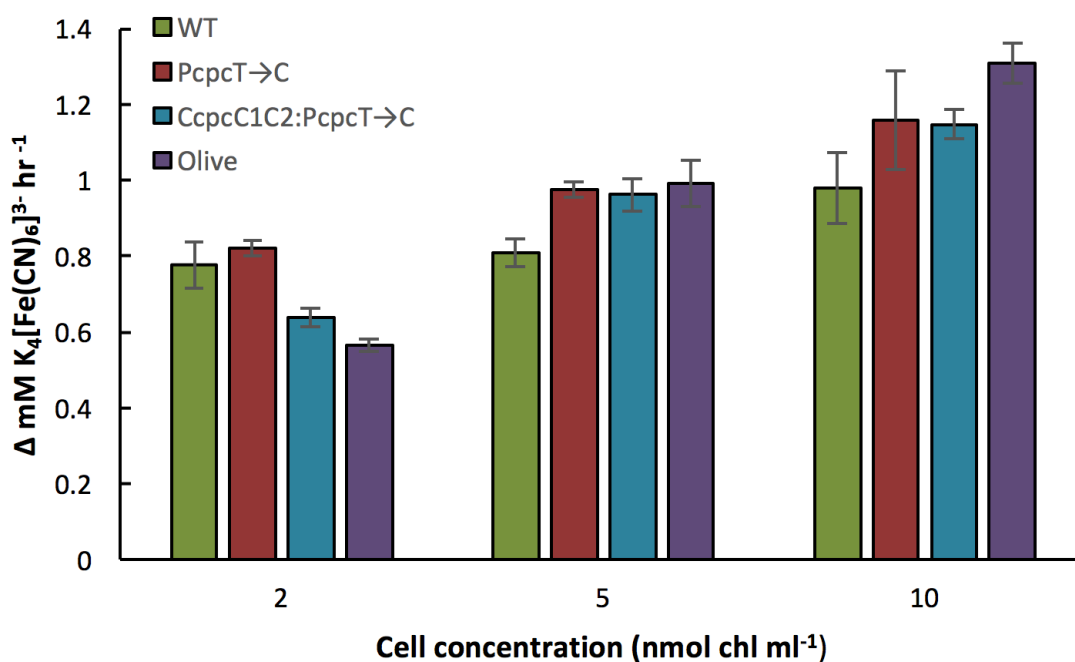


**Fig. 3.12:** Rates of reduction of ferricyanide over 24 hours under 60  $\mu\text{E}$  light intensity at 632 nm in the wild type *Synechocystis*,  $p_{cpC1} \rightarrow C$ ,  $\Delta CpcC1C2:p_{cpC1} \rightarrow C$ , and olive mutants at increasing concentration of 2, 5, and 10 nmol of chlorophyll per ml in suspended culture. The assay was performed in triplicate and error bars show the standard deviation, asterisks indicate significant difference from the wild type in each concentration group ( $p < 0.05$ ).

### 3.2.3.3. PBS truncation enhances the rate of photo-induced ferricyanide reduction at medium light intensity:

To test conditions similar to those to be used in the BPV devices, the ferricyanide reduction assay was performed at a higher light intensity of 200  $\mu\text{mol photons m}^{-2} \text{ s}^{-1}$  and higher cell concentration of 5 nmol Chl ml<sup>-1</sup>. In the 5 ml wells this led to a cell number equivalent to 25 nmol Chl, the same amount to be used in later BPV experiments. Because the assay was set up to maximise replicates and control for mixing and temperature in a shaker incubator, the light intensity was limited by the need to ensure even light distribution from the 9 warm white lights, and avoid overheating. Ferricyanide concentration was determined using the slower scan

method incorporating the peak at 263 nm as detailed in Methods 2.3.3. This method incorporated lower wavelengths where the contribution of ferrocyanide could be taken into account for a more accurate picture of the rate of reduction of ferricyanide. The rate of ferricyanide reduction over 20 hours in Fig. 3.13 was similar between the wild type and  $p_{cpc}T \rightarrow C$ , slightly higher from  $\Delta CpcC1C2:p_{cpc}T \rightarrow C$ , and 2.5 fold greater from the olive mutant. Rates of reduction were more varied than expected in the dark, with the olive nearly 7-fold faster than the wild type. Despite variation in the dark, the increase in ferricyanide reduction rate on exposure to light for the olive strain was still higher at  $0.0542 \pm 0.00299 \text{ mM K}_4[\text{Fe}(\text{CN})_6]^4 \text{ hr}^{-1}$  compared to the wild type at  $0.0320 \pm 0.00361 \text{ mM K}_4[\text{Fe}(\text{CN})_6]^4 \text{ hr}^{-1}$ . The  $p_{cpc}T \rightarrow C$  and  $\Delta CpcC1C2:p_{cpc}T \rightarrow C$  mutants had relatively high dark currents and reduction rate in the light similar to the wild type, meaning the light effects were smaller at  $0.00927 \pm 0.00694$  and  $0.0234 \pm 0.00236 \text{ mM K}_4[\text{Fe}(\text{CN})_6]^4 \text{ hr}^{-1}$ . At  $25 \text{ nmol Chl ml}^{-1}$  light is almost completely absorbed by the culture, and path length, or light penetration depth, is limiting. Although 6 replicates were completed for each condition, it is possible that the low dark reduction rate from the wild type was an outlying result. These results show that in replicates at higher cell concentration and light intensity performed side by side in light and dark, the rate of reduction of ferricyanide over 20 hours increased with illumination. Removing phycoerythrin completely resulted in higher rates of reduction over the wild type in the light and the dark. However due to the low dark rate of reduction from the wild type the rate of reduction increased by a factor of 4.83 times in the wild type and 1.95 times in the olive.

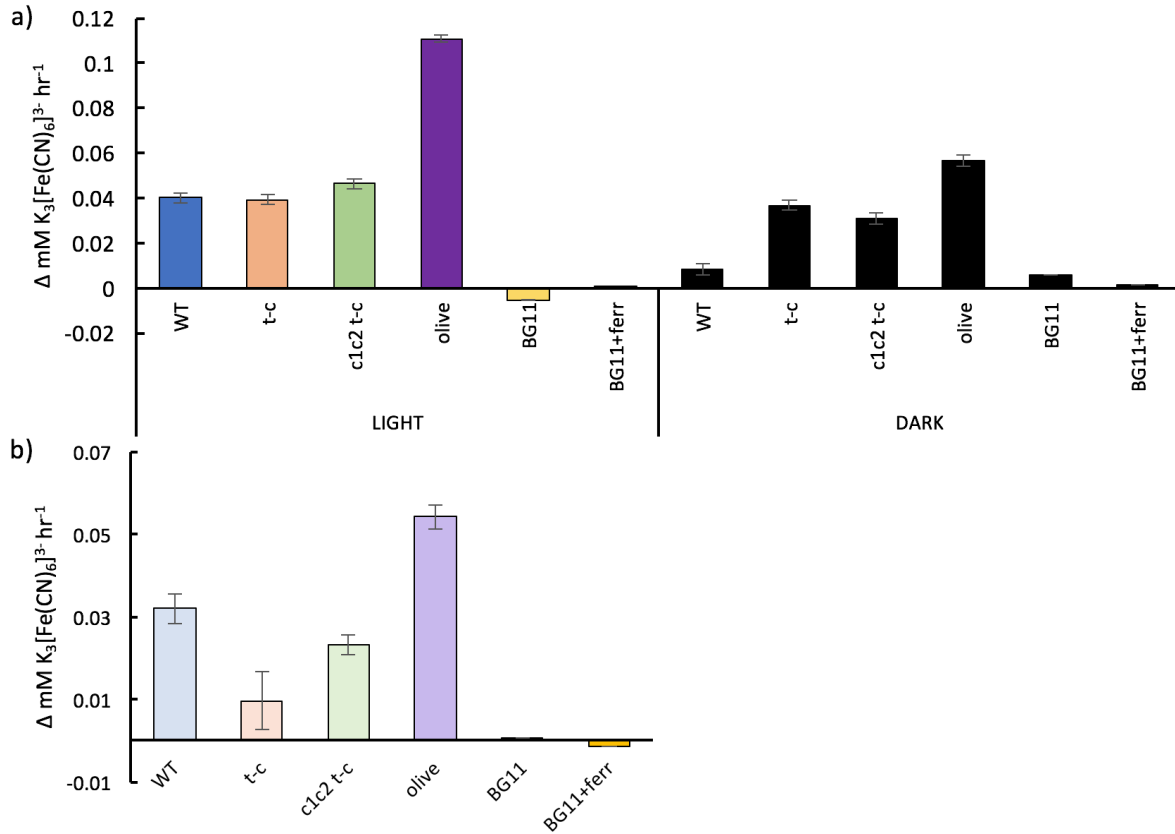
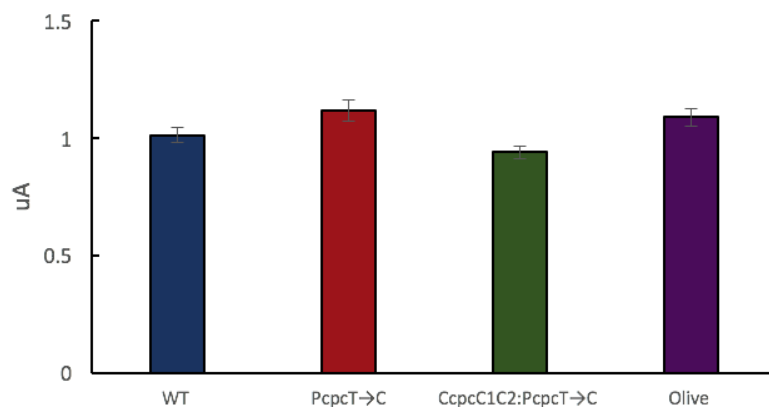


**Fig. 3.13:** Rate of reduction of ferricyanide from the wild type,  $\text{pcpC1C2}:\text{pcpC1C2} \rightarrow \text{C}$ ,  $\Delta\text{CpcC1C2}:\text{pcpC1C2} \rightarrow \text{C}$ , and olive strains, and a BG11 medium control with and without ferricyanide, a) under  $200 \mu\text{mol photons m}^{-2} \text{s}^{-1}$  and in the dark at  $25 \text{ nmol Chl ml}^{-1}$  cell concentration. b) The rate of photo-reduction of ferricyanide from subtracting the dark from the light. Results are an average of at least 6 replicates taken at 0 and 20 hours, and error bars show the standard error.

#### 3.2.3.4. Biophotovoltaic output from biofilms of PBS truncated mutants:

In order to test how antenna truncation affected biophotovoltaic output, BPV devices were set up with light from above in the configuration in Fig. 3.3b. The equivalent of  $25 \text{ nmol Chl}$  of cells was used in each, resulting in a thick biofilm in which penetration path length was limiting, in order to highlight any effects of decreasing individual cell light absorption. In order to encourage the development of an electroactive biofilm, cells were allowed to settle over the

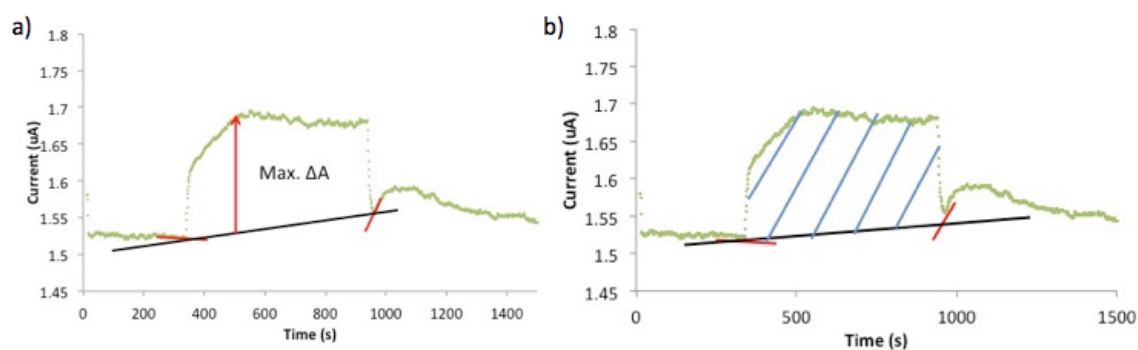
steel mesh anode for 72 hours under low light intensity. Cells were dark adapted for 30 minutes prior to beginning a sequence of 5 minute illumination periods interspersed by 15 minutes recovery in the dark, administered by warm white LEDs controlled by a computer linked power box. The light intensity was increased in a step wise fashion from low ( $60 \mu\text{mol photons m}^{-2} \text{s}^{-1}$ ) to extreme high light ( $5370 \mu\text{mol photons m}^{-2} \text{s}^{-1}$ ) over 13 illumination periods. *Synechocystis* still produces a ‘dark’ current from the metabolism of stored carbon sources. This was measured prior to exposure to the BPV light sequences and showed no significant differences between the wild type and the antenna mutants (Fig. 3.14), unlike the measurement of ferricyanide reduction in the dark. The wild type produced  $1.01 \pm 0.0327 \mu\text{A}$ , and  $p_{cpc}T \rightarrow C$ ,  $\Delta CpcC1C2:p_{cpc}T \rightarrow C$ , and the olive mutants produced  $1.12 \pm 0.0454$ ,  $0.938 \pm 0.0275$ , and  $1.09 \pm 0.0360 \mu\text{A}$  respectively.



**Fig. 3.14:** Dark current prior to BPV light sequence for wild type *Synechocystis*,  $p_{cpc}T \rightarrow C$ ,  $\Delta CpcC1C2:p_{cpc}T \rightarrow C$ , and olive strains. Error bars represent the standard error.

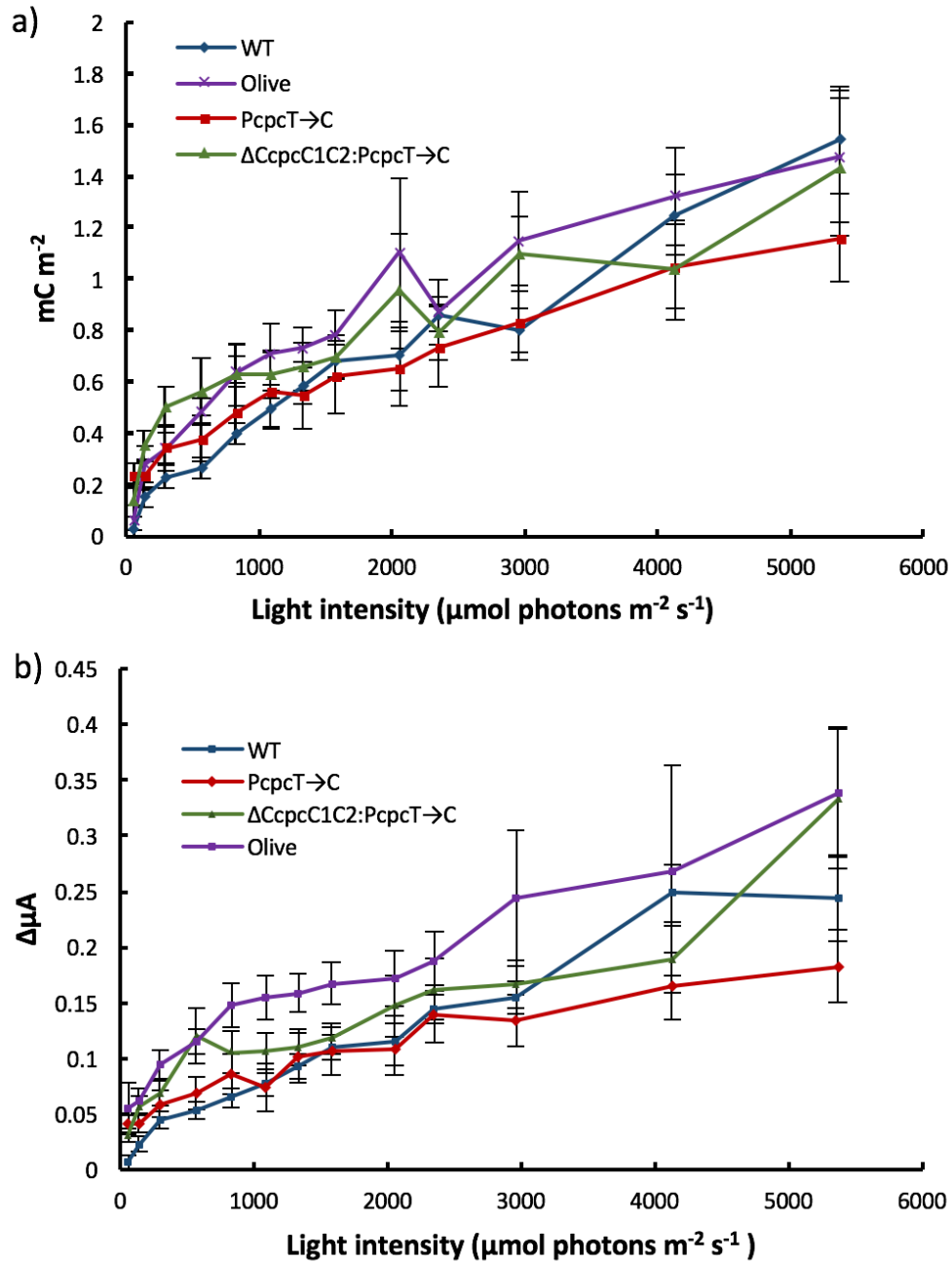
The maximum current increase at each light intensity was calculated by subtracting the projected dark current from the maximum current reached during illumination as in Fig. 3.15a. Due to the variable shape of the chronoamperometric response to light (as seen in Figs. 3.5 and 3.6) the total BPV output from each illumination period was quantified as in

Fig. 3.15b by integrating the area under the chronoamperometry curve and subtracting the integral of the projected dark current. It is worth noting that although a range of response dynamics were observed, there was no correlation between strain of *Synechocystis* and the shape of the light response trace. The origins of the fluctuating current trace and reasons for observing different traces at different times were beyond the scope of this thesis. Proper characterization of photocurrent output will likely require taking into account the mechanisms behind this, however for the purposes of this study the method of calculating the total charge accumulation over the projected dark current was kept the same, including when initial current reduction during the illumination period subtracted from the total. The frequency of observation of different trace shapes was approximately 50%, without any discernable common factor as to why the initial response varied. Total BPV charge was adjusted to the anode surface area, giving a measure of charge density in Coulombs per metre squared.



**Fig. 3.15:** Diagram illustrating analysis of chronoamperometry with *Synechocystis* in a BPV device with ITO anode over one illumination period with the methods used to calculate a) the maximum current increase over the projected dark current, and b) the total charge accumulation from chronoamperometry traces of the illuminated BPV devices.

BPV charge density from biofilms of wild type *Synechocystis* increased in a relatively linear fashion from  $0.0275 \pm 0.0000673$  to  $1.54 \pm 0.209$  mC m<sup>-2</sup> between 60 and 5370  $\mu\text{mol photons m}^{-2} \text{ s}^{-1}$ . Maximum biophotovoltaic charge densities reached by the PBS antenna mutants at 5370  $\mu\text{mol photons m}^{-2} \text{ s}^{-1}$  (with dark current subtracted) were  $1.16 \pm 0.170$ ,  $1.44 \pm 0.265$ , and  $1.48 \pm 0.259$  mC m<sup>-2</sup> in p<sub>cpc</sub>T→C, ΔCpcC1C2:p<sub>cpc</sub>T→C, and the olive mutants respectively (Fig. 3.16a). This shows that at extreme high light, removal of PC no longer confers an advantage for BPV output, probably because the biofilm is saturated with light. At extreme high light the maximum BPV current increase over the dark also had a high degree of variability, with an average BPV current of  $0.245 \pm 0.0386$   $\mu\text{A}$  from the wild type,  $0.182 \pm 0.0325$   $\mu\text{A}$  from p<sub>cpc</sub>T→C,  $0.334 \pm 0.0626$   $\mu\text{A}$  from ΔCpcC1C2:p<sub>cpc</sub>T→C, and  $0.334 \pm 0.0582$   $\mu\text{A}$  from the olive mutant (Fig. 3.16b). Above 1580  $\mu\text{mol photons m}^{-2} \text{ s}^{-1}$  the variation between biological replicates masked any significant differences between the wild type and the mutants in both charge density and current increase over the dark.



**Fig. 3.16:** a) BPV charge density for the wild type *Synechocystis*, pcpct→C, ΔCpcC1C2:p<sub>cpct</sub>→C, and olive strains over the full range of light intensities used from 60 to 5370 μmol photons m<sup>-2</sup> s<sup>-1</sup>. b) Maximum biophotovoltaic current increase over the dark current for the wild type, pcpct→C, ΔCpcC1C2:p<sub>cpct</sub>→C, and olive strains over the full range of light intensities used. Error bars represent the standard error.

Fig. 3.17a-c shows the charge density and Fig. 3.17d-f the maximum BPV current between of each antenna truncated strain 60 and 1580  $\mu\text{mol photons m}^{-2} \text{s}^{-1}$  compared to the wild type. At these low to medium light intensities, removal of just one PC disk in  $p_{\text{cpc}}T \rightarrow C$  did not result in significant difference from the wild type, although removing two PC disks in  $\Delta\text{CpcC1C2}:p_{\text{cpc}}T \rightarrow C$  resulted in significantly higher ( $p < 0.05$ ) charge density between 140 and 570  $\mu\text{mol photons m}^{-2} \text{s}^{-1}$ , before reaching a plateau and tend back to the charge density of the wild type. The maximum current increase from  $p_{\text{cpc}}T \rightarrow C$  is also similar to the wild type, however for  $\Delta\text{CpcC1C2}:p_{\text{cpc}}T \rightarrow C$  it is significantly higher between 60 and 830  $\mu\text{mol photons m}^{-2} \text{s}^{-1}$ . Charge density from the olive, with no PC, is higher than the wild type at 570 and 830  $\mu\text{mol photons m}^{-2} \text{s}^{-1}$  but also tends back to the level of the wild type at higher light intensities. The maximum BPV current from the olive, however, is significantly higher for the whole range between 60 and 1580  $\mu\text{mol photons m}^{-2} \text{s}^{-1}$ . This may be due to interference with certain photoprotective mechanisms that have been disrupted by the removal of PC, such as the orange carotenoid protein ( $\text{OCP}^{\text{O/R}}$ ) which binds to the PBS to re-emit excess exciton energy from excess light absorption as heat. The light intensity at which the greatest advantage of  $\Delta\text{CpcC1C2}:p_{\text{cpc}}T \rightarrow C$  over the wild type is seen is 570  $\mu\text{mol photons m}^{-2} \text{s}^{-1}$ , where the charge density and maximum BPV current are 2-fold greater than the wild type at  $0.565 \pm 0.132 \text{ mC m}^{-2}$  and  $0.121 \pm 0.0110 \mu\text{A}$  compared to  $0.267 \pm 0.0423 \text{ mC m}^{-2}$  and  $0.0536 \pm 0.00714 \mu\text{A}$ . The olive also had a 2-fold increase in charge density and maximum BPV current over the wild type at 830  $\mu\text{mol photons m}^{-2} \text{s}^{-1}$  with  $0.641 \pm 0.0620 \text{ mC m}^{-2}$  and  $0.148 \pm 0.0191 \mu\text{A}$ . These results demonstrate that at a certain range of low to medium light intensities, removal of PC can yield higher rates of DEET in a BPV device. It seems likely that between 300 and 830  $\mu\text{mol photons m}^{-2} \text{s}^{-1}$  the path length of light though the biofilm is sufficiently attenuated that removing PC allows

deeper light penetration relative to the wild type, leading to greater net light absorption and production of extracellular reducing power.

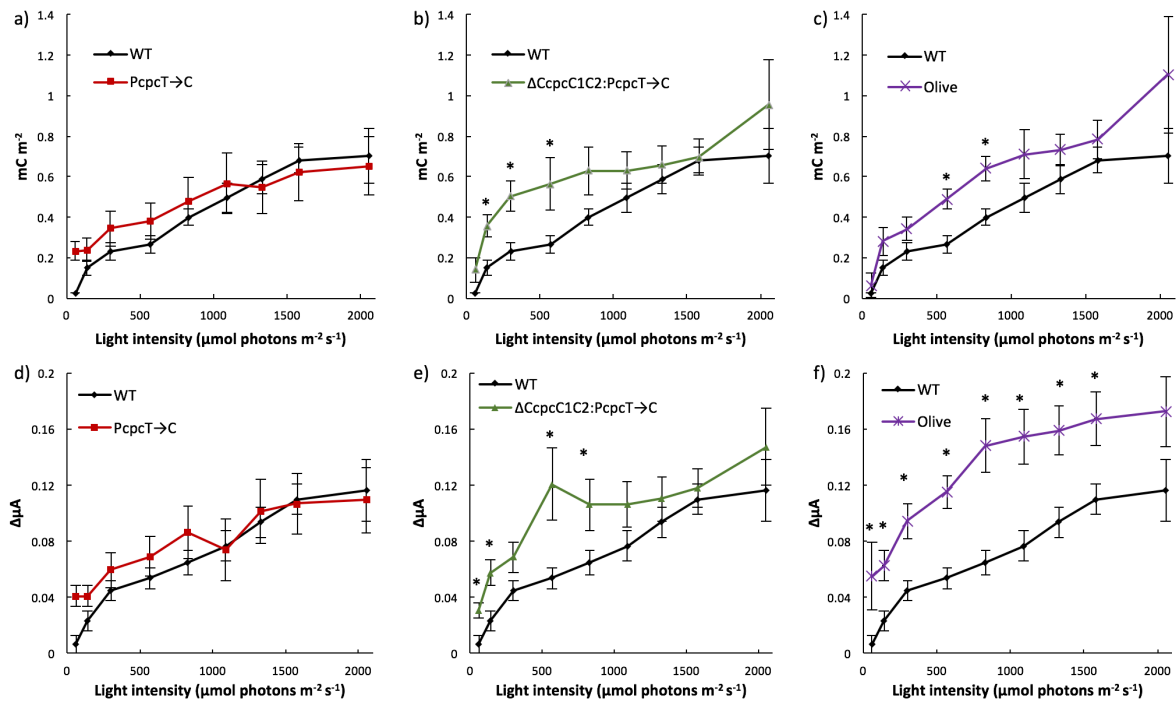


**Fig. 3.17:** a-c) Comparison of the charge accumulation per unit area due to light from the wild type and antenna truncation mutants during 10 minute periods of illumination over a range of light intensities from 60 to 2000  $\mu\text{mol photons m}^{-2} \text{s}^{-1}$ . Each mutant is displayed relative to the wild type; a)  $\text{pcpcT} \rightarrow \text{C}$ , b)  $\Delta\text{CpcC1C2}:\text{pcpcT} \rightarrow \text{C}$ , and c) olive. Charge density or accumulation is calculated as the integral of the light effect under the chronoamperometry plot. Light intensities where the charge accumulation is significantly greater than the wild type are marked with an asterisk ( $p < 0.05$ ). d-f) Comparison of each antenna truncation mutant to the maximum increase in current due to illumination over the dark current. Each mutant is displayed relative to the wild type; d)  $\text{pcpcT} \rightarrow \text{C}$ , e)  $\Delta\text{CpcC1C2}:\text{pcpcT} \rightarrow \text{C}$ , and f) olive. Light intensities where the peak light effect current is significantly greater than the wild type are

marked with an asterisk ( $p < 0.05$ ), results are an average of at least 8 biological replicates and error bars show the standard error.

### **3.3. Discussion:**

#### **3.3.1. Cells in a biofilm exhibit faster BPV kinetics:**

The move from suspended cells to biofilms in the BPV devices was a clear advance in experimental efficiency when potentiostat channel capacity was limited; being able to perform a full light cycle in 2-3 hours as opposed to a full day was a huge advantage. Operating with cells in suspension and ferricyanide as an extracellular electron carrier took many hours to reach a stable plateau of current output to each light intensity. By contrast, upon illumination *Synechocystis* biofilms produced rapid current spikes and reached a current plateau for a given light intensity in the space of seconds to minutes (Fig. 3.7c). A rapid photocurrent response allowed sequential measurements of a range of light intensities over much shorter time periods, reducing variation due to time between each light exposure and the risk of photodamage at higher light intensities confounding results. Reduction of the anode without an external electron carrier must be mediated by endogenous mechanisms of DEET but is not limited by the rates of diffusion of ferrocyanide to the anode.

The faster current kinetics also revealed interesting characteristics that may belie multiple underlying charge transfer processes either directly involved in, or responding to the changes in EET. Possible redox mechanisms contributing to the fluctuating current profile could include electron transport chain protective mechanisms such as putative flavodiirons, the terminal oxidases. Cytosolic electron sinks such carbon fixation, storage compound synthesis, and

uptake of extracellular metabolites including reduction of iron compounds could also play a role. However, chronoamperometry curves with a similar profile have been reported by Ciesielski et al. (2010) when using only isolated PSI on electrodes, and by Cereda et al. (2014) when using cells dried onto the electrode before rehydration. Recently, Zhang et al. (2017) reported chronoamperometry curves using isolated PSII that did not display the fluctuations, as well as whole cell chronoamperometry that did. This may indicate the charge rebalancing as described in Fig. 3.6, or at least part of it, may be occurring at PSI. The chronoamperometry trace from PSI only had one initial spike at lights-on, and one dip at lights-off, whereas the whole cell trace exhibited multiple charge rebalancing components. Use of a combination of knockouts, isolated components, and electron transfer inhibitors could provide a framework to determine the mechanisms contributing to the light dependent fluctuations the chronoamperometry trace and ultimately processes governing the rate of EET and biophotovoltaic output.

The light exposures we report were all done using a ‘square-wave’ light on/light off approach which does not mimic natural light exposure and would impair growth and even prove lethal without the protective terminal oxidases (Lea-Smith et al. 2013). It would be interesting to compare the application of a diurnal light gradient to chronoamperometry, although this was difficult in our set up using LEDs with low modularity resulting in step changes in luminescence. A filament bulb with a computer controlled dimmer or apparatus to vary the distance from a light source in a controlled manner could easily solve this. The current from the example BPV device in figure 3.7 shows a response to light at the lowest light intensity of  $60 \mu\text{mol photons m}^{-2} \text{ s}^{-1}$ . If the spikes represent different components balancing the charge it would be interesting to see how they respond to different rates of constant light increase. An interesting observation is that the start of the chronoamperometry trace often resembles an

action potential. Prindle et al. (2015) report the occurrence of action potential like signals traversing biofilms that aid in coordinating metabolism across different regions. They observed potassium ion mediated waves of depolarization propagating from cell to cell by positive feedback loops. If such phenomena exist in cyanobacteria it is conceivable they might be involved in rapid communication about changing light conditions or coordination on resource use such as iron depletion to avoid a tragedy of the commons situation impeding biofilm growth. Experiments using filters to keep the cells at a defined distance from anode, or other means of testing ion concentrations could investigate the involvement of ion channels.

### **3.3.2. The role of type IV pili as conductive nanowires in *Synechocystis*:**

The debate continues about the existence or involvement of conductive Type IV pili in DEET from anodic biofilms. Our SEM results clearly indicate an abundance of filamentous structures connecting cells to the anodic ITO surface, although their function remains unknown. Given the previous difficulty in the lab of successfully imaging pili from *Synechocystis* perhaps we were lucky to have observed them on the first attempt, and the conditions required for their expression are either not controlled for in our apparatus or we were simply unaware of what they are. A follow up experiment using a pili knockout strain was expected to show obvious differences, although neither the knockout or the parent wild type strain exhibited pili like structures as seen in the initial SEM round, and the only phenotypic difference was the lack of extracellular polysaccharide excretions holding together a biofilm of cells in the knockout line and there was no apparent difference in their biophotovoltaic current output. The deletion of the RNA chaperone *hfq* was linked to the loss of motility and lack of Type IV pili expression (Dienst et al. 2008), which may explain why cells were only seen in a monolayer on the anode surface if part of the motility function is to organise into 3-dimensional biofilms. The wild type *Synechocystis* sp. PCC6803 strain in Fig. 3.9 is the parent strain for the *hfq* knockout from Dr.

Annegret Wilde's lab, and may have significant differences from the Howe lab wild type strain. Type IV pili in *Synechocystis*, known as fimbriae, have been well characterised in for enabling phototaxis by twitch motility (Bhaya et al. 2000). They also appear to occur in two distinct morphotypes: thick and thin, depending on whether they have been bundled together or not, and play a key role in cell adhesion in biofilms (Chandra et al. 2017). The pili visible in our SEM in Figure 3.8 are most likely serving as anchors to the surface, and seem to be more common in cells attached directly to the surface rather than higher in the z-stack of the biofilm. The fact that fimbriae or pili are well known to bundle could explain the branching of pili before they contact the surface in our images. Type IV pili have been shown to be involved in the reduction of extracellular iron oxide compounds (Lamb et al. 2014), whether this could make them conductivity as claimed by Gorby et al. (2009) is unclear. The bundles of pili can be quite large, and inhibit further motility (Yoshihara et al. 2001). However, these may not explain the much more extensive structures that seem to be connecting regions of the biofilm tens to hundreds of micrometres apart. These may be an artefact of extracellular polysaccharide (EPS) contraction during cryopreservation for SEM, however the EPS may still play role as its intrinsic charge has been shown to have electrophoretic properties and protect against iron depletion and salt stresses. It may therefore play an integral role in conduction of electrons from many layers of the biofilm to the anode.

#### **3.3.4. Tuning light absorbance to optimize BPV light use efficiency:**

Truncation of the PBS antenna by removing PC yielded three mutant phenotypes with 2 or 1 PC disks in partially complete antenna and with no PC, leaving the bare AC core unit. Complete removal of the PBS by deletion of AC as well produces a phenotype with low viability that is

difficult to test at the same physiological conditions as the wild type (Schuurmans et al. 2015). Keeping the AC core retains some of the functionality of an intact PBS, however there are still organism-wide implications for the cell proteome of removing such a significant proportion of protein. Liberton et al. (2017) found removal of PC to increase the proportion of PSII to PSI, reported to be due specifically to a reduction in PSI expression (Nagarajan et al. 2014), and an increase in abundance of cytochrome- $b_6/f$ , which would directly affect electron transport to PSI. Significant changes in metabolite transport were also seen - an iron depletion phenotype, nitrate uptake increase, and bicarbonate transport decrease. Interestingly they also found their CB mutant, equivalent to our  $\Delta CpcC1C2:p_{cpc}T \rightarrow C$  mutant with one PC disk left from each antenna on the AC core, to have reduced levels of ATP synthase. PBS truncation also causes significant changes to thylakoid membrane curvature (Collins et al. 2012), with potential implications for overall cell size. The increased rate of ferricyanide reduction in the antenna truncated mutants therefore may only represent a partial validation of light absorption optimization theory. Under illumination greater stimulation of cell metabolism deeper into the culture mostly resulted in increased EET. We found the rate of ferricyanide reduction in the olive mutant to be more sensitive to concentration than the wild type, and importantly the reduction rate was lower than the wild type at low cell concentrations, meaning that intrinsic proteomic, metabolic, and physiological differences cannot be the only factor affecting EET. If they were then the reduction rate of ferricyanide would be expected to scale in proportion to the cell concentration and still be higher than the wild type at low cell concentration. As cell concentration increases the limiting factor likely shifts from light absorption efficiency to light path length or shading of lower layers. Increased ferricyanide reduction in the dark from the olive does potentially reveal some key differences in cellular metabolism that may be due to changes identified by Liberton et al. (2017), or the diversion of resources from synthesis of large quantities of PC. The very low reduction rate from wild type assay samples kept in the dark is potentially

anomalous. However, the partial truncation mutants were found to be most similar to the wild type and exhibited fewer proteomic changes, so the differences between them and the olive still support these conclusions.

### **3.4. Conclusions:**

Reduction of the PBS antenna size proved to be a successful strategy to increase EET in suspended culture and in a biofilm. The precise mechanism of electron export has yet to be elucidated. For an industrial context the removal of PC may be an interesting intervention to increase productivity due increased light use efficiency, although the broader implications on whole cell metabolism and photoprotection must be considered.

## **4. COMBINING SIMULTANEOUS FLUORESCENCE AND ELECTROCHEMICAL MEASUREMENTS TO MONITOR BIOPHOTOVOLTAIC EFFICIENCY AND NON-PHOTOCHEMICAL QUENCHING IN *SYNECHOCYSTIS***

### **4.1. Introduction:**

#### **4.1.1. Coupling photosynthetic electron generation to extracellular electron transfer:**

Photosynthesis in cyanobacteria is highly regulated by light stress and other growth limiting factors that could present a major bottleneck in energy transduction from light to electricity in a BPV device. Understanding how photosynthetic efficiency is regulated in the unnatural environment of an anodic biofilm could lead to improving the efficiency of BPV devices. McCormick et al. (2011) estimated the efficiency of BPV devices, based on incident light power and power output, from BPV devices containing the cyanobacteria *Synechococcus* sp. WH5701 and *Synechocystis* sp. PCC6803 at ca. 0.1 and 0.01% respectively. Comparing incident light energy to the electrical output gives an overview estimate of how efficient the BPV system is, but treats the biological component as a black box. The rate of photosynthesis can be measured by the rate of oxygen evolution from photolysis by the oxygen evolving complex (OEC). McCormick et al. (2011) did observe a positive correlation between rates of oxygen evolution and BPV power output. However, it is not possible to measure the rate of oxygen evolution using an oxygen electrode at the same time as measuring EET using a potentiostat. Both measure electrochemical changes and would interfere with each other, so measurements have to be taken from separate samples. The oxygen electrode also requires constant stirring of cultures in suspension to normalise the rate of oxygen diffusion to the electrode, which is not compatible with biofilm based devices. Another technique to measure the photosynthetic efficiency is pulsed amplitude modulation (PAM) fluorescence. Ng et al.

(2014) investigated the photosynthetic efficiency of various electrogenic algal and cyanobacterial strains using pulsed amplitude modulated fluorescence. They found higher BPV output to be correlated with lower rates of photoprotective mechanisms, or non-photochemical quenching (NPQ), and a higher relative electron transport rate (rETR) in *Synechococcus* sp. UMACC105 in particular. Ciniciato et al. (2016) went a step further and compared the rETR to the poised potential of the BPV device, finding an increase in rETR at more positive potentials. If the anode is more positive, EET becomes more energetically favourable for cells, and may promote a more oxidized electron transport chain, which may in turn downregulate NPQ.

#### **4.1.2. Quantifying intracellular photosynthetic electron flux to EET:**

Combining PAM and BPV measurements in the same device could yield a more in depth understanding of how electrons are transported from the photosynthetic electron transport chain to the outer cell membrane by giving a measure of internal light driven electron flux. The rETR is a measure of  $\mu\text{mol electrons s}^{-1}$ , and so could be compared to the rate of electron flow out of the same cells quantified simultaneously by electrical current. This would be possible by measuring the photocurrent produced by the measuring light, actinic light, and saturating pulses emitted by the PAM device. From this it may be possible to make an analogy with metabolic electron flux and electrical current, and quantify internal 'metabolic resistance' of electron sinks or the photosynthetic electron export efficiency.

#### **4.1.3. Effect of phycocyanin removal on NPQ:**

The photosynthetic electron transport chain of cyanobacteria is protected from excess reduction by electron sinks such as terminal oxidases and flavodiiron proteins that reduce oxygen to water. Adaptive strategies to protect the photosynthetic machinery can alter light absorption,

or re-emit excess energy as heat or fluorescence before electron production by PSII and the OEC. NPQ in *Synechocystis* is mediated either by the orange carotenoid protein (OCP<sup>O/R</sup>), which attaches to the PBS in its activated form to channel exciton energy away for dissipation as heat, or by state transitions of PBS dislocation between PSI and PSII to manage the production of reducing power (Acuña et al. 2015) (Fig. 4.1). Both of these mechanisms are closely tied to the PBS, with OCP<sup>O/R</sup> being triggered by blue light and state transitions controlled by the redox state of the electron transport chain (Gorbunov et al. 2011; Mullineaux & Allen 1990). How these mechanisms tie in with extracellular electron transfer to an anode or the voltage of the biofilm substrate has not yet been investigated in *Synechocystis*. By altering the PBS antenna size, as in Chapter 3, NPQ regulation may be altered by changes in light absorption, and dynamics of mechanisms directly involving the PBS may be affected.

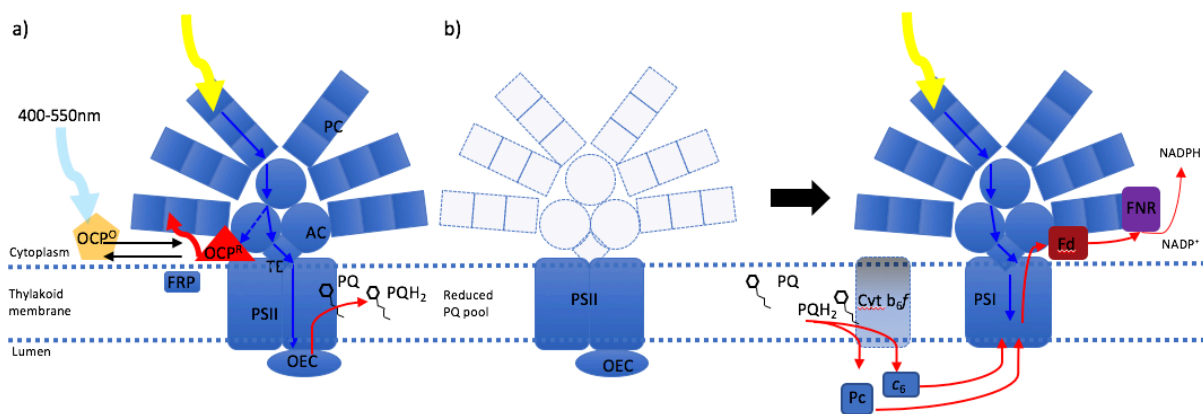


**Fig. 4.1:** Diagram illustrating photoprotection of the photosynthetic electron transport chain of *Synechocystis*. a) Fluorescence quenching by the blue light activated orange carotenoid protein (OCP<sup>O</sup> → OCP<sup>R</sup>), thought to attach to the allophycocyanin (AC) core at the base of the phycobilisome (PBS), channelling exciton energy away (blue arrows) from the terminal emitter (TEM) responsible for transmitting energy to photosystem II (PSII) and the oxygen evolving complex. Excess reduction of the plastoquinone (PQ) pool leads to b) dissociation of the PBS from PSII migration to PSI, lowering the rate of reduction of the PQ pool, which is oxidised by the proton pump cytochrome-*b<sub>6</sub>f* (Cyt-*b<sub>6</sub>f*). Electrons are passed *via* plastocyanin (Pc) or

cytochrome- $c_6$  on to PSI and on to ferredoxin and ferredoxin-NADP<sup>+</sup>-reductase (FNR) to reduce NADP<sup>+</sup> to NADPH.

Here, we adapted the BPV design to incorporate the fibre optic probe of a PAM device in order to measure simultaneously fluorescence and electrochemical output from biofilms of *Synechocystis*. The effect of anode potential was found to alter the basal fluorescence of the biofilm, increasing the fluorescence at more positive potentials, and the current and fluorescence from a PAM induction curve were used to compare the current and rETR. The percentage of electrons from rETR leaving the cell as current was calculated as a demonstration of a new kind of approach to quantify BPV systems. Finally, NPQ from the antenna mutants was measured at different light intensities, and although PC is found to interfere with fluorescence, reduction of antenna size is concluded to reduce NPQ.

## **4.2. Results:**

### **4.2.1. Effects of bias potential on basal fluorescence of anodic biofilms:**

To test how the basal fluorescence from cells in an electrogenic biofilm responds to a changing anode potential, a PAM/BPV device was inoculated with wild type *Synechocystis* and the anode potential varied using a potentiostat. Basal fluorescence ( $F_t$ ) was excited by a pulsed low intensity red measuring light (655 nm) from the PAM device designed to stimulate fluorescence, but not photochemistry. Prior to the measurement, the current and fluorescence were allowed to stabilize fully at the open circuit potential. No other lights were used, and the potential of the anode was altered in discrete periods of 330 seconds from -0.5 V to 0.5 V in 0.1 V steps, and the newly stabilized current recorded for each bias potential (Fig. 4.2). Inset

in Fig. 4.2 is a cyclic voltammogram of the same device, which showed an oxidation peak at 0.2 V. The *Synechocystis* anodic biofilm showed changes in response to the application of a positive bias potential. A negative bias potential of -0.5 V to 0 V had little effect on fluorescence, but above 0 V, an increasingly positive bias potential caused a striking shift in  $F_t$ . At -0.5 V the current was reversed as the biofilm was reduced, but it quickly stabilized around 0 A, as in the CV plot. Current from the biofilm increased to 2  $\mu$ A at 0.2 V and stabilized, as in the cyclic voltammogram, while  $F_t$  continued to rise. Finally, the anode potential was dropped to 0 V, and  $F_t$  dropped rapidly (in seconds) to a stable level slightly above the starting level. When the anode potential was switched rapidly back to 0.5 V,  $F_t$  rose sharply again to the level attained after the step potential increase. This experiment showed that increasing the potential of the biofilm substrate directly affected both biofilm fluorescence, and the rate of EET, i.e. current. In the dark, when the reaction centres and PSII  $Q_A$  bound PQ are fully oxidized, fluorescence is minimal. But when they become reduced, the excited light harvesting apparatus releases energy as fluorescence. Facilitating EET with a positive bias potential may have a number of knock on effects that could influence the redox state of the electron transport chain and cause reaction centres to close, resulting in an increase in fluorescence. The increase in  $F_t$  began around 0.1 V, before the oxidation peak visible in the CV plot, so the  $F_t$  increase may not be linked to the mechanism of EET. As this experiment was performed with the PAM measuring light only, the interlinked respiratory electron transport chain sharing the thylakoid PQ pool could be implicated if a positive bias potential increased the rate of respiratory PQ pool reduction. Other possibilities could be down to electrostatic repulsive forces from a positively charged anode affecting either directly movement of protons across the membrane and therefore pH, which could in turn increase the rate of electron flow through the PETC (Sukhova et al. 2017). State transitions are also upregulated by reduction of the electron transport chain, and slow fluorescence rises as seen

here have been attributed to state II to state I transitions in *Synechocystis* (Mullineaux & Allen 1990; Kodru et al. 2015).

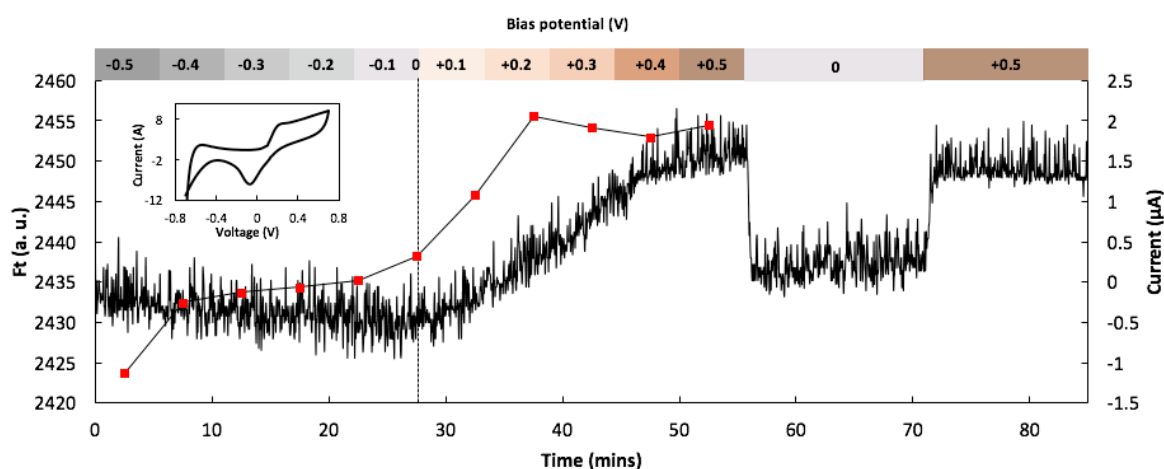


**Fig. 4.2:** Basal fluorescence ( $F_t$ ) from a wild type *Synechocystis* anodic biofilm in the dark during step change voltammetry (black line). The anode potential was increased at regular intervals by 0.1 V from -0.5 V to 0.5 V, and the stabilized current recorded after each change (red squares). After 0.5 V the anode potential was dropped to 0 V for a period of time, then taken back up to 0.5 V. Inset: a cyclic voltammogram of the same biofilm revealing a strong oxidation and reduction peak pair at 0.2 V and -0.03 V.

The increase in fluorescence at positive bias potentials is arguably unexpected, as withdrawing electrons might be expected to encourage the oxidation of the electron transport chain. To compare changes in fluorescence in the light and the dark,  $F_t$  was recorded from a newly set up device whilst again varying the anode potential over roughly an hour in the dark, then under high light at  $2000 \mu\text{mol photons m}^{-2} \text{s}^{-1}$ . Fig. 4.3 shows the change in fluorescence from a biofilm of *Synechocystis* as the anode was once again changed in 0.1 V increments between -0.5 V and 0.5 V, in both the light and the dark. The main difference were a brief reduction in  $F_t$  as the bias potential is changed from OCP to -0.5 V at the start, and a lower average  $F_t$  value in under light. This effect may be related to the drop in  $F_t$  when changing potential from 0.5 V

to 0 V in Fig. 4.2, possibly caused by the shift from positive to negative potential. In the dark, after the initial drop,  $F_t$  rose gradually before reaching an inflection point at ca. 0.32 V whereupon it rises more steeply. In the light-exposed device  $F_t$  remains stable and from the application of -0.5 V through to around 0.2 V, when it begins to drop slightly, before increasing sharply at the same potential as the dark adapted run. These results show that the state of the photosynthetic reaction centres, whether they are closed or open, or reduced or oxidized, is directly affected by the potential of the electrochemical cell. Ciniciato et al. (2016) recorded fluorescence based parameters changing alongside the applied potential, although they only took measurements in the region of 0 V to 0.24 V, and although they did see an effect on rETR, they saw little or no effect on quantum efficiency, suggesting higher potentials could have yielded more interesting results.

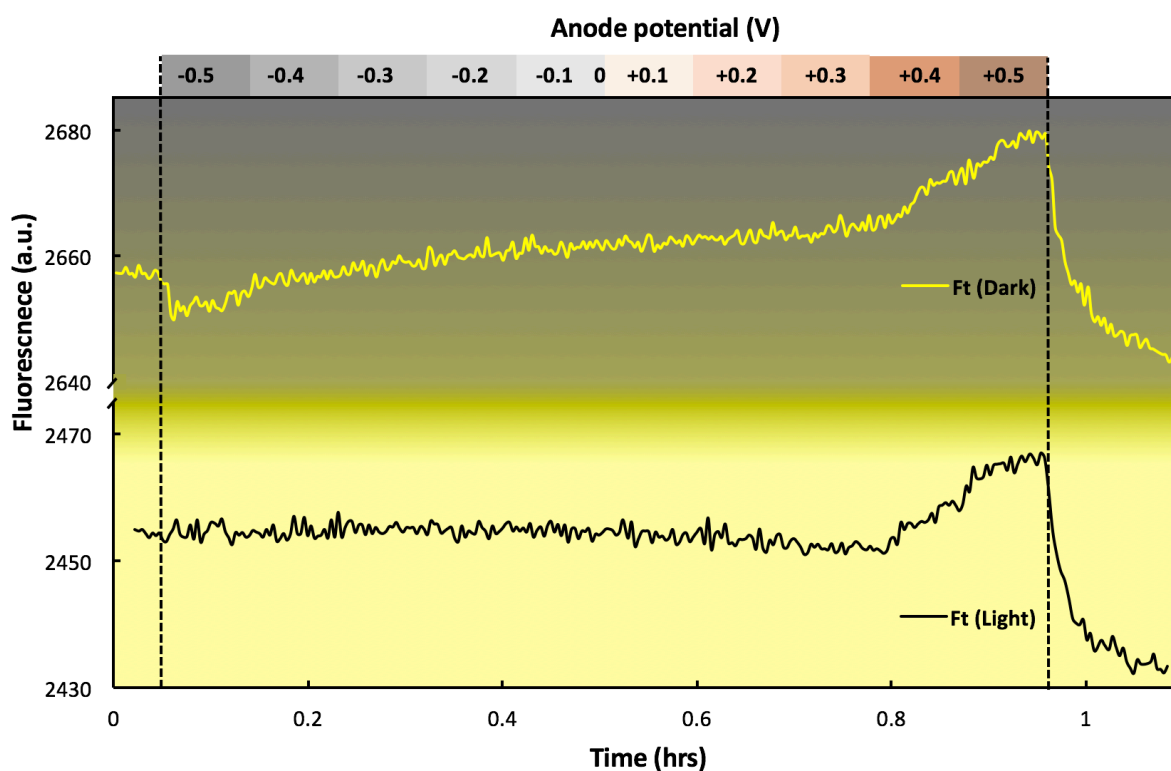


**Fig. 4.3:** PAM chlorophyll fluorescence from a wild type *Synechocystis* anodic biofilm in a BPV device during step change voltammetry in dark versus vs high light ( $2000 \mu\text{mol photons m}^{-2} \text{s}^{-1}$ ) conditions.

#### 4.2.2. Coupling fluorescence to chronoamperometry:

By recording the current produced by the biofilm during the induction curves we may be able to gain an insight into how the cells are performing in terms of photosynthesis and EET simultaneously. To test this, PAM  $F_t$  and BPV chronoamperometry traces were recorded using an induction curve light regime. Fig. 4.4 shows the PAM fluorescence trace and current from a dark adapted wild type *Synechocystis* biofilm throughout an induction curve in a PAM/BPV device. The light regime of the induction curve began with a saturating pulse of light after at least 30 minutes dark adaptation from which the maximum quantum efficiency was calculated. It is possible that the intense saturating pulses could have induced some photovoltaic effect, however the electrical response at relatively low actinic light indicates the biological current production is significant. Whilst ITO is known for its inorganic photovoltaic applications, the ITO coated PET anode material in the BPV set up we used never displayed any noticeable photovoltaic activity in the absence of cells (Bombelli et al. 2012; Tobias Wenzel, personal communication). After a two minute recovery period in the dark the biofilm was lit by continuous actinic light for thirteen minutes with a series of saturating pulses one minute apart. Photosynthesis was induced by the actinic light, while the saturating pulses allowed measurement of the accompanying change in quantum efficiency and photoprotective responses. The peaks in fluorescence from saturating pulses coincided with peaks in current and current increases from 0.14 to 0.18  $\mu\text{A}$  with the constant actinic light, in this example at 54  $\mu\text{mol photons m}^{-2} \text{s}^{-1}$ . From the maximal fluorescence during a saturating pulse from dark adapted cells and maximal fluorescence under actinic light, the quantum efficiency (YII) and relative electron transport rate (rETR) can be calculated.

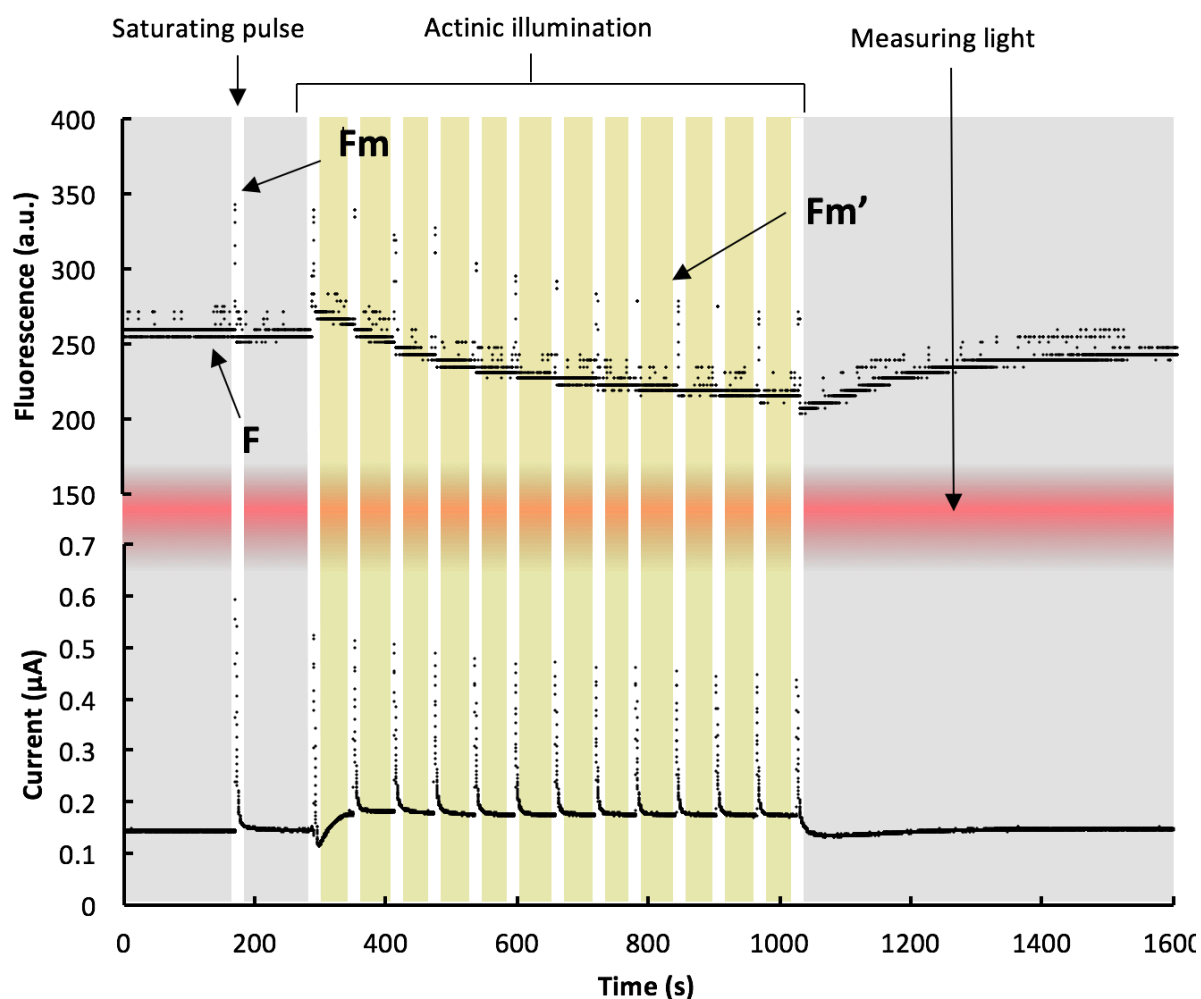


**Fig. 4.4:** Simultaneous PAM fluorescence and chronoamperometry from a single representative wild type *Synechocystis* anodic biofilm in a PAM modified BPV device loaded with 4 ml of cells in BG11 at  $5 \text{ nmol Chl ml}^{-1}$  with a cross sectional area of  $1.32 \text{ cm}^2$ . The background illustrates the light regime for the induction curve, with saturating pulses in white, the actinic illumination in yellow ( $54 \text{ } \mu\text{mol photons m}^{-2} \text{ s}^{-1}$  in this case), and the constant measuring light in red, with some key parameters labelled.

#### 4.2.3. Using PAM fluorescence and chronoamperometry to probe BPV efficiency:

By comparing the rate of production of photosynthetic electrons inferred by PAM measurements with the rate inferred from chronoamperometry we may be able to gain deeper insight into the biophotovoltaic efficiency of the anodic biofilms and limitations lying between

photolysis of water by the OEC and EET. An attempt was made to build a device capable of measuring all three of bioelectrochemical output, PAM fluorescence, and oxygen evolution using an oxygen fluorescence probe. The oxygen probe, however, proved unreliable and we could not obtain consistent measurements. ETR in  $\mu\text{mol electrons m}^{-2} \text{s}^{-1}$  was calculated from the quantum efficiency, i.e. the proportion of photons used for photochemistry, multiplied by the absorbance of photosynthetically active radiation (PAR) reaching the cross sectional area of the biofilm (Touloupakis et al. 2015). We found the absorbance of intense white light ( $3150 \mu\text{mol photons m}^{-2} \text{s}^{-1}$ ) by the nearly opaque biofilms was found to be close to 88%, and although dynamically regulated, the ratio of PSII to PSI for *Synechocystis* biofilms has been reported as 0.3 by Murakami & Fujita (1993) in high light conditions. The biofilm cross sectional area was also factored in (Kuhne et al. 2013). The emission spectrum of the PAM actinic white light from the halogen lamp peaked around 590 nm, and tailed off into the infra-red, so the proportion within the usually accepted 400-700 nm PAR range is approximately 0.7 (Walz Mini-PAM manual). rETR could be approximated by:

$$rETR = \frac{Fm' - F0}{Fm'} \times PAR \times Area \times 0.3 \times 0.7 \times 0.88$$

A comparison between rETR and BPV photocurrent from the actinic light induced photocurrent is shown in Fig. 4.5 At low light –  $54 \mu\text{mol photons m}^{-2} \text{s}^{-1}$  (light blue line), rETR increased slightly, but remained relatively constant, as did the photocurrent. rETR at medium light –  $208 \mu\text{mol photons m}^{-2} \text{s}^{-1}$  (light green line), rose to around double that of low light, as did the photocurrent. At high light –  $741 \mu\text{mol photons m}^{-2} \text{s}^{-1}$  (light red line), rETR was more variable, rising above rETR from medium light after 3 minutes, and declining gradually.

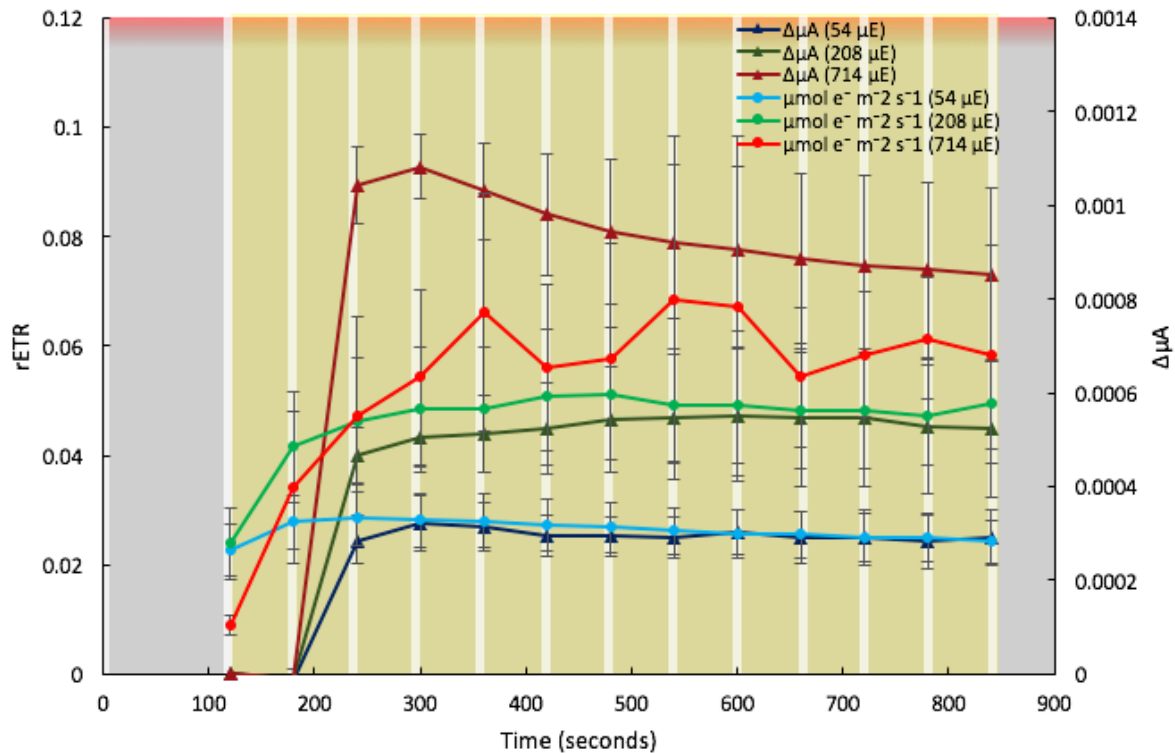


**Fig. 4.5:** Relative electron transport rate from actinic light PAR and stabilised photocurrent from wild type *Synechocystis* anodic biofilms. rETR and photocurrent at 54 (light red and dark red respectively), 208 (light green and dark green), and 714 (light blue and dark blue)  $\mu\text{mol photons m}^{-2} \text{s}^{-1}$  actinic light. Results are an average of three biological replicates and error bars show the standard error.

To compare rETR and current from the saturating pulses as well as during actinic light, the same method was applied, using the quantum efficiency calculated from the previous saturating pulse. Fig. 4.6 shows the rETR for the saturating pulses as opposed to actinic light throughout the induction curve, as well as the maximum increase in current. As expected, the rETR from each of the actinic light intensities was similar and started high given quantum efficiency measured from the initial saturating pulse. rETR for the second saturating pulse in the sequence drops for each actinic light condition before increasing steadily to a stable level, the difference being that the pattern is reversed compared to rETR calculated from actinic light where rETR

was highest at low light intensity and lowest at high light intensity. The EET current spikes from saturating pulses follow a similar pattern to rETR with the magnitude of the current spike highest at low light intensity and lowest at high light intensity.

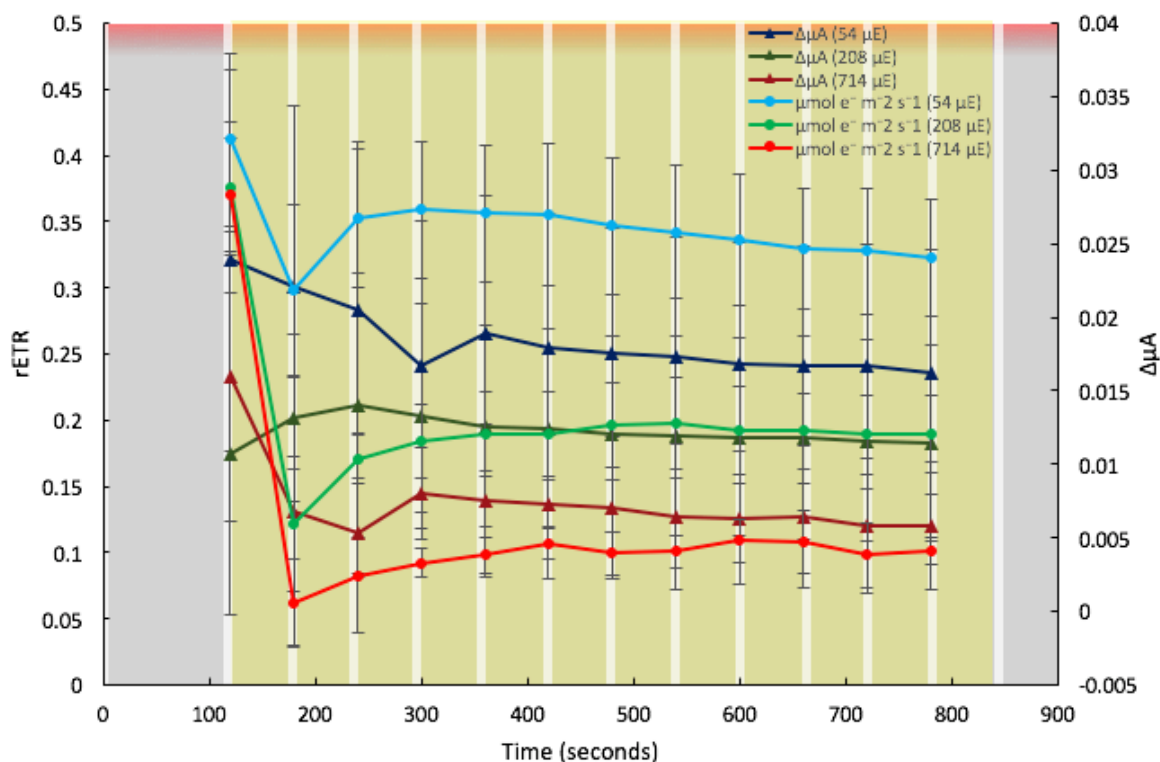


**Fig. 4.6:** Relative electron transport rate and photocurrent from saturating pulse illumination PAR ( $4450 \mu\text{mol photons m}^{-2} \text{s}^{-1}$ ) and pulse linked current spikes from a wild type *Synechocystis* anodic biofilm. rETR and photocurrent at 54 (light red and dark red), 208 (light green and dark green), and 741 (light blue and dark blue)  $\mu\text{mol photons m}^{-2} \text{s}^{-1}$  actinic light. Results are an average of three biological replicates and error bars show the standard error.

In order to estimate the proportion of photosynthetic electrons being exported per second, EET was expressed as a percentage of rETR. rETR ( $\mu\text{mol e}^{-} \text{s}^{-1}$ ) was converted to number of electrons by Avogadro's constant ( $6.02214 \times 10^{23}$ ), and current ( $\mu\text{C s}^{-1}$ ) to electrons by the charge of one electron being  $1.60271 \times 10^{-19} \text{C}$ . The results in Fig. 4.7 express the percentage

of electrons approximately produced by photochemistry that reach the anode *via* EET for actinic light and the saturating pulses. This was greatest at the highest actinic light of 741  $\mu\text{mol photons m}^{-2} \text{ s}^{-1}$  (0.23%), but after 13 minutes of high actinic light the percentage dropped to just above the level of low and medium light intensities. At 54 and 208  $\mu\text{mol photons m}^{-2} \text{ s}^{-1}$  the EET percentage remained relatively stable at c. 0.10%. These results are a proof of concept due to limited equipment and assumptions made about light absorption, but the methodology could be applied to more accurate data in future. Photosynthetic electron export efficiency at actinic light may be viewed as the ‘steady state’ BPV efficiency, and the percentage of electrons leaving the cell due to the effect of saturating pulses may yield information about rapid light changes and associated electron export. The change in percentage of photosynthetic electrons being exported during the saturating pulses also appeared to vary with the level of actinic light (Fig. 4.7b). The initial EET percentage was very low, due possibly to the high initial quantum efficiency before actinic light stress reduced it. The overall levels are also much lower than for actinic light. The percentage electron export at the second saturating pulse yielded the greatest differences between the actinic light levels, with 0.13%, 0.050% and 0.019% at 54, 208, and 741  $\mu\text{mol photons m}^{-2} \text{ s}^{-1}$ . It is conceivable that the rapid export of electrons during saturating pulses is down a ‘shunt’ mechanism that is relieved as other photoprotective mechanisms or EET pathways are upregulated during actinic illumination. This may account for the decline in percentage electron export from 741 and 208  $\mu\text{mol photons m}^{-2} \text{ s}^{-1}$ .

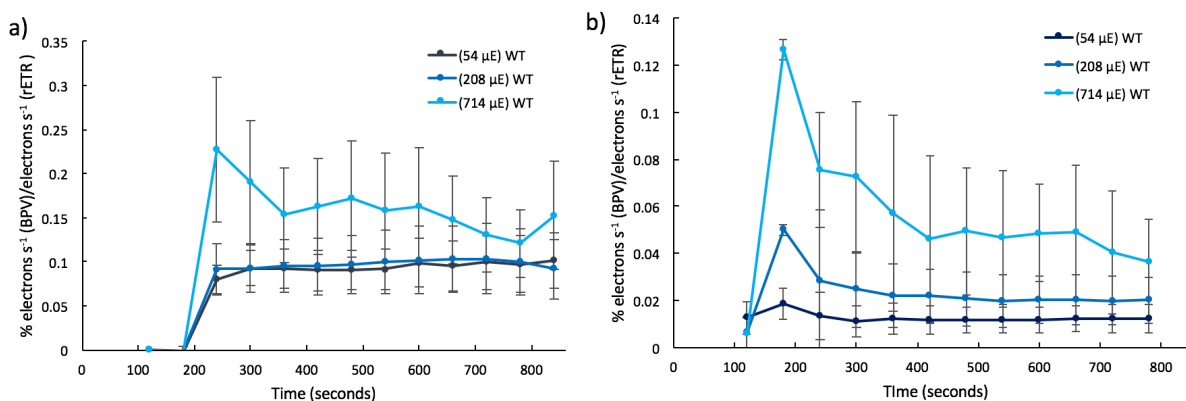


**Fig. 4.7:** Percentage estimates of electrons produced from photosynthetic light capture during a) actinic light and b) saturating pulses exiting cells in the anodic biofilm as current during saturating pulses and constant actinic light illumination at 74, 208, and 741  $\mu\text{mol photons m}^{-2} \text{s}^{-1}$ . Results are an average of three biological replicates and error bars show the standard error.

#### 4.2.4. Pulse amplitude modulation fluorescence analysis of PBS truncated mutants in custom PAM/BPV devices:

In Chapter 3 the effect on PBV output of truncating the PBS antennae was characterized. Reduced antenna size was seen to increase charge accumulation at low to medium light intensities, which may have been due to more efficient distribution of light throughout the biofilm, but there is also the possibility that the stimulation and mechanism of photoprotective mechanisms is being affected. To test levels of NPQ regulation in the PBS antenna mutants the fluorescence from biofilms in the PAM/BPV devices was measured during induction curves, although chronoamperometry data of sufficient quality to calculate the photosynthetic electron export efficiency as above were not obtained.

##### 4.2.4.1. PBS truncated mutants have reduced fluorescence changes under actinic light:

To compare the effect of PBS antenna truncation and light intensity on  $F_t$ , the  $F_t$  traces of wild type and antenna truncated mutants in BPV devices at open circuit potential (with no bias

potential applied) were plotted with the same scale axes in Fig. 4.8. During actinic light illumination  $F_t$  decreased in the wild type, reaching a new lower stable level after a 5-10 minutes, with intermittent spikes from saturating pulses. As light intensity increased between 54, 208, and 741  $\mu\text{mol photons m}^{-2} \text{ s}^{-1}$  the decline in  $F_t$  increased, leading to a lower actinic light baseline. This decline was apparent in the wild type,  $\text{pcpcT} \rightarrow \text{C}$ , and  $\Delta\text{CpcC1C2}:\text{pcpcT} \rightarrow \text{C}$  strains, although in  $\text{pcpcT} \rightarrow \text{C}$  fluorescence increased for the first few minutes before declining. Fluorescence in the olive mutant declined rapidly in the first minute after the initial actinic light spike and stabilized at the pre-illumination level at 54, slightly higher at 208  $\mu\text{mol photons m}^{-2} \text{ s}^{-1}$ , and only marginally lower at 741  $\mu\text{mol photons m}^{-2} \text{ s}^{-1}$ . The fluorescence drop may also have been due to NPQ of the photosynthetic electron transport chain by state transitions of phycobilisomes from PSII to PSI, with less excitation energy reaching the reaction centres in PSII leads to lower fluorescence (Mullineaux & Allen 1990). Lacking PC altogether, the difference in  $F_t$  change in the olive compared to the wild type due to light is likely to be caused by differences light adaptations mediated by the PBS, such as state transitions.

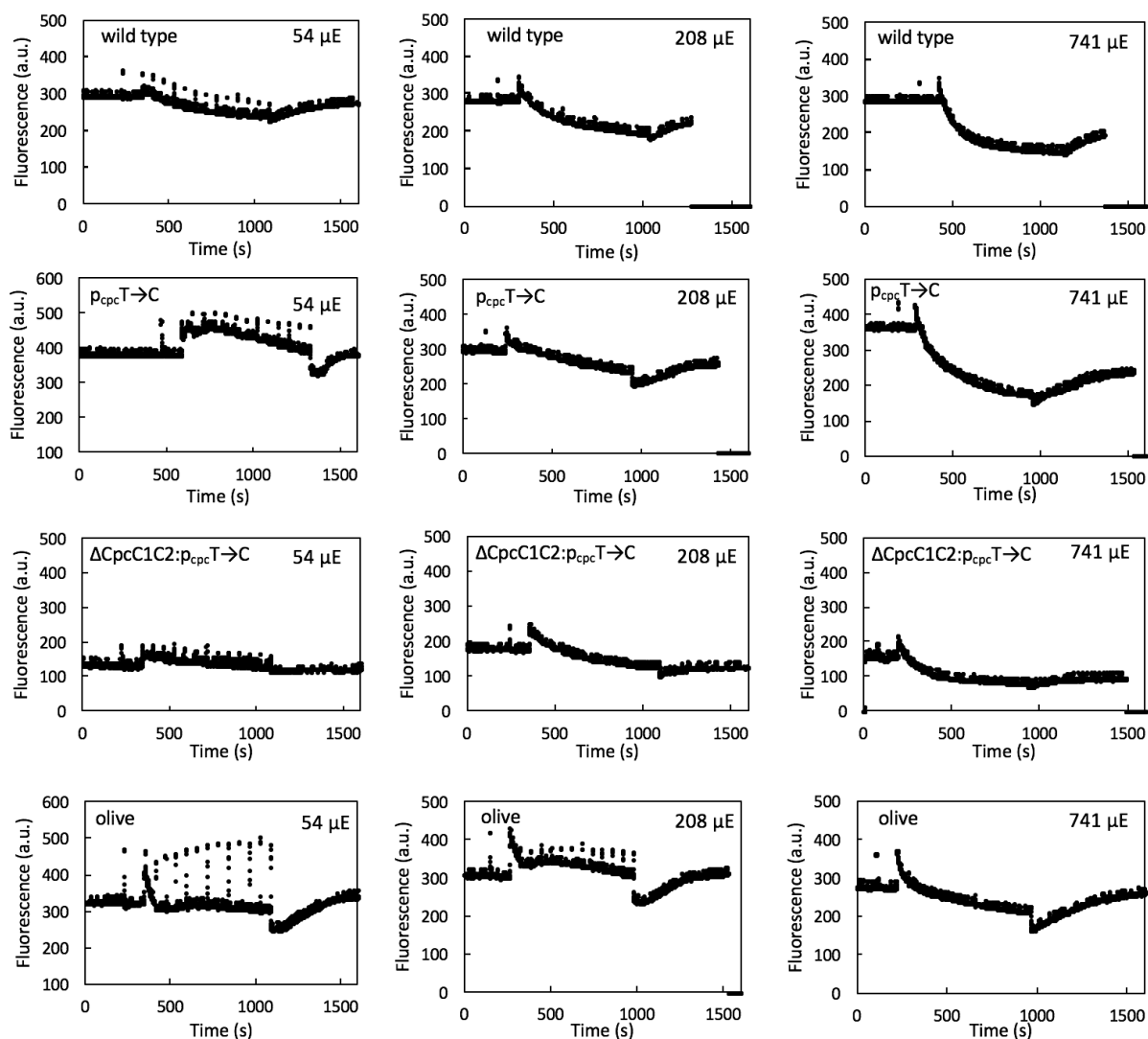


**Fig. 4.8:** Fluorescence profiles of representative samples from induction curves of the wild type,  $p_{cpc}T \rightarrow C$ ,  $\Delta CpcC1C2:p_{cpc}T \rightarrow C$ , and olive at 54, 208, and 741  $\mu mol photons m^{-2} s^{-1}$  from electrogenic biofilms in PAM adapted BPV devices.

#### 4.2.4.2. PBS antenna mutants confound derivation of photosynthetic parameters:

To compare the efficiency of photosynthetic light use, several parameters were calculated from the induction curves in PAM/BPV devices containing biofilms of wild type *Synechocystis* and the antenna mutants. These were quantum efficiency ( $Y(II)$ , or  $F_v/F_m$ ) – the proportion of absorbed light being used for photochemistry, heat dissipation ( $Y(NO)$ ) – the proportion of absorbed energy dissipated as heat, and non-photochemical quenching ( $Y(NPQ)$ ) – the

proportion of absorbed energy dissipated as a result of photoprotective mechanisms upregulated in response to sustained light exposure. Fig. 4.9 shows the stacked proportions of the coefficients of quantum efficiency, heat dissipation, and non-photochemical quenching. At low light we saw a slight reduction in  $Y(II)$  in the  $p_{cpc}T \rightarrow C$  and  $\Delta CpcC1C2:p_{cpc}T \rightarrow C$  mutants, and despite complete removal of PC the olive mutant retained similar  $Y(II)$  to the wild type at  $54 \mu\text{mol photons m}^{-2} \text{ s}^{-1}$  actinic light. However, at medium and high light the quantum efficiency was higher than the wild type.  $Y(NPQ)$  from both  $p_{cpc}T \rightarrow C$  and the olive mutants was significantly lower than the wild type at  $54 \mu\text{mol photons m}^{-2} \text{ s}^{-1}$ ; at  $208 \mu\text{mol photons m}^{-2} \text{ s}^{-1}$   $Y(NPQ)$  from  $p_{cpc}T \rightarrow C$  was still lower than the wild type but only by a small margin, as was  $Y(NPQ)$  from  $\Delta CpcC1C2:p_{cpc}T \rightarrow C$ , whereas  $Y(NPQ)$  from the olive remained less than half that of the wild type. At  $714 \mu\text{mol photons m}^{-2} \text{ s}^{-1}$   $Y(NPQ)$  was similar between the wild type and  $p_{cpc}T \rightarrow C$ , slightly lower in  $\Delta CpcC1C2:p_{cpc}T \rightarrow C$ , and significantly lower from the olive mutant. These results suggest that removing PC increases quantum efficiency and reduces sensitivity to NPQ upregulation as actinic light intensity increases. However, as will be discussed in the following sections, measurements of quantum efficiency obtained from cyanobacteria are known to be lower than for eukaryotic algae due to the interference of the phycobilisome (Schuurmans et al. 2015).

To test whether the total amount of PC in the cell affected measurements of NPQ, a strain with the PC antenna linker protein knocked out without the *cpc* promoter single base pair substitution causing a downregulation of PC expression (Lea-Smith et al. 2014),  $\Delta CpcC1C2$ , was tested using the same protocol in the PAM/BPV device (Fig. 4.9). If PC content had no effect we would have expected similar results from the  $\Delta CpcC1C2$  and  $\Delta CpcC1C2:p_{cpc}T \rightarrow C$  mutants. However,  $Y(NPQ)$  from  $\Delta CpcC1C2$  had slightly lower  $Y(II)$  and  $Y(NPQ)$  at low light, but otherwise a similar profile to the wild type and  $\Delta CpcC1C2:p_{cpc}T \rightarrow C$ . Therefore, the

calculation of PAM fluorescence parameters using  $F_0$  and  $F_M$  is likely to be dependent on total amount of PC rather than light harvesting PBS antenna length, and care must be taken in interpreting results.

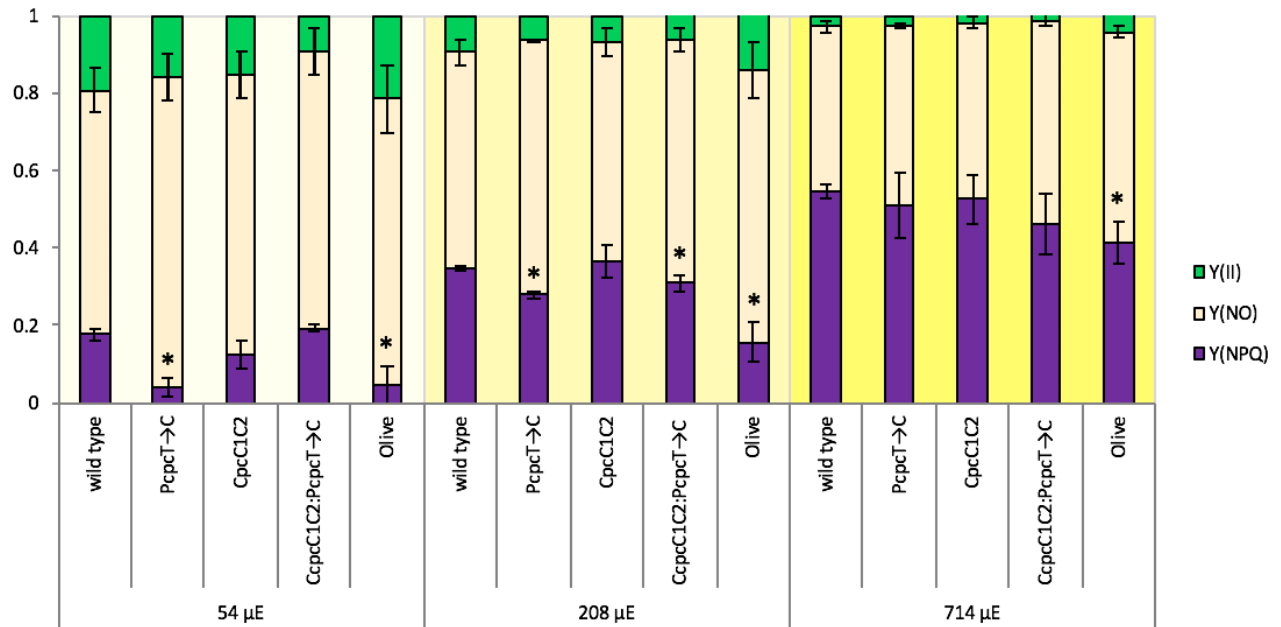


**Fig. 4.9:** The relative coefficients of quantum efficiency (Y(II)), rapid, uncontrolled heat dissipation (Y(NO)), and regulated non-photochemical quenching (Y(NPQ)), are shown for each strain at each actinic light intensity. Results are an average of at least 3 biological replicates and obtained from PAM induction curves on wild type *Synechocystis* and the pcpct→C, ΔCpcC1C2, ΔCpcC1C2:pcpcT→C, and the olive strains in PAM adated BPV devices. Three different light intensities are shown, 54, 208, and 714 μmol photons m<sup>-2</sup> s<sup>-1</sup>. Asterisks indicate a statistically significant difference from the wild type in each actinic light condition (Student's t-test with Welch's correction, p<0.05). Error bars show the standard error for Y(NPQ) and Y(II).

The magnitude of  $F_0$  measured from cyanobacteria is sensitive to phycobiliprotein content (Campbell et al. 1998). However, there is an alternative means of calculating NPQ which

compares the ratio of actinic light induced change in saturating pulse fluorescence without depending on the absolute value of the initial dark adapted  $F_0$ . In order to test whether PC interference still affected NPQ without taking  $F_0$  into consideration, NPQ was recalculated using the equation in Methods section 2.3.9. This effectively gave a measure of the reduction in the magnitude of the saturating pulse fluorescence peak relative to the initial dark adapted saturating pulse. At low light ( $54 \mu\text{mol photons m}^{-2} \text{s}^{-1}$ ), NPQ, as calculated by this method for  $\text{pcpcT} \rightarrow \text{C}$  and the olive mutant, was lower compared to the wild type (Fig. 4.10). All three antenna truncation mutants had lower NPQ at  $208 \mu\text{mol photons m}^{-2} \text{s}^{-1}$ , however, due to an increase in variation at  $714 \mu\text{mol photons m}^{-2} \text{s}^{-1}$ , only the olive mutant had significantly lower NPQ at high actinic light. The  $\Delta\text{CpcC1C2}$  strain has slightly lower NPQ at low actinic light, but similar levels to the wild type at medium and high light. Given two primary mechanisms of NPQ –  $\text{OCP}^{\text{O/R}}$  exciton energy shunting and state transitions – involve the PBS, and if we assume to have avoided the affect of PC by omitting  $F_0$  then these data would support the idea that reducing antenna size reduces NPQ, either by lowering the threshold for activation by lowering light absorption or by interfering with the mechanism. However, the  $\Delta\text{CpcC1C2}$  results being similar to the wild type show that despite the functional PBS being significantly truncated to antennae with one PC disk, the remaining free floating PC in the cell still contributes to the fluorescence profile.

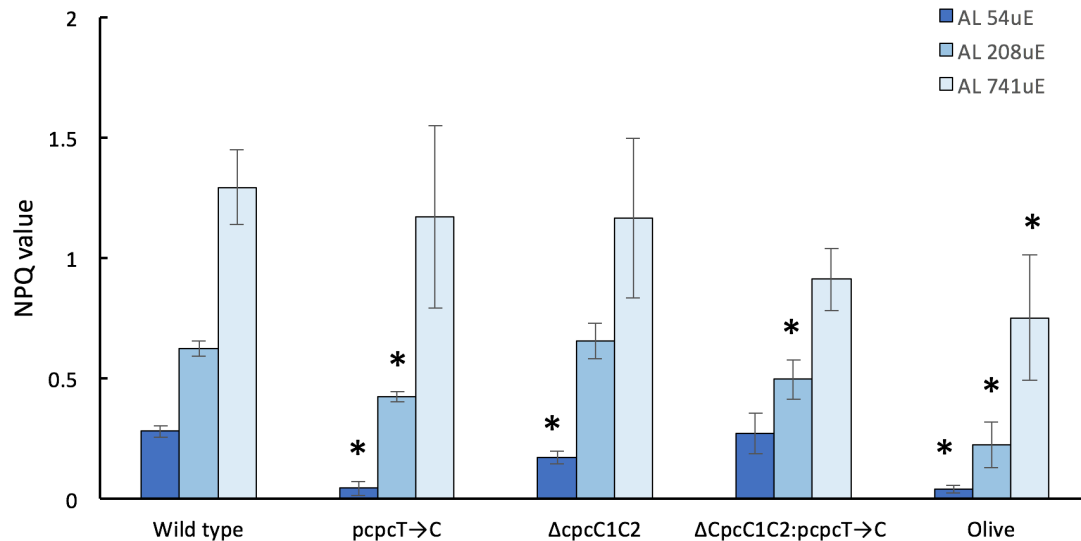


**Fig. 4.10:** NPQ values for the wild type,  $pcpcT \rightarrow C$ ,  $\Delta CpcC1C2$ ,  $\Delta CpcC1C2:pcpcT \rightarrow C$ , and the olive strains taken from the end of the induction curve, at three different light intensities. Asterisks denote values significantly different from the wild type, from at least three biological replicates and error bars show the standard error.

#### 4.2.4.5. Relative NPQ changes within strain:

Although the data appear to show a decrease in NPQ from the antenna mutants, the results from the  $\Delta CpcC1C2$  strain show that PC interference is a potentially confounding factor when comparing NPQ changes between strains. In order to test how NPQ changes within strain, a separate set of PAM/BPV experiments were conducted using just the wild type and the olive strains over the same range of actinic light intensities. Fig. 4.11a shows the NPQ values for the wild type and the olive over the course of induction curves. The absolute level of calculated NPQ in the wild type was much higher than in the olive even at low light of  $70 \mu\text{mol photons m}^{-2} \text{s}^{-1}$ , and increased to 3-fold higher than the olive at  $700 \mu\text{mol photons m}^{-2} \text{s}^{-1}$ . In both wild type and olive strains the step increase in NPQ between  $70$  and  $320 \mu\text{mol photons m}^{-2} \text{s}^{-1}$  was greater than between  $320$  and  $700 \mu\text{mol photons m}^{-2} \text{s}^{-1}$ , suggesting a low light threshold for NPQ activation. NPQ at low light from the olive was almost at ground state, suggesting it had

barely been triggered. The factor of increase of NPQ (Fig. 4.11b) was greater for the olive between low and medium light intensity and between low and high intensity, although this could be an artefact of very low NPQ at low light. Between medium and high light, however, the factor of increase in NPQ was smaller overall, but relatively larger in the wild type than the olive, although not statistically significant. This may be down to decreased sensitivity to high light stress in the olive strain, and once a low level of NPQ is occurring it may be less sensitive to further increases in light intensity.

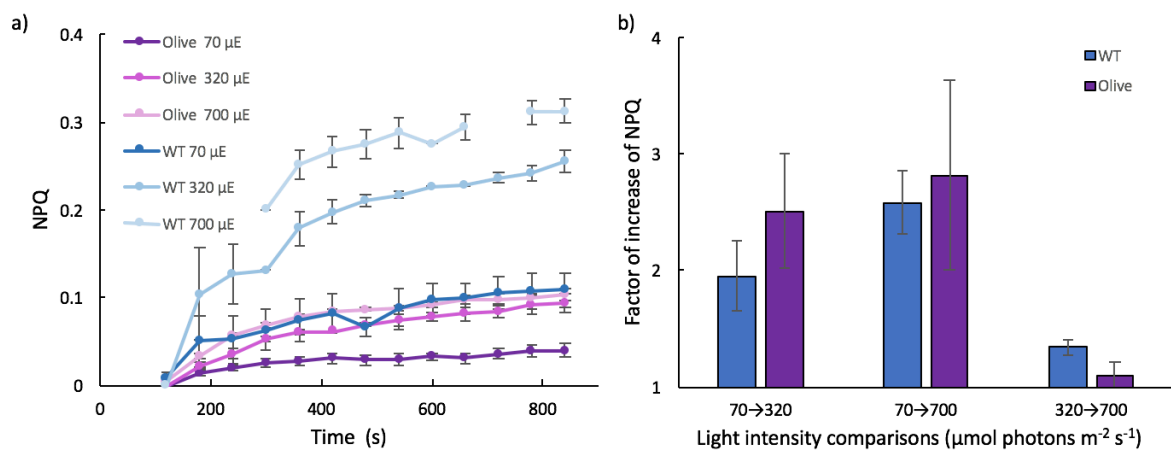


**Fig. 4.11:** a) NPQ values from induction curves from wild type, *pcpcT*→C,  $\Delta\text{CpcC1C2}$ ,  $\Delta\text{CpcC1C2}:\text{pcpcT}→C, and the olive strains from 70, 320, and 700  $\mu\text{mol photons m}^{-2} \text{s}^{-1}$  in PAM adapted BPV devices. b) Ratios of the increase in NPQ from 70 to 320, 320 to 700, and 70 to 700  $\mu\text{mol photons m}^{-2} \text{s}^{-1}$  at the end of the induction curve. Results are an average of three biological replicates for the olive and two for the wild type and error bars show the standard error.$

#### 4.2.4.6. Effect of bias potential on NPQ:

The effect of bias potential on fluorescence was demonstrated earlier, and because anode potential interferes somehow with the photosynthetic machinery, it is possible that it could

influence NPQ and other parameters. Previous PAM experiments were performed in the PAM/BPV device at OCP; without applying a bias potential, open circuit potential typically stabilizes between -0.1 V and -0.3 V for *Synechocystis*. To test if bias potential affects how NPQ changes as actinic light increases, NPQ was measured as above from two PAM/BPV devices with a negative bias potential – set at the positive value opposite to the OCP of each sample to cancel out any biologically produced electrochemical potential – and at a positive bias potential of 0.4 V – ‘encouraging’ the transfer of electrons to the anode. Fluorescence from the biofilms in the PAM/BPV devices was stabilized at each bias potential and dark adapted before commencing PAM induction curves. In Fig. 4.12, at low actinic light of 70  $\mu\text{mol photons m}^{-2} \text{s}^{-1}$ , the magnitude of NPQ is similar between the olive and the wild type, however applying 0.4 V appeared to have the opposite effect, decreasing NPQ slightly in the wild type, and increasing it slightly in the olive. At 320  $\mu\text{mol photons m}^{-2} \text{s}^{-1}$  and -0.4 V, NPQ from the olive had increased slightly at OCP, but decreased marginally when exposed to the positive bias potential 0.4 V. This supports the idea that removing PC reduces sensitivity to NPQ upregulation from low to medium light, and suggests that a positive bias potential may also reduce the sensitivity to NPQ upregulation. The threshold for activation of NPQ may be increased by facilitating EET as an alternative route to oxidise the electron transport chain. NPQ from the wild type sample is reduced by a greater factor at 320 compared to 70  $\mu\text{mol photons m}^{-2} \text{s}^{-1}$ , suggesting that any photoprotection increases in magnitude at higher light. Unfortunately, equipment error meant only a single measurement could be made for each strain, so only limited conclusions can be drawn. Further work to test possible photoprotection mechanisms or interference with NPQ regulation from a positive bias potential may yield insights into the electron transfer pathway from thylakoid to extracellular electron transfer.

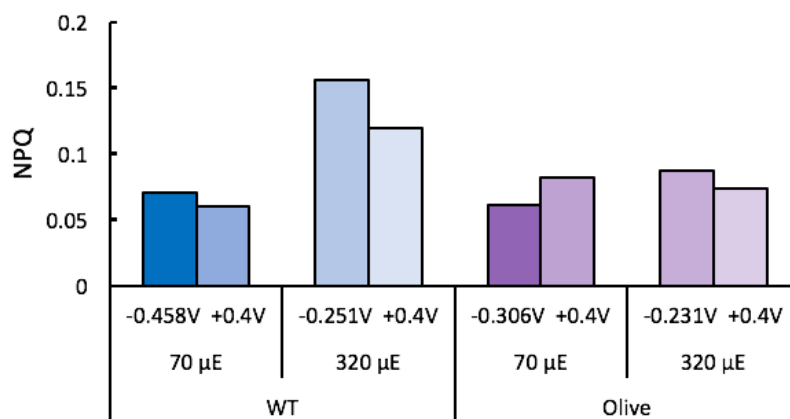


**Fig. 4.12:** NPQ values for the wild type and olive strains subjected to positive and negative bias potentials, taken from the end of an induction curve at 70 and 320  $\mu\text{mol photons m}^{-2} \text{s}^{-1}$ . Results are from single replicate each.

### 4.3. Discussion:

#### 4.3.1. Simultaneous PAM fluorescence and chronoamperometry as a technique to probe BPV efficiency:

PAM fluorescence is increasingly being used as a complementary tool to electrochemical measurements to investigate the link between photosynthetic efficiency and EET (Ciniciato et al. 2016; Ng et al. 2017; Fu et al. 2017). Using custom designed PAM/BPV devices we tested how the photosynthetic machinery responds to the unnatural environment of the anodic chamber. We demonstrated a direct effect of anode potential on PAM fluorescence from *Synechocystis*, with basal fluorescence increasing steadily from 0.1 V to 0.5 V. Further work will be needed to pin down the underlying mechanisms linking external potential to photosystem redox state, and could inform future device and experimental designs to optimize photosynthetic efficiency in BPV outputs. In figures 4.5 – 4.7 we apply a methodology correlating PAM fluorescence with chronoamperometry to estimate the efficiency of

photochemically produced electrons reaching the anode as BPV current. Light absorbance was adjusted as much as possible with some measured and some existing and accepted parameters. McCormick et al. (2015) cite the biophotovoltaic efficiency calculated by an early study from Ochiai et al. (1983) as 0.5%, close to our estimates of 0.1-0.2%. This is far from the near 100% efficiency of carbon substrate conversion achieved by anaerobic bacteria species in MFCs such as *Geobacter* (Nevin et al. 2008), but may be due to the evolution of efficient metabolic use of photosynthetic electrons for carbon fixation and growth and photoprotective mechanisms. Data collection was in part hampered by the temperamental nature of the PAM device. The Walz Mini-PAM is designed for field work and the halogen lamp regularly overheated after repeated use causing measurements to be skipped without warning. The inbuilt calculation of ETR also did not function, but it could be calculated from the quantum efficiency, PAR, approximated light absorbance. Further work to develop this method with a more defined system could provide more precise measurements of BPV efficiency. Successful incorporation of a non invasive oxygen probe could increase precision, ultimately paving the way to a more complete electrochemical characterization of cyanobacteria with quantification of internal cell current and treatment of metabolic electron sinks as internal resistors.

#### **4.3.2. PBS truncation may reduce NPQ in *Synechocystis*:**

Another potential consequence of altering light absorbance is reduced energy dissipation by regulated mechanisms, especially in the light saturated upper layers of a biofilm. Tian et al. (2013) found that the fluorescence quenching by NPQ was reduced in PBS truncated mutants, with fewer PBSs quenched by blue light induced OCP<sup>O/R</sup>. We used PAM fluorimetry to characterize changes in photosynthetic efficiency and NPQ. However, this was not without its drawbacks, and conclusions had to be drawn cautiously. Use of PAM techniques in cyanobacteria is known to be complicated by interference from the PBS and overlapping

respiratory and cyclic electron flow pathways (Laczko-Dobos et al. 2008), making it difficult to compare quantum efficiency of photosynthesis between species, and particularly between cyanobacteria and eukaryotic algae. High  $F_0$  values due to PBS and PSI fluorescence lead to an underestimation of cyanobacterial photosynthetic efficiency compared to eukaryotic algae (Campbell et al. 1998; Acuña et al. 2015; Schuurmans et al. 2015). Nevertheless, the technique is valid for monitoring photosynthesis related fluorescence from a single species as in this study, except that by altering the phycobilisome antennae we are potentially interfering with apparent fluorescence values. The PAM fluorescence signal is influenced by the abundance of PBS-PSII, free PSI, and PBS-PSI complexes (Acuña et al. 2015) as well as  $OCP^{O/R}$  mediated NPQ (Wilson et al. 2006), so state transitions should be apparent from the fluorescence trace of the induction curves. Therefore the  $F_t$  profile throughout the induction curve sequence offers an indication of NPQ independent of the relative magnitude of fluorescence between PC knockouts. The drop in fluorescence is less pronounced for the olive mutant in figure 4.8, which may be attributable to both the  $OCP^{O/R}$  and state transitions. The threshold for triggering state transitions may be altered by not just reduced light absorption, but by the altered state of electron transport in the thylakoid membrane caused by increased proportion of PSII. The olive mutant is still capable of state transitions (Bernát et al. 2009), however, decreased size of PBS may affect migration rates between PSII and PSI, although this has not been proven. The attachment of  $OCP^{O/R}$  may also be affected, however the site of attachment is the TEM under the AC core (Maksimov et al. 2014), which should not be affected by PC loss. A strategy to overcome the complications of interference by PC was the comparison within the olive mutant and the wild type, showing that the relative change in NPQ from medium to high light may be reduced in the olive compared to the wild type. This suggests that although removing PC may reduce the amount of light absorbed per cell, the window of optimal light intensity to BPV current conversion throughout the biofilm is increased not only by deeper light path length and

less shading, but also less sensitive activation of energy dissipation by NPQ. In eukaryotic algae truncation of light harvesting antenna was shown to reduce NPQ (Shin et al. 2016), and NPQ related proteins have been targeted to artificially reduce NPQ in order to increase productivity (Berteotti et al. 2016). So, engineering  $OCP^{O/R}$  and state transitions in cyanobacteria could also lead to improved productivity or EET, for example by  $OCP^{O/R}$  knockout or potentially by locking the PBS in state I attached to PSII. It may also be possible that BPV output is complementary to NPQ, relieving stress from excess light by EET, however the electron export pathway from the thylakoid membrane to the outer cell membrane and the anode remains to be elucidated.

#### **4.4. Conclusions:**

Here we show that the anode potential has a direct effect on fluorescence from photosynthetic reaction centres, posing further questions as to how EET and photosynthesis are linked. We relate photosynthetic electron production directly to biophotovoltaic current, and propose the further development of this technique as an analytical tool to help characterize the biology underlying and powering the electrochemical interaction. Finally, the effect of PBS antenna truncation on NPQ is investigated, and although inherently confounded by altering PC content, NPQ is tentatively concluded to be reduced in the olive mutant.

## 5. ENHANCED BIOPHOTOVOLTAIC PHOTOCURRENT FROM KNOCKOUTS OF COMPETING ELECTRON SINKS IN *SYNECHOCYSTIS*

### 5.1 Introduction:

#### 5.1.1. Electron sinks in the electron transport chains of *Synechocystis*:

The photosynthetic electron transport chain (PETC) is buffered by electron sinks that help regulate the redox state of components such as the PQ pool to prevent overreduction and potentially damaging production of reactive oxygen species. In a physiological context these mechanisms prevent the rate of electron excitation and NADP<sup>+</sup> or ferredoxin reduction by PSI from being the rate limiting step, which would lead to a back log of reduced PQ in the thylakoid membrane. In the context of a BPV device, removing competing electron sinks may therefore be another strategy to increase the rate of extracellular electron transfer. Bradley et al. (2013) showed that removal of the three cyanobacterial terminal oxidases cytochrome *c*-oxidase (COX), cytochrome *bd*-quinol oxidase (Cyd), and the alternative respiratory terminal oxidase (ARTO) effected a 24-fold increase in rate of ferricyanide reduction in the dark compared to wild type along with a lesser, non- statistically significant further increase under low light (14-40  $\mu$ E), where carbon dioxide would be the preferred terminal electron acceptor. They also observed an increase in power output from a ferricyanide mediated BPV device. This was likely to be due to the rate of PSII reduction not exceeding the rate of carbon fixation and/or demand from other electron sink pathways. The triple mutant was also found to have increased sensitivity to square wave light changes (Lea-Smith et al. 2013), suggesting the terminal oxidases allow the cell to adapt to increasing oxidative stress caused by rapid increases in light intensity. The flavodiiron (Flv) proteins also offer photoprotection of the PETC, with Flv2/4 putatively accepting electrons from PSII and Flv1/3 from PSI to prevent overreduction,

especially during fluctuating light levels (Allahverdiyeva et al. 2013). Deletion of Flv1/3 results in decreased carbon fixation and nitrogen assimilation in constant and fluctuating light conditions, and an increase in Flv2/4 expression in fluctuating light (Mustila et al. 2016). Flv2/4, found in only cyanobacteria, may dissipate up to 30% of PSII generated electrons to reduce oxygen water, providing a vital alternative electron pathway to protect vulnerable PSII from ROS (Luca Bersanini et al. 2014). Flavodiiron protein deletion may reduce the proportion of electrons dissipated in order to protect the PETC, although their importance for cell viability may negate any increase in electron export.

#### **5.1.2. Metabolic electron sinks downstream of the thylakoid electron transport chain:**

Downstream from the PETC, other electron sink pathways could be targeted to reduce the competition for reducing power. The pathway for electron transfer between the thylakoid electron transport chain and the outer cell membrane is not known, although inhibitor studies have shown electrons reaching the anode leave the PETC *via* PSI (Bradley et al. 2012). It is likely that the electron export mechanism is supplied by electron carriers such as NADPH, ferredoxin, or ferredoxin NADP<sup>+</sup> reductase (FNR), so there will be significant competition from other metabolic pathways.

**Nitrate uptake and conversion to ammonia:** The assimilation of nitrate is essential for a wide range of physiological functions and a growth limiting factor in natural environments, and nitrate/nitrite uptake is closely regulated alongside bicarbonate uptake to balance nitrogen and carbon metabolism (Koropatkin et al. 2006). Nitrates permeating into the periplasm are brought into the cytoplasm by a specific binding complex (NrtA) and transmembrane porin channel before they are reduced to ammonia. The two-gene nitrate assimilation pathway in *Synechocystis* consists of *narB* (nitrate reductase). and *nirA* (nitrite reductase). NarB and NirA

convert nitrates ( $\text{NO}_3^-$ ) to ammonia ( $\text{NH}_4^+$ ), utilizing 2 and 6 electrons respectively from ferredoxin (Baebprasert *et al.* 2011). Gutthann *et al.* (2007) found that inhibition of nitrogen uptake by impairment of NarB synthesis was found to divert significant electron flux to increasing hydrogen production.

**Bi-directional hydrogenase activity:** Baebprasert *et al.* (2011) demonstrated an increase in hydrogen output from *Synechocystis* after inactivating *nirA* and *narB*, and diverting electron flux to the bi-directional NiFe-hydrogenase. The bi-directional NiFe-hydrogenase HoxEFUYH in *Synechocystis* is unusual in that it can reversibly catalyze the formation of hydrogen gas from  $\text{H}^+$  and reduction by ferredoxin, allowing temporary storage of reducing power as  $\text{H}_2$  that can be converted back into  $2\text{H}^+ + 2\text{e}^-$  and transferred into the PQ pool via cyclic electron flow. It acts as a redox regulator that may help the cell adapt to conditions such as rapid light changes and oxidative and sugar stresses (Gutthann *et al.* 2007, Ortega-Ramos *et al.* 2014). HoxH plays a key role in the cyanobacterial electron transport network and readily oxidises ferredoxin, so for our purposes of electricity production we targeted one of the subunits, *hoxH*, for deletion. The bi-directional NiFe-hydrogenase has been shown to be an essential electron sink under conditions mimicking phytoplankton blooms i.e. large amounts of dissolved organic carbon and dissolved nitrogen (Gutekunst *et al.* 2014).

**Reduction of external cell signaling mediators:** The fourth electron sink targeted was the nitric oxide reductase NorB, which forms an N-N bond to reduce toxic nitric oxide (NO) to nitrous oxide ( $\text{N}_2\text{O}$ ) in *Synechocystis* (Busch *et al.* 2002) as a side effect of respiratory denitrification. In a non-denitrifying organism NorB may serve principally as a detoxifying agent or to regulate intercellular communication mediated by NO (Richardson 2000). *NorB* in *Synechocystis* is thought to be dependent on quinol oxidation from the cytoplasmic membrane, rather than cytochrome-*c* dependent (Büsch *et al.* 2002; Gonska *et al.* 2018), therefore we

expected it to be a good candidate for increasing electron output by inactivation.

Here we describe the generation of knockout mutants in *Synechocystis* of a combination of multiple electron sinks. We demonstrate that removing the nitrate assimilation pathway reduces growth rate, but increases the rate of EET to ferricyanide and an electrode in a BPV system, and that sequential inclusion of the other knockouts results in a cumulative increase in BPV output.

## **5.2. Results:**

### **5.2.1. Generation of unmarked electron sink knockouts in *Synechocystis*:**

In order to test whether the removal of electron sinks affects extracellular electron transport from *Synechocystis*, unmarked knockout strains were generated that removed a bi-directional hydrogenase, the nitrate uptake pathway, and a nitric oxide reductase from both wild type background and in a strain already lacking all three terminal oxidases.

### **5.2.2. *Synechocystis* knockout vector construction:**

To perform genetic modification of *Synechocystis* by homologous recombination, two plasmid vectors were assembled using standard cloning techniques as detailed in the Methods section. The first plasmid contained a kanamycin and sucrose sensitivity selection cassette between flanking regions surrounding the target gene to create a marked knockout by homologous recombination. The second plasmid was the intermediary step in the construction of the first, containing only the flanking regions, and was used to remove the selection cassette and create a stable unmarked knockout of the target gene. PCR amplification of vector fragments was

performed using Phusion high fidelity polymerase (NEB) to ensure identity between the target flanking regions in the vector and the genomic target. Primers used to amplify flanking regions with restriction digest sites and to verify gene knockout are listed in Table 5.1.

The gene knockout vector for the nitric oxide reductase *norB* (sll0450) was constructed by amplifying a 904bp 3' fragment upstream (left) of sll0450 from *Synechocystis* using primers Sll0450leftfor and Sll0450leftrev and a 914bp 5' fragment downstream (right) using primers Sll0450rightfor and Sll0450rightrev. The amplified fragment PCR products were purified and inserted into the restriction digest sites *XbaI/BamHI* and *SacI/EcoRI* sites of pUC19 respectively to synthesize pSll0450-1 (Fig. 5.1a). pSll0450-1 was introduced into competent *Escherichia coli* DH5- $\alpha$  by transformation before plating on LB ampicillin (100  $\mu$ g/ml) agar. Successful incorporation of upstream and downstream flanking region insertions, replacing the  $\beta$ -galactosidase encoding *lacZ* was confirmed using IPTG induced Xgal blue/white selection. White colonies were picked and grown overnight in LB, plasmids were extracted using a MoBio® miniprep kit, digested with the same enzymes and checked by gel electrophoresis before verification by sequencing. The kanamycin resistance and levansucrase cassette *npt1/sacB* was then digested from pUM24Cm (Ried & Collmer 1987) and inserted into the *BamHI* site between the left and right target gene flanking regions in pSll0450-1 to generate pSll0450-2 (Fig. 5.2a). Verification of insertion was confirmed by growth on kanamycin plates and gel electrophoresis after *BamHI* digestion. Glycerol stocks were made from cells streaked on ampicillin and ampicillin + kanamycin plates using LB with 25% glycerol.

**Table 5.1 Primers used for vector construction and knockout diagnosis:**

<b>Primer:</b>	<b>Name</b>	<b>Sequence:</b>
HoxH left flanking region forward + <i>Sac</i> I	HoxHleftfor	GCATGAGCTCATTACACCGCTCACATTGG
HoxH left flanking region reverse + <i>Bam</i> H1	HoxHleftrev	GCATGGATCCATGATGTGCAAGAAGGGTTT
HoxH right flanking region forward + <i>Bam</i> H1	HoxHrightfor	GCATGGATCCAAATGGAGATTTGGCATGG
HoxH right flanking region reverse + <i>Xba</i> I	HoxHrightrev	GCATTCTAGACGAGCAACGCTAGAACCATT
NarB left flanking region forward + <i>Sac</i> I	NarBleftfor	GCATGAGCTCGAATACAGCGGAGGGAATCA
NarB left flanking region reverse + <i>Bam</i> H1	NarBleftrev	GCATGGATCCTTAGACCACAGTCGGGGATT
NarB right flanking region forward + <i>Bam</i> H1	NarBrightfor	GCATGGATCCAGGGCTGCTCCCAACTAAT
NarB right flanking region reverse + <i>Xba</i> I	NarBrightrev	GCATTCTAGACGATCGCCTAGTGATGATGA
NirA left flanking region forward + <i>Sac</i> I	NirAleftfor	GCATGAGCTCAATGGGGTTCCTACGCTAC
NirA left flanking region reverse + <i>Bam</i> H1	NirAleftrev	GCATGGATCCTAACCCTCAAGCGCAGA
NirA right flanking region forward + <i>Bam</i> H1	NirArightfor	GCATGGATCCATTTGGGTACCTGTGTCC
NirA right flanking region reverse + <i>Xba</i> I	NirArightrev	GCATTCTAGACACCGTCCCTAAAAGCTTGA
sll0450 left flanking region forward + <i>Sac</i> I	Sll0450leftfor	GATCTCTAGACACAAAACACTTCCTGCCGTA
sll0450 left flanking region reverse + <i>Bam</i> H1	Sll0450leftrev	GATCGGATCCTGCTGGGACTCCGGTATTTA
sll0450 right flanking region forward + <i>Bam</i> H1	Sll0450rightfor	GATCGAGCTCAACGGTGCAACACATCC
sll0450 right flanking region reverse + <i>Xba</i> I	Sll0450rightrev	GATCGAATTCGGATCGGACAATGAAAAAT
HoxH knockout verification forward	HoxHverfor	GGTGATGCCGGGGTATTT
HoxH knockout verification reverse	HoxHverrev	TCCGTACAACAAAATTTCCCTA
NarB knockout verification forward	NarBverfor	TCGCAACTAAATCCTGACTTTT
NarB knockout verification reverse	NarBverrev	CCGGTCATGCCATAAAAAT
NirA knockout verification forward	NirAverfor	TTAACGAAACGGGAACCCTA
NirA knockout verification reverse	NirAverrev	GACATTAACGATGGGGAAGC
sll0450 knockout verification forward	Sll0450verfor	AAAAATTCAGCGGCATACG
sll0450 knockout verification reverse	Sll0450verrev	GGCAGGGGCTGCTATCTATAA
COX knockout verification forward	COXf	CAGAAAAGGTGGATGGCATT
COX knockout verification reverse	COXr	CCACCAGGAACAGGACAACCT
ARTO knockout verification forward	Ctaf	GAGCGGTGGGTTAATTGATG

ARTO knockout verification reverse	Ctar	GCCAAAGCTGGGGTAAAGAT
Cyd knockout verification forward	Cydf	TAGGGTGGGCACAACCTCTCT
Cyd knockout verification reverse	Cydr	GGGATCAGGAAACCAATGAA

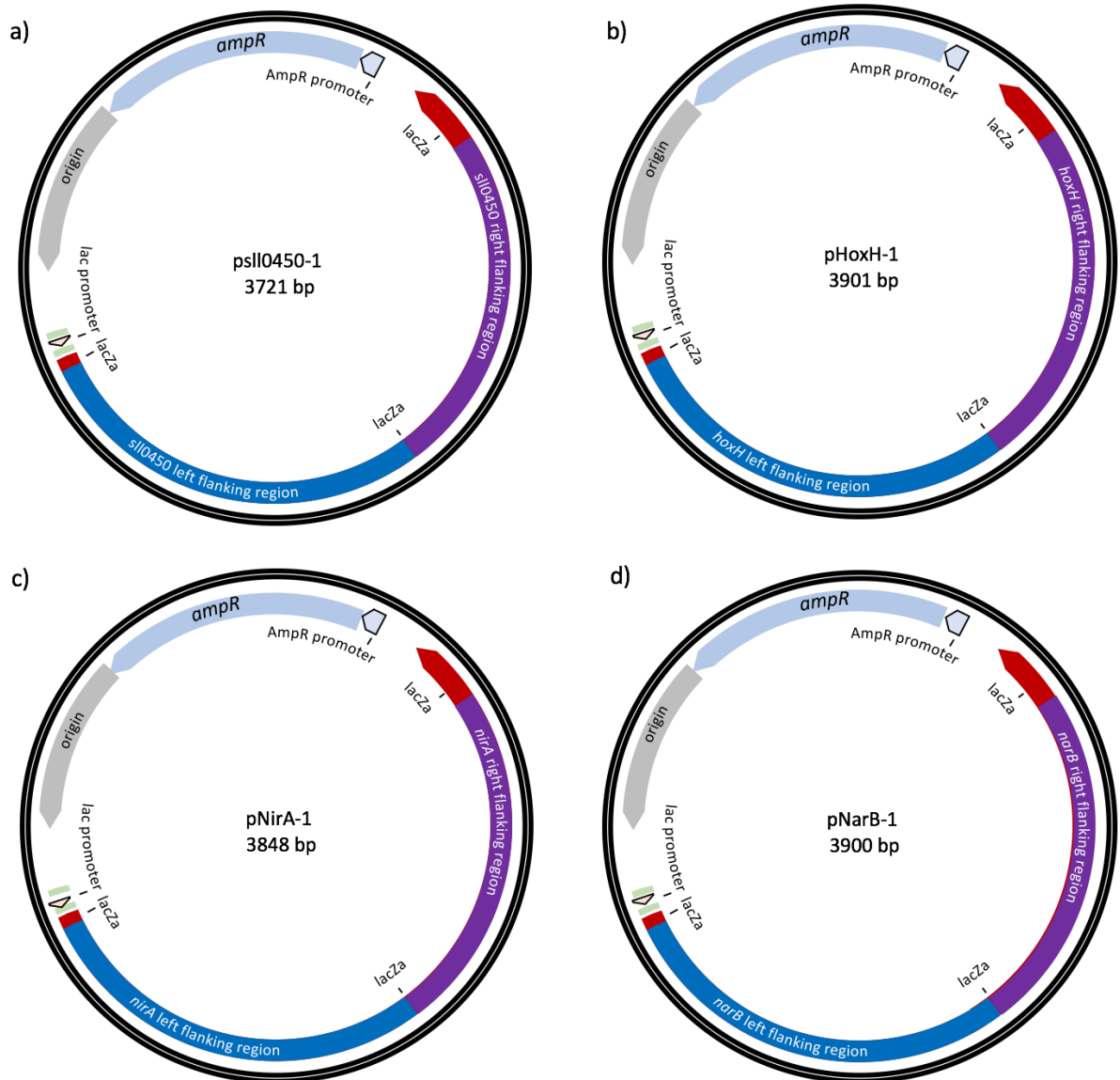


**Fig. 5.1:** Circular plasmid maps for the first stage vectors with the left and right flanking regions successfully cloned into pUC19 between *Xba*I and *Bam*HI and *Sac*I and *Eco*RI respectively, disrupting the *lacZ* gene and containing an  $amp^R$   $\beta$ -lactamase ampicillin

resistance selection marker. a) psl10450-1 for removal of the selection cassette from the  $\Delta norB$  knockout, b) pHoxH-1 for  $\Delta hoxH$ , c) pNirA-1 for  $\Delta nirA$ , and d) pNarB-1 for  $\Delta narB$ .

The gene knockout vector for *hoxH* was constructed by amplifying a 996bp 3' fragment upstream (left) of *hox* using primers HoxHleftfor and HoxHleftrev and a 1002bp 5' fragment downstream (right) using primers HoxHrightfor and HoxHrightrev. The amplified fragment PCR products were purified and inserted into the *XbaI/BamHI* and *SacI/EcoRI* sites of pUC19 respectively to synthesize pHoxH-1 (Fig. 5.1b). The *nptI/sacB* was then inserted into the *BamHI* site between left and right flanking regions in pHoxH-1 to generate pHoxH-2 (Fig. 5.2b). Knockout vectors for the nitrate reductase *narB* and the nitrite reductase *nirA* had already been generated by David Lea-Smith as follows. The gene knockout vector for *nirA* was constructed by amplifying a 975bp 3' fragment upstream (left) of *nirA* using primers NirAleftfor and NirAleftrev and a 970bp 5' fragment downstream (right) using primers NirArightfor and NirArightrev. The amplified fragment PCR products were purified and inserted into the *XbaI/BamHI* and *SacI/EcoRI* sites of pUC19 respectively to synthesize pNirA-1 (Fig. 5.1c). The *nptI/sacB* was then inserted into the *BamHI* site between left and right flanking regions in pNirA-1 to generate pNirA-2 (Fig. 5.2c). The gene knockout vector for *narB* was constructed by amplifying a 998bp 3' fragment upstream (left) of *narB* using primers NarBleftfor and NarBleftrev and a 999bp 5' fragment downstream (right) using primers NarBrightfor and NarBrightrev. The amplified fragment PCR products were purified and inserted into the *XbaI/BamHI* and *SacI/EcoRI* sites of pUC19 respectively to synthesize pNarB-1 (Fig. 5.1d). The *nptI/sacB* was then inserted into the *BamHI* site between left and right flanking regions in pNarB-1 to generate pNarB-2 (Fig. 5.2d).

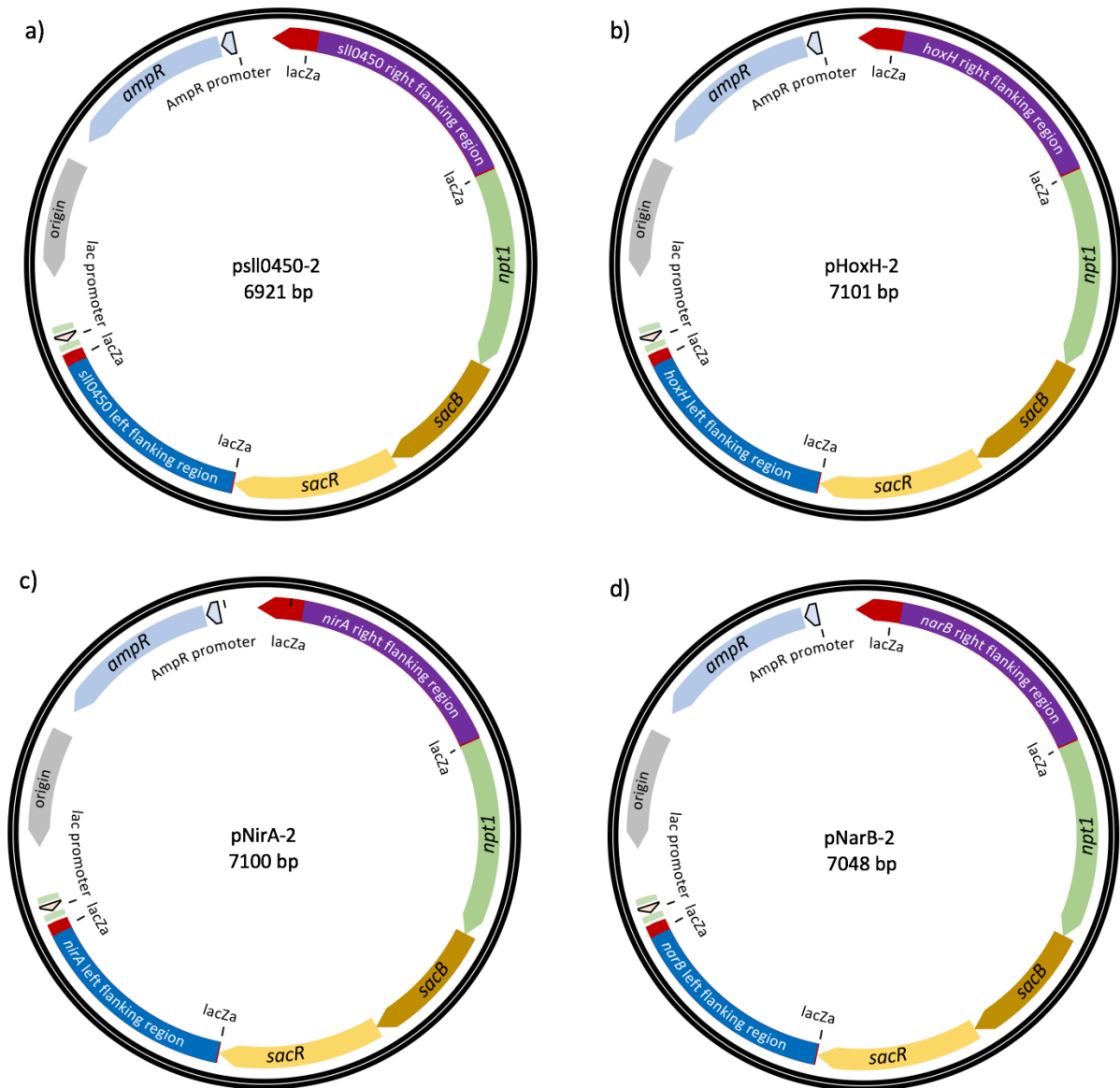


**Fig. 5.2:** Circular plasmid maps for the second stage vectors with the *npt1/sacBR* cassette cloned successfully into the *Bam*HI restriction site between the flanking regions in pUC19. a) pslI0450-2 for generation of the  $\Delta norB$  knockout, b) pHoxH-2 for  $\Delta hoxH$ , c) pNirA-2 for  $\Delta nirA$ , and d) pNarB-2 for  $\Delta narB$ .

### 5.2.3. Generation of unmarked gene knockouts in *Synechocystis* sp. PCC6803:

Unmarked gene knockouts of the terminal oxidase genes *COX*, *cyd*, and *ARTO*, were generated previously by David Lea-Smith and Robert Bradley (Bradley et al. 2013a). The terminal oxidase knockouts were confirmed by colony PCR amplification and observation of smaller

amplified fragments of expected length in the knockouts compared to the wild type (Fig. 5.4).

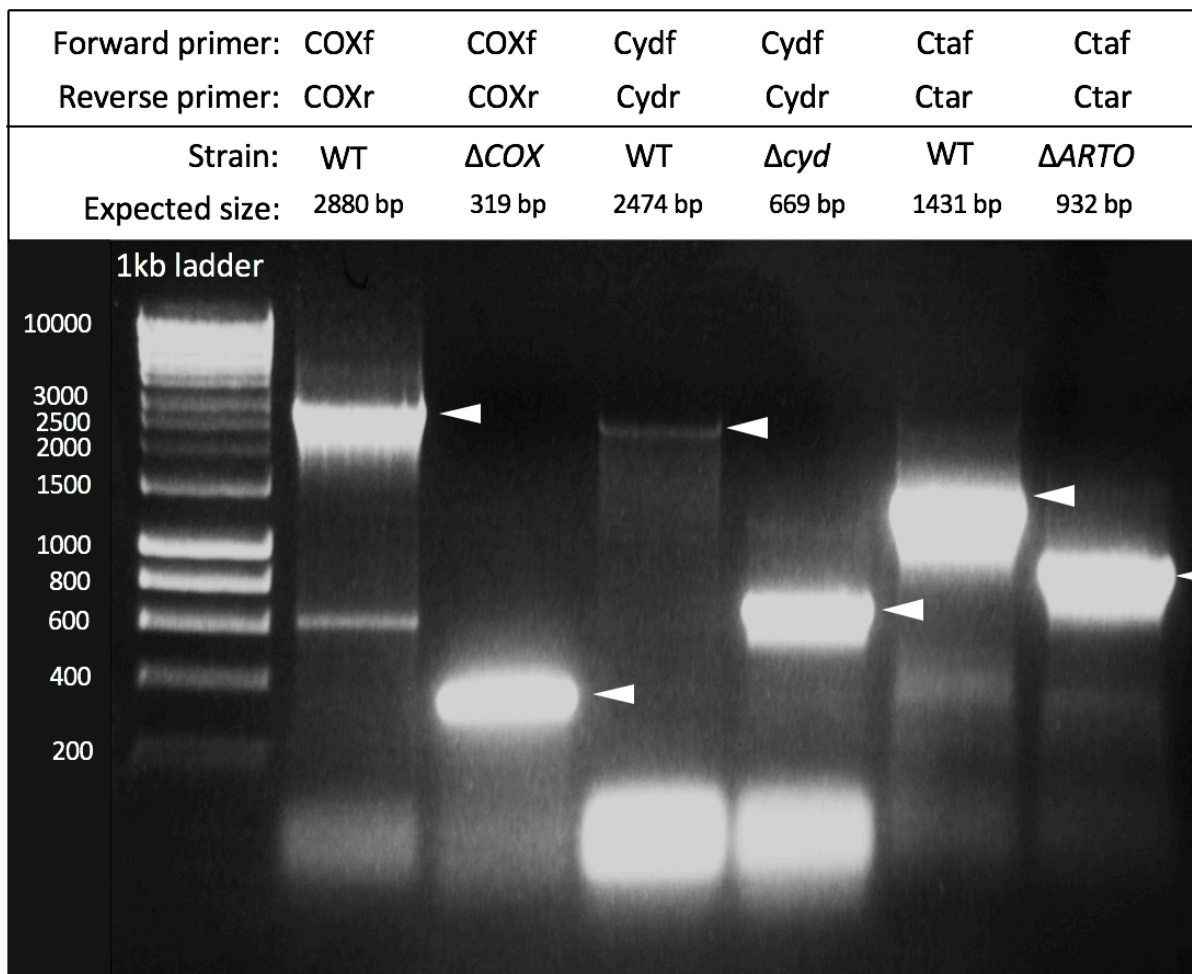


**Fig. 5.3:** Gel electrophoresis of PCR products from the wild type and unmarked terminal oxidase knockouts using their respective primers to amplify by colony PCR, with predicted fragment sizes. A white arrow indicates the faint amplification band of *Cyd* in the WT strain.

Marked knockouts for *norB*, *hoxH*, *narB*, and *nirA* were generated in both the wild type and the triple terminal oxidase backgrounds by transforming each with the knockout vector plasmid for each gene: psl10450-2, pHoxH-2, pNarB-2, or pNirA-2, containing the target gene flanking regions and the *nptI/sacB* cassette. The parent cyanobacterial strain was inoculated in freshly autoclaved BG11 medium and grown to early log phase before collection of cells by

centrifugation at 3000 rpm in a benchtop centrifuge for 10 minutes, washing once by resuspending in 2 ml BG11 and centrifugation again, before bringing to a final volume of 200  $\mu$ l with fresh BG11 medium. 1  $\mu$ g of plasmid was added to the cells at the base of a 20 ml tube sealed with cotton wool. The cells were incubated under 20  $\mu$ mol photons  $\text{m}^{-2} \text{s}^{-1}$  for 6 hours at 30°C, with mixing every 2 hours before recovery by adding 1.8 ml of BG11 medium and incubation for a further 4 days in a shaker incubator. 20 and 80  $\mu$ l of transformation culture was plated on BG11 plates (plus  $\text{NH}_4\text{Cl}$  for *narB* and *nirA* knockouts), followed by pouring over each plate 3 ml of 0.6% agar plus kanamycin (0.5 mg/ml), cooled to 42°C. After incubation under 40  $\mu$ mol photons  $\text{m}^{-2} \text{s}^{-1}$  at 30°C for c. 1 week, roughly 20 colonies were streaked on BG11-kanamycin (30  $\mu$ g/ml) plates and incubated for a further week. Replacement of the target genes between the flanking regions with the *nptII/sacB* cassette as in Fig. 5.4a,i was tested by colony PCR with Promega Taq polymerase using the reverse primer of the upstream 5' flanking region and forward primer of the downstream 3' flanking region.

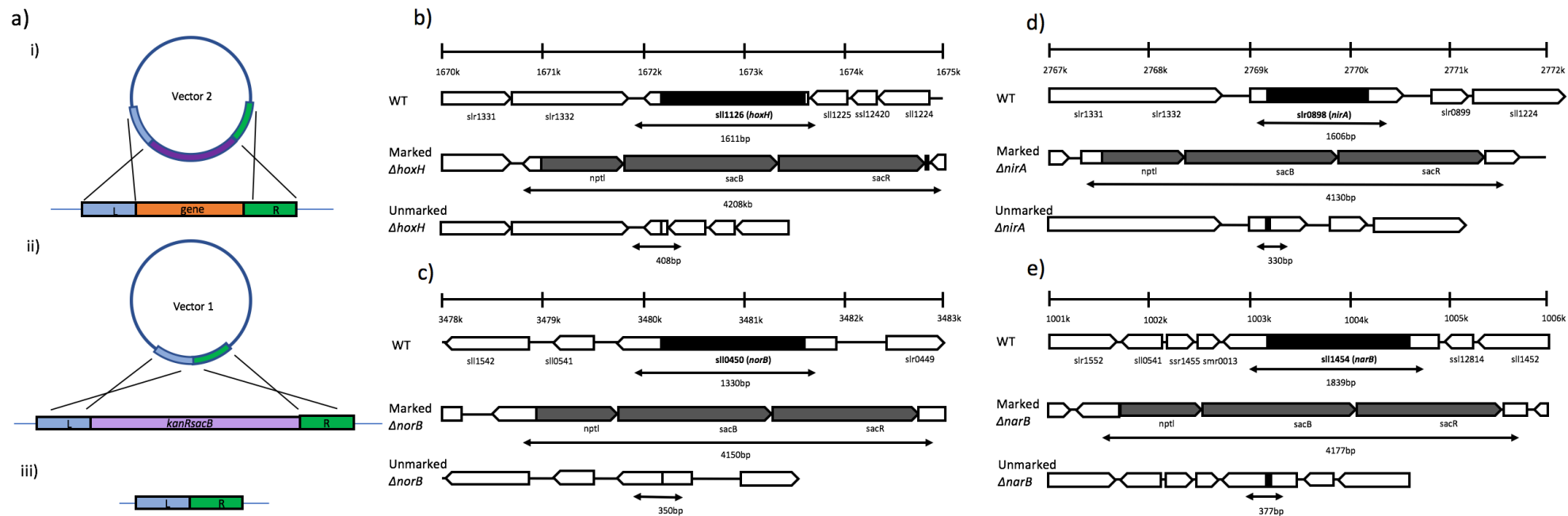


**Fig. 5.4:** a) Diagrams of gene knockout strategy in *Synechocystis* showing i) insertion of the *nptI/sacB* cassette by homologous recombination on the two flanking sites using the stage 2 vector, ii) a second homologous recombination using the stage 1 vector to remove the *nptI/sacB* cassette, leaving iii) an unmarked knockout of the target region. The strategy for each gene with expected amplification sizes of wild type, marked, and unmarked strains is shown in a) for *hoxH*, b) for *norB*, d) for *nirA*, and d) for *narB*.

Fig. 5.5b-e illustrates the target sequences, the resulting marked knockout region containing the *nptI/sacB* cassette, and the unmarked knockout with the loss of the *nptI/sacB* cassette and the predicted amplification product sizes for each. To generate unmarked knockouts, the confirmed marked knockout was inoculated in freshly autoclaved BG11 medium and grown to early log phase before collection of cells by centrifugation at 3000 rpm in a benchtop centrifuge for 10 minutes, washing once by resuspending in 2 ml BG11 and centrifugation again, before bringing to a final volume of 200  $\mu$ l with fresh BG11 medium. 1  $\mu$ g of plasmid containing only the flanking regions (psll0450-1, pHoxH-1, pNarB-1, or pNirA-1) was added to the cells at the base of a 20 ml tube sealed with cotton wool. The cells were incubated under low light - 20  $\mu$ mol photons  $\text{m}^{-2} \text{s}^{-1}$  - for 6 hours at 30°C, with mixing every 2 hours before recovery by adding 1.8 ml of BG11 medium and incubation for a further 4 days in a shaker incubator. Aliquots of 5  $\mu$ l, 20  $\mu$ l, and 1 ml were plated onto BG11-sucrose (5% w/v) agar plates. Appearing after c. 1 week, 12 colonies were streaked in a grid patch on both BG11-kanamycin and BG11-sucrose plates. Patches that were sensitive to kanamycin but resistant to sucrose were streaked on BG11 agar without sucrose. 12 resulting colonies were analysed by colony PCR using verification primers for each gene to confirm the unmarked knockout by observation of fragments of the expected reduced size (Fig. 5.5).

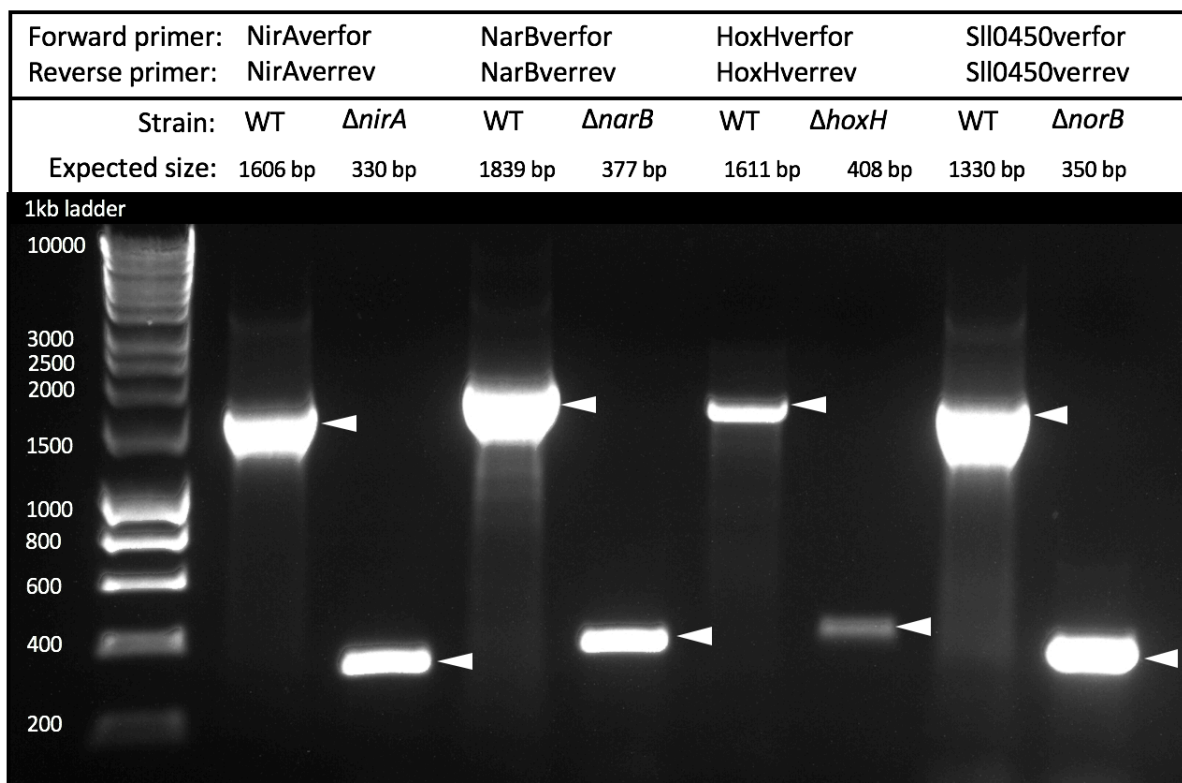


**Fig. 5.5:** Gel electrophoresis of PCR products from the wild type and unmarked knockouts of *nirA*, *narB*, *hoxH*, and *norB* using their respective primers to amplify by colony PCR, with the predicted band sizes.

Generation of serial unmarked knockouts was performed in the same manner, using the previous unmarked knockout strain as the parent strain to generate a marked knockout via a first homologous recombination step with the selectable knockout vector plasmid to insert the *nptII/sacB* cassette, followed by a second homologous recombination step with the vector containing only the flanking region to remove the cassette. All combinatorial knockouts beyond the single gene knockout stage were generated by David Lea-Smith, and all knockout combinations are listed in Table 2. This represents one of the largest knockout studies to date in *Synechocystis*, and provides a basis for physiological quantification of electron export to determine the importance of electron sink knockout in enhancing biophotovoltaic output.

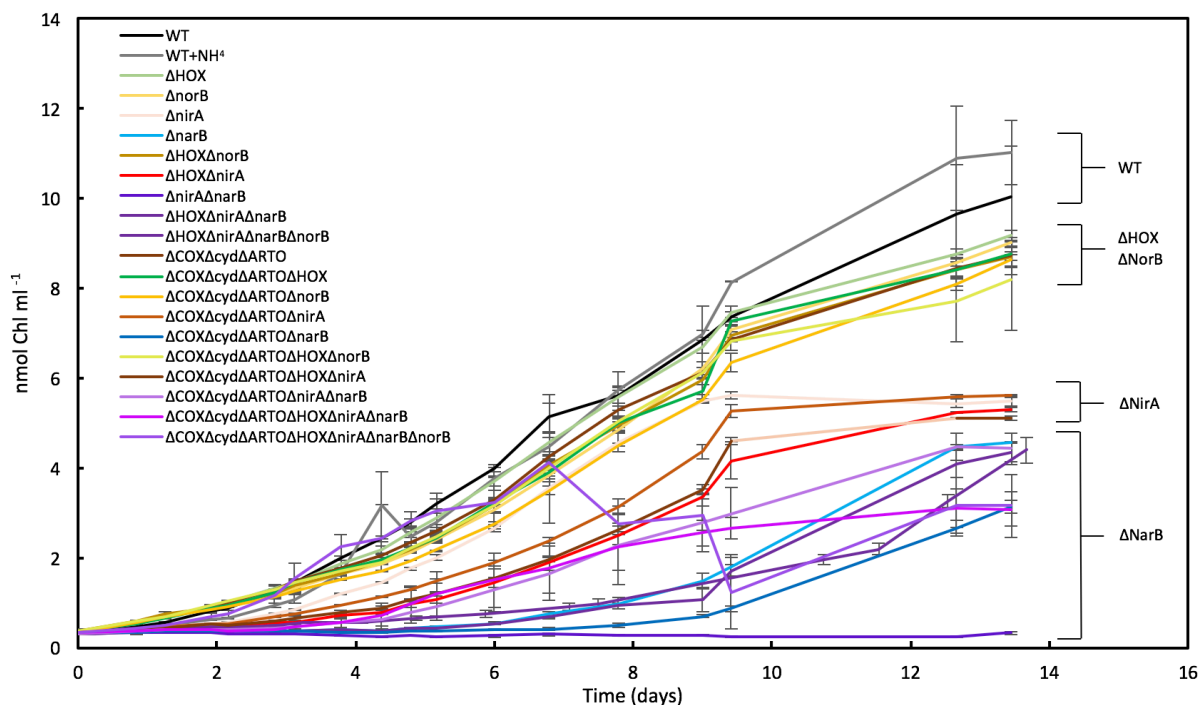
**Table 5.2: List of gene knockout combinations generated in *Synechocystis***

Background strain	Knockout strain name
Wild type	$\Delta hox$
Wild type	$\Delta norB$
Wild type	$\Delta narB$
Wild type	$\Delta nirA$
Wild type	$\Delta hox \Delta norB$
Wild type	$\Delta narB \Delta nirA$
Wild type	$\Delta hox \Delta nirA$
Wild type	$\Delta hox \Delta nirA \Delta narB$
Wild type	$\Delta hox \Delta nirA \Delta narB \Delta norB$
$\Delta COX \Delta Cyd \Delta ARTO$	$\Delta hox$
$\Delta COX \Delta Cyd \Delta ARTO$	$\Delta norB$
$\Delta COX \Delta Cyd \Delta ARTO$	$\Delta narB$
$\Delta COX \Delta Cyd \Delta ARTO$	$\Delta nirA$
$\Delta COX \Delta Cyd \Delta ARTO$	$\Delta hox \Delta norB$
$\Delta COX \Delta Cyd \Delta ARTO$	$\Delta hox \Delta nirA$
$\Delta COX \Delta Cyd \Delta ARTO$	$\Delta nirA \Delta narB$
$\Delta COX \Delta Cyd \Delta ARTO$	$\Delta hox \Delta nirA \Delta narB$
$\Delta COX \Delta Cyd \Delta ARTO$	$\Delta hox \Delta nirA \Delta narB \Delta norB$

**5.2.4. Growth assay of electron sink knockout strains:**

To test whether the knockouts affected the fitness of each strain a growth assay was performed over two weeks, recording absorbance at 750 and 680 nm respectively in order to compare both the growth rate and the Chl content. Each strain was grown in triplicate from starter cultures grown from streaked glycerol stocks and adjusted to 0.15 nmol Chl ml<sup>-1</sup> in 40 ml NUNC flasks with freshly autoclaved BG11, or where *nirA* or *narB* were knocked out, BG11 with the addition of ammonium chloride to assist growth. The assay was housed in an Infors shaker incubator at 30°C with illumination by fluorescent bulbs at 40 μmol photons m<sup>-2</sup> s<sup>-1</sup>. The absorbance was taken directly through the NUNC flask, and adjusted by a factor of 2.4 to account for the increased path length compared to a 1 cm cuvette, and each time the flasks were

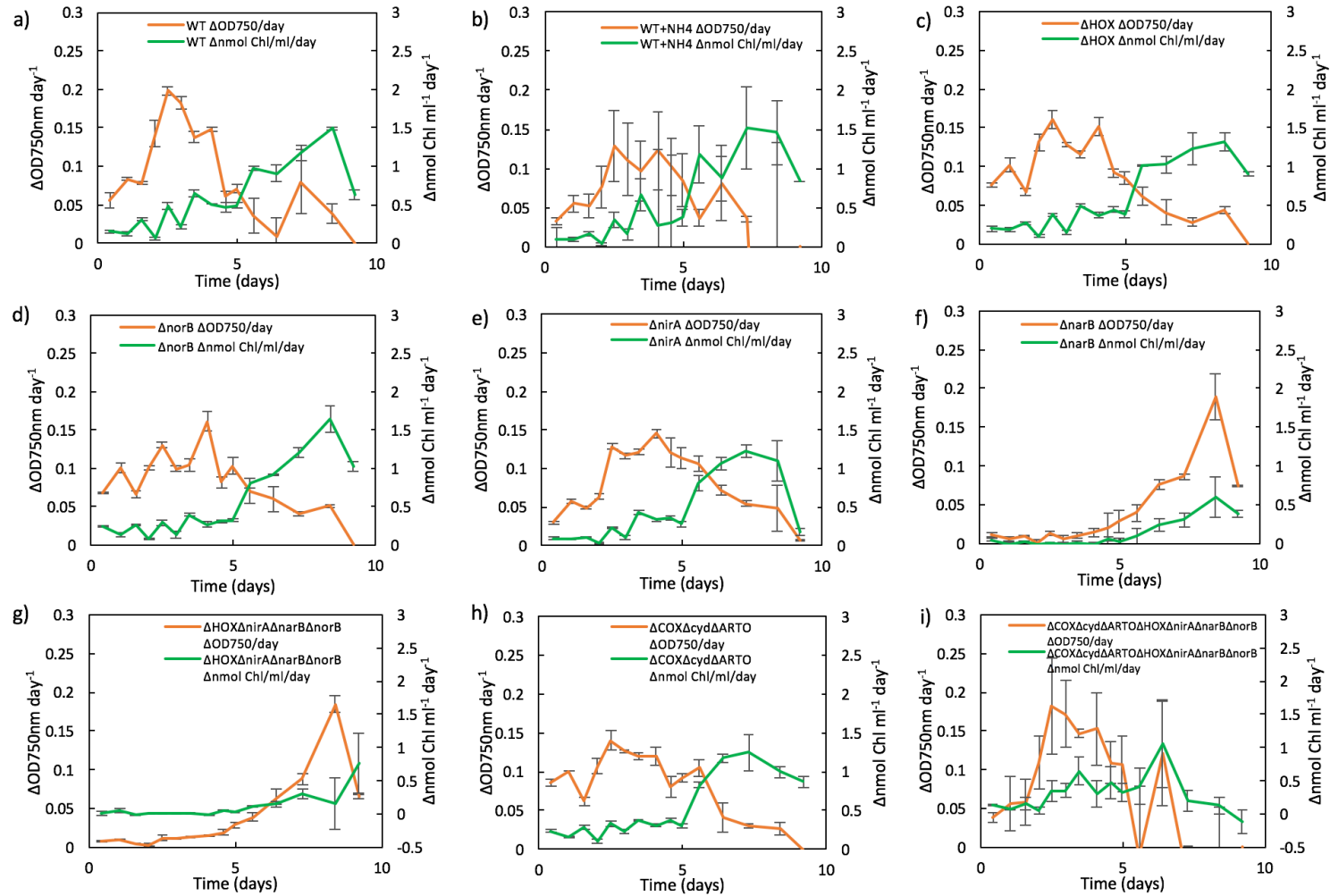
returned to the incubator their position was randomised to eliminate biases due to slight differences in light intensity or temperature gradients. Fig. 5.6 shows the concentration of Chl (see Materials and Methods) over the course of the assay, with regular measurements every day for 9 days, when many of the cultures began to bleach, and with a final few measurements around day 13. Colour coding reveals strains with an intact nitrate assimilation pathway,  $\Delta hoxH$  (green),  $\Delta norB$  (yellow),  $\Delta hoxH\Delta norB$  (dark yellow), and  $\Delta COX\Delta cyd\Delta ARTO$  (brown) did not seem to have any significant effect on Chl concentration compared to the wild type (black). Where the nitrate assimilation pathway was disrupted by  $\Delta nirA$  (red),  $\Delta narB$  (blue), and  $\Delta nirA\Delta narB$  (purple), Chl accumulation measurements clustered at a lower rate relative to the wild type control with added ammonium chloride (grey). Removal of NarB, reducing imported nitrate into nitrite, appeared to cause the most Chl deficient phenotype, whereas retention of NarB but lack of NirA for the next step of nitrite to ammonia conversion caused an intermediate phenotype.



**Fig. 5.6:** Chlorophyll concentration measured throughout the growth assay in all 20 strains plus a wild type control with ammonium chloride over 14 days. Each point is the average of three

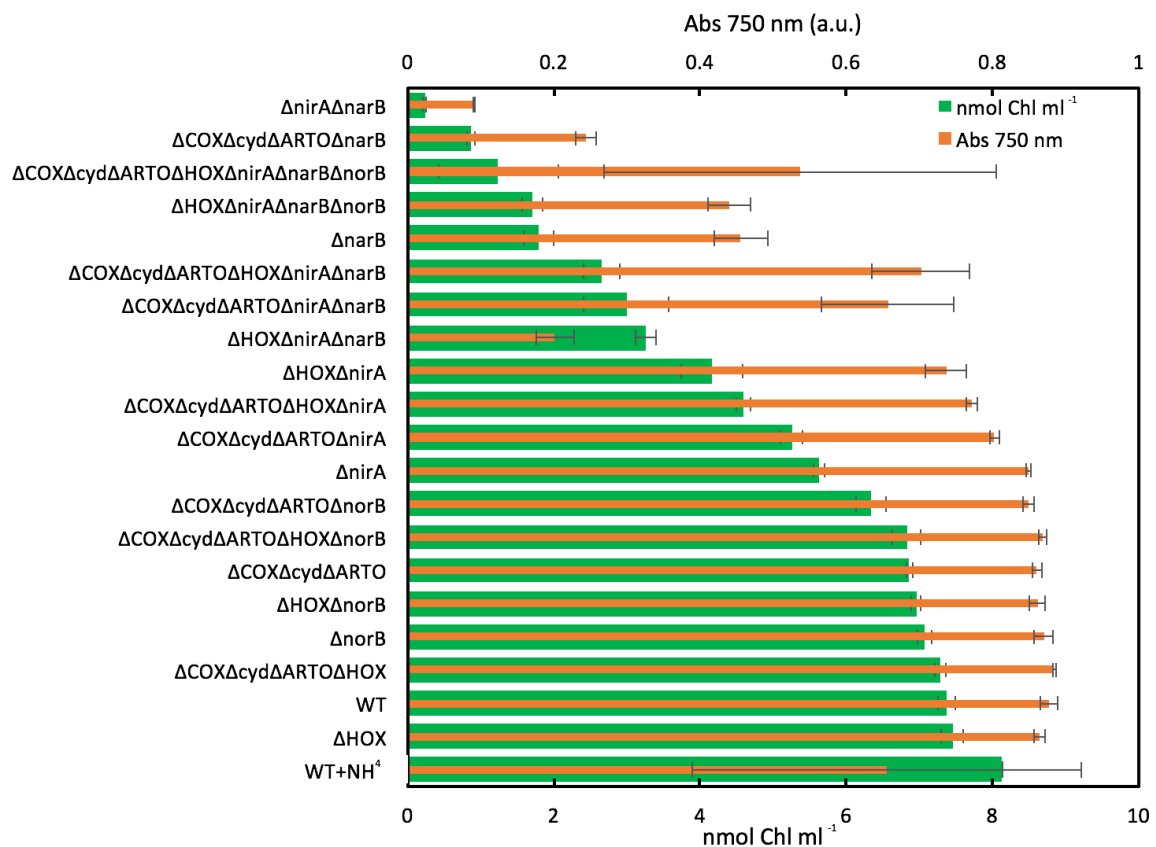
biological replicates grown under identical conditions, and error bars show the standard error. Novel common denominator knockouts have been highlighted at the end of the plot.

Fig. 5.7 shows rates of change of absorbance at 750 nm and the rate of change of Chl concentration for the wild type, wild type with ammonium chloride,  $\Delta hoxH$ ,  $\Delta nirA$ ,  $\Delta narB$ ,  $\Delta norB$ ,  $\Delta hoxH\Delta nirA\Delta narB\Delta norB$ , and  $\Delta COX\Delta cyd\Delta ARTO$  strains up to day 9 at the end of the exponential growth phase for most of the strains. The rate of cell growth in the wild type peaked before the rate increase of Chl concentration, and a similar pattern was observed for most of the other strains including the triple terminal oxidase knockout  $\Delta COX\Delta cyd\Delta ARTO$ , but with the exception of  $\Delta narB$  and  $\Delta hoxH\Delta nirA\Delta narB\Delta norB$ . The pattern persisted within all other strains (not shown) containing the unmarked knockout of  $\Delta narB$ . The addition of ammonium chloride to nitrate assimilation knockout strains was necessary to achieve sufficient growth. However, the maximum levels of Chl reached in these strains may reflect nitrogen depletion by exhaustion of the ammonium chloride supplement in the medium by day 9. In the wild type with ammonium chloride this supply was also likely to be preferentially consumed, but once depleted, the wild type could then resort to the nitrate assimilation pathway to continue Chl synthesis and growth. The seven gene knockout strain  $\Delta COX\Delta cyd\Delta ARTO\Delta hoxH\Delta nirA\Delta narB\Delta norB$  began the assay with seemingly no deficit in the rate of Chl synthesis, however after day seven it decreases rapidly fall in line with other strains lacking NarB. Nitrogen limitation in *Synechocystis* is well known to stunt growth and reduce content of chlorophyll as well as phycocyanin and other nitrogen storage compounds like cyanophycin (Kolodny et al. 2006). Although ammonium chloride is supporting growth of the nitrate assimilation knockouts to some extent, its concentration may not be optimal to restore growth to the wild type level.



**Fig. 5.7:** The rate of change in  $OD_{750}$  and chlorophyll concentration over 9 days in BG11 of wild type *Synechocystis*, wild type plus ammonium chloride,  $\Delta hoxH$ ,  $\Delta nirA$ ,  $\Delta narB$ ,  $\Delta norB$ ,  $\Delta hoxH\Delta nirA\Delta narB\Delta norB$ ,  $\Delta COX\Delta cyd\Delta ARTO$ , and  $\Delta COX\Delta cyd\Delta ARTO\Delta hoxH\Delta nirA\Delta narB\Delta norB$ . Axes for each plot show the same range, each point is the average of three biological replicates, and error bars show the standard error.

The difference in growth rate and Chl synthesis resulted in not only a lower OD<sub>750</sub> reading by day 9 but a relative decrease in Chl content. This is apparent in Fig. 5.8, where nitrate assimilation deficient strains cluster without exception at lower growth and relative Chl content. Knocking out upstream *narB*, should have had the same effect as removing *nirA*, with the addition of removing the 2 electron nitrate to nitrite reduction step. Nitrate uptake in *Synechocystis* is stimulated by nitrite and 2-oxoglutarate build up, but metabolism of ammonium causes depletion of 2-oxoglutarate, inhibiting nitrate uptake (Ohashi et al. 2011). So nitrite build up in  $\Delta nirA$  may continue to further stimulate nitrate uptake, which is inhibited in  $\Delta narB$  by lack of nitrite and abundance of ammonium chloride. The growth deficit caused by  $\Delta nirA$  is not as great as when  $\Delta narB$  is included, suggesting that *Synechocystis* may have other means of using nitrite generated by NarB accumulating in the cytoplasm.



**Fig. 5.8:** Comparison of absorbance at 750 nm and concentration of chlorophyll at day 9 of growth in BG11 for all electron sink knockout strains. Results are an average of three biological replicates and error bars show the standard error.

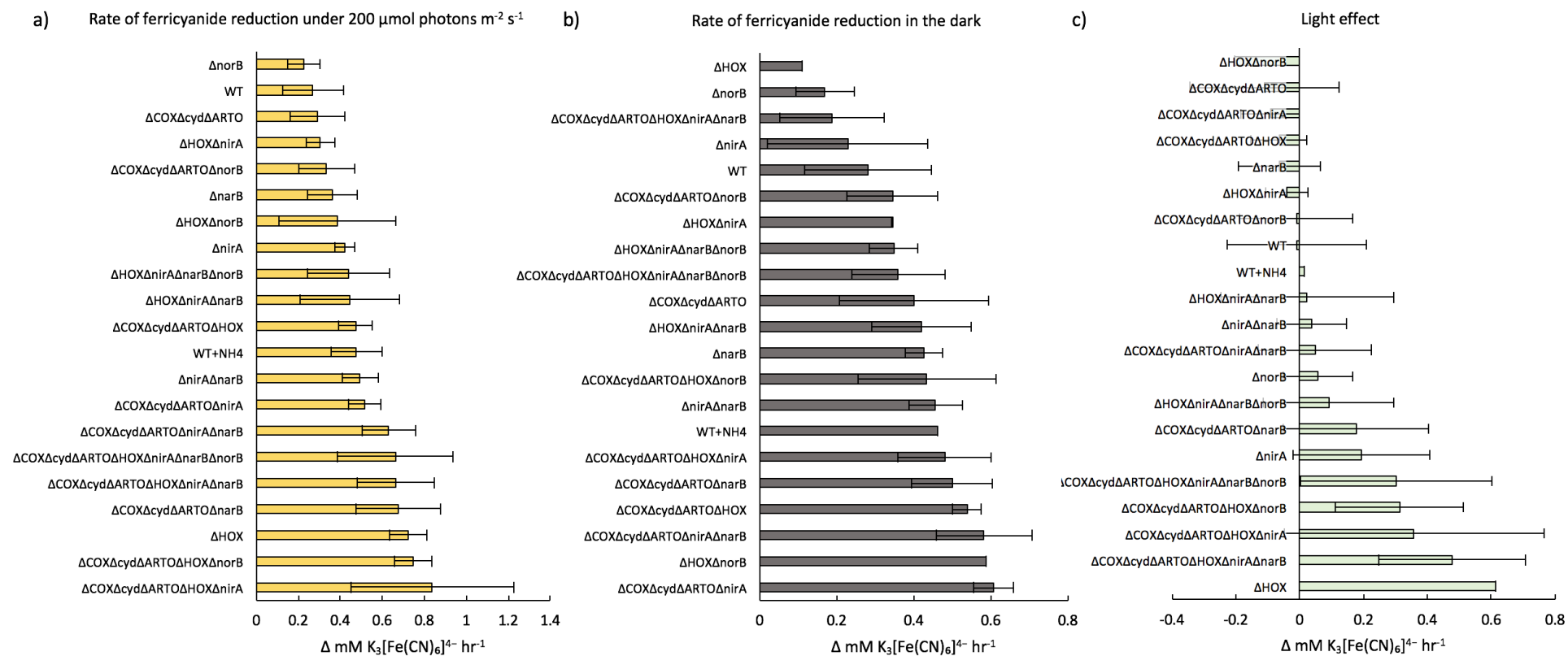
### **5.2.5. Electron sink knockouts enhance extracellular electron transfer:**

In order to test whether rate of extracellular electron transfer was altered by knocking out electron sinks in *Synechocystis*, each knockout strain was characterised by its rate of reduction of an external electron acceptor – potassium ferricyanide – and its bioelectrochemical charge accumulation in a biophotovoltaic system. More specifically, the rate of electron export directly due to photosynthetic light stimulation was quantified.

#### **5.2.5.1. How does the rate of ferricyanide reduction by *Synechocystis* change over time?**

To investigate the rate of EET to an external electron acceptor the rate of ferricyanide reduction from each strain was measured using a multi-well plate assay. Each strain was adjusted to the same starting concentration in triplicate in 3 ml total volume from the same starter cultures as the growth assay. After adding ferricyanide, the assay plates were kept in a shaker incubator at 30°C under a diffuse, uniform light source. Measurements of individual samples could have the full absorption spectra from 230 to 750 nm recorded, but for the time sensitive large scale assay it was only possible to do single wavelength recordings at 420 and 750 nm to estimate ferricyanide concentration. Initial experiments established that ferricyanide was almost completely reduced to ferrocyanide over 48 hours. It was not possible to take multiple measurements every hour in the large scale assay to calculate the initial rate of reduction, so samples were taken at two timepoints: 0 h and 10 h, and the rate of reduction of ferricyanide calculated as the gradient between the two. A smaller scale assay (Chapter 3, Fig. 3.11b) taking

samples every hour from the wild type confirmed the rate of reduction was approximately linear in the initial stages, and so could be quantified using two timepoints.



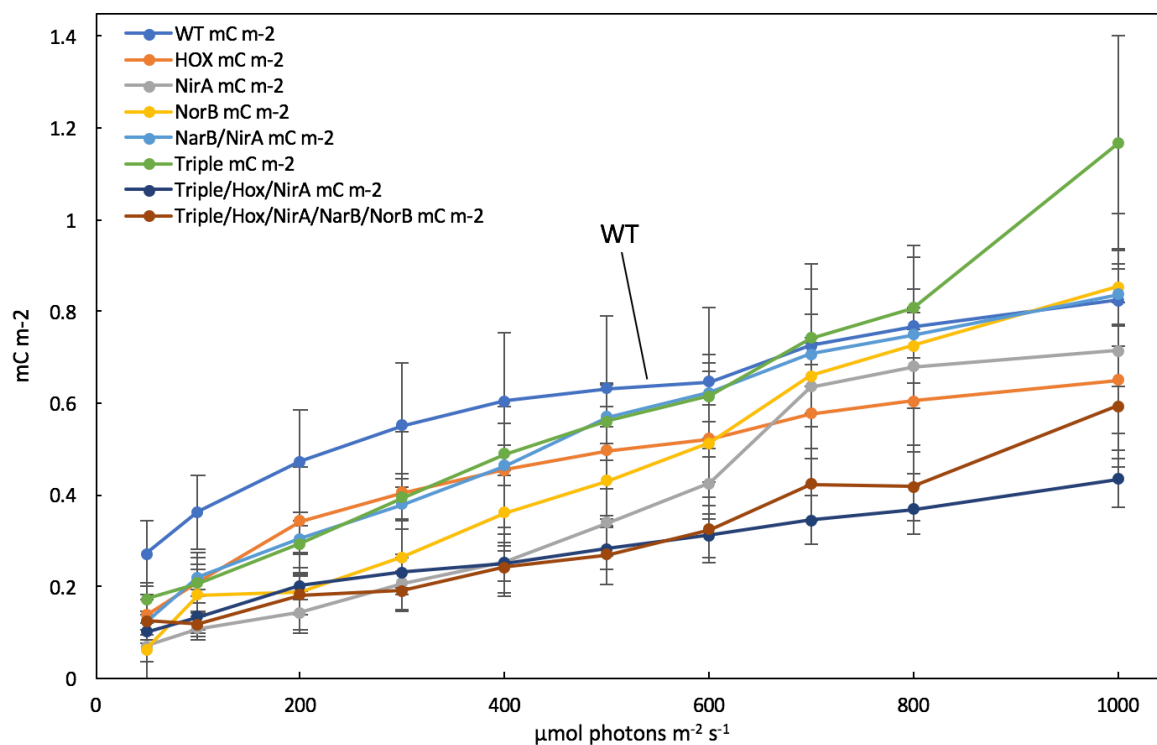
**Fig. 5.9:** Rates of ferricyanide reduction over eight hours between the wild type and electron sink mutant combinations of *Synechocystis* under  $200 \mu\text{mol photons m}^{-2} \text{s}^{-1}$  red light in BG11 media. Results are an average of 3 biological replicates and error bars show the standard error.

Fig. 5.9 a, b) shows the rates of reduction for each strain of *Synechocystis* both under 200  $\mu\text{mol photons m}^{-2} \text{ s}^{-1}$  and in the dark, and c) shows the light-dependent effect, estimated by subtracting the rate of reduction in the dark from the rate of reduction under light. Variation was quite large, and was later attributed in part to poor mixing during dilution of the extracted samples, a challenge when manually handling so many samples in a time sensitive assay. When comparing each strain to wild type, or the wild type plus ammonium chloride, using unpaired, two tailed T-tests, none of them yielded a probability of significance below 0.05. The wild type had a rate of reduction of ferricyanide of  $0.271 \pm 0.0771 \text{ K}_3[\text{Fe}(\text{CN})_6]^{4-} \text{ hr}^{-1}$  in the light, which was no different or even slightly less than the rate in the dark of  $0.281 \pm 0.165 \text{ K}_3[\text{Fe}(\text{CN})_6]^{4-} \text{ hr}^{-1}$ . The wild type would have been expected to show an increase in ferricyanide reduction due to light, so it is possible that an external effect such as evaporation of light exposed samples had skewed the light vs dark comparison. This might explain the number of experiments in which light appeared to decrease the rate of ferricyanide reduction, as in Fig. 5.10c. However, the principal trend observable within each light condition was that, under illumination, strains with more electron sinks knocked out tended to exhibit a higher rate of ferricyanide reduction, supporting the hypothesis that removing electron sinks would increase EET.  $\Delta\text{COX}\Delta\text{cyd}\Delta\text{ARTO}\Delta\text{hoxH}\Delta\text{nirA}$  had the highest rate of reduction under light of  $0.839 \pm 0.289 \text{ K}_3[\text{Fe}(\text{CN})_6]^{4-} \text{ hr}^{-1}$ , with  $\Delta\text{COX}\Delta\text{cyd}\Delta\text{ARTO}\Delta\text{hoxH}\Delta\text{norB}$  just behind with much lower variation at  $0.747 \pm 0.0898 \text{ K}_3[\text{Fe}(\text{CN})_6]^{4-} \text{ hr}^{-1}$ . The triple terminal oxidase knockouts tended to be towards the higher end of the range, especially in combination with one or more other additional knockouts. With fewer electron sinks, more reducing power was being directed out across the cell membrane. In the dark,  $\Delta\text{COX}\Delta\text{cyd}\Delta\text{ARTO}\Delta\text{nirA}$  had the highest rate of reduction at  $0.607 \pm 0.0521 \text{ K}_3[\text{Fe}(\text{CN})_6]^{4-} \text{ hr}^{-1}$ .  $\Delta\text{norB}$  may have a less important effect on rate of ferricyanide reduction as it was present in only two of the top ten strains in both the light and the dark,  $\Delta\text{hoxH}$  was present in four in the dark and five in the light,  $\Delta\text{nirA}$  four in the dark

and six in the light,  $\Delta narB$  four in the dark and five in the light, and  $\Delta COX\Delta cyd\Delta ARTO$  six in the dark and seven in the light.

#### **5.2.5.2. Initial, 'slow', BPV experiments:**

To measure the effect of mutations on bioelectrochemical activity, each strain was characterised using BPV devices developed in the Howe lab, and described in the methods section. Initially, the protocol involved growing each strain sequentially before concentrating them and inoculating in 4 ml of BG11 medium in all 12 BPV devices. Once inoculated, measurements were taken after 3 days to allow cells to settle on the anode and form a biofilm. This assumed that each strain would grow at a similar rate, which was often not the case, as confirmed in the growth assay. The time taken to settle as a biofilm also meant all 12 BPV devices had to be disassembled, cleaned, and reassembled each time due to cell attachment and possible resulting contamination. This introduced small differences each time, and meant the results were not deemed reliable enough to compare potentially subtle differences between knockouts at different times. Results from this initial approach are presented in Fig. 5.11, showing the magnitude of BPV light effect expressed as charge density over the 10 minute illumination periods at increasing light intensity. A steady increase in all strains was seen as light intensity increased, but the error bars were quite large given each data point is an average of at least 10 replicates, and the wild type appeared to produce the highest charge density at low to medium light intensity until overtaken by  $\Delta COX\Delta cyd\Delta ARTO$  (Triple). This ran contrary to conclusions on EET from the ferricyanide reduction assays and to previous experiments showing increased BPV output from  $\Delta COX\Delta cyd\Delta ARTO$  and  $\Delta hoxH$  (not shown). Only a portion of strains were characterized sequentially in this way before a new protocol was devised to improve reliability of inter-strain BPV comparison.



**Fig. 5.10:** BPV Charge density over ten minute periods from wild type *Synechocystis* and a selection of knockouts in individual block BPV devices at varying light intensity. 50 nmol Chl was inoculated into 4 ml of BG11 and allowed to form a biofilm over 3 days. Results are an average of at least 10 replicates and error bars show the standard error.

### 5.2.5.3. Revised 'Fast' BPV protocol:

A revised, more reliable protocol was developed to characterize biophotovoltaic activity from each strain. 3 BPV devices were assembled with transparent electrode materials with light from below as in Chapter 3. 50 ml of each the same starter cultures used for the ferricyanide reduction assay and growth assays were centrifuged at 4000 rpm in a benchtop centrifuge and adjusted to 200 nmol Chl ml<sup>-1</sup> by resuspending in BG11. Inoculating each device with just 500 μl of highly concentrated cells was found to yield a biophotovoltaic light response within minutes, permitting a much faster turnover of samples. Immediately after inoculation the light protocol and chronoamperometric recording by the potentiostat were started simultaneously.

The light protocol was designed to allow each sample 30 minutes to stabilize its bioelectrochemical current enough to be able to analyse the change in current output due to light. The stabilization period included 3 minutes of illumination at  $500 \mu\text{mol photons m}^{-2} \text{s}^{-1}$ , as during the course of method development, pre-illumination had been found to enhance the rapidity of photocurrent response. In the revised protocol, summarized in Fig. 5.12 each strain was in the BPV devices for the same length of time and received the same pre-illumination. 5 light exposures calibrated to 20, 80, 200, 500, and  $1000 \mu\text{mol photons m}^{-2} \text{s}^{-1}$  for five minutes each were chosen to characterize photocurrent at low, medium, and high light intensity, with 5 minutes recovery in between and 10 minutes at the end to allow the current to return to a stable 'dark' level. Once the light protocol was completed, cyclic voltammetry was performed on each device, recording the second of two scans from -500 to +500 mV at  $10 \text{ mV s}^{-1}$ . The photocurrent response from the electron sink knockouts showed the extent to which electron flux had been diverted from metabolic processes to the anode, and the cyclic voltammograms yielded information on cell to anode interaction. This protocol condensed BPV characterization from 3 days to 80 minutes, including cleaning the devices with ethanol and rinsing with de-ionized water before loading the next sample.

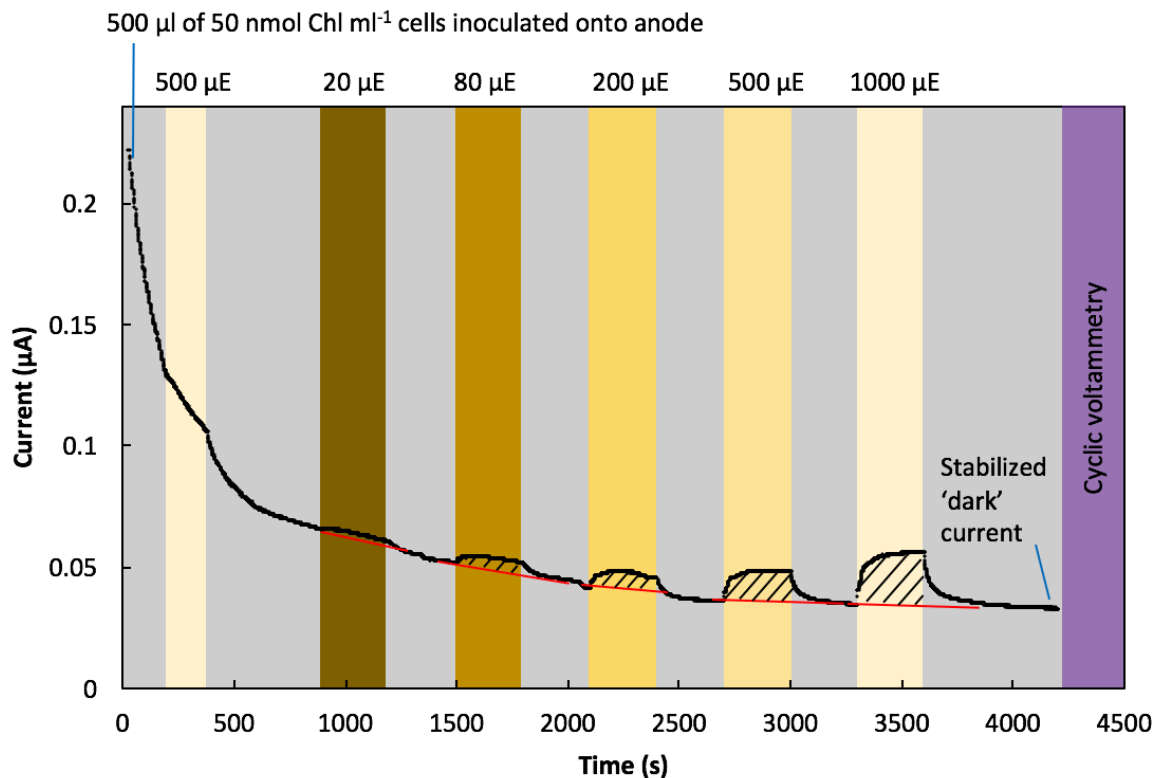


**Fig. 5.11:** Illustration of the revised 'fast' BPV method, showing data from an example chronoamperometry trace recorded with wild type cells from inoculation over 70 minutes using 100 nmol Chl highly concentrated in 500  $\mu\text{l}$  on the anode of the BPV device and immediate measurement. Each light exposure is illustrated, with light intensity abbreviated from  $\mu\text{mol photons m}^{-2} \text{s}^{-1}$  to  $\mu\text{E}$ . The projected dark current, calculated from the gradient of points preceding the illumination period is shown (red lines), and the photoeffect highlighted (black lines) as the area corresponding to the total charge accumulated. Chronoamperometry was followed by cyclic voltammetry in the dark.

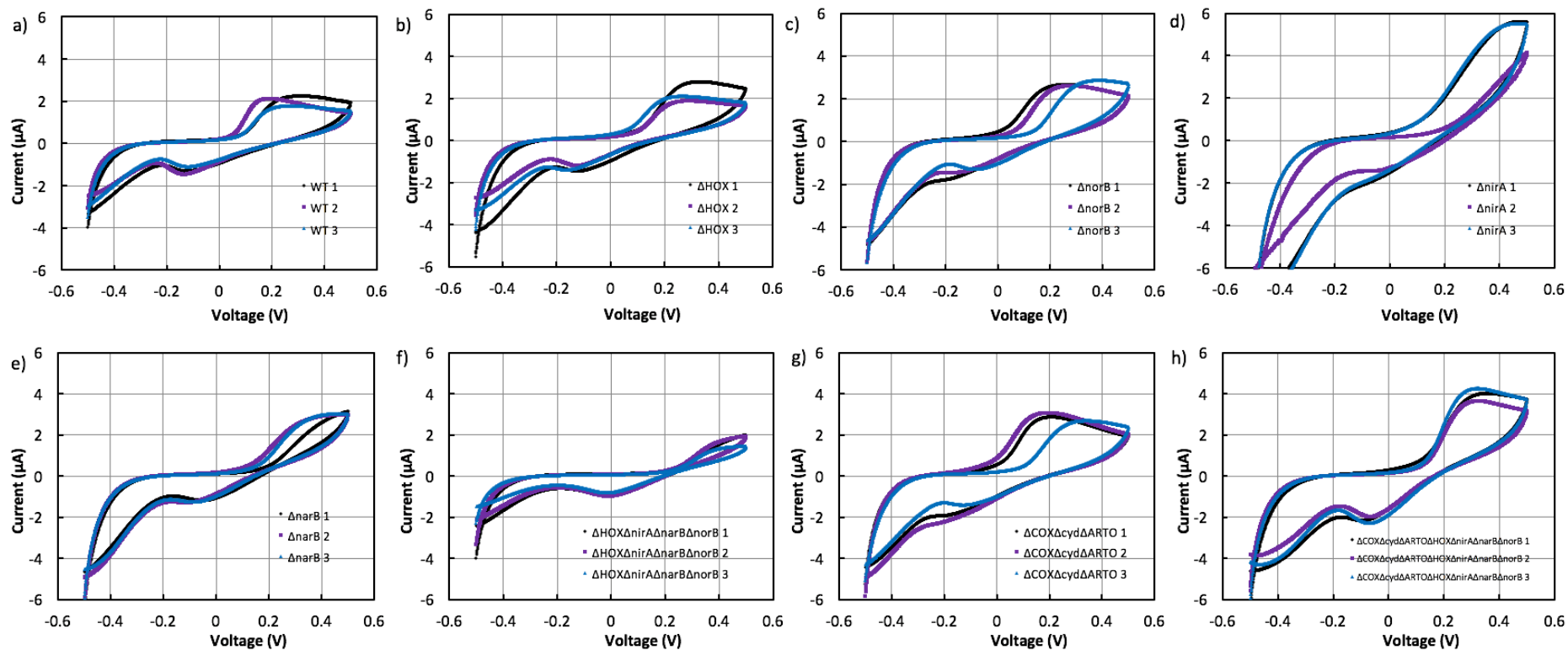


**Fig. 5.12:** Cyclic voltammograms showing each of the three replicates of key electron sink knockouts between -500 and 500 mV at  $1 \text{ mV s}^{-1}$  with axes adjusted to the same heights. Cyclic voltammetry was performed at the end of the fast chronoamperometry protocol with highly concentrated cells.

#### **5.2.5.4. Cyclic voltammetry confirmed electrochemical interaction in fast BPV protocol:**

Cyclic voltammograms (CVs) in Fig. 5.12 were taken at the end of the chronoamperometry sequence and revealed interactions from cells to the anode, confirming an electrochemical association. The wild type showed a typical pattern for wild type *Synechocystis* with a strong oxidation peak around 200 mV and a reduction peak around -150 mV. This pattern is the same as observed from previous BPV experiments where the inoculum was allowed to settle and form a biofilm over several days. Similar peaks were visible for most of the strains, with the peak heights varying. The CV shape was similar between  $\Delta hoxH$ ,  $\Delta norB$ , and  $\Delta COX\Delta cyd\Delta ARTO$ , although  $\Delta nirA$  and  $\Delta narB$  produced peaks that were shifted to a more positive potential as did  $\Delta hoxH\Delta nirA\Delta narB\Delta norB$  consistent with the  $\Delta nirA$  and  $\Delta narB$  results. The oxidation peak from  $\Delta nirA$  alone was nearly three times the height, or current, of the wild type. However, the seven gene knockout strain  $\Delta COX\Delta cyd\Delta ARTO\Delta hoxH\Delta nirA\Delta narB\Delta norB$  displayed an oxidation peak at only a slightly higher potential than the wild type, but with double the current output. The CV traces from each of the strains tested (not all shown) confirmed that in the revised, fast method of BPV analysis, each strain was able to associate electrochemically with the anode in the short time allocated, and that the traces were similar to previous measurements of *Synechocystis*.

#### **5.2.5.5. Chronoamperometry revealed increasing biophotovoltaic response from electron sink knockouts:**

Fig. 5.13 summarizes the increase in charge accumulation with increasing light intensity for each strain. While the magnitude of charge accumulation was around 5-fold lower than from the previous, slow protocol in Fig. 5.11, due possibly to the reduced time for cells to attach as a biofilm on the anode surface, the results followed a similar pattern to those obtained from the initial slow protocol. The faster protocol permitted characterization of all strains in 3.5 days,

with every effort made to keep conditions identical, including reuse of the same BPV electrode assemblies, leading to smaller error bars (with the exception of  $\Delta nirA$ ) and more confidence in the reliability of the results than the slower protocol spread over several months. The electron sink knockouts also mostly yielded greater light effects and dark currents than the wild type, in line with the trend from the ferricyanide reduction assays.

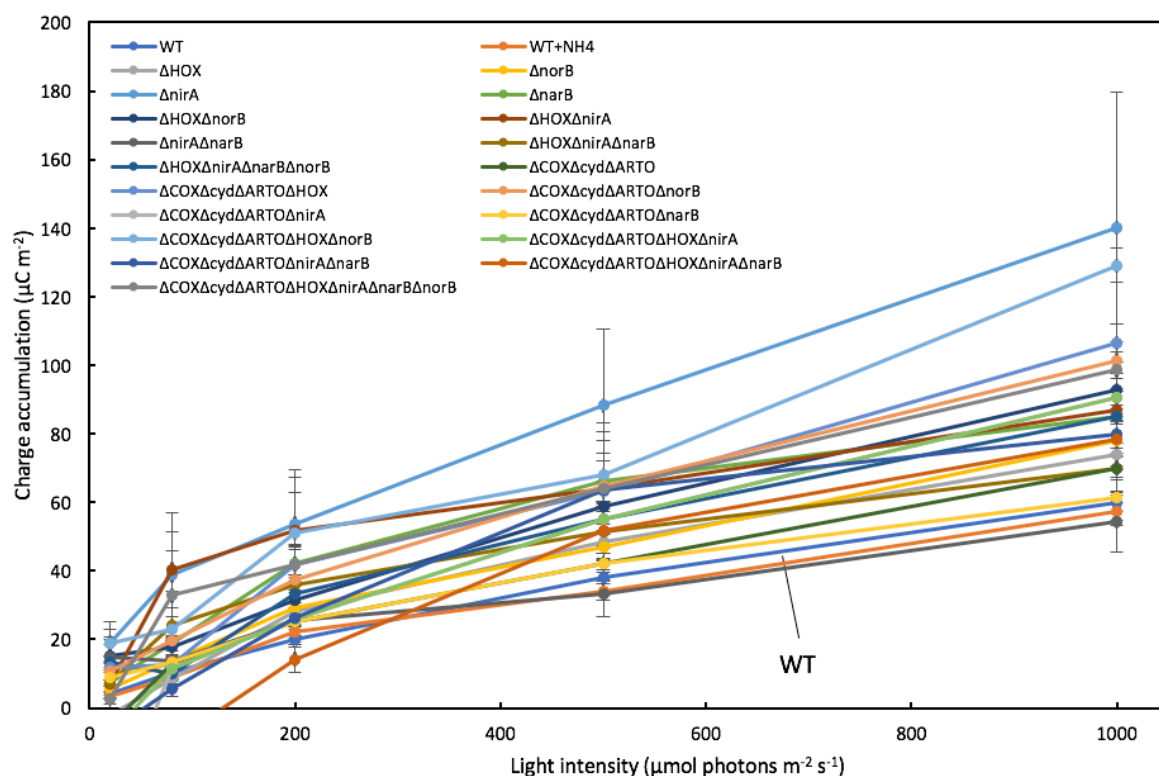


**Fig. 5.13:** Overview of charge accumulation with the ‘fast’ BPV protocol from each *Synechocystis* strains at 20, 80, 200, 500, and 1000  $\mu\text{mol photons m}^{-2} \text{s}^{-1}$  using 100 nmol Chl highly concentrated in 500  $\mu\text{l}$  on the anode of the BPV device and immediate measurement. Results are an average of three biological replicates and error bars show the standard error.

Bioelectrochemical output in the dark was measured by taking the final current level at the end of the run, having stabilized for 80 minutes. The final current value was taken as calculation of charge accumulation would have been affected by the previous illumination period. The average stabilized dark current for each strain and charge accumulation for each light intensity

is shown ranked in increasing order in Fig. 5.15a. Dark current ranged from  $0.318 \pm 0.00539$  A m<sup>-2</sup> in the wild type to  $1.18 \pm 0.104$  A m<sup>-2</sup> from  $\Delta nirA$ . The addition of ammonium chloride did not seem to affect the bioelectrochemical output from the wild type. Charge accumulation was calculated for each illumination period. The lowest light condition of 20  $\mu\text{mol photons m}^{-2} \text{s}^{-1}$  resulted in difficulties in accurate estimation of the photoeffect as the action potential-like response to light stimulation caused a net reduction in current output at low light compared to the projected dark current (as in Chapter 3, Fig. 3.5b). At higher light intensities the reduction of current in the minute just after the initial spike from illumination did not dip below the projected dark current before recovering, so the current measured per second could be summed as the total charge generated due to light stimulation.

Deletion of the nitrate assimilation pathway had variable effects on charge accumulation with *narB* or *nirA* disrupted in different combinations. The individual knockout of *narB* resulted in a roughly 2 – fold increase in dark current and charge accumulation over the wild type with ammonium chloride at all light intensities except 20  $\mu\text{mol photons m}^{-2} \text{s}^{-1}$ . *p*-values of results significantly different to the wild type are listed: dark current: *p*=0.007; 80  $\mu\text{mol photons m}^{-2} \text{s}^{-1}$ : *p*=0.027; 200: *p*=0.048; 500: *p*=0.031, 1000: *p*=0.0014). Knockout of just *nirA* led to a greater 3 – fold increase in dark current and charge accumulation across all light intensities, although due to its large variation, this difference is not statistically significant. However, the combination of  $\Delta nirA \Delta narB$  produced the same dark current and charge accumulation as the wild type, except under 20  $\mu\text{mol photons m}^{-2} \text{s}^{-1}$  where charge accumulation was slightly higher. Other knockout combinations containing  $\Delta nirA \Delta narB$  were distributed across the range of relative outputs, making it difficult to conclude the double  $\Delta nirA \Delta narB$  knockout was detrimental, whereas the individual gene knockouts enhanced EET. NirA, however, is

presumed to be the most significant electron sink in terms of the cost in reducing power, requiring 6 electrons from ferredoxin to reduce nitrite to ammonia.

The triple terminal oxidase knockout strain,  $\Delta COX\Delta cyd\Delta ARTO$ , produced only slightly higher dark current than the wild type ( $p=0.0005$ ) and a higher charge accumulation at 200  $\mu\text{mol photons m}^{-2} \text{ s}^{-1}$  ( $p=0.006$ ). The bi-directional hydrogenase and nitric oxide reductase knockouts,  $\Delta hoxH$  and  $\Delta norB$ , also displayed only a few, marginal increases over the wild type.  $\Delta hoxH$  yielded a slightly higher dark current ( $p=0.002$ ) and charge accumulation at 1000  $\mu\text{mol photons m}^{-2} \text{ s}^{-1}$  ( $p=0.02$ ), and although  $\Delta norB$  consistently ranked higher in terms of its average dark current and charge accumulation, at no light intensity was it statistically higher than the wild type. While  $\Delta COX\Delta cyd\Delta ARTO$ ,  $\Delta hoxH$ , and  $\Delta norB$  resulted only in small increases in the rate of EET individually, the combinatorial effect was greater.  $\Delta hoxH\Delta norB$  produced significantly higher dark current ( $p=0.013$ ) than the wild type, and charge accumulation at 200 ( $p=0.039$ ), 500 ( $p=0.004$ ), and 1000  $\mu\text{mol photons m}^{-2} \text{ s}^{-1}$  ( $p=0.004$ ). The combinations of  $\Delta COX\Delta cyd\Delta ARTO$  with  $\Delta hoxH$ , and  $\Delta norB$  were consistently ranked towards the upper end in terms of photoeffect and dark current.  $\Delta COX\Delta cyd\Delta ARTO\Delta norB$  produced over 2-fold higher dark current ( $p=0.01$ ) and charge accumulation at 200  $\mu\text{mol photons m}^{-2} \text{ s}^{-1}$  ( $p=0.003$ ) than the wild type, and just under 2-fold greater charge accumulation at 500 ( $p=0.006$ ), and 1000  $\mu\text{mol photons m}^{-2} \text{ s}^{-1}$  ( $p=0.005$ ).  $\Delta COX\Delta cyd\Delta ARTO\Delta hoxH$  showed a similar pattern with increased dark current ( $p=0.003$ ), and increased charge accumulation at 500 ( $p=0.003$ ) and 1000  $\mu\text{mol photons m}^{-2} \text{ s}^{-1}$  ( $p=0.006$ ). The five gene knockout strain  $\Delta COX\Delta cyd\Delta ARTO\Delta hoxH\Delta norB$  produced around 2.5-fold higher dark current ( $p=0.0007$ ) and was consistently amongst the highest ranked for charge accumulation at 20 ( $p=0.045$ ), 80 ( $p=0.043$ ), and 1000  $\mu\text{mol photons m}^{-2} \text{ s}^{-1}$  ( $p=0.0009$ ).

Interestingly, combinations of the terminal oxidase knockouts, bi-directional hydrogenase and nitric oxide reductase knockouts with the nitrate assimilation pathway gene knockouts did not lead to the highest outputs. Compared to the wild type plus ammonium chloride in the dark there was higher current output from  $\Delta COX\Delta cyd\Delta ARTO\Delta narB$  ( $p=0.00002$ ), the seven gene knockout strain  $\Delta COX\Delta cyd\Delta ARTO\Delta hoxH\Delta nirA\Delta narB\Delta norB$  ( $p=0.001$ ),  $\Delta COX\Delta cyd\Delta ARTO\Delta hoxH\Delta nirA$  ( $p=0.001$ ),  $\Delta COX\Delta cyd\Delta ARTO\Delta hoxH\Delta nirA\Delta narB$  ( $p=0.007$ ),  $\Delta COX\Delta cyd\Delta ARTO\Delta hoxH\Delta nirA$  ( $p=0.001$ ), and  $\Delta COX\Delta cyd\Delta ARTO\Delta nirA\Delta narB$  ( $p=0.00000009$ ). The photoeffect was greater than the wild type plus ammonium chloride at  $500 \mu\text{mol photons m}^{-2} \text{s}^{-1}$  from  $\Delta COX\Delta cyd\Delta ARTO\Delta hoxH\Delta nirA$  ( $p=0.001$ ), and at  $1000 \mu\text{mol photons m}^{-2} \text{s}^{-1}$  from  $\Delta COX\Delta cyd\Delta ARTO\Delta hoxH\Delta nirA$  ( $p=0.03$ ) and  $\Delta COX\Delta cyd\Delta ARTO\Delta nirA\Delta narB$  ( $p=0.013$ ). The electron sink knockout combinations retaining the terminal oxidases,  $\Delta hoxH\Delta nirA\Delta narB$  and  $\Delta hoxH\Delta nirA\Delta narB\Delta norB$  also produced a slightly higher dark current ( $p=0.002$  and  $0.001$  respectively) but variation mean their photoeffect was never significantly higher than the wild type plus ammonium chloride.

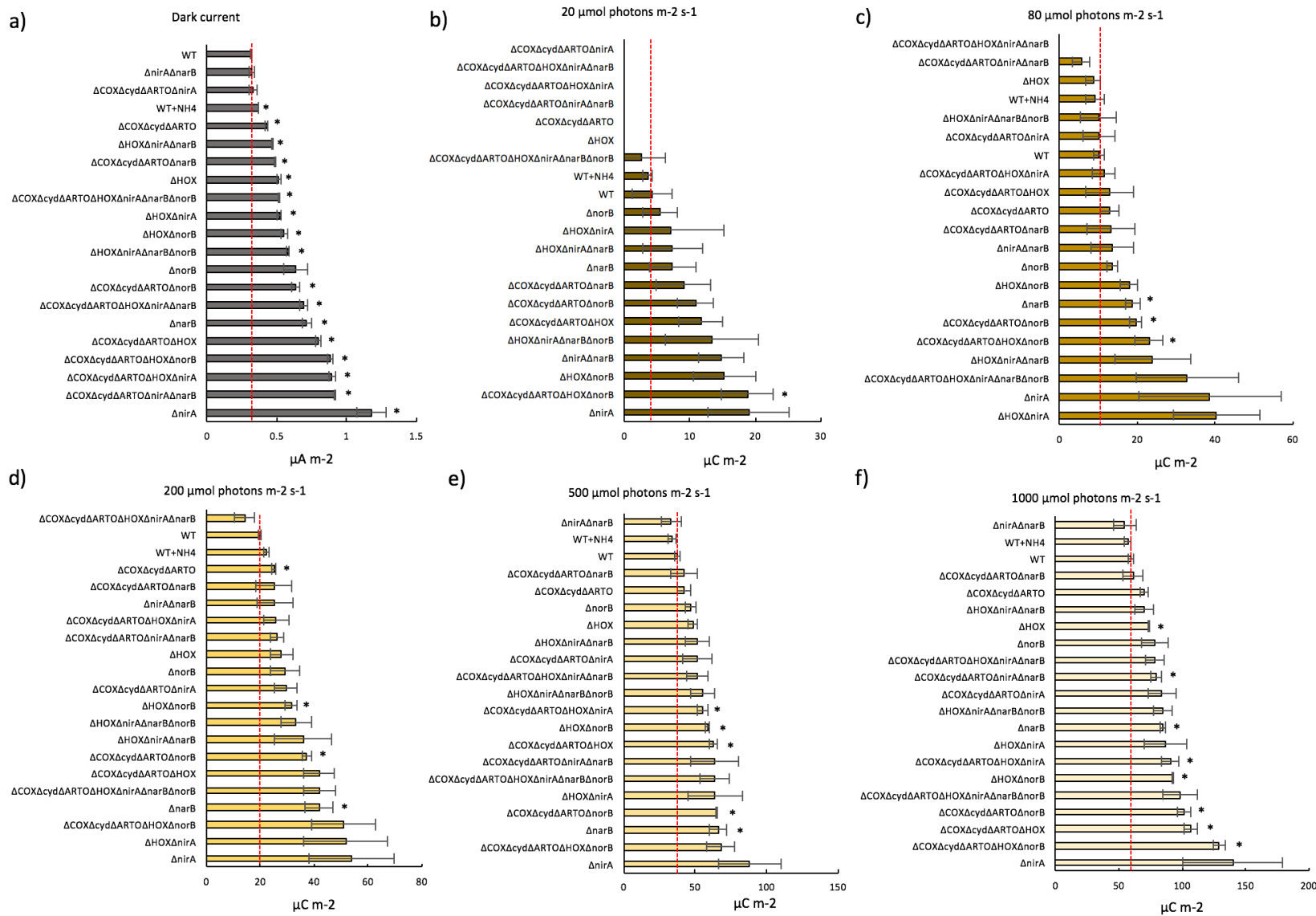


**Fig. 5.14:** Plots showing a) the stabilized ‘dark current’ from each *Synechocystis* electron sink knockout strain in BG11, and b-f) ranked total charge density from each 5 minute light exposure in the fast BPV protocol. Results are the average of three biological replicates and error bars show the standard error. Asterisks indicate a  $p$ -value  $< 0.05$  from unpaired, two-tailed T-tests comparing to the appropriate wild type, a red line indicates the level of the wild type for comparison.

The  $\Delta nirA$  knockout produced the greatest charge accumulation over the 5 minute light period at 1000  $\mu\text{mol photons m}^{-2} \text{ s}^{-1}$  at  $140 \pm 15.8 \mu\text{C m}^{-2}$ , over twice the output of the wild type with ammonium chloride at  $57.1 \pm 2.63 \mu\text{C m}^{-2}$ . This may reflect the importance of the nitrate assimilation pathway as a major electron sink, without which reducing power is preferentially directed towards the unknown EET mechanism. This major increase may also suggest the EET mechanism uses ferredoxin as an electron donor rather than NADPH. However, deletion of the nitrate assimilation pathway and necessary addition of ammonium to the BG11 medium is a major disruption to cell metabolism and the inclusion of further knockouts of electron sinks in addition to  $\Delta nirA$  and  $\Delta narB$  may cause too great an imbalance in redox regulation for the cells as seen with growth rate deficits in NirA and NarB deficient cells. The combination of the other five electron sinks may represent individually less disruptive interventions, explaining the cumulative increase in photoeffect. At 1000  $\mu\text{mol photons m}^{-2} \text{ s}^{-1}$  the wild type ( $59.8 \pm 2.63 \mu\text{C m}^{-2}$ ),  $\Delta COX\Delta cyd\Delta ARTO$  ( $70.0 \pm 3.29 \mu\text{C m}^{-2}$ ),  $\Delta hoxH$  ( $73.9 \pm 0.531 \mu\text{C m}^{-2}$ ),  $\Delta norB$  ( $78.0 \pm 10.5 \mu\text{C m}^{-2}$ ),  $\Delta hoxH\Delta norB$  ( $92.7 \pm 0.484 \mu\text{C m}^{-2}$ ),  $\Delta COX\Delta cyd\Delta ARTO\Delta norB$  ( $101 \pm 5.26 \mu\text{C m}^{-2}$ ),  $\Delta COX\Delta cyd\Delta ARTO\Delta hoxH$  ( $107 \pm 5.58 \mu\text{C m}^{-2}$ ), and  $\Delta COX\Delta cyd\Delta ARTO\Delta hoxH\Delta norB$  ( $129 \pm 4.97 \mu\text{C m}^{-2}$ ) produced a steady increase in power output that likely reflected the compounded reduction in buffering of the redox state of the cell or demand for reducing power. Fig. 5.15 shows the photoeffect of the wild type subtracted from the five non-nitrate assimilation pathway knockouts. The sum of the increases from  $\Delta hoxH$  and  $\Delta norB$  ( $\Sigma = 32 \pm 10.9 \mu\text{C m}^{-2}$ ) was very similar to the increase over the wild type from  $\Delta hoxH\Delta norB$  ( $32 \pm 2.32 \mu\text{C m}^{-2}$ ). Inclusion of the triple terminal oxidase knockout, however, resulted in photoeffect enhancements greater than the sum of the charge accumulation increase over the wild type from  $\Delta hoxH$  and  $\Delta norB$  and  $\Delta COX\Delta cyd\Delta ARTO$  strains individually.

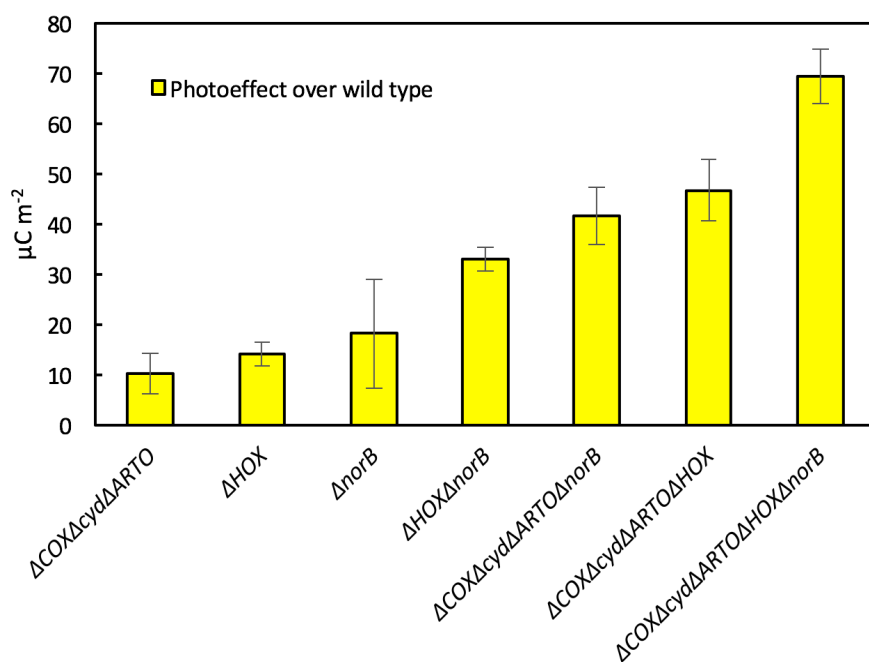


**Fig. 5.15:** Charge accumulation enhancement from the triple terminal oxidase, bi-directional hydrogenase, and nitric oxide reductase knockouts at 1000  $\mu\text{mol photons m}^{-2} \text{s}^{-1}$  with charge accumulation from wild type *Synechocystis* subtracted. Error bars show the standard error and results are an average of three biological replicates.

### 5.3. Discussion:

#### 5.3.1. Cumulative electron sink knockout in *Synechocystis* enhances biophotovoltaic output:

Altering the BPV protocol to a faster, higher throughput method proved an effective way to manage the quantification of a large number of strains in conditions that were as standardized as possible. Comparison of (i) the rate of reduction of ferricyanide and (ii) BPV output from the electron sink knockouts with the wild type showed that removing these electron sinks increased the rate of extracellular electron transfer. This suggests that the internal redox balance of the cell has been altered such that electron flux is being redirected *via* an as yet undefined

mechanism of extracellular electron transfer in order to maintain an optimal redox state. The knockouts of the respiratory terminal oxidases, bi-directional hydrogenase, and nitric oxide reductase appeared to increase BPV output cumulatively as seen in Fig. 5.16. The inclusion of the  $\Delta nirA$  knockout led to the greatest increases in BPV output over the wild type. NirA is the largest individual electron sink, requiring 6 electrons to reduce nitrite to ammonia, and so assuming equal enzyme concentrations to others, it was the most effective knockout, however NirA abundance likely varies as its expression is tied to nitrate and ammonia levels (Frias & Flores 2015).  $\Delta narB$ , upstream of  $\Delta nirA$ , always produced lower BPV output than  $\Delta nirA$ , suggesting continued reduction of nitrate to nitrite is beneficial for EET. The cyclic voltammogram of  $\Delta nirA$  showed a stronger cell to anode interaction, which may have been due to the effect of nitrite reductase removal and further suggest that nitrite accumulation facilitates EET, or belie an artefact particular to those samples. However, high variation in charge accumulation from  $\Delta nirA$  means its BPV output is never statistically significantly higher than the wild type. The cyclic voltammogram of  $\Delta narB$  is much more similar to the wild type, and yet BPV output is significantly higher at  $80 \mu\text{mol photons m}^{-2} \text{s}^{-1}$  and above. The double knockout  $\Delta nirA\Delta narB$  did not seem to grow well and often had lower rates of EET than the wild type. This is likely to be a chance effect from the poor viability of the original starter culture as  $\Delta nirA$  and  $\Delta narB$  knockouts in other strains was not as detrimental.  $\Delta nirA\Delta narB$  may also have triggered a shift in electron flux away from the putative EET mechanism that the single knockouts did not, which could explain why  $\Delta COX\Delta cyd\Delta ARTO\Delta hoxH\Delta norB$  was consistently ranked higher than  $\Delta COX\Delta cyd\Delta ARTO\Delta hoxH\Delta nirA\Delta narB\Delta norB$ . The triple terminal oxidase mutant alone yielded no difference in the rate of ferricyanide reduction, and only a small increase in dark current and photoeffect at all light intensities. The combination of  $\Delta COX\Delta cyd\Delta ARTO$ , with  $\Delta hoxH$  and  $\Delta norB$  in particular, was most often among those with the highest photoeffect BPV results. The combination of  $\Delta COX\Delta cyd\Delta ARTO$  with  $\Delta nirA$  and

$\Delta narB$ , however, was often in the lower half of the ranked BPV outputs, but performed equally well in terms of ferricyanide reduction.

### **5.3.2. Nitrate assimilation knockout impedes redox balancing regulation:**

The individual effects of nitrate assimilation pathway knockouts on EET were often greater than when in combination with other knockouts. This may reflect the importance of *nirA* and *narB* as both electron sink and nitrogen source - knockout of the nitrate assimilation leads to a surplus of reducing power that is ejected from the cell, and although any further knockouts might marginally increase the flux to EET, they may also become detrimental for the cell, leading to the growth deficits and Chl reduction as seen in Fig. 5.7. The difference in chlorophyll concentration compared to cell density as measured by OD<sub>750</sub> was greatest for the six- and seven-gene knockout strains lacking NarB and NirA, whereas  $\Delta nirA$  by itself had only a slightly different profile of chlorophyll to OD<sub>750</sub> ratio. The apparent reduction in Chl in nitrate assimilation deficient mutants raises a concern that cell concentration, adjusted by Chl content for BPV and ferricyanide experiments had been underestimated, and the higher BPV output could be due to a higher cell number. However, some of the strains with highest current outputs retained the nitrate assimilation pathway, and single knockouts of NarB or NirA that have high BPV output and rates of ferricyanide reduction only have a slight difference in Chl to OD<sub>750</sub> ratio compared to the wild type (Fig. 5.9).

### **5.3.3. Ferricyanide reduction rates and biophotovoltaic output may not be equivalent:**

The ranks of ferricyanide reduction rate under 200  $\mu\text{mol photons m}^{-2} \text{s}^{-1}$  and the BPV output under the same light conditions showed some differences. This may be due to the different modes of oxidation of *Synechocystis* by ferricyanide and the anode. Ferricyanide diffuses amongst cells cultured in otherwise favourable conditions in a suspended culture in a shaker

incubator kept at 30 degrees. The anode accepts electrons by surface contact of cellular EET redox mediating mechanisms coming from cells in a biofilm on the anode, or at least in high enough concentrations to mimic a biofilm. The conditions in a biofilm at the bottom of an anodic chamber may differ from a well plate culture, especially in terms of light exposure. In the ferricyanide assay cells were exposed to constant light with mixing, whereas in the BPV, square wave light periods only illuminated the anode for a few minutes.

### **5.3. Conclusions:**

In conclusion, the sequential deletion of multiple electron sinks in *Synechocystis* resulted in increased biophotovoltaic photoeffect, with removal of the nitrate assimilation pathway having the greatest effect, and therefore being the most significant electron sink, but at a risk of reducing cell viability. Further work looking at the effect of flavodiiron or other pathway deletion could test whether the limits on electron sink deletion had been reached in terms of redirecting the highest proportion of intracellular reducing power towards the anode.

## **6. EFFECT OF DELETION OF GLYCOGEN AND POLY- $\beta$ -HYDROXYBUTYRATE SYNTHESIS IN *RHODOPSEUDOMONAS PALUSTRIS* ON BIOELECTROCHEMICAL OUTPUT IN A MICROBIAL FUEL CELL**

### **6.1. Introduction:**

#### **6.1.1. *R. palustris* in microbial fuel cells:**

While the removal of electron sink pathways in *Synechocystis* was shown to have increased the efficiency of electricity production from light, more industrially relevant bioelectrochemical systems (BESs) fall into the category of microbial fuel cells (MFCs). Microorganisms exploited in the anodic chamber of an MFC are fed organic substrates and MFCs rely on microorganisms with exoelectrogenic capability to reduce an electrode directly. The purple non-sulphur alpha proteobacterium *Rhodopseudomonas palustris* has a number of advantages over using a heterotrophic cyanobacterium in an MFC that warranted the development of tools for its genetic manipulation. *R. palustris* has remarkable metabolic diversity, reportedly being able to switch between aerobic chemoheterotrophy and chemoautotrophy and anaerobic photoheterotrophy and photoautotrophy (Larimer et al. 2004), making it robust to variable conditions. It has been shown to be able to degrade a number of pollutants including aromatic compounds (Harwood & Gibson 1988), and to grow on waste products such as crude glycerol (Pott et al. 2013). *R. palustris* forms robust biofilms, producing the protein adhesin at one end of the cell to help adhere to the anode. These biofilms do not require an electron mediator such as ferricyanide, and can reduce the anode by direct physical contact (Sure et al. 2016). The surface area of the anodic substrate is key to maximising cell contact and output - Morishima et al. (2007) used a porous polyaniline coated carbon fibre sheet to increase surface area to

produce  $18.3 \mu\text{W m}^{-2}$ , and Xing et al. (2008) produced 2.3 times the power density when using a graphite fibre brush anode compared to a flat carbon paper anode.

### **6.1.2. Extracellular electron transport from *Rhodopseudomonas palustris*:**

*R. palustris* has been found to produce high power densities in MFCs, and has been shown to produce conductive type IV pili, or nanowires (Venkidusamy et al. 2015; Xing et al. 2008). The best described transmembrane electron transport in *R. palustris* so far is the *pioABC* electron uptake operon allowing photoferrotrophic growth by oxidising ferrous iron. Bose *et al.* (2014) discovered that knocking out the *pioABC* operon significantly reduced electron uptake from a poised electrode, and reduced biomass in an illuminated cathodic chamber. The operon codes for a putative periplasmic decaheme cytochrome (*pioA*), an outer membrane porin (*pioB*), and a periplasmic high potential Fe-S cluster protein. Given the *OmcA-MtrCAB* respiratory pathway in *Shewanella oneidensis* has been found to facilitate both electron import and export, it is possible the related *pioABC* pathway, or a related pathway, may also facilitate EET (Bücking et al. 2012). However, there is no direct homologue for the outer membrane cytochrome OmcA in *R. palustris* and the latter's mechanisms of electron export have yet to be elucidated.

### **6.1.3. Glycerol as a proxy substrate to waste crude glycerol:**

*R. palustris* can metabolise a wide range of compounds, which affect the rate of bioelectricity production. Xing *et al.* (2008) found the highest MFC output with acetate, lactate, and ethanol, and while yeast extract yielded around a fifth of the power density of acetate, Inglesby *et al.* (2012) demonstrated high output using whole cell cyanobacteria, *Arthrospira maxima*, as the growth substrate for *R. palustris*. Axenic cultures were found to produce better results than mixed cultures, and with its metabolic versatility and tolerance to harsh substrates, an extreme

environment could be maintained that gives *R. palustris* a selective advantage to avoid contamination. Crude glycerol, a by-product of glycerol biodiesel production, is one such environmentally hazardous waste product that is uneconomical to purify further and is therefore increasingly often discarded. Despite highly alkaline pH, around 10 due to NaOH or KOH left over from the purification process, and a varied composition of glycerol, saponified fatty acids, methanol, fatty acid methyl-esters, free fatty acids, glycerides, and ash (Hu et al. 2012), untreated crude glycerol has been found to support growth and hydrogen production from *R. palustris* (Pott et al. 2013). A few simple treatments such as reduction of the pH to precipitate saponified fatty acids were found to support similar growth rates as pure glycerol (Pott et al. 2014). As a step towards testing crude glycerol as a cheap substrate for electricity production from genetically engineered *R. palustris*, we used pure glycerol.

#### **6.1.4. Removing key storage compounds may divert electron flux to the anode:**

The conditions in an MFC anodic chamber are potentially not dissimilar from the swampy, anaerobic environments *R. palustris* strains have been isolated from. The dark, unstirred chamber, sealed to promote an anaerobic environment and supplied only with minimal medium and glycerol, may simulate scarcity conditions for other nutrients and stimulate the production of storage molecules from glycerol. Synthesis of storage molecules could be a significant electron sink and hinder the production of power from an MFC by competing for reducing power. *R. palustris* employs a number of pathways to regulate the redox state of the cell dynamically: regulation of cell mass and storage compound synthesis is closely balanced with hydrogen production from nitrogen fixation, and carbon dioxide assimilation by RuBisCo (Mckinlay & Harwood 2010). Poly- $\beta$ -hydroxybutyrate (PHB) synthesis is thought to serve as an electron sink to balance the redox state of the cell, as it is not as energy dense as glycogen, but requires a large amount of reducing equivalents to synthesise. Thus, in the presence of an

external electron acceptor, deletion of PHB synthesis may divert electron flux towards EET. Previously, electron sink knockouts of the nitrogenase and uptake hydrogenase enzymes, NifHD and HupSL, demonstrated an increase in MFC output relative to the wild type (Morishima et al. 2007), avoiding the loss of electrons by H<sub>2</sub> production. A 1.7 times increase in hydrogen production was achieved by knocking out the poly- $\beta$ -hydroxybutyrate synthesis gene *phbC* in *R. palustris* (Yang et al. 2011). Glycogen synthesis is a key energy storage compound that allows cells to survive periods of nitrogen and carbon scarcity and contributes to the longevity of individual cells (Pechter et al. 2017). Inactivation of glycogen synthesis may increase the rate of transfer of electrons out of the cell. We therefore investigate the removal of both glycogen and PHB synthesis in *R. palustris* and the effect on the MFC output.

Unmarked genome knockouts of *glgAC* (glycogen synthase) and *phaAB* (PHB synthesis) were generated in *R. palustris* CGA009, and tested for power and current output using glycerol as a substrate. The concentration of glycerol was also measured, but difficulties obtaining accurate measurements impeded a direct comparison of electron flux from glycerol to the anode. Growth rate was found to be reduced in the glycogen knockout, but strangely not the double knockout, and the glycogen knockout showed an increased rate of glycerol consumption. There was no difference in maximum power output between the wild type and knockouts, although glycogen knockout may have caused a slight decrease in power after several days, and an increase in total charge accumulation during chronoamperometry. This chapter finds storage molecule removal not to give direct and obvious enhancement of MFC output in the conditions used, highlighting the variability inherent in studying bioelectrochemical systems. A novel genetic modification protocol for *R. palustris* is demonstrated, and groundwork laid for future experiments to vary MFC conditions and improve analytical techniques for glycerol quantification in particular.

## **6.2. Results:**

### **6.2.1. Generation of glycogen and PHB synthesis knockouts in *R. palustris*:**

To test the effect of removal of key storage molecules on microbial fuel cell activity in *R. palustris*, a novel protocol, developed by David Lea-Smith in the Howe lab, was used to make unmarked gene knockouts of key genes involved in the synthesis of glycogen and PHB. Knockout vectors were constructed consisting of regions flanking the target gene and a *nptI/SacB* cassette, conferring kanamycin resistance and sucrose sensitivity, inserted in the plasmid pK18*mobsacB*. Unlike the situation after transformation of *Synechocystis*, only a single homologous recombination event occurs initially. This leads to insertion of the construct, including the selection cassette, by recombination across the target gene flanking sequences and generating marked knockouts. The selection cassette is then removed by a second round of selection after marked knockouts have been confirmed. This generates either an unmarked knockout or the wild type. Primers used to assemble vectors and verify knockouts are listed in table 5.1.

**Table 6.1. Primers used for vector construction and knockout diagnosis:**

<b>Primer:</b>	<b>Name</b>	<b>Sequence:</b>
Pha left flanking region forward	Phaleftfor	GATCAAGCTTGCTCGAAGATCTGTGC
Pha left flanking region reverse	Phaleftrev	GTACTCTAGATGGTAACCGTTGAAGGCATC
Pha right flanking region forward	Pharightfor	GATCGGATCCGCGGAGAAATTCAAAAACGA
Pha right flanking region reverse	Pharightrev	GATCGAATTCGCGTGATAACCGAACAATCC
Glg left flanking region forward	glgleftfor	GATCAAGCTTATCCGGAGATGAACTCGTTG
Glg left flanking region reverse	glgleftrev	GTACTCTAGAGGTCGTATCGGTGTGCATC
Glg right flanking region forward	glgrightfor	GTACTCTAGACGGCGATCTCGATCTATTTG
Glg left flanking region reverse	glgrightrev	GATCGGATCCATAGCGCAAGGCCGAGAG
Pha knockout verification forward	Rhodophafor	ACTGATGAACGGCGACTCC
Pha knockout verification reverse	Rhodopharev	CTCGAGCGTCATCTTGTGAA
Glg knockout verification forward	Rhodoglgfor2nd	CGACATCATCGAGAGCTACG
Glg knockout verification reverse	Rhodoglgrev2nd	AGCACATCCGGCTTGTAGTG

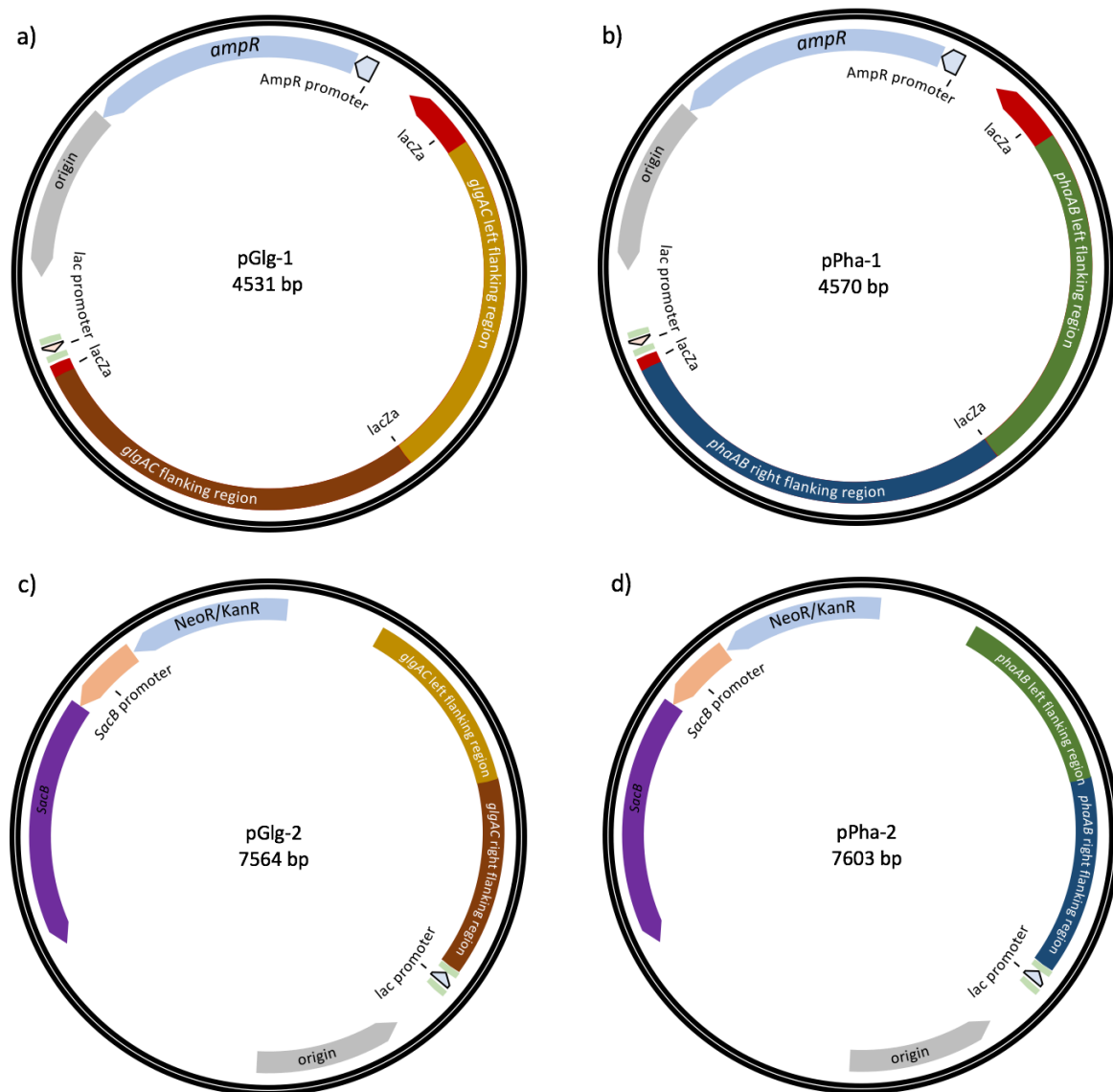


**Fig. 6.1:** Plasmid diagrams of two stage assembly of knockout vectors for *R. palustris* showing a,b) amplification of flanking regions into pUC19 for *glgCA* and *phaAB* respectively, and c,d) flanking regions cloned into pK18*mobsacB* knockout vectors for *glgCA* and *phaAB* respectively.

### 6.2.2. *R. palustris* pK18*mobsacB* knockout vector construction:

The genome sequence of *R. palustris* CGA009 (Larimer et al. 2004) for primer design was accessed via JCVI (<http://cmr.jcvi.org/tigr-scripts/CMR>). High fidelity Phusion (NEB) DNA polymerase was used to PCR amplify fragments. The knockout vector for *glgAC* was generated

by amplification of a 902bp fragment upstream of *glgA*, with primers *glgleftfor* and *glgleftrev*, and a 943bp fragment downstream of *glgC* with primers *glgrightfor* and *glgrightrev*, which were then inserted into the *HindIII/XbaI* and *BamHI/EcoRI* sites of pUC19, generating pGlg-1. The combined left and right flanking regions were excised from pUC19 by digestion with *HindIII* and *EcoRI*, purified after gel extraction, and inserted into the same restriction sites in pK18mobsacB, generating pGlg-2. pK18mobsacB contains the *np111* kanamycin resistance gene, and *sacB* levansucrase, which confers sucrose sensitivity by converting sucrose into toxic levans. The knockout vector for *phaAB* was generated by amplification of a 942bp fragment upstream of *phaA*, with primers *phaleftfor* and *phaleftrev*, and a 924bp fragment downstream of *phaB* with primers *pharightfor* and *pharightrev*. Each fragment was serially into the *HindIII/XbaI* and *BamHI/EcoRI* sites of pUC19 respectively, generating pPha-1 (Fig. 6.1). The combined left and right flanking regions were excised from pUC19 by digestion with *HindIII* and *EcoRI*, purified after gel extraction, and inserted into the same restriction sites in pK18mobsacB (Schafer et al. 1994), generating pPha-2.

### **6.2.3. Generation of unmarked knockouts in *R. palustris*:**

The knockout vectors pPha-2 and pGlg-2 were transformed into exponential phase *R. palustris* by electroporation. Cells were grown in recovery medium and then streaked onto YP-kanamycin agar plates to select for successful transformants, where the plasmid had been inserted at one of the flanking regions (Fig. 6.2a). Kanamycin resistant colonies were checked by colony PCR with Promega Taq polymerase for insertion of pPha-2 and pGlg-2 using primers *Rhodophafor* and *Rhodopharev*, and *Rhodoglgfor2nd* and *Rhodoglgrev2nd*. To generate unmarked knockouts, one PCR verified single-crossover colony for each knockout was inoculated into 2 ml of YP medium and incubated for 24 hours at 30°C under 60  $\mu\text{mol photons m}^{-2} \text{s}^{-1}$  with shaking at 120 rpm before plating on YP-sucrose (5%) agar plates. Sucrose resistant

colonies appearing after 3 or 4 days were patched in a grid onto both YP-kanamycin and YP-sucrose plates to screen for loss of the *nptI**sacB* cassette. Patches both sensitive to kanamycin and resistant to sucrose were analysed by colony PCR to distinguish the unmarked knockout of the target gene from colonies reverting to the wild type (Fig. 6.2d). As with the *Synechocystis* knockouts, serial knockout steps were performed to generate the double  $\Delta pha\Delta glg$  knockout strain.

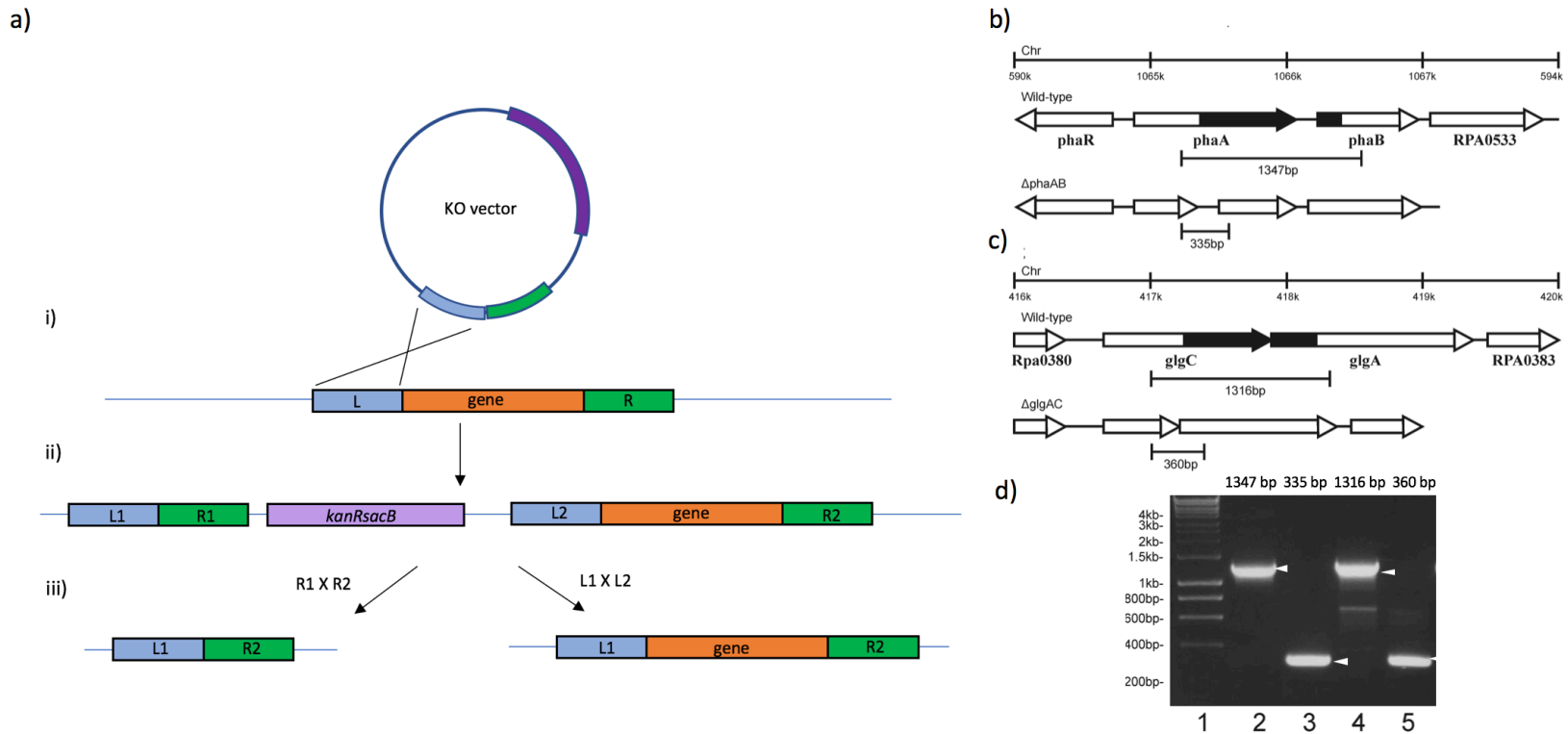


**Fig. 6.2:** a) Diagram illustrating gene knockout strategy i) the knockout vector is inserted at one of the flanking regions, giving ii) the selectable marker cassette and between the combined flanking sites and the target gene. iii) A single homologous recombination event between the left flanking sites restores the wild type, or between the right flanking regions excises the target gene. Diagrams demonstrating gene locus and disruption of b) *phaAB* and c) *glgAC* in the *Rhodospseudomonas palustris* genome. PCR amplification product size from primers flanking the deleted sequence, with the deletion shaded in black the wild-type and unmarked knockout strain are shown. d) Colony PCR amplification using primers Rhodophafor and Rhodopharev of WT (lane 2) and  $\Delta$ *phaAB* (lane 3), and primers Rhodoglgfor2nd and Rhodoglgrev2nd of WT (lane 4) and  $\Delta$ *glgAC* (lane 5), with predicted band sizes.

#### 6.2.4. Effects on growth and glycerol consumption by storage molecule gene knockouts:

In order to test the effect of storage molecule knockout on cell fitness the wild type and knockout strains were grown in minimal medium with 50 mM glycerol in sealed, anaerobic, 40 ml NUNC flasks at 30°C and 60  $\mu\text{mol photons m}^{-2} \text{s}^{-1}$  in an Infors shaker-incubator. Starter cultures were adjusted to  $\text{OD}_{660}$  0.15. The absorption at 660 nm was measured through the flasks over 12 days and adjusted to allow for the width of the NUNC flask compared to a standard cuvette. This avoided the need to open flasks for sample extraction and maintained an anaerobic environment. The growth rates in Fig. 6.3a initially varied with the single knockouts growing slightly more slowly than the wild type, and the double growing faster than the wild type over the first 2 days. The  $\Delta\text{phaAB}$  strain reached the fastest growth rate by day 5, but levelled off in stationary phase from day 8.  $\Delta\text{glgAC}$  showed the biggest growth deficit, starting off at a similar rate to  $\Delta\text{phaAB}$ , ending up with the lowest final  $\text{OD}_{660}$ . The growth advantage of the double knockout initially over the wild type could reflect the diversion of assimilated carbon toward growth and division rather than accumulating stores of glycogen or PHB. The growth deficit of  $\Delta\text{glgAC}$  could be down to the resources being directed toward PHB synthesis, the breakdown of which is less favourable for growth than glycogen, yielding pyridine nucleotides and acetyl-CoA rather than ATP and NADPH from glycogen (Philippis et al. 1992). There is also the possibility of secondary mutations arising during the knockout stages with unknown effects on growth.

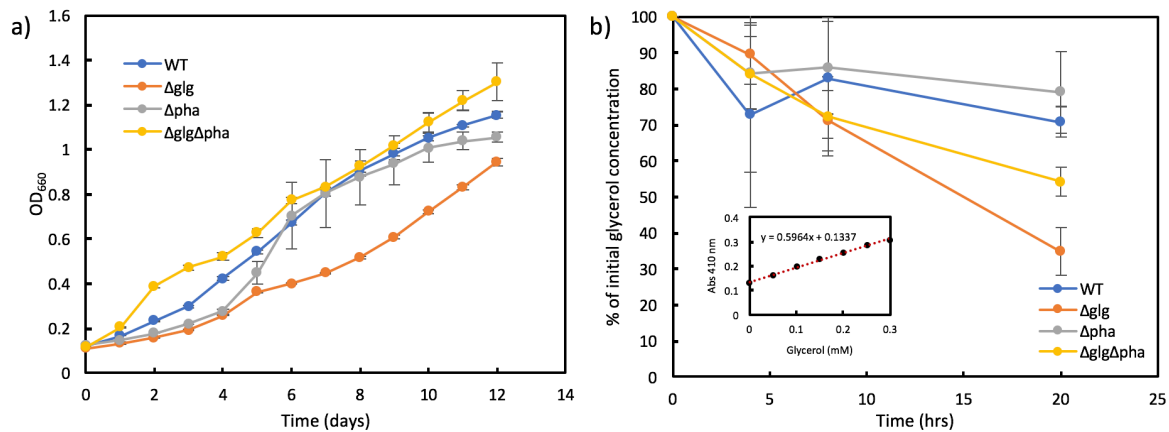


**Fig. 6.3:** a) Growth as measured by taking the absorption at 660 nm over 12 days for wild type *R. palustris*,  $\Delta glgAC$ ,  $\Delta phaAB$ , and  $\Delta glgAC\Delta phaAB$ , and b) glycerol concentration at increasing culture incubation times from a separate experiment, with the standard curve inset. Values are an average of three biological replicates and error bars show the standard error.

The concentration of glycerol from *R. palustris* proved difficult to measure accurately, and the level of glycerol in samples appeared to reduce rapidly over the course of a few days. So an experiment was set up growing the wild type and each knockout strain in sealed 50 ml tubes using lids assembled with silicon sealed needle syringes to extract sub millilitre samples every few hours. The colorimetric assay method was very sensitive and yielded variable results over the first few hours in Fig. 6.3b, but by 20 hours the  $\Delta glgAC$  strain had reduced the glycerol to c. 35% of the starting amount, the double knockout  $\Delta glgAC\Delta phaAB$  had reduced the glycerol concentration to 55% and the wild type and  $\Delta phaAB$  strain to 70% and 80% respectively. Growth on glycerol is associated with high levels of glycogen synthesis in *Escherichia coli* (Martínez-Gómez et al. 2012), however the  $\Delta glgAC$  cells grown prior to the assay will not have been able to accumulate stores of glycogen, and so had a higher rate of glycerol import.

### 6.2.5. Cyclic voltammetry confirmed bioelectrochemical output from *R. palustris* in a single chamber microbial fuel cell:

To compare the bioelectrochemical output of wild type *R. palustris* to the knockout strains, the same design developed for BPV devices was used to build MFCs with a similar electrode configuration. The anode chambers in MFCs adapted for *R. palustris* were not illuminated and were sealed to promote an anaerobic environment, as would be the case in MFC applications for waste remediation, using an externally supplied carbon source in chemoheterotrophic conditions. High surface area electrode materials were employed to maximise the cell to anode surface contact and promote biofilm adhesion. Cyclic voltammetry (Fig. 6.4) confirmed the emergence of bioelectrochemical activity of *R. palustris* as it formed a biofilm over a carbon fibre anode. The results showed a nearly flat CV trace at day 0, followed by the emergence of oxidation and reduction peaks by day 4 in the same device.

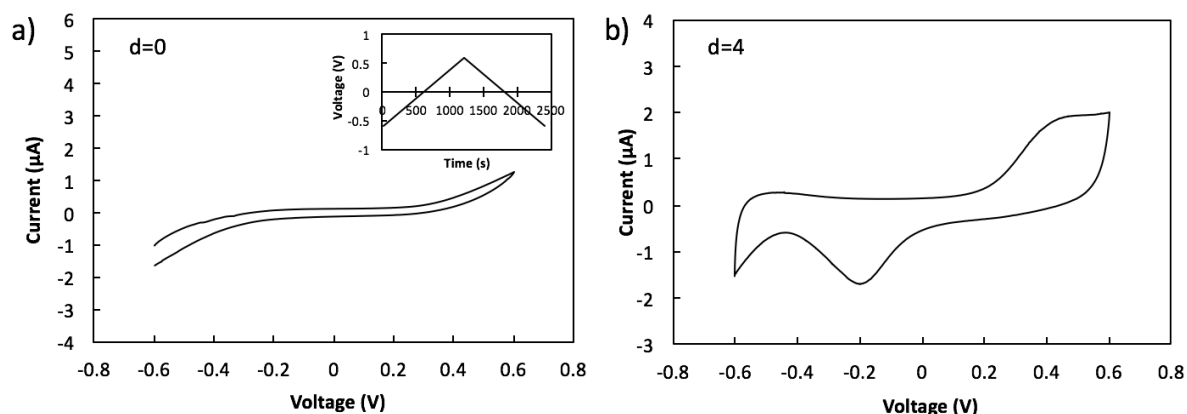


**Fig. 6.4:** Cyclic voltammograms of an MFC device with carbon fibre anode containing *R. palustris* a) immediately after inoculation, with the change in anode potential at  $1 \text{ mV s}^{-1}$  displayed inset, and b) 4 days after inoculation.

### 6.2.6. Maturation of bioelectrochemical interaction and glycerol consumption over initial three days was similar between wild type, $\Delta glgAC$ , $\Delta phaAB$ , and $\Delta glgAC\Delta phaAB$ :

To test whether bioelectrochemical characteristics and rates of glycerol consumption differed between the wild type,  $\Delta glg$ ,  $\Delta pha$ , and  $\Delta pha\Delta glg$ , each was tested in MFC devices adapted for small volume sample extraction using syringes. In the anodic chamber, graphene based aerogels, described in detail in Chapter 7, were clamped as anode extensions on top of a stainless steel mesh. Linear sweep voltammetry was performed at multiple time points over 74 hours, following extraction of 50  $\mu$ l culture to measure glycerol concentration in the media. Cultures were centrifuged and washed by twice resuspension in minimal media without glycerol, before bringing to OD<sub>660</sub> 3.0. Glycerol was added to each device to a concentration of 50 mM at the second timepoint. Fig. 6.5 shows the open circuit potential (OCP), sheet resistance ( $R_S$ ), maximum current density ( $I_D$ ) and maximum volumetric power ( $P_V$ ) at each timepoint. There were no significant differences between wild type and each of the knockouts, although they all followed a similar pattern with the OCP increasing over 74 hours from c.350 mV to c.650 mV.  $R_S$  increased for each strain, for the wild type from  $44.5 \pm 20.1$  to  $78 \pm 23.3 \Omega m^{-2}$ , for  $\Delta glg$  from  $45.8 \pm 0.347$  to  $61.3 \pm 1.85 \Omega m^{-2}$ , for  $\Delta pha$  from  $51.4 \pm 18.5$  to  $65.1 \pm 8.16 \Omega m^{-2}$ , and for  $\Delta pha\Delta glg$  from  $48.6 \pm 20.7$  to  $69.7 \pm 30.2 \Omega m^{-2}$ .  $I_D$  appeared to stay relatively constant for each strain, with wild type increasing until 28 hours before dropping back to a similar value as the knockout strains.  $P_V$  increased for the wild type from  $4.27 \pm 2.22$  to  $13.6 \pm 4.25 W m^{-3}$  after 74 hours, for  $\Delta glg$  from  $5.19 \pm 0.844$  to  $10.4 \pm 0.814 W m^{-3}$ , for  $\Delta pha$  from  $4.68 \pm 2.01$  to  $11.1 \pm 1.61 W m^{-3}$ , and for  $\Delta pha\Delta glg$  from  $4.73 \pm 2.00$  to  $10.8 \pm 3.97 W m^{-3}$ . Fig. 6.6 shows the concentration of glycerol as determined by the colorimetric assay from the MFC devices characterized in Fig. 6.5. Again, there was no clear difference between the wild type and storage molecule knockouts, variation in the starting concentrations of glycerol indicate potential issues with residual glycerol or issues with the extraction process.

By 74 hours all strains showed a reduction in glycerol concentration; in the wild type to  $6.67 \pm 4.23$  mM glycerol, in  $\Delta glg$  to  $6.03 \pm 2.34$  mM, in  $\Delta pha$  to  $6.00 \pm 4.41$  mM, and in  $\Delta pha\Delta glg$  to  $4.32 \pm 1.57$  mM. These results demonstrate some of the difficulties of generating timecourse data from MFC devices. The anodic chamber is unstirred so EET without an external electron shuttle is highly dependent on cells having a physical interaction with the anode as a biofilm, which could be disrupted by sample extraction. With the anode and majority of the cells at the bottom of the chamber it is possible that substrates the in medium will not be evenly distributed.

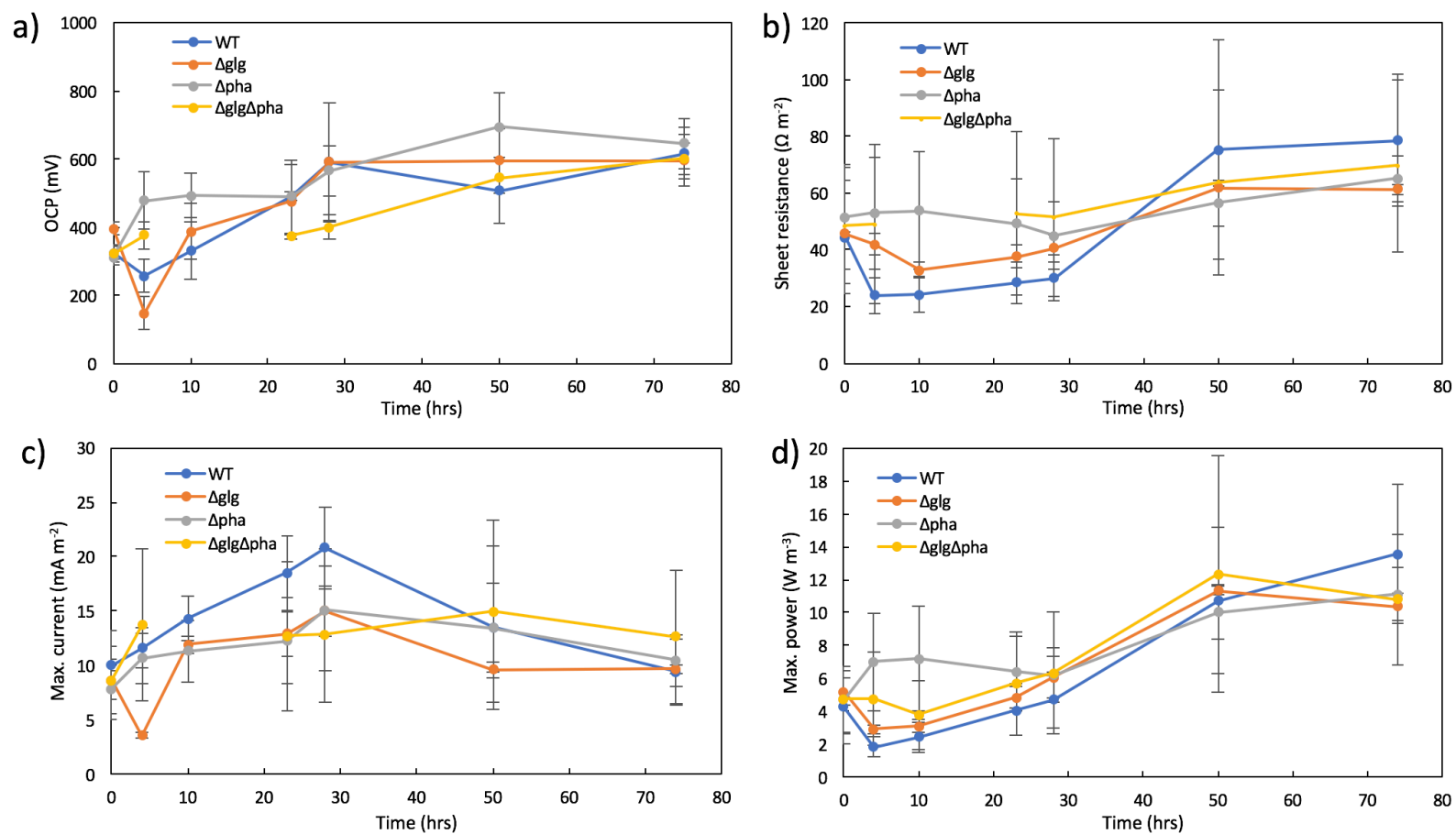


**Fig. 6.5:** Bioelectrochemical parameters of MFC assay showing a) Open circuit potential, b) sheet resistance, c) maximum current density, and d) maximum power density from MFC devices using wild type *R. palustris*,  $\Delta glgAC$ ,  $\Delta phaAB$ , and  $\Delta glgAC\Delta phaAB$  with graphene based aerogel anodes over 74 hours. Results are an average of three biological replicates and error bars show the standard deviation.

The samples extracted were relatively small (50  $\mu$ l), and no active mixing was permitted so as not to disrupt the anodic biofilm and fragile aerogel anode extensions, so the samples may not have been representative of the overall concentration, until most of the glycerol had been consumed. The MFC results show that over 74 hours cells in the anodic chamber the increase in power output was due to a more negative potential being generated by cells within the graphene aerogel anodic matrix, and not an increase in maximum current density. While limited reliable conclusions can be drawn from the first part of the assay for glycerol concentration, based on previously measured reduction of glycerol concentration in Fig. 6.3 and the trend of all strains to lower concentrations, glycerol has become largely depleted by 50 hours.  $P_V$ , as calculated from linear sweep voltammetry in Fig. 6.5, seems to peak at 50 hours before reducing slightly by 74 hours in  $\Delta glgAC$  and  $\Delta glgAC\Delta phaAB$ , whereas  $P_V$  from the wild type and, to a lesser extent,  $\Delta phaAB$ , continues to rise from 50 to 74 hours. This may show the power output is directly related to the rate of glycerol consumption, and that *R. palustris* retains electrogenic activity after depletion of glycerol by metabolising stores of glycogen.

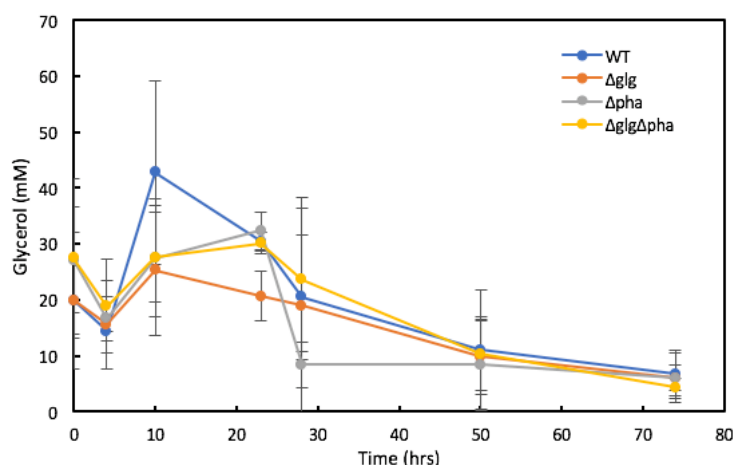


**Fig. 6.6:** Concentration of glycerol over 74 hours from MFC assay using wild type *R. palustris*,  $\Delta glgAC$ ,  $\Delta phaAB$ , and  $\Delta glgAC\Delta phaAB$  with graphene based aerogel anodes over 74 hours. Results are an average of three biological replicates and error bars show the standard deviation.

### **6.2.7. Electrochemical interaction and glycerol consumption from established MFC biofilms:**

In order to test whether storage molecule knockout altered current output from glycerol consumption by established biofilms of *R. palustris*, a second run of MFC experiments was set up for each strain simultaneously in triplicate. Carbon fibre was used at the anode as it was more durable than the graphene aerogels over longer time periods. No glycerol was added to the anodic chamber for the first week; on day six, cyclic voltammetry and linear sweep voltammetry were used to characterize each device. On the seventh day, glycerol was added during chronoamperometric recording, and the resulting current with the baseline subtracted converted to total charge accumulated. Fig. 6.7 shows from the averaged cyclic voltammograms from the wild type and knockout out strains that there were no major differences in electrochemical interaction of cells with the anode. The wild type showed a slightly more pronounced oxidation peak at 200 mV than the knockouts, but was otherwise similar to the knockouts. The current was much higher and redox peaks were less pronounced than in the example cyclic voltammogram in Fig. 6.4 which is from a device with carbon fibre at the anode. This is likely to be due to the differences in anode to cell interaction between carbon fibre and graphene.

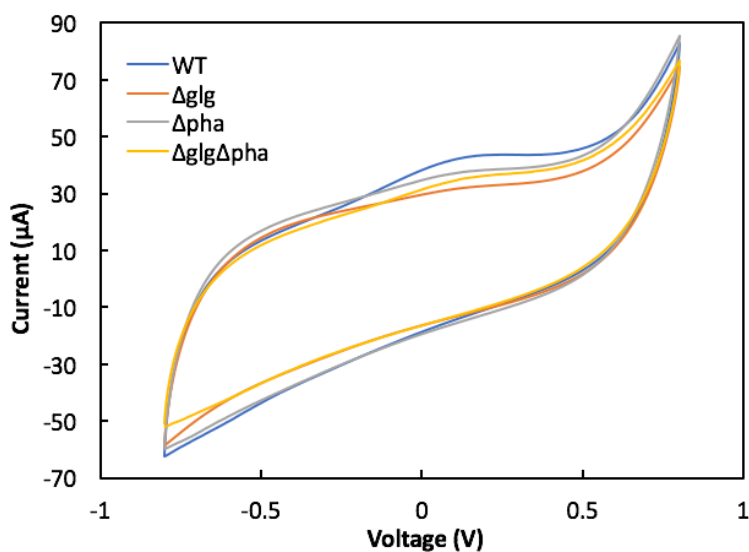


**Fig. 6.7:** Cyclic voltammograms at day six averaged from the three biological replicates of wild type *R. palustris*,  $\Delta glgAC$ ,  $\Delta phaAB$ , and  $\Delta glgAC\Delta phaAB$  in MFC devices.

With little apparent difference in mechanism of EET caused by lack of storage molecule synthesis, LSV was conducted to test for differences in bioelectrochemical parameters (Fig. 6.8). Again, there was no clear bioelectrochemical difference between wild type and knockouts, although it is interesting to compare these results to the previous, shorter timescale experiment.  $I_D$  was higher from the carbon fibre anodes at day six compared to the graphene aerogels at day three, possibly due to the small size of the aerogels and resulting larger volume of carbon fibre being used (c.10 times). OCP and  $P_V$  with carbon fibre anodes at day 6 were similar to the graphene aerogels at day 1, around 400 mV and 3-4 W m<sup>-3</sup>, but after three days the OCP, and resulting  $P_V$  had increased with the graphene aerogels to over 600 mV and c. 10 W m<sup>-3</sup>. Increased OCP with the graphene anodes is likely to be due to differences in the electrochemical interactions of graphene with *R. palustris*, which is covered in the next chapter. However, overall this experiment showed that there was no appreciable difference in OCP,  $I_D$ ,  $R_S$ , or  $P_V$  caused by storage molecule knockout.

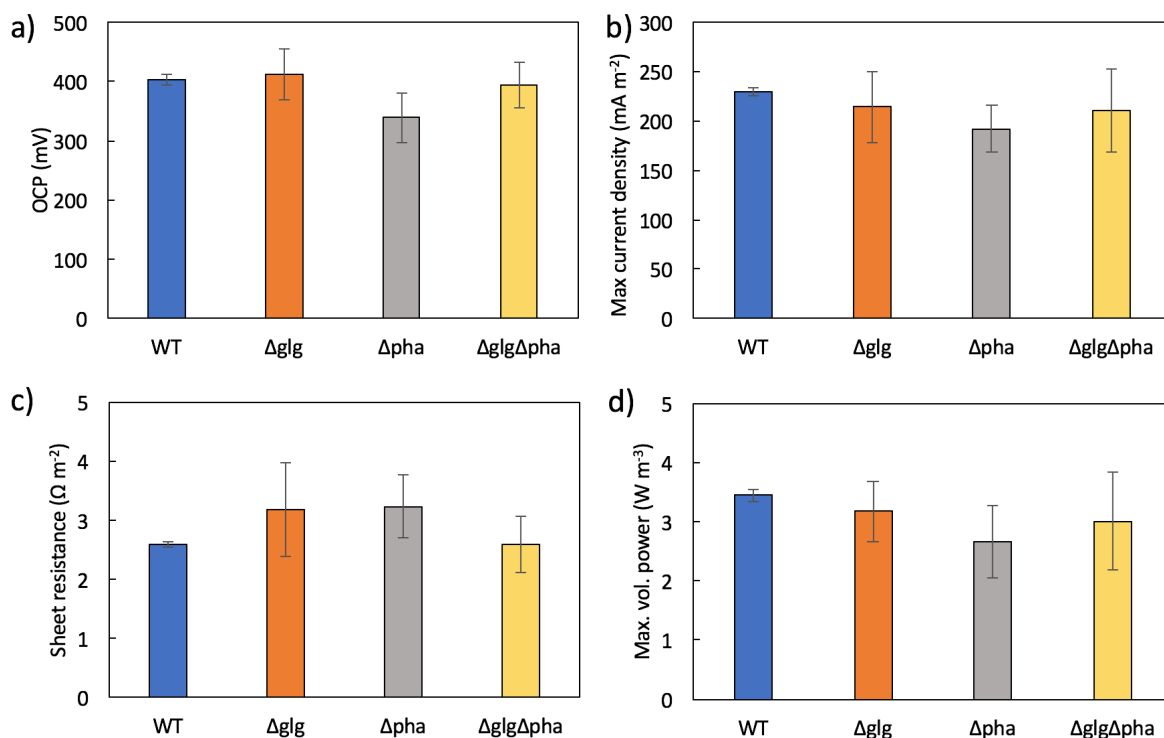


**Fig. 6.8:** a) Open circuit potential, b) maximum current density, c) sheet resistance, and d) maximum power density from MFC devices using wild type *R. palustris*,  $\Delta glgAC$ ,  $\Delta phaAB$ , and  $\Delta glgAC\Delta phaAB$  with carbon fibre anodes after six days. Results are the average of three biological replicates and error bars show the standard error.

### 6.2.8. Chronoamperometric responses to glycerol spiking in depleted MFCs:

LSV offers essentially a snapshot into the electrochemical activity of the MFC at a given time. By recording the rate of EET, or current, being generated by *R. palustris* we may be able to see different patterns in response to glycerol metabolism, and compare the total charge accumulated over an extended time period. At day seven of glycerol was added to a final concentration of 50 mM to each device by syringe injection at 9000 seconds after starting to record chronoamperometry, and the current was recorded for 60,000 seconds, or just under 17 hours. Fig. 6.9 shows the current response to the addition of glycerol over time for each replicate of the wild type and knockout strains. Each strain showed variation in in the initial

current and although they were pre-acclimated to the bias potential of 0V, stabilizing the current from most of the devices, the current from some devices was still declining more than others during the experimental run. To allow for these initial starting point differences, the initial, pre-glycerol, current was used to plot a projected curve, predicting the progression of current output had there been no glycerol added at 9000s. Previous experiments by Clayton Rabideau (personal communication) have suggested projected decline in current could be modelled by an exponential decay (Fig. 6.10). The current output was then normalised to the pre-glycerol current for each replicate and the flattened to account for the stabilization, or decay. This gives in Fig. 6.11 a comparison of the current due directly to the addition of glycerol for each replicate. Interestingly, there was an initial perturbation upon addition of glycerol with a spike in current immediately after, followed in some cases by a rapid reduction before a slow but steady increase in all cases.

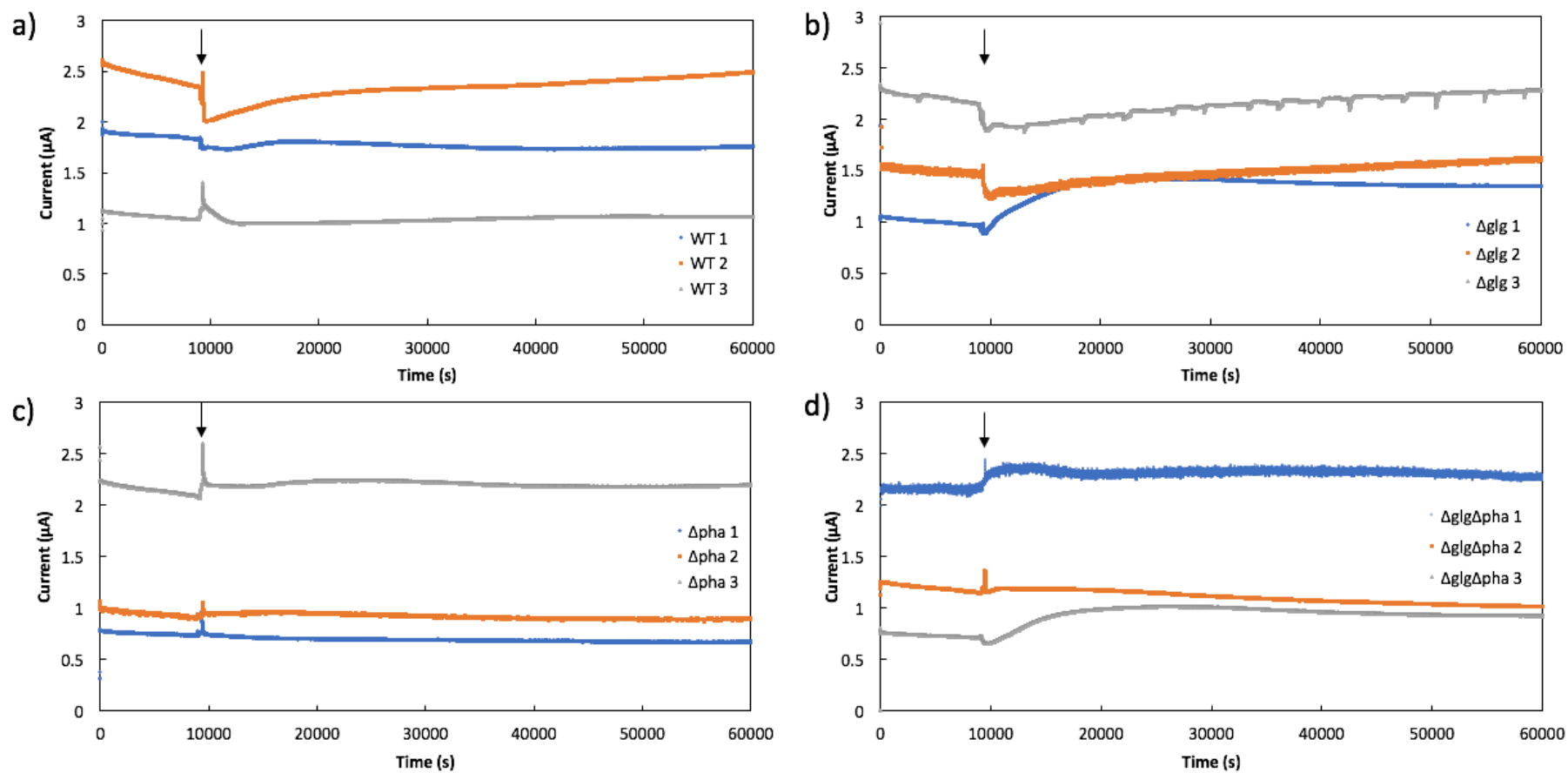


**Fig. 6.9:** Chronoamperometry from three MFC device replicates of a) wild type *R. palustris*, b)  $\Delta glgAC$ , c)  $\Delta phaAB$ , and d)  $\Delta glgAC\Delta phaAB$  at day 6. The total run lasted 60,000 seconds and 50 mM glycerol was added at 9000 seconds (black arrow).

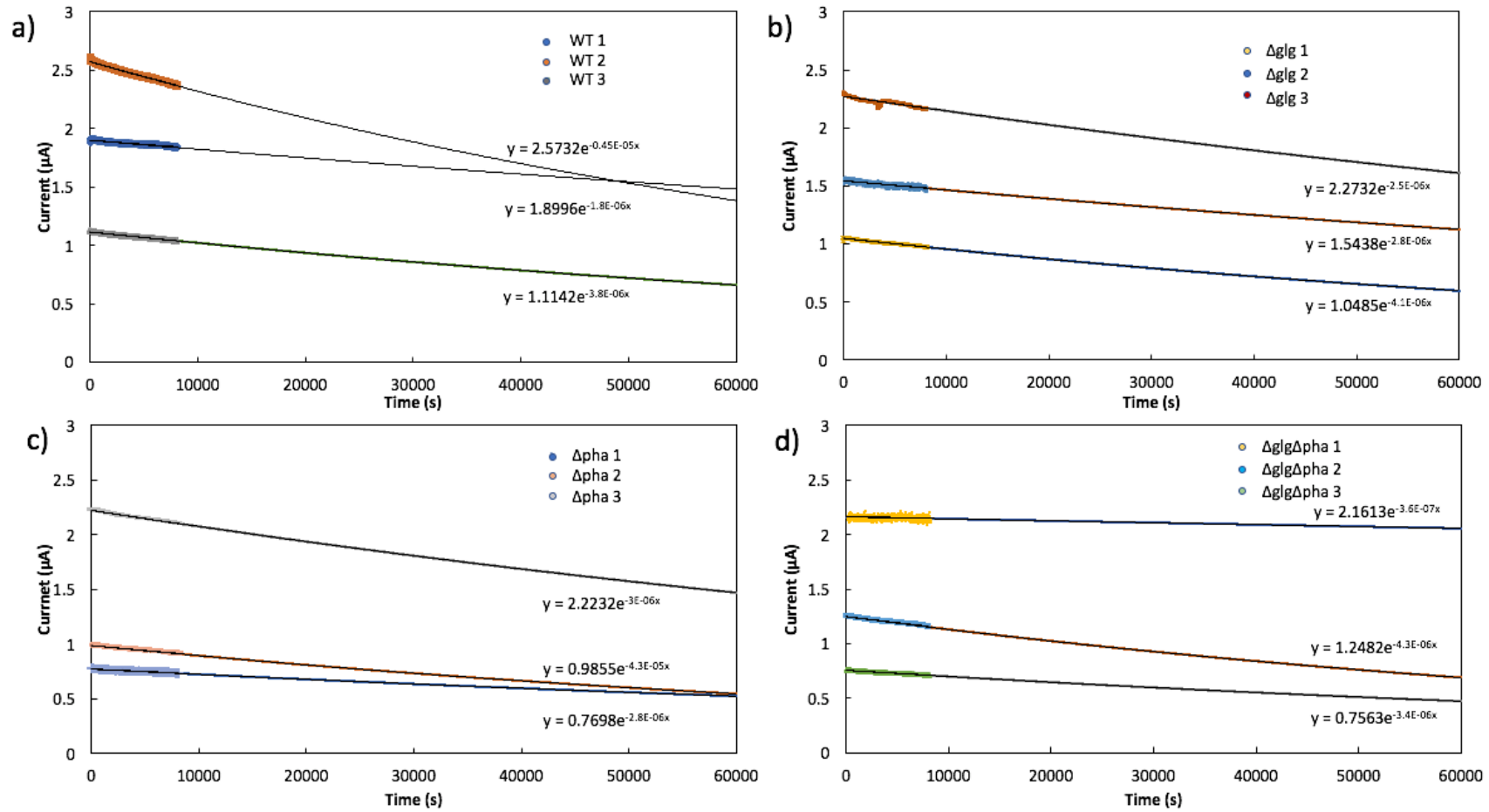


**Fig. 6.10:** Plots of the projected dark current according to the initial, pre-glycerol, current decay for each replicate of a) wild type *R. palustris*, b)  $\Delta glgAC$ , c)  $\Delta phaAB$ , and d)  $\Delta glgAC\Delta phaAB$ , assuming an inverse exponential decline.

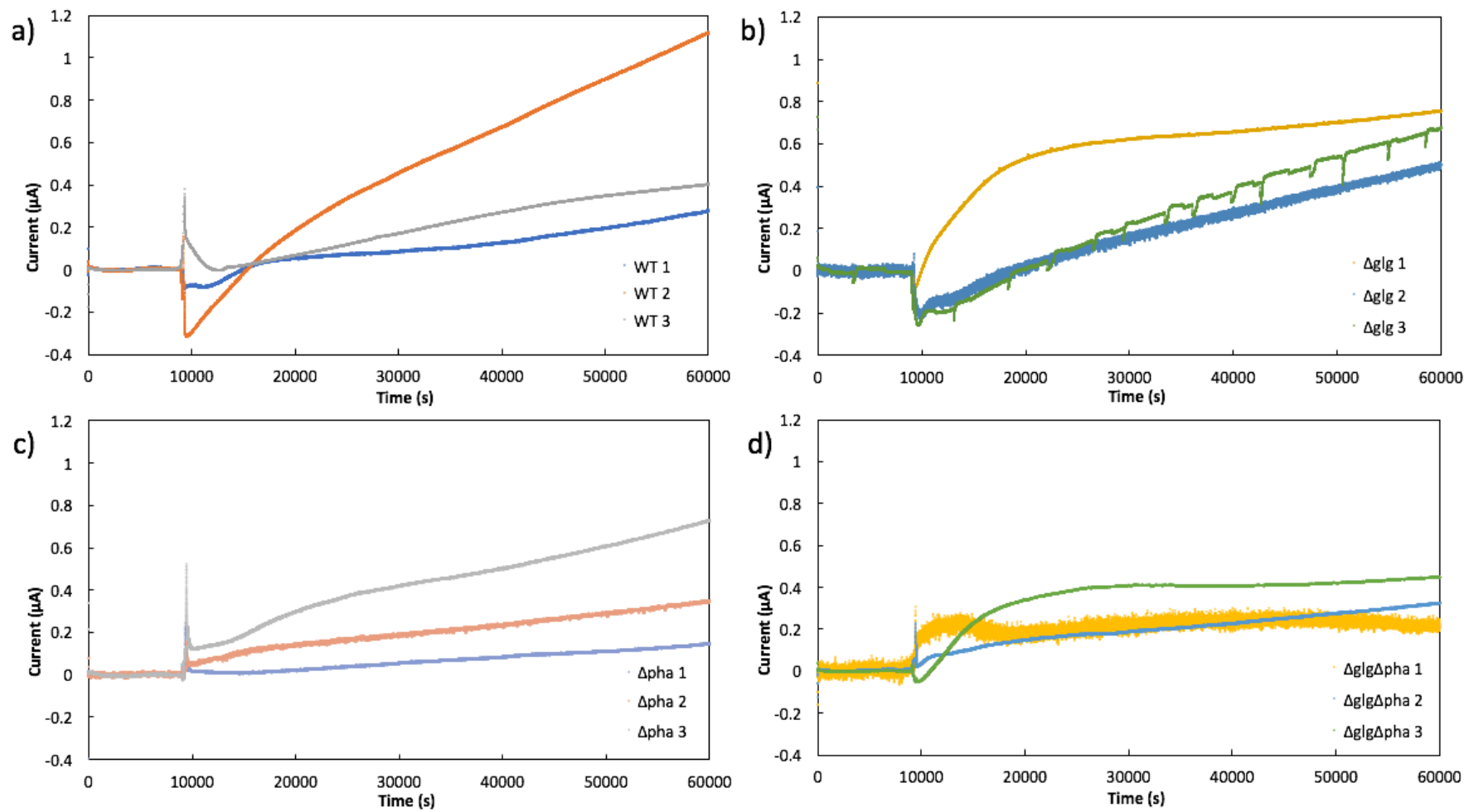


**Fig. 6.11:** Normalised current output due to glycerol supplementation in depleted MFCs for each replicate of a) wild type *R. palustris*, b)  $\Delta glgAC$ , c)  $\Delta phaAB$ , and d)  $\Delta glgAC\Delta phaAB$ .

The spikes may be due to a change in osmotic balance due to glycerol and/or a sudden effect on *R. palustris* metabolism. Rather than decline as glycerol was consumed, the current from each sample either continued to increase throughout the timecourse, or increased until a higher plateau, where it was maintained. One possible difference between the knockouts was the lack of an initial reduction in current after glycerol addition in the  $\Delta phaAB$ , with only a slight reduction in one of the  $\Delta glgAC\Delta phaAB$  replicates. If genuine, this may be linked to the role of PHB synthesis in redox balancing of the cell, the effect of which may be discernible as the initial current reduction. Fig. 6.12 shows the corrected cumulative charge over the time course of the experiment, and total charge accumulated due to glycerol over 51,000 seconds in Coulombs. The averaged charge accumulation shows the initial slight reduction from  $\Delta phaAB$  and  $\Delta glgAC\Delta phaAB$  preceding a steeper rate of charge accumulation than  $\Delta glgAC$  and the wild type. This means that the wild type has converted the least glycerol to electrical charge until it overtakes  $\Delta phaAB$  at 48,000 seconds, and  $\Delta glgAC\Delta phaAB$  at 56,000 seconds.  $\Delta glgAC$  overtakes  $\Delta phaAB$  at 30,000 seconds and  $\Delta glgAC\Delta phaAB$  at 42,000 seconds to reach the greatest amount of charge accumulated. The  $\Delta glgAC$  strain results in a slightly greater, although no statistically significant, charge accumulation –  $0.664 \pm 0.229 \mu\text{C m}^{-3}$  – than the wild type –  $0.536 \pm 0.235 \mu\text{C m}^{-3}$ .  $\Delta phaAB$  and  $\Delta glgAC\Delta phaAB$  yielded  $0.461 \pm 0.210$  and  $0.499 \pm 0.096 \mu\text{C m}^{-3}$ .

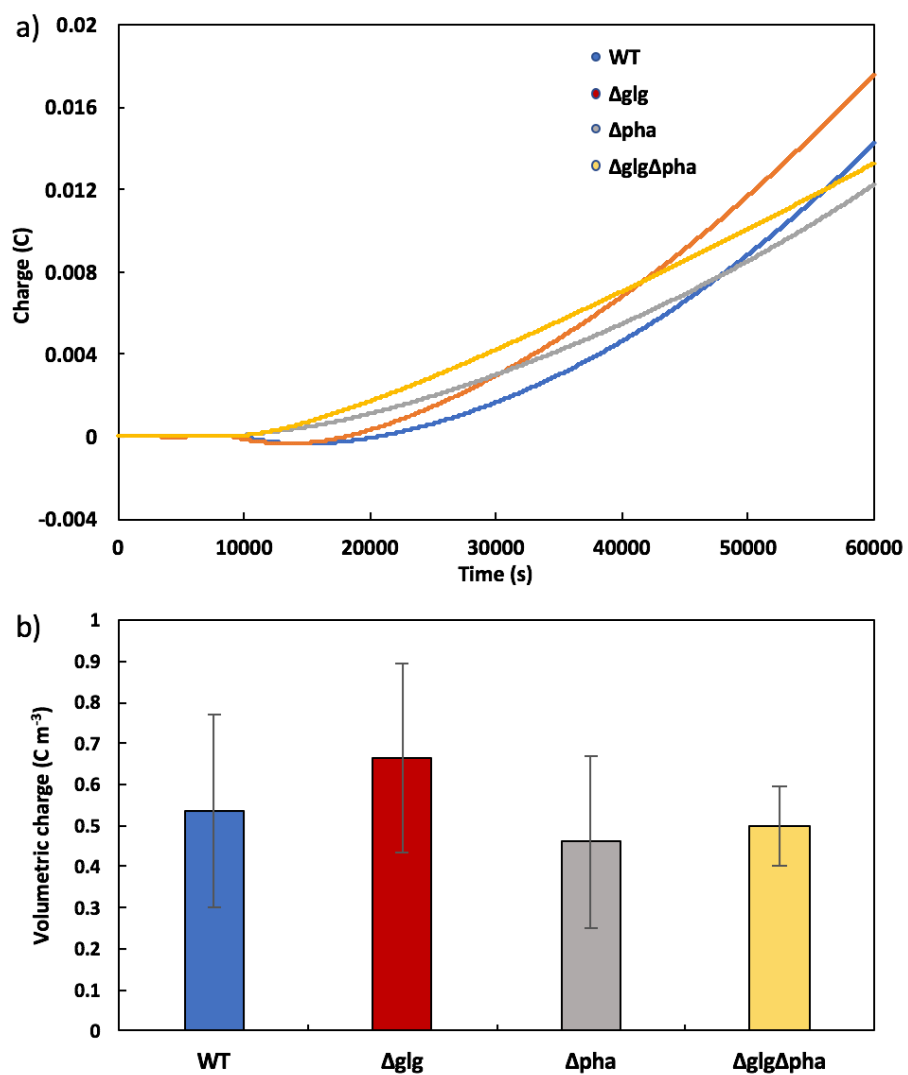


**Fig. 6.12:** a) Total summed charge over time from the metabolism of 50 mM of glycerol added to glycerol depleted MFC devices containing wild type *R. palustris*,  $\Delta glgAC$ ,  $\Delta phaAB$ , and  $\Delta glgAC\Delta phaAB$ . b) Average final charge accumulated over 51,000 seconds from glycerol from three biological replicates with error bars showing the standard error.

### 6.3. Discussion:

#### 6.3.1. Deletion of storage molecule synthesis had little effect on EET:

Somewhat surprisingly, the removal of glycogen and PHB synthesis had little effect on power output relative to the wild type. Growth rates of the biofilm in the MFC device were not measured as this would have disrupted the electrogenic biofilm, but they are unlikely to have caused much of a difference as each device was normalised to the same concentration at the start. Although the functional knockouts were not confirmed by subsequent complementation, glycogen staining and Nile Red assays (staining PHB) have confirmed significantly reduced levels glycogen and PHB in the knockout strains (Ruth Laing – personal communication). A suggestion of a difference in bioelectrochemical output appears at the end of the comparison of glycerol consumption with power output in Fig. 6.5, where the  $\Delta glgAC$  and  $\Delta glgAC\Delta phaAB$  strains seemed to plateau in power density at the penultimate time point, whereas the wild type and  $\Delta phaAB$  continued to rise (although caution must be exercised here, given the size of the error bars). Were the experiment extended and this trend continued, the effect might be attributed to a lack of glycogen synthesised in the first few days and thus a deficit in energy reserves when glycerol levels decrease. In Fig. 6.3  $\Delta glgAC$  had a growth deficit compared to the wild type, and, coupled with the apparent faster rate of consumption of glycerol, it could be concluded that knocking out glycogen synthesis reduces the efficiency of glycerol usage such that  $\Delta glgAC$  is catabolising the external carbon source rapidly and without diverting any carbon to energy dense glycogen. In this respect rhodopseudomonads may be different to many other bacteria, synthesising glycogen to optimum storage levels during exponential growth phase with plentiful nutrient supply, as opposed to only during periods of carbon or nitrogen scarcity or imbalance (Wilson et al. 2011). So being unable to synthesise glycogen, it might be expected to divert reducing power to other compounds, or towards EET. The total charge

accumulated from metabolising glycerol in 51,000 seconds from glycerol depleted MFCs was slightly, but not significantly, higher than the wild type (Fig. 6.12). These suggestive differences were less apparent from the double knockout  $\Delta glgAC\Delta phaAB$ , in which growth actually accelerated compared to the wild type in the first few days, and the glycerol consumption rate was intermediate between the wild type and  $\Delta glgAC$ . This could suggest opposing roles in a redox state balancing network that counteracted each other, or perhaps the reduced burden to the cell of storage molecule synthesis promoted early growth. Removal of PHB was predicted to have an effect on MFC output because it can accumulate up to 30% dw in stationary phase cells that, while not dividing, retain a high rate of metabolism (McKinlay et al. 2014). However, little or no effect was observed relative to the wild type. Although glycogen granule synthesis is thought to be central to the robust longevity of *R. palustris* (Pechter et al. 2017), little is known about the effect of glycerol in particular on glycogen or PHB synthesis in purple non-sulphur bacteria. However, glycerol was found to inhibit PHB synthesis in a pseudomonad bacterium (Zevenhuizen & Ebbink 1974). It may also be that the conditions of the MFC were not conducive to PHB synthesis to the degree that a knockout strain would show a significant deficit, and that having an external electron acceptor, the anode, negated the need to use storage molecules as an electron sink in the first place.

### **6.3.2. MFC conditions may not have been optimised:**

Previous experiments in the lab had found an increase in power output over the wild type from a triple mutant lacking both glycogen and PHB synthesis as well as a hydrogen uptake enzyme HupL (Paolo Bombelli – personal communication). It is possible that deletion of *hupL* in this triple knockout strain was the most effective knockout as MFC conditions can induce hydrogen formation, however differences in MFC design for these experiments may have resulted in suboptimal conditions to compare storage molecule knockouts. The experiment with the triple

mutant also used anaerobic digestate as the feedstock, creating a very different environment to the glycerol enriched media used here. Glycerol was chosen for these experiments as a precursor to subsequent experiments using crude glycerol that were not completed, however other carbon sources such as acetate may be more suited to electricity generation in *R. palustris*. The current increase after adding glycerol to the depleted MFCs varied in shape, even between replicates of each strain, with some reaching a plateau, and others continuing on an upwards trajectory with no sign of reducing. The amount of glycerol added was in all likelihood excessive, and because the anode chambers were not mixed, the local concentration could have varied greatly as it may not have been able to disperse effectively throughout the carbon fibre anodic mass. Excessive concentrations of glycerol could also be inhibitory, effectively fixing the cells. Initially, many attempts were made to perform the experiment with lower concentrations of glycerol that would ideally be entirely consumed within the chronoamperometry window and result in a clear increase followed by a return to previously stable current. However, there was often no visible change in current after the addition of glycerol, which, given the lengthy run time, led to prioritizing of other MFC/BPV experiments. Eventually the conditions eliciting a current response to the addition of glycerol in these experiments ensured the MFCs were fully depleted of glycerol in the medium, and were protected from contamination by careful preparation, before adding a large quantity of glycerol. To define the optimal set of conditions for comparing knockout strains, a greater variety of different substrates, anode materials, bias potentials, light conditions, and other factors should be explored.

### **6.3.3. Glycerol concentration quantification:**

A major problem with coming to conclusions about the efficiency of bioelectricity generation from glycerol is the high variability of glycerol concentrations measured in samples extracted

from MFCs. The colorimetric assay protocol had to be adapted from its original form to be able to fit a high number of samples at lower volumes. The time sensitive addition of sodium metaperiodate by individual manual pipetting introduced a degree of error. In addition, there were slight differences in the length of the heat step, although iced water was used to cool the samples down rapidly. As a result, standard curves were included with every assay run. With practice and careful implementation, the standards curves became more reliable, and although they needed to be run every time, the absorption peaks at 410 nm corresponding to 0 to 0.3 mM of glycerol followed a linear relationship (see example in inset, Fig. 6.3b). The variation in glycerol measurements, therefore, must come from the sample extraction or storage. It is unlikely that glycerol would be unstable in the storage conditions used. However, there may be inherent difficulties with sampling medium from MFC anodic chambers with an anode chamber packed with dense carbon fibre and very dense culture ( $OD_{660}$  3.0) that has formed a biofilm on the anode surface. Although mixing the anode chamber fully would mean any sample extracted would be representative of the overall glycerol concentration, any electrogenic biofilms would be disrupted. Future experiments could be designed with a gently stirred anodic chamber that would still allow cells to attach and form a biofilm on the anode, but ensure the medium components are evenly dispersed. A further challenge in sample extraction from MFCs was maintaining an anaerobic environment. Whilst a level of oxygen contamination was accepted as inevitable, removing a medium sample creates negative pressure, bringing in air and oxygen, which have an inhibitory effect on *R. palustris*. A bespoke extraction system or argon gas sparging system incorporated into an MFC device could be beneficial.

#### **6.4. Conclusions:**

In conclusion, unmarked genomic knockouts of glycogen and PHB synthesis were successfully generated in *R. palustris*, but the mutations were found to have little effect on the rate of glycerol conversion to EET as measured in a MFC. Given the importance of glycogen and PHB evident from the literature as storage molecules and electron sinks, they are still likely to have an effect measurable as in an MFC relative to the wild type if conditions are found that mimic a situation in which the cell would be dependent on the synthesis, or existing reserves of, glycogen or PHB.

## **7. EFFECT OF CELL TO ELECTRODE INTERACTIONS IN**

### ***R. PALUSTRIS* MFC OPERATION**

#### **7.1. Introduction:**

##### **7.1.1. Optimizing electrode properties for applied use of MFCs:**

One of the most significant factors limiting the efficiency of BESs today is the charge transfer of electrons from the cell to the anode (Xie et al. 2015). Power output from MFC electrode materials is linked to surface area, conductivity, and biocompatibility, and facilitate current generation by catalysing the oxidation of microorganisms at the anode and the reduction of O<sub>2</sub> to H<sub>2</sub>O at the cathode (Yu et al. 2016; P. Bombelli et al. 2012; M. Mustakeem 2015). This chapter investigates how surface area and conductivity can be optimized for electrode materials in collaboration with Dr. Felice Torrisi and Tian Carey at the Cambridge Graphene Centre (CGC).

##### **7.1.2. Surface area of MFC electrodes is an important factor contributing to power output:**

Carbon-based materials such as carbon felt, carbon fibre, carbon paper and graphite granules have been used extensively as anode materials due to their chemical stability and resistance to corrosion in an aqueous environment, electrical conductivity, and their high surface area (Y. Z. Zhang et al. 2011; Ringeisen et al. 2006; Yu et al. 2016). Higher power outputs can be reached by fabricating 3D porous structures incorporating conductive materials that maximise available surface area for biofilm colonization and cell to anode contact (Oh & Logan 2006). Aerogels are increasingly yielding high volumetric power outputs thanks to their extremely high surface area and tuneable composition (Y. Yang et al. 2016).

### **7.1.3. Graphene based MFC electrodes:**

Graphene has a higher theoretical surface area than many commonly used MFC electrode materials, up to 2630 m<sup>2</sup>/g (Stoller et al. 2008), it has the potential for cost-effective mass production (Paton et al. 2014), high electrical conductivity (L. Wang et al. 2013), impressive mechanical strength (Lee et al. 2008), and shows good biocompatibility (Fabbro et al. 2016). These properties mean graphene has garnered much interest across a variety of applications including flexible electronics, energy harvesting and storage, biomedical applications (Ferrari et al. 2014), as well as proving an effective material for MFC electrodes.

### **7.1.4. Use of graphene oxide in MFC electrodes:**

Most applied graphene based MFC electrodes to date have used graphene oxide (GO). MFC electrodes enhanced with chemically modified GO have produced some of the highest power densities to date: a 3-fold increase to 0.0525 W m<sup>-3</sup> from carbon cloth (Liu et al. 2012), an 18-fold increase to 2.67 W m<sup>-2</sup> from stainless steel mesh (Y. Zhang et al. 2011), and a 19-fold increase to 661 W m<sup>-3</sup> from nickel oxide foams (H. Wang et al. 2013). Furthermore, a modified GO-based aerogel anode yielded the highest volumetric power density so far reported at 750 W m<sup>-3</sup> (normalised to anode volume) (Y. Yang et al. 2016). GO owes its electrode performance in part due to oxygen and nitrogen-containing functional groups and impurities imparting a catalytic effect and improving EET efficiency *via* an electron shuttling processes. The low density, high surface area, and high conductivity of GO aerogels establish them as high performance MFC anodes (Nardecchia et al. 2013; Chen et al. 2014; X. Yang et al. 2016), however chemical oxidation introduces basal plane defects detrimental to the mechanical and electrical properties of GO. Partial recovery of performance loss can be attained by chemical

reduction to reduced GO (rGO) (Mattevi et al. 2009), alternatively, pristine graphene flakes with the basal plane unaltered can be used.

#### **7.1.5. Use of pristine graphene in MFC electrodes:**

The most common methods for growing pristine graphene structures involve intensive and costly procedures such as acid etching, to remove a copper or nickel template, that can leave chemical residuals, or gas precursors like methane for chemical vapour deposition (CVD) (Das et al. 2013). A nickel mesh template has been used to grow porous and conductive pristine graphene structures with  $850 \text{ m}^2 \text{ g}^{-1}$  specific surface area (H. Wang et al. 2013). A simpler alternative is freeze gelation of graphene inks, performed at room temperature and using a freezer, and producing pristine graphene aerogels with superior electrical properties to GO or rGO (Lin et al. 2016). In this chapter we use pristine graphene flakes produced by liquid phase exfoliation (LPE) of graphite or cracking of sustainably sourced methane biogas (from Cambridge Nanosystems) to make custom graphene based inks to modify existing electrodes and produce customized aerogels (Lotya et al. 2009).

#### **7.1.6. Conductive polymers in aerogels:**

Aerogels made from biomass derived scaffold molecules such as alginate, pectin, or the food thickening agent carboxymethylcellulose (CMC) are cost effective and result in highly porous yet robust structures (Antonyuk et al. 2015; Wang & Sanchez-Soto 2015). Their electrical properties can be enhanced by conductive polymers such as polyaniline (PANI) and polyacrylamide (PAm), leading to potential applications as supercapacitors (Zhao et al. 2016). Along with pristine graphene, we incorporate the conjugated conductive polymer Poly(3,4-ethylenedioxythiophene)-poly(styrenesulfonate) (PEDOT:PSS) into aerogels used as MFC anodes. PEDOT:PSS has been extensively used in the development of flexible and printed

electronics thanks to its high conductivity and ease of processing, including combination with graphene to enhance catalytic and structural properties. Graphene has been shown to interact synergistically with the PEDOT:PSS polymer matrix via non-covalent  $\pi$ - $\pi$  stacking interactions between aromatic rings in each compound (Seekaew et al. 2014). It has been used to enhance electron transfer characteristics of graphite felt and carbon cloth (Kang et al. 2015) and to provide conductive bridges between graphene flakes (Soltani-Kordshuli et al. 2016).

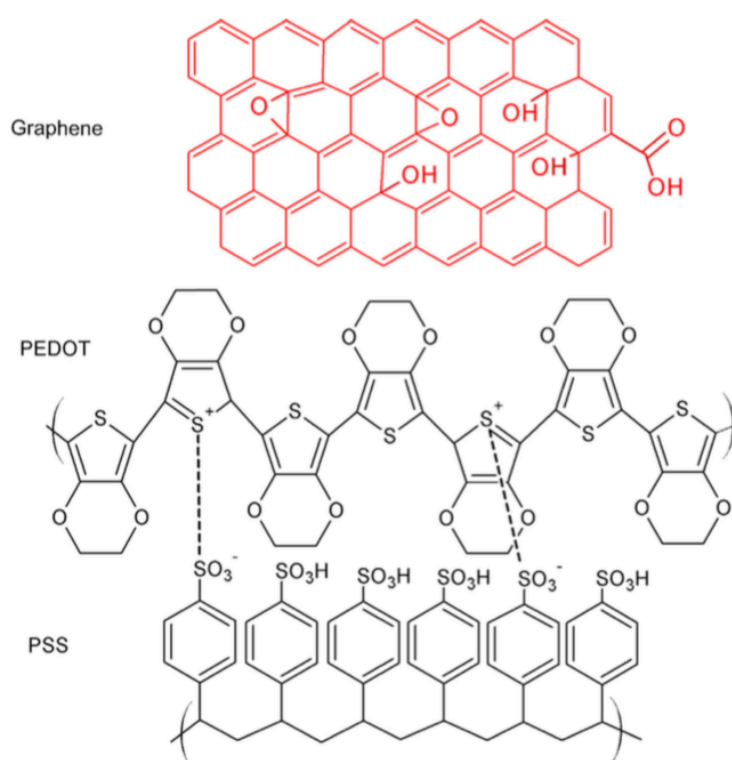


**Fig. 7.1:** Illustration of the structures of graphene and PEDOT:PSS (Reproduced from Seekaew et al. 2014).

### 7.1.7. Graphene as a cathodic catalyst:

Platinum is often used at the cathode to maximise catalytic efficiency (Winter & Brodd 2004), but high and fluctuating costs (~£26/g) limit its commercial viability in MFC technology. Graphene in various doped forms has been developed for use as a cathode in microelectronics

(Chang et al. 2015) and battery technology (Sun et al. 2012; Li et al. 2012), and graphene oxide has been used recently as an MFC cathode (Santoro et al. 2017). However pristine graphene has not been tested for cathodic catalytic activity, neither has an all graphene MFC device been demonstrated to date.

#### **7.1.8. Aims:**

In this chapter we aim to test the effects of surface area and material conductivity of electrode materials on the power output of MFCs containing *R. palustris*. Electrode materials will be assembled and characterized in terms of their specific surface area and conductivity, before bioelectrochemical characterization using cyclic and linear sweep voltammetry. The basic anode configuration is a single layer of marine grade stainless steel mesh, upon which anode extensions made from commercially available conductive carbon foam (Maplins) and custom CMC based aerogels will be placed. The effect of surface area will be tested by comparing the power output from MFCs using marine grade lower surface area stainless steel mesh and carbon foam, and high surface area CMC based aerogels. The effect of material conductivity will be tested by incorporating pristine graphene flakes and PEDOT:PSS as a coating on the carbon foam, and as a composite part of the aerogel. As a novel MFC anode material, the effect of graphene and PEDOT:PSS will also be compared separately. Pristine graphene coated stainless steel will be tested for its function as an air cathode, and as a demonstration of applications a graphene anode – graphene cathode MFC and a graphene anode powered digital clock will be described.

## **7.2. Results:**

### **7.2.1. Alternative electrode material fabrication and characterization:**

The bioelectrochemical performance in terms of MFC power output from stainless steel (SS) mesh was compared to commercially available carbon foam (Maplin) and custom fabricated aerogel anodes. Graphene flakes were used to modify these materials to alter conductivity and catalytic function. All graphene based electrodes and aerogels were fabricated by Tian Carey and Dr. Felice Torrasi in the Cambridge Graphene Centre (CGC) as described in the methods section and summarised here in Table 4.1. They performed Raman spectroscopy, mercury porosimetry, electrochemical impedance spectroscopy, and SEM on the dry aerogels prior to use as anodic substrates in our MFC devices. Bioelectrochemical characterization of electrode materials in the MFC, and SEM of aerogels extracted from MFC devices after operation with *R. palustris*, was done by Toby Call in the Department of Biochemistry and the Cambridge Advanced Imaging Centre (CAIC) respectively. It is worth noting that although the aerogel samples made with 20% PEDOT:PSS ultimately yielded the highest current density and volumetric power, it proved impractical to make sufficient samples to characterize fully as at high concentrations PEDOT:PSS no longer acted as a dispersant for graphene and it became difficult to produce an even distribution of components in the ink. Unless otherwise stated A-CMC-PD or A-CMC-Gr-PD refers to 10% PEDOT included in the initial ink.

**Table 7.1: Electrode materials used in this study:**

Electrode materials	Electrode name/abbreviation	Fabrication method	MFC function
Marine grade stainless steel	SS	-	Anode
Carbon foam	CF	-	Anode
Stainless steel-graphene-PEDOT:PSS (1%)	SS-Gr-PD	Vacuum deposition	Cathode
Carbon foam-graphene-PEDOT:PSS (1%)	CF-Gr-PD	Drop casting	Anode
Carbon paper-platinum	CP-Pt	-	Cathode
Carbon-platinum coated PEM membrane	Nafion® catalyst	-	Cathode
CMC aerogel	A-CMC	Freeze gelation	Anode
CMC-PEDOT:PSS (10%) aerogel	A-CMC-PD (10%)	Freeze gelation	Anode
CMC-PEDOT:PSS (10%) aerogel	A-CMC-PD (20%)	Freeze gelation	Anode
CMC-graphene	A-CMC-Gr	Freeze gelation	Anode
CMC-graphene-PEDOT:PSS (10%)	A-CMC-Gr-PD (10%)	Freeze gelation	Anode

### 7.2.2. Raman spectroscopy:

Raman spectroscopy was used to test whether the anode materials had the expected composition, looking in particular for peaks identifying graphene and PEDOT:PSS present where expected in the aerogels, modified carbon foam and modified stainless steel electrodes. The results in Fig. 4.2a showed the expected signature peaks from PEDOT:PSS (PD, pink line), graphene flakes made by liquid phase exfoliation, and the presence of both in the composite graphene-PEDOT:PSS ink (Gr-PD, green line), stainless steel with graphene-PEDOT:PSS deposits (SS-Gr-PD, blue line), and graphene-PEDOT:PSS coated carbon foam (CF-Gr-PD, red line). Both graphene and carbon foam (CF, black line) have D and G peaks attributed to them, however the 2D peak appears unique to graphene. Presence of the 2D peak indicates the graphene layers are electronically decoupled (Ferrari et al. 2006). Fig. 4.2b shows the Raman spectra of graphene flakes from Cambridge Nanosystems both alone and incorporated with

CMC in the A-CMC-Gr aerogel, as well as PEDOT:PSS incorporated with CMC in the A-CMC-PD aerogel. Peaks for both graphene and PEDOT:PSS confirm they are both present in the A-CMC-Gr-PD aerogel. Although we used pristine graphene flakes in our materials, as opposed to reduced graphene oxide like many other contemporary studies (H. Wang et al. 2013; X. Yang et al. 2016; Y. Z. Zhang et al. 2011), analysis of the dispersion of the G peak (by Tian Carey) indicates defects along the graphene flake edges and plane (Beams et al. 2015).

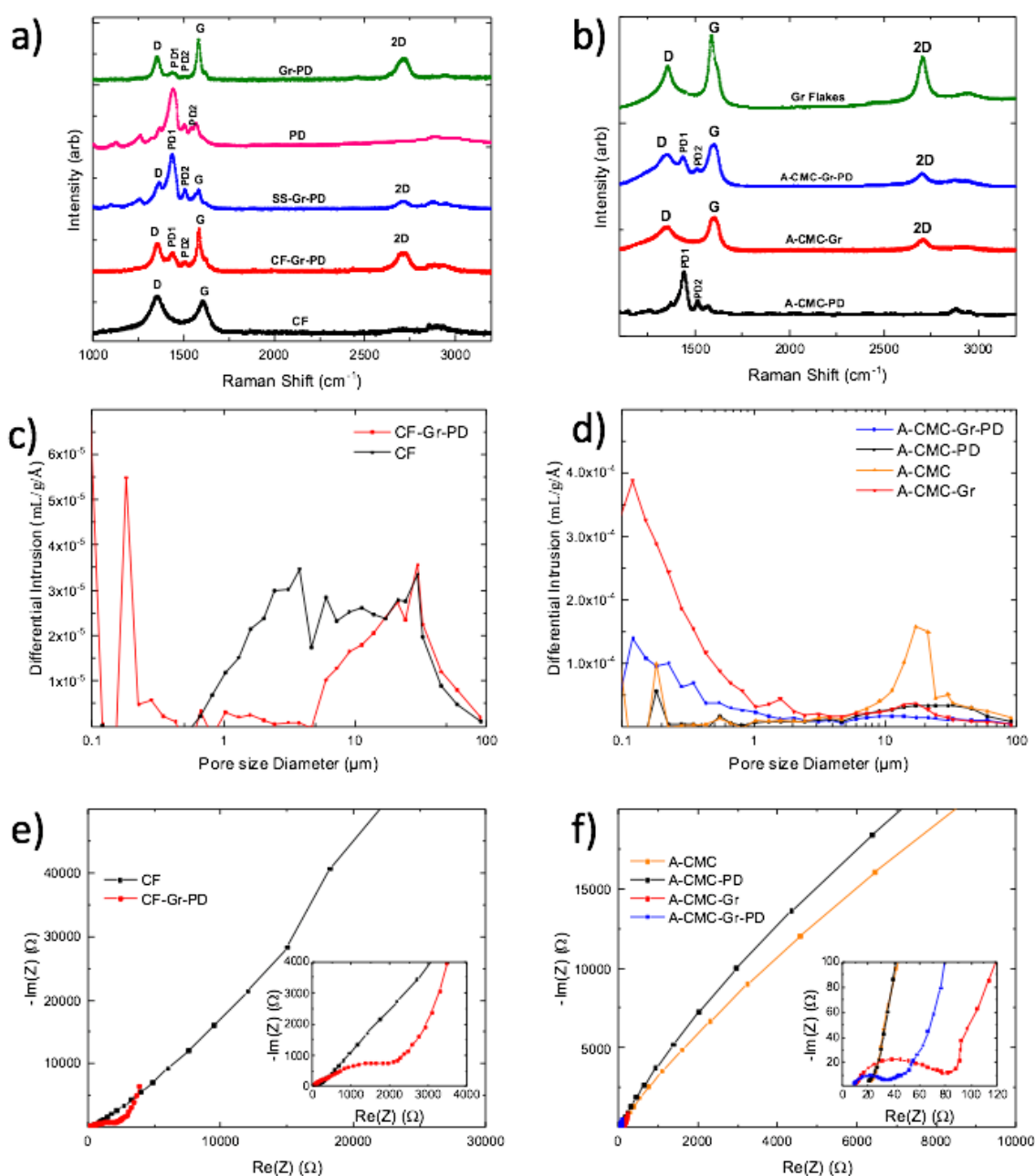


**Fig. 7.2:** Raman spectroscopy of the anode materials showing key peaks of the a) carbon foam (black line - CF), graphene and PEDOT ink (green line – Gr-PD), PEDOT alone (pink line - PD), carbon foam with graphene and PEDOT ink coating (red line – CF-Gr-PD), and stainless steel with graphene and PEDOT coating (blue line – SS-Gr-PD). b) Raman spectra of the graphene flakes alone (green line – Gr flakes), the CMC with graphene aerogel (red line – A-CMC-Gr), the CMC with PEDOT aerogel (black line – A-CMC-PD), and the CMC with graphene and PEDOT aerogel (blue line – A-CMC-Gr- PD). Mercury porosimetry showing differential intrusion and pore size distribution of c) the carbon foam anode material (black line – CF), and carbon foam with graphene and PEDOT coating (red line – CF-Gr-PD). d) Differential intrusion and pore size distribution in each of the aerogels: A-CMC (yellow line), A-CMC-PD (black line), A-CMC-Gr (red line), A-CMC-Gr-PD (blue line). Electrochemical impedance spectroscopy derived Nyquist plots of e) carbon foam (black line), and carbon foam with graphene and PEDOT coating (red line). f) Nyquist plots of each of the aerogels: A-CMC (yellow line), A-CMC-PD (black line), A-CMC-Gr (red line), A-CMC-Gr-PD (blue line).

### **7.2.3. Specific surface area and morphological characteristics from mercury porosimetry and SEM:**

The average pore size and specific surface area of the carbon foam CMC aerogel based materials were characterised by differential intrusion in mercury porosimetry, revealing key differences in pore size and potential cell to anode surface contact area between the aerogels and other anode materials. Fig. 4.2c shows that the carbon foam (CF) had a smaller average pore size (2  $\mu\text{m}$ ) and almost twice the corresponding calculated specific surface area (3.7  $\text{m}^2 \text{g}^{-1}$ ) compared to carbon foam coated with graphene (CF-Gr-PD) (5  $\mu\text{m}$  and 2  $\text{m}^2 \text{g}^{-1}$ ). The carbon foam based anodes had a primary pore size in the range of 100  $\mu\text{m}$ , with an abundance of smaller pores pitting the surface which might be expected to aid adherence of the 1-2  $\mu\text{m}$  long

*R. palustris* cells. SEM images (Fig 4.3) did not reveal any obvious differences between CF and CF-Gr-PD, so the difference in average pore size may be due to filling in of the smallest pores with graphene flakes bridging the gaps.

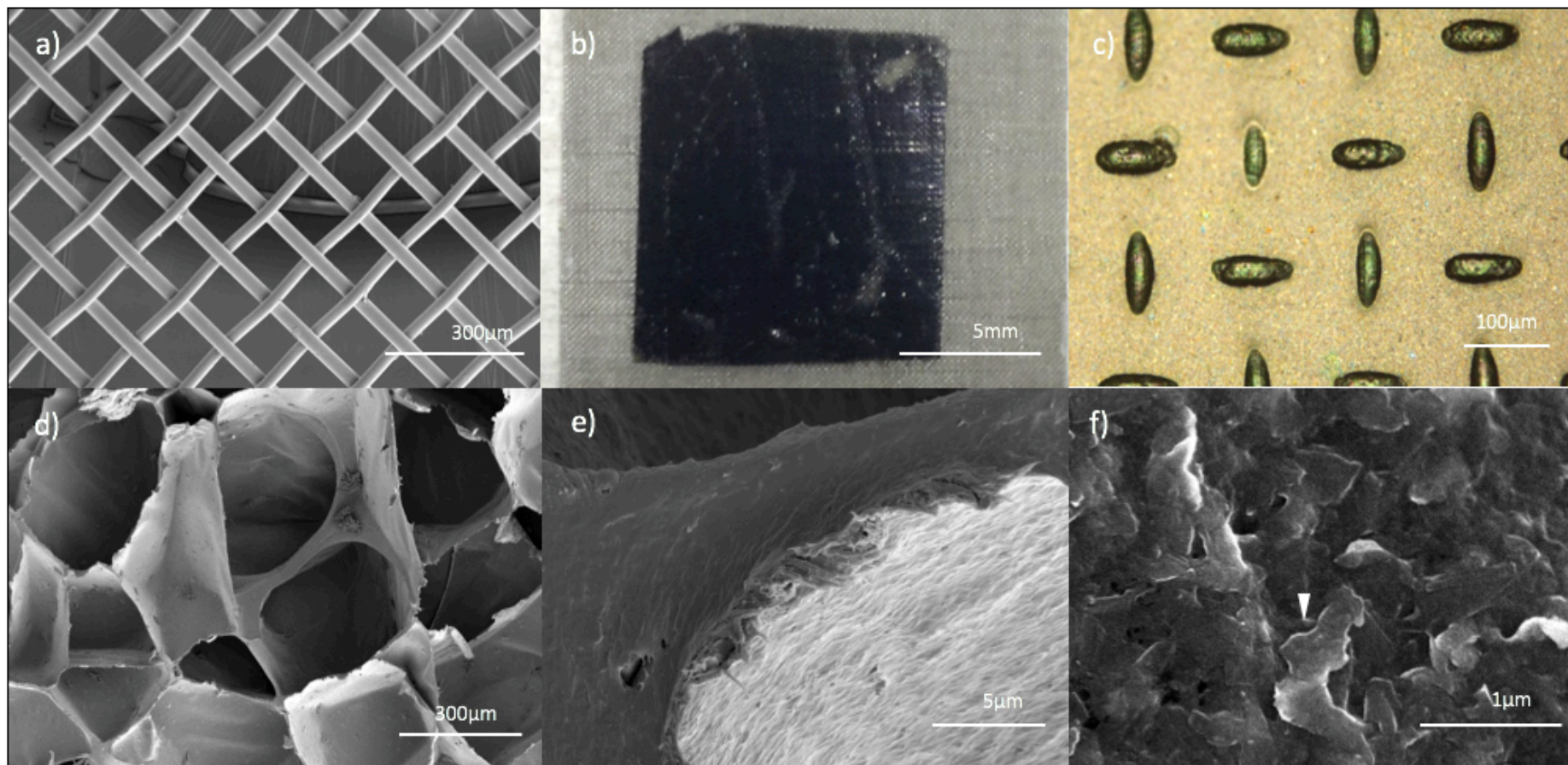


**Fig. 7.3:** SEM image of a) marine grade stainless steel mesh, b) Photograph of vacuum filter deposited graphene-PEDOT over stainless steel mesh, and c) optical microscopy showing the deposition plane between the stainless steel mesh wires. SEM images of d) carbon foam anode (CF) material at low magnification, e) at higher magnification and f) carbon foam coated with graphene-PEDOT-IPA ink (CF-Gr-PD) showing the surface bonded graphene flakes (white arrow).

The average pore size and specific surface area of the aerogels were also measured and calculated by mercury porosimetry (Fig. 4d). The predominant peak for pore size distribution in the carboxymethylcellulose base aerogel (A-CMC) was 17  $\mu\text{m}$ , with some smaller peaks towards 100 nm. Addition of 10% poly(3,4-ethylenedioxythiophene)-poly(styrenesulfonate) (PEDOT:PSS) in A-CMC-PD resulted in a broader pore size distribution between 10 and 90  $\mu\text{m}$ . SEM of the dry A-CMC-PD revealed a smoother surface with larger pores and filamentous structures, probably resulting from polymerization of water-insoluble PEDOT in the water based ink during the freeze drying process. SEM images of A-CMC-PD after use in the MFC showed cells embedded in a filamentous mesh (Fig. 4.8), suggesting that despite the smooth appearance of dry A-CMC-PD, in the conditions of the MFC partial disintegration led to high cell to anode material surface contact. With the addition of graphene to make A-CMC-Gr and A-CMC-Gr-PD, the pore size distribution dropped to predominantly in the range of 0.1 – 1  $\mu\text{m}$ .

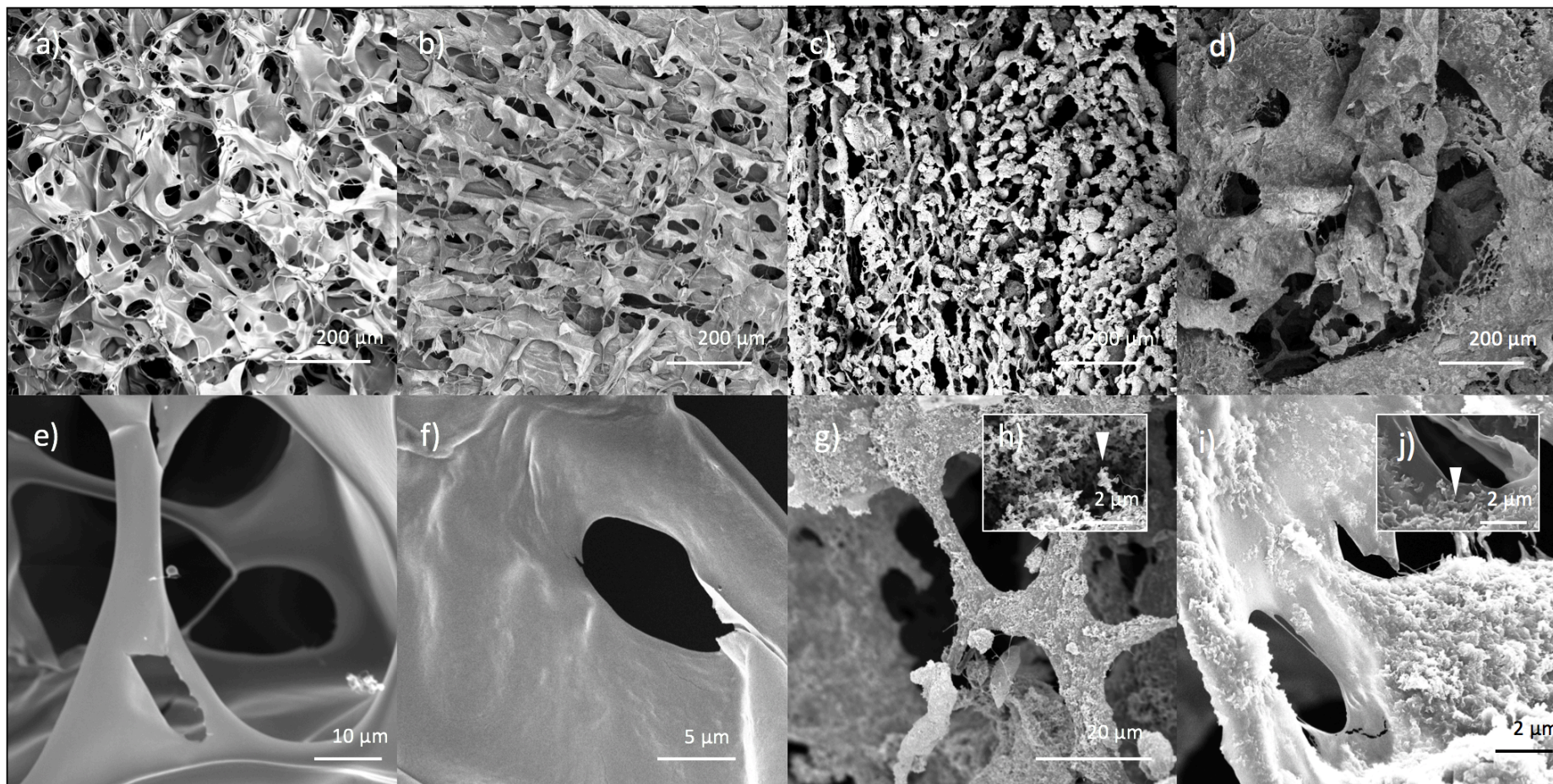


**Fig. 7.4:** SEM images show aerogels A-CMC, A-CMC-PD, A-CMC-Gr, and A-CMC-Gr-PD at low magnification (a-d respectively), and A-CMC, A-CMC-PD, A-CMC-Gr, and A-CMC-Gr-PD at higher magnification (e-g, i) respectively. Inset in g), h) shows under high magnification stacked graphene flake structures from A-CMC-Gr, and inset in i), j) shows graphene flakes embedded in the surface of A-CMC-Gr-PD.

The calculated surface areas for the aerogels were  $7.1 \text{ m}^2 \text{ g}^{-1}$  for A-CMC,  $3.9 \text{ m}^2 \text{ g}^{-1}$  for A-CMC-PD, increasing to  $20.2 \text{ m}^2 \text{ g}^{-1}$  for A-CMC-Gr and  $8.2 \text{ m}^2 \text{ g}^{-1}$  for A-CMC-Gr-PD. Comparison of the calculated surface areas for the aerogels shows that graphene flakes help to increase the potential cell to surface contact area. However, we suspect the true surface area values to be much higher. This is because the high pressure injection of mercury to probe intrusion resistances may damage and deform many of the smaller pores and filamentous extensions due to the fragile nature of the aerogel scaffold (Drake 1949; Leofanti et al. 1998). SEM images of dry A-CMC-Gr showed filamentous stacks of graphene flakes bound end to end (Fig. 4.4h). During experimental runs it became clear that the graphene was not strongly bound to the aerogel as the medium turned black from loose graphene flakes, indicating disintegration of the A-CMC-Gr aerogel. SEM images of A-CMC-Gr after use in the MFC showed agglomerated graphene connected by underlying filamentous CMC scaffold, and cells dispersed in amongst the material. With PEDOT added to the ink the A-CMC-Gr-PD aerogels maintained their integrity during MFC operation. SEM images of A-CMC-Gr-PD also showed regions of agglomerated graphene flakes, although sitting on thicker planes of underlying CMC and PEDOT material, which most likely helped to bind the graphene to the aerogel and provide conductive bridges between graphene dense regions.

#### **7.2.4 Electrochemical impedance spectroscopy (EIS):**

EIS was used by Tian Carey to measure the conductivity and determine the charge transfer resistance ( $R_{ct}$ ) of the anode materials before the addition of *R. palustris* cells. Nyquist plots were generated by plotting imaginary impedance  $\text{Im}(Z)$  versus real impedance  $\text{Re}(Z)$  of the electrode material as the working electrode or anode immersed in an electrolyte shifted from high to low frequency alternating current (AC) (from 10 mHz to 10 kHz) (Zhao, Robert C T

Slade, et al. 2009). At high frequencies, when the system follows kinetic dynamics and local concentration gradients of electroactive species, such as ions and molecules, are negligible. Where Nyquist plots show a semicircle, the diameter can be interpreted as the charge transfer resistance ( $R_{ct}$ ). A straight line appears at lower AC frequencies, when the system changes to follow diffusive dynamics due to mass transport of electroactive species entering or leaving the electrode surface (Lin et al. 2016). For the carbon foam based electrodes (Fig. 4.2e)  $R_{ct}$  of CF was 41.4 k $\Omega$ , which decreased with the addition of graphene in CF-Gr-PD to 0.930 k $\Omega$ , showing that coating with graphene flakes increased the conductivity of the carbon foam material. EIS measurements of the aerogels (Fig. 4.2f) gave  $R_{ct}$  for A-CMC and A-CMC-PD as ~101 k $\Omega$  and ~176 k $\Omega$  respectively, showing that although they possess a conductive backbone, PEDOT did not increase electrochemical conductivity, with the single semicircle suggesting kinetic control of the electrochemical reaction, limited by the electrical resistance of the CMC and PEDOT. With graphene flakes included in A-CMC-Gr and A-CMC-Gr-PD,  $R_{ct}$  dropped to 46.2  $\Omega$  and 21.0  $\Omega$  respectively. The graphene flakes were presumably responsible for the decrease in  $R_{ct}$ , although it is possible that the PEDOT acted synergistically to reduce  $R_{ct}$  below A-CMC-Gr by providing conductive bridges between graphene flakes.

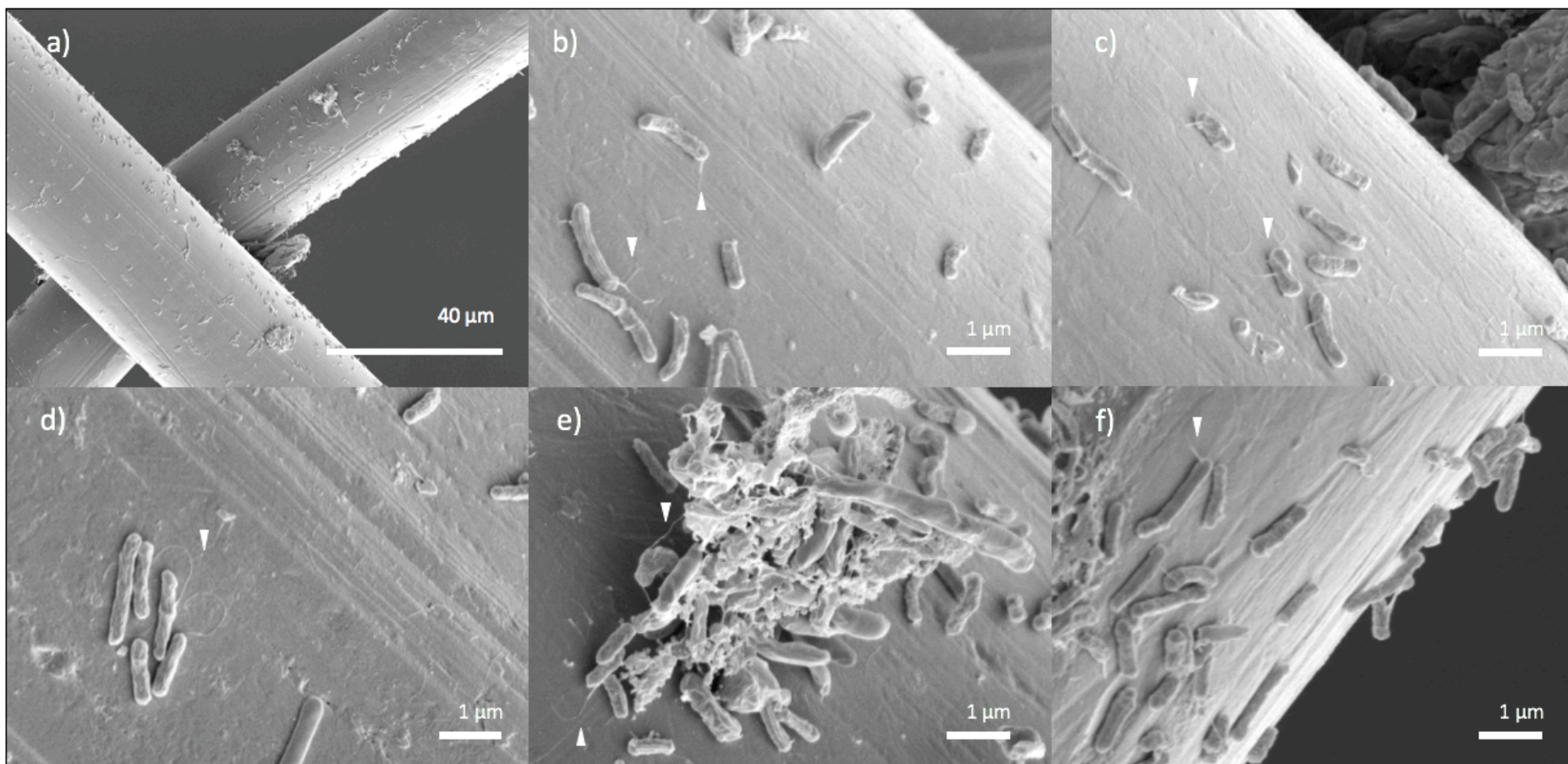


**Fig. 7.5:** SEM images of marine grade stainless steel mesh after use in the MFC with *R. palustris* cells attached. a) SEM image showing the low cell retention by the stainless steel mesh, and b-f) higher magnification SEM images showing cells attached with nanowires connecting cells to the stainless steel surface (white arrows).

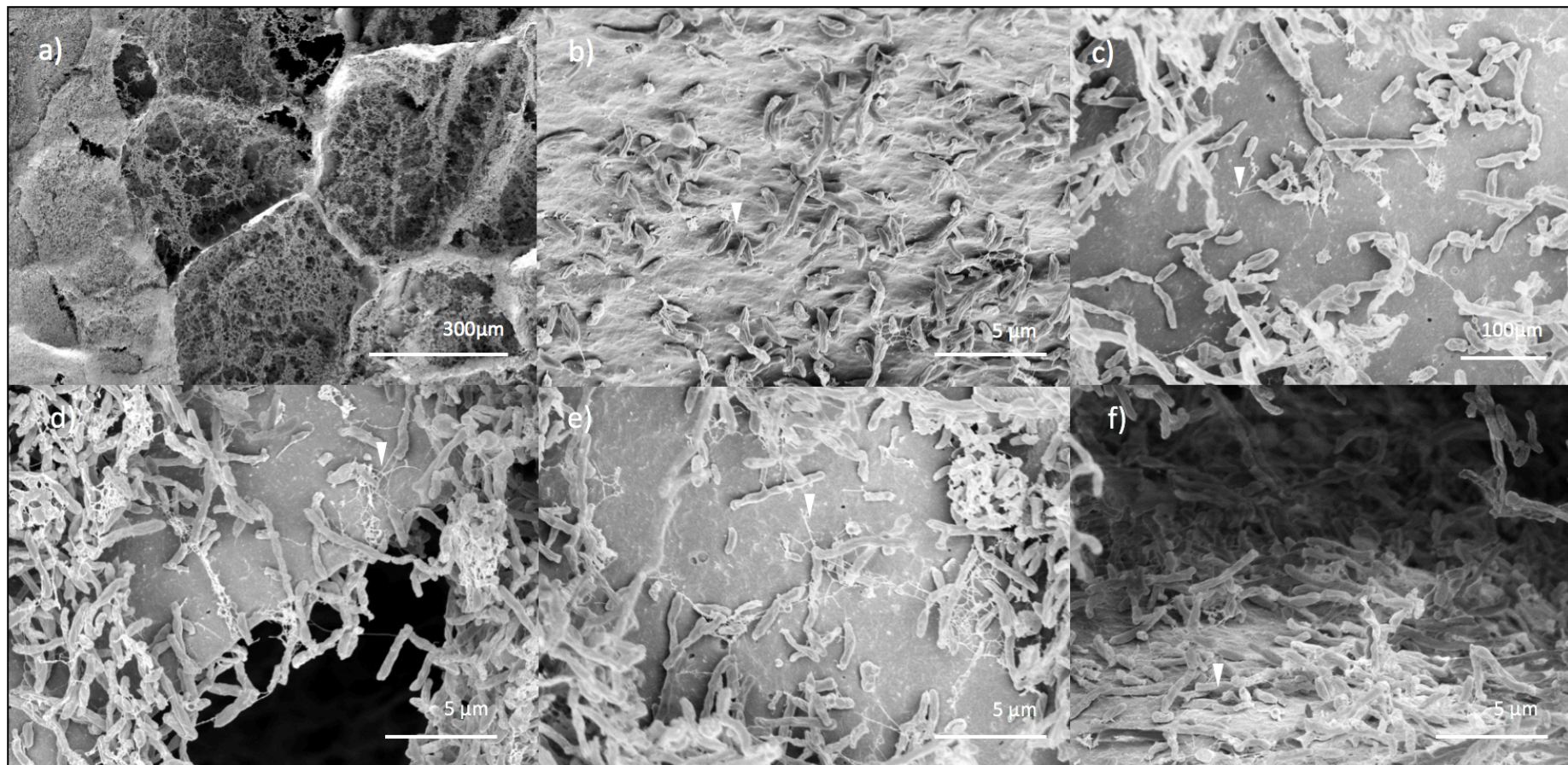


**Fig. 7.6:** SEM images of (a-c) carbon foam and (d-f) carbon foam with graphene coating after use in the MFC with *R. palustris* cells attached. a) SEM image showing high cell retention by the carbon foam, and b-f) higher magnification SEM images showing cells attached with nanowires connecting cells to the carbon foam (white arrows).

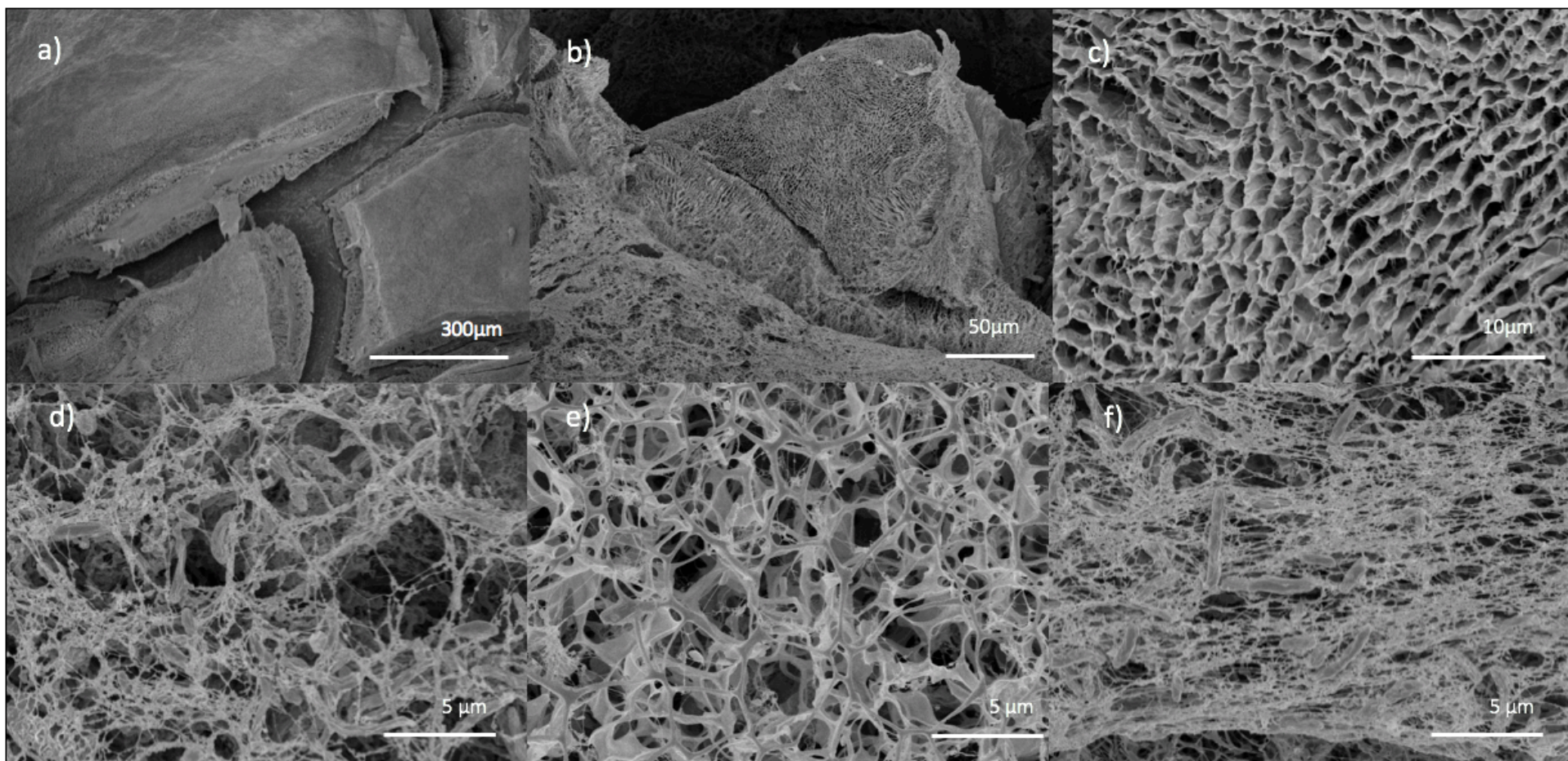


**Fig. 7.7:** SEM images of the A-CMC aerogel after use in the MFC at a) low magnification, b, c) medium magnification showing porous internal structure, and d-f) high magnification showing individual *R. palustris* cells embedded in the rehydrated aerogel matrix.

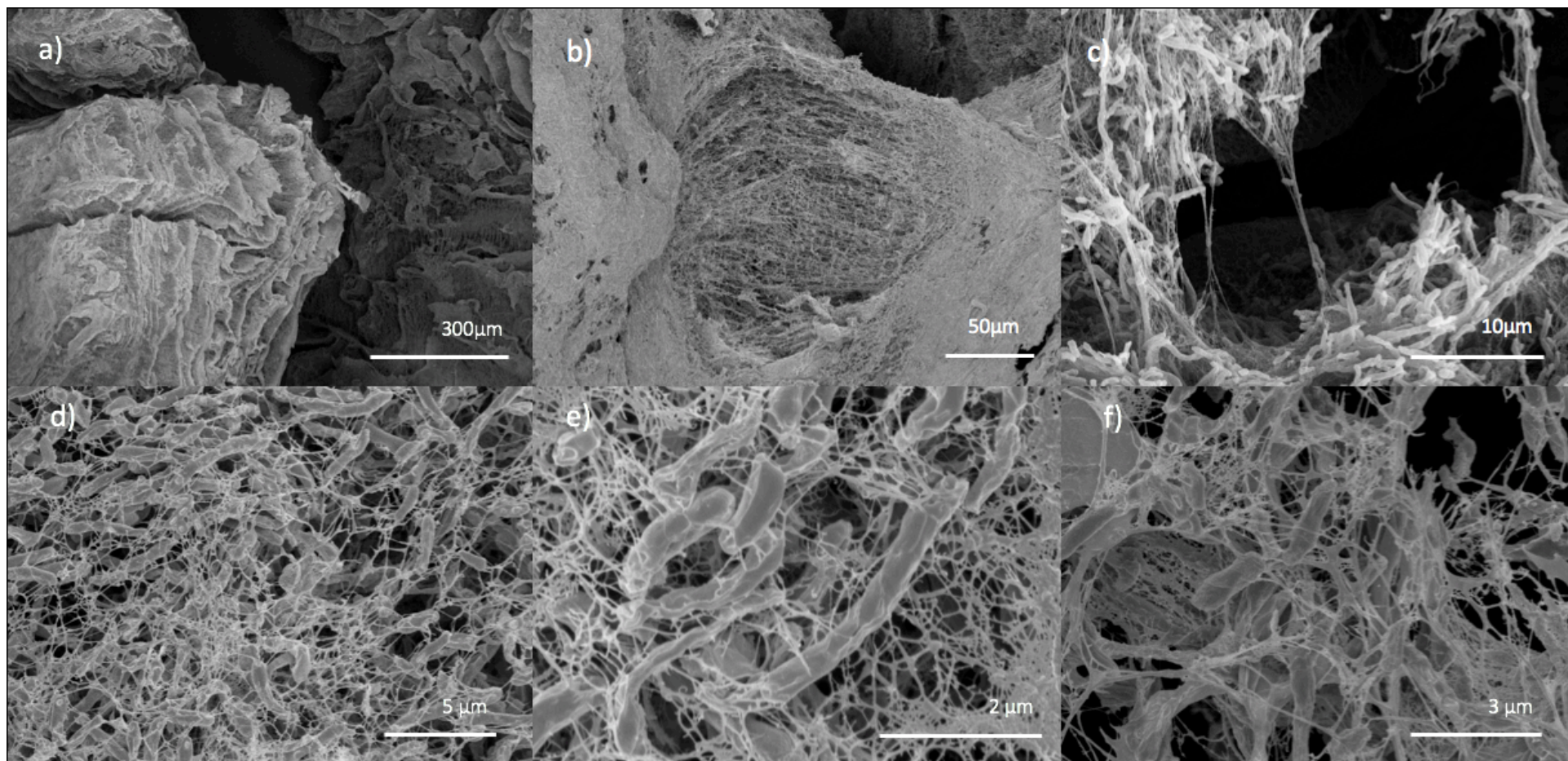


**Fig. 7.8:** SEM images of the A-CMC-PD (10%) aerogel after use in the MFC at a) low magnification, b, c) medium magnification showing porous internal structure, and d-f) high magnification showing individual *R. palustris* cells embedded in the rehydrated aerogel matrix.

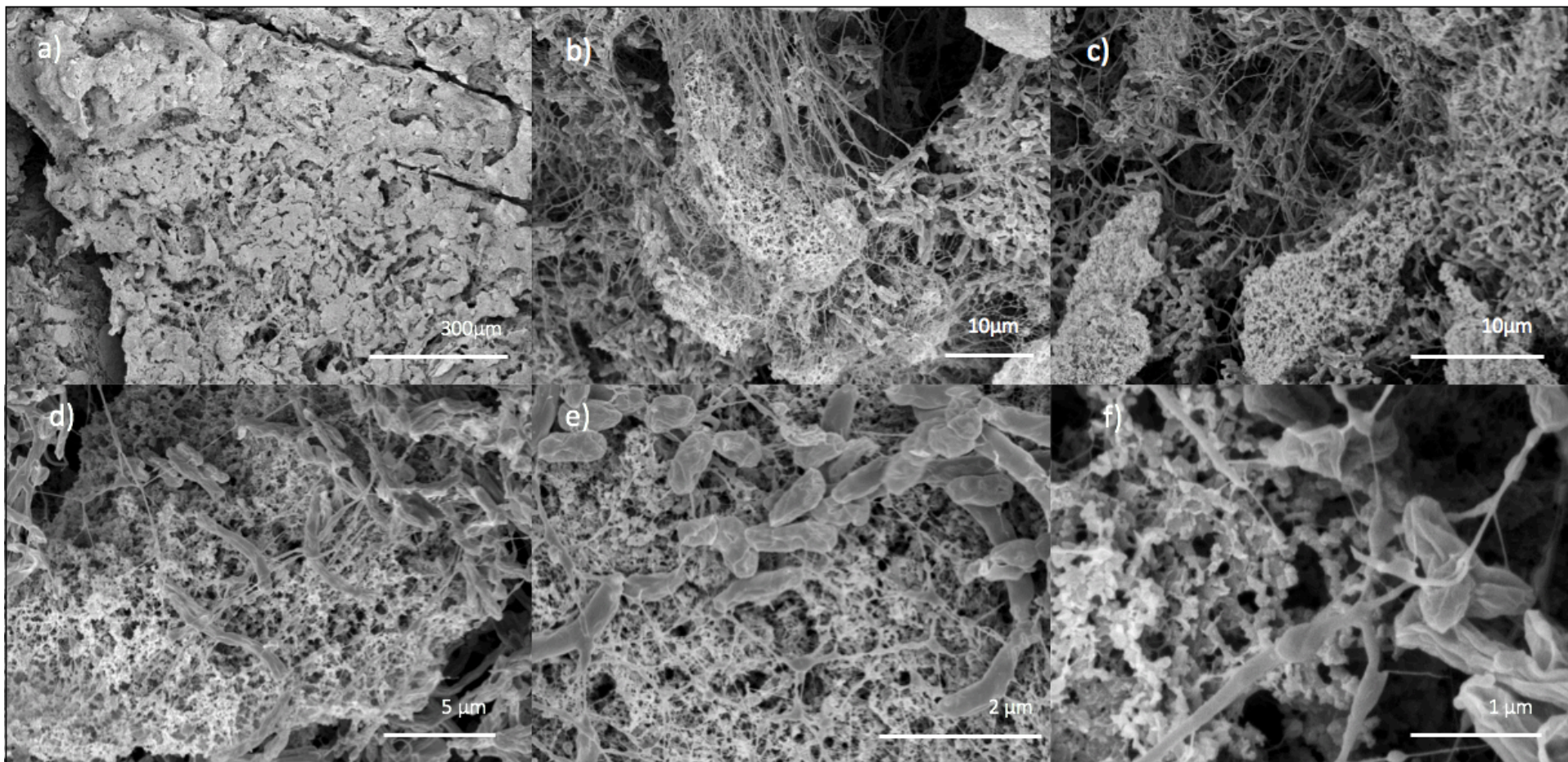


**Fig. 7.9:** SEM images of the A-CMC-Gr aerogel after use in the MFC at a) low magnification, b, c) medium magnification showing internal structure with regions of graphene flakes, and d-f) high magnification showing individual *R. palustris* cells embedded in the rehydrated aerogel in contact with graphene flakes.

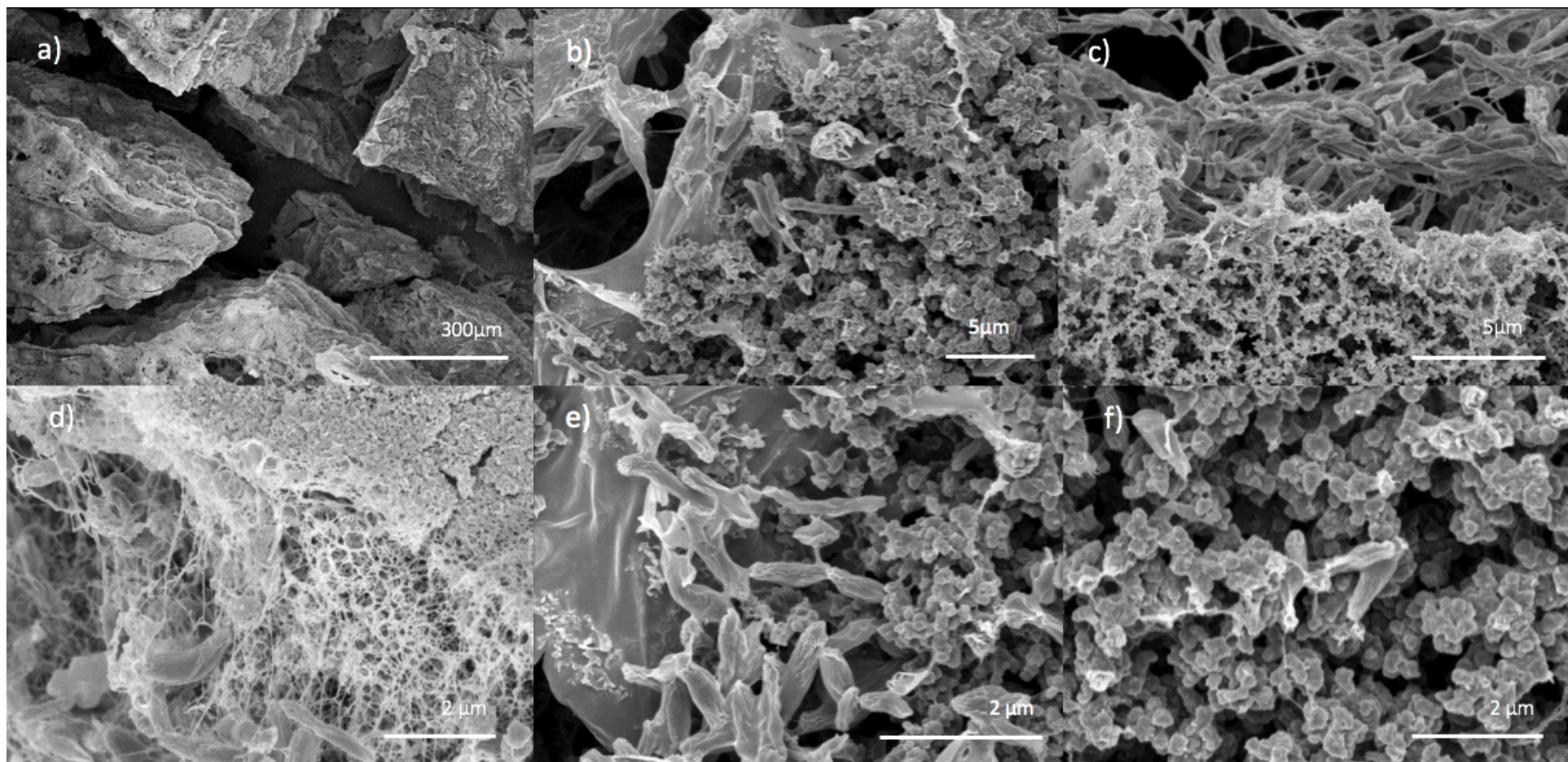


**Fig. 7.10:** SEM images of the A-CMC-Gr-PD aerogel after use in the MFC at a) low magnification, and b-f) high magnification showing internal structure with regions of graphene flakes and individual *R. palustris* cells embedded in the rehydrated aerogel in contact with graphene flakes.

### **7.2.5. Loading of MFC devices:**

The electrochemical performance of MFC devices containing the different anode materials was then determined. After loading with 4 ml of  $OD_{660} = 3.0$  culture of *R. palustris* the MFC devices were sealed with assay plate tape to provide anaerobic conditions, and cells were left to colonize the anode material. Due to their rigid structure, MFC devices containing the carbon foam based anode materials were left for 72 hours in order for the culture to percolate fully into the material and form a biofilm on the surface. The open circuit potential (OCP) was monitored over this period, and found to have stabilized by 72 hours, so that the devices were ready for bioelectrochemical characterization. The aerogel anode extensions required less time to stabilize OCP because of the nature of the aerogel material upon rehydration. Upon rehydration with cell culture the media was rapidly absorbed into the aerogel structure, which visibly contracted and partially deformed. This presumably had the consequence of embedding cells in the conductive matrix of the aerogel, analogous to 'shrink-wrapping' them. MFC devices operated with aerogels required only 12 hours to reach stable OCP and be ready for measurement, an indication of the high degree of cell to anode material contact.

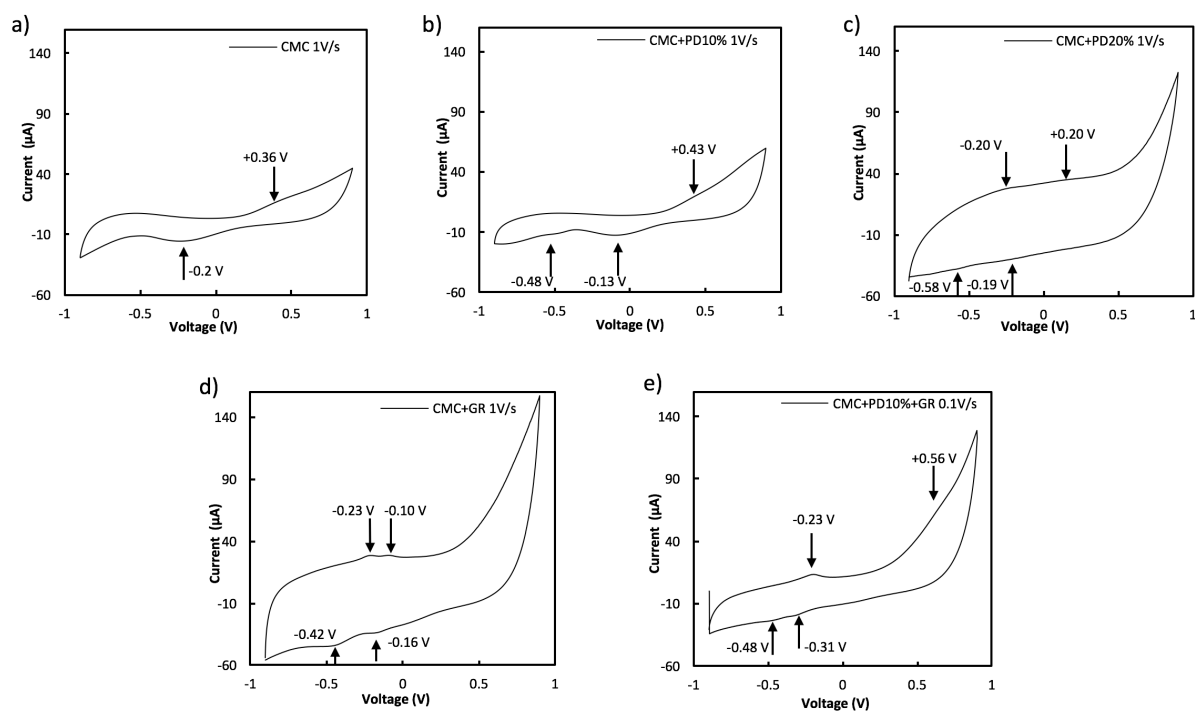


**Fig. 7.11:** Cyclic voltammograms for each aerogel showing the change in current as the anode bias potential is swept from -900 mV to 900 mV from MFC devices containing a) A-CMC, b) A-CMC-PD (10%), c) A-CMC-PD (20%), d) A-CMC-Gr, f) A-CMC-Gr-PD (10%).

### 7.2.6. Cyclic voltammetry of operational microbial fuel cells:

Cyclic voltammetry (CV) was used to characterize the redox properties of the aerogel anodes, revealing peaks in current at anode potentials where charge transfer is facilitated between cells and the anode. CVs of each of the aerogel anodes were taken from MFC devices with *R. palustris* between -900 mV and 900 mV 72 hours after loading the devices with cells, after other bioelectrochemical measurements had been taken (Fig. 4.11). For A-CMC a broad oxidation-reduction pair of peaks was apparent at around 360 mV and -200 mV, probably resulting from interaction of the aerogel with the stainless steel anode connector (Xie et al. 2015), but demonstrating establishment of a conductive biofilm (Muthukumaran et al. 2016). Inclusion of 10% PEDOT with CMC did not yield many changes apart from a small reduction peak appearing at -480 mV from A-CMC-PD. At 20% However, at 20% a substantial increase

in the current magnitude was observed, with tentative oxidation-reduction peak pairs visible at -580 mV and -200 mV, and -190 mV and 200 mV. Including graphene flakes in A-CMC-Gr yielded two oxidation-reduction peak pairs at -230 mV and -420 mV, and -100 mV and -160 mV, corresponding to similar CV peak pairs from *R. palustris* on a carbon paper substrate (Xing et al. 2008). These peak pairs show that graphene catalyses electron transfer using at least two extracellular electron transfer mechanisms from *R. palustris*, with proximity of the oxidation and reduction peak pairs suggesting an easily reversible reaction with facilitated charge transfer (Peng et al. 2010). The combination of graphene and PEDOT in A-CMC-Gr-PD led to the disappearance of the oxidative peak at -100 mV from A-CMC-Gr, although the -230 mV peak became more prominent, and a oxidative peak at 560 mV emerged.

Previous reports highlight the graphene's effectiveness at supporting EET from biofilms attached to the surface (Liu et al. 2012; Yong et al. 2014). These results show CV profiles similar to other, better characterized, organisms such as *Shewanella oneidensis* which possesses metal reducing outer membrane OmcA cytochromes and the Mtr pathway (Peng et al. 2010), although *R. palustris* does not possess obvious homologs to OmcA, with the closest candidates having low structural and genetic similarity (Venkidusamy et al. 2015). *R. palustris* does have a number of other extracellular electron transfer pathways, such as the phototrophic iron oxidation (Pio) pathway that can oxidise extracellular iron and import electrons.

#### **7.2.7. Effect of graphene on cell to anode material adherence:**

One possible way graphene might affect MFC power output is by increasing the strength of adherence of cells to the anodic substrate. In collaboration with Shiyao Wang in the Department of Chemical Engineering, the adherence of *R. palustris* to carbon paper and carbon paper coated with graphene was measured. A novel sterile chamber fluid dynamic gauging

system was developed by Shiyao Wang that could precisely measure the forces required to dislodge cells from the surface. Although it was not possible to complete the measurements, it was noted in initial experiments that *R. palustris* biofilms appeared to adhere more weakly to carbon paper with a graphene coating. This might be consistent with the fact that graphene is used as an industrial lubricant; the upper layers of the coating may be easily dislodged, taking any cells with them. Another possibility is that the graphene coating may have filled in or blocked micropores in the carbon paper. Qualitative observations from SEM imaging did not reveal any obvious differences in cell to surface adhesion on carbon foam (Fig. 4.6a-c) and carbon foam coated with graphene (Fig. 4.6 d-f). However, in SEM images of the graphene containing aerogels after use in the MFC, there appeared to be a much lower frequency of cells attached to the dense graphene agglomerate regions than to the surrounding CMC or CMC/PEDOT:PSS polymers (Figs. 4.9d and 4.10f). We performed a simple experiment to compare the dry mass change from carbon foam ( $5 \pm 1.6$  mg) with and without a graphene coating ( $6 \pm 2.0$  mg) after 4 days incubation with *R. palustris*, however we saw no significant difference between the dry mass changes ( $p = 0.406$ , unpaired T-test).

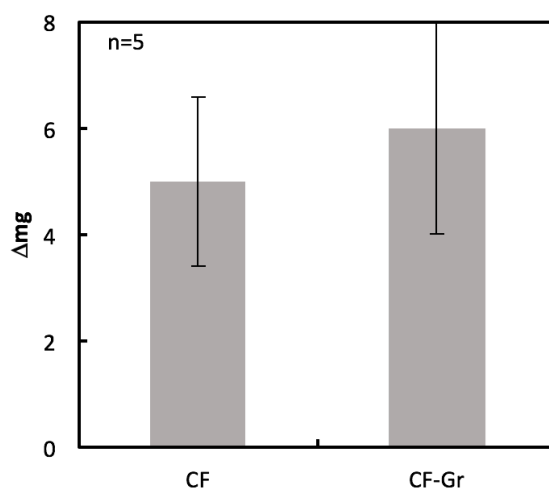


**Fig. 7.12:** Dry weight changes of biomass between carbon foam (CF) and carbon foam coated with graphene (CF-Gr) anodes after 4 days in the MFC, error bars show the standard deviation, and  $n=6$ .

### 7.2.8. Power output enhancement by anode extension materials:

In order to compare the power output from the enhanced carbon foam and aerogels, linear sweep voltammetry (LSV) was used to record the current produced between the open circuit potential and 0V. From this region polarization and power curves could be derived, allowing calculation of the overall resistance ( $R_{sur}$ ) from the slope of the polarization curve, maximum current density ( $I_D$ ), normalized to the cathode surface area, and maximum volumetric power output ( $P_V$ ), normalized to the anode material volume.  $R_{sur}$  is distinct from  $R_{ct}$  because it is calculated from the slope of the current-potential polarization, which is a measure of the surface resistance including cell to anode interactions, rather than direct electrochemical charge transfer properties as determined by EIS. OCP,  $R_{sur}$ ,  $I_D$ , and  $P_V$  from MFC devices operated with *R. palustris* on the aerogel anode extensions are summarized in Fig. 4.13.

The OCP from CF-Gr-PD after 72 hours was  $669 \pm 6.92$  mV, higher than  $480 \pm 30.9$  mV from CF and  $392 \pm 21.4$  mV with only SS at the anode. CF and CF-Gr-PD yielded similar values for  $R_{sur}$  -  $30.8 \pm 5.30 \Omega \text{ m}^{-2}$  and  $23.7 \pm 3.48 \Omega \text{ m}^{-2}$  respectively, lower than  $R_{sur}$   $86.4 \pm 25.5 \Omega \text{ m}^{-2}$  for SS.  $I_D$  and  $P_V$  for SS were the lowest at  $4.47 \pm 1.06 \text{ mA m}^{-2}$  and  $43.6 \pm 10.1 \text{ mW m}^{-3}$  respectively. Using CF as an anode extension yielded a 3-fold increase compared to SS in  $I_D$  and  $P_V$  of  $15.9 \pm 2.80 \text{ mA m}^{-2}$  and  $138 \pm 28.2 \text{ mW m}^{-3}$  respectively. A graphene coating on CF-Gr-PD increased  $I_D$  and  $P_V$  a further 2-fold to  $25.7 \pm 1.113 \text{ mA m}^{-2}$  and  $265 \pm 12.1 \text{ mW m}^{-3}$ . Since the CF and CF-Gr-PD have similar surface area, these results indicate that the conductive graphene coating was responsible for improving the MFC performance, resulting in higher  $P_V$  and  $I_D$ , and lower  $R_{sur}$ .

12 hours after inoculation with *R. palustris*, the stable OCP of A-CMC, A-CMC-PD (10%), A-CMC-PD (20%), A-CMC-Gr and A-CMC-Gr-PD reached  $522 \pm 47.7$  mV,  $476 \pm 35.0$  mV,  $535$

$\pm 57.5$  mV,  $391 \pm 38.9$  mV, and  $456 \pm 38.0$  mV respectively. Given that CMC is an electrically insulating polymer, as expected  $R_{sur}$  at  $146 \pm 17.3 \Omega \text{ m}^{-2}$  was not surprisingly the highest amongst aerogel anodes. The increase in  $I_D$  and  $P_V$  over SS and CF, yielding  $4.04 \pm 0.618 \text{ mA m}^{-2}$  and  $0.648 \pm 0.178 \text{ W m}^{-3}$  may mean that A-CMC promoted the formation of a conductive biofilm in contact with the SS anode connector. Inclusion of 10% PEDOT:PSS in A-CMC-PD lowered  $R_{sur}$  to  $63.5 \pm 5.09 \Omega \text{ m}^{-2}$ , while  $I_D$  and  $P_V$  marginally increased over A-CMC to  $7.91 \pm 0.923 \text{ mA m}^{-2}$  and  $1.01 \pm 0.178 \text{ W m}^{-3}$ . At 20% PEDOT the anode resistance dramatically decreased to  $3.71 \pm 1.24 \Omega \text{ m}^{-2}$ , and increased  $I_D$  to  $44.2 \pm 2.78 \text{ mA m}^{-2}$  and  $P_V$  to  $7.12 \pm 0.893 \text{ W m}^{-3}$ . With the inclusion of graphene in A-CMC-Gr,  $R_{sur}$  was  $26.3 \pm 3.24 \Omega \text{ m}^{-2}$  and  $I_D$  and  $P_V$  were  $17.9 \pm 3.09 \text{ mA m}^{-2}$  and  $2.59 \pm 0.514 \text{ W m}^{-3}$ , a 4-fold increase over A-CMC and A-CMC-PD. The combination of graphene and 10% PEDOT:PSS in in A-CMC-Gr-PD improved  $R_{sur}$  over A-CMC-Gr and A-CMC-PD (10%) to  $16.7 \pm 2.86 \Omega \text{ m}^{-2}$ , and  $I_D$  and  $P_V$  reached  $34.61 \pm 5.84 \text{ mA m}^{-2}$  and  $3.51 \pm 0.504 \text{ W m}^{-3}$ , a 13-fold increase in power output over A-CMC and A-CMC-PD, but still only half that of A-CMC-PD (20%).

**Table 7.2:** Summary of electrochemical and surface area measurements from electrode materials tested here:

Material	OCP (mV)	$R_{sur}(\Omega m^{-2})$	$R_{ct}(k\Omega)$	$I_d(Am^{-2})$	$P_v(Wm^{-3})$	$S_a(m^2 g^{-1})$
SS	$392 \pm 21.4$	$86.4 \pm 25.5$	-	$0.00447 \pm 0.00106$	$0.0436 \pm 0.0101$	-
CF	$480 \pm 30.9$	$30.8 \pm 5.30$	41.4	$0.0159 \pm 0.00280$	$0.138 \pm 0.0282$	3.7
CF-Gr-PD	$669 \pm 6.92$	$23.7 \pm 3.48$	0.930	$0.0257 \pm 0.00111$	$0.265 \pm 0.0121$	2.0
CFi (0.13 cm <sup>3</sup> )	$605 \pm 70.9$	$15.3 \pm 1.21$	-	$0.0397 \pm 0.00486$	$5.37 \pm 1.16$	0.14
CFi (4 cm <sup>3</sup> )	$565 \pm 8.39$	$0.895 \pm 0.036$	-	$0.672 \pm 0.152$	$5.01 \pm 0.302$	0.14
A-CMC	$522 \pm 47.7$	$146 \pm 17.0$	101	$4.04 \pm 0.618$	$0.648 \pm 0.178$	7.1
A-CMC-PD (10%)	$476 \pm 35.0$	$63.5 \pm 5.09$	176	$7.91 \pm 0.923$	$1.01 \pm 0.178$	3.9
A-CMC-PD (20%)	$535 \pm 57.5$	$3.71 \pm 1.24$	-	$44.2 \pm 2.78$	$7.12 \pm 0.893$	-
A-CMC-Gr	$391 \pm 38.9$	$26.3 \pm 3.24$	0.0462	$17.9 \pm 3.09$	$2.59 \pm 0.514$	20.2
A-CMC-Gr-PD (10%)	$456 \pm 38.0$	$16.7 \pm 2.86$	0.021	$34.61 \pm 5.84$	$3.51 \pm 0.504$	8.2

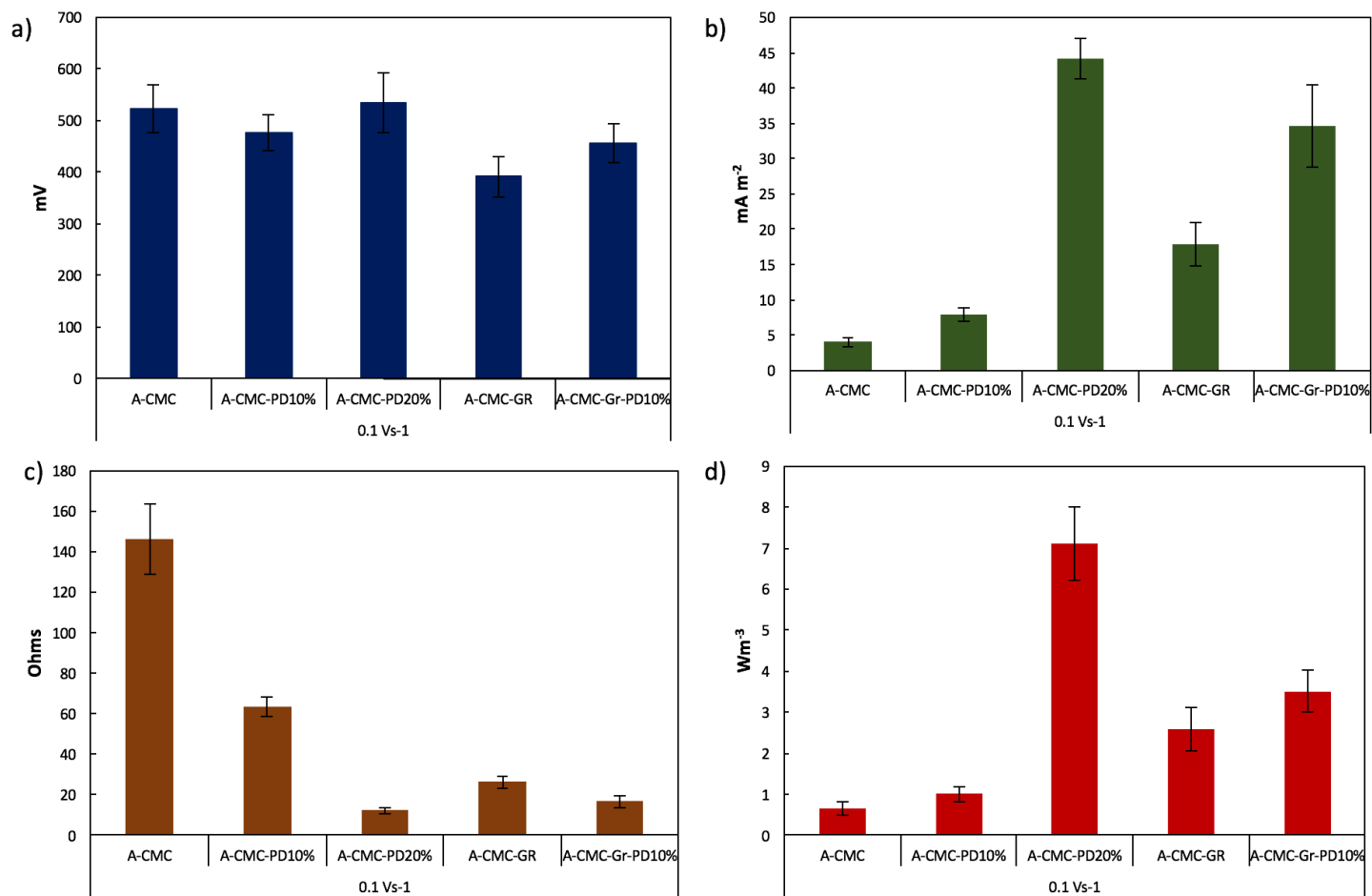


**Fig. 7.13:** Analysis of linear sweep voltammetry from MFC devices with with *R. palustris* and the aerogels A-CMC, A-CMC-PD (10%), A-CMC-PD (20%), and A-CMC-Gr-PD (10%). a) Open circuit potential, b) current density, c) resistance, and d) volumetric power output. Averages are from at least 8 biological replicates, and all sweeps were performed at 1 mV per second.

**7.2.9. An MFC powered digital clock:** As proof of principle that the MFCs could be used to power a small electrical device, 10 MFCs using the best performing graphene based anodes in terms of power output (A-CMC-Gr-PD) and Nafion® carbon-Pt cathodes were connected with two series of five MFCs in parallel (Fig. 4.14a). This configuration provided sufficient voltage to operate the digital clock. LSV and chronovoltammetry measurements and data analysis were carried out jointly with Paolo Bombelli. Fig. 4.14b shows the results of chronovoltammetry measurement of the effect on circuit voltage when the clock was connected. The results showed a steady potential drop from 1.38 to 1.10 V, recovering after the clock was disconnected. This voltage drop may have been caused by an internal short circuit due to faster oxidation-reduction kinetics at the anode than the cathode (Kim et al. 2012; Estrada-Arriaga et al. 2017). Polarization and power curves (Fig. 4.14 c and d) from data before and after the clock was connected indicate  $I_D$  and  $P_V$  decreasing from 8.3 to 6.5  $\mu\text{A}$  and from 4.19 to 2.76  $\mu\text{W}$ , respectively.

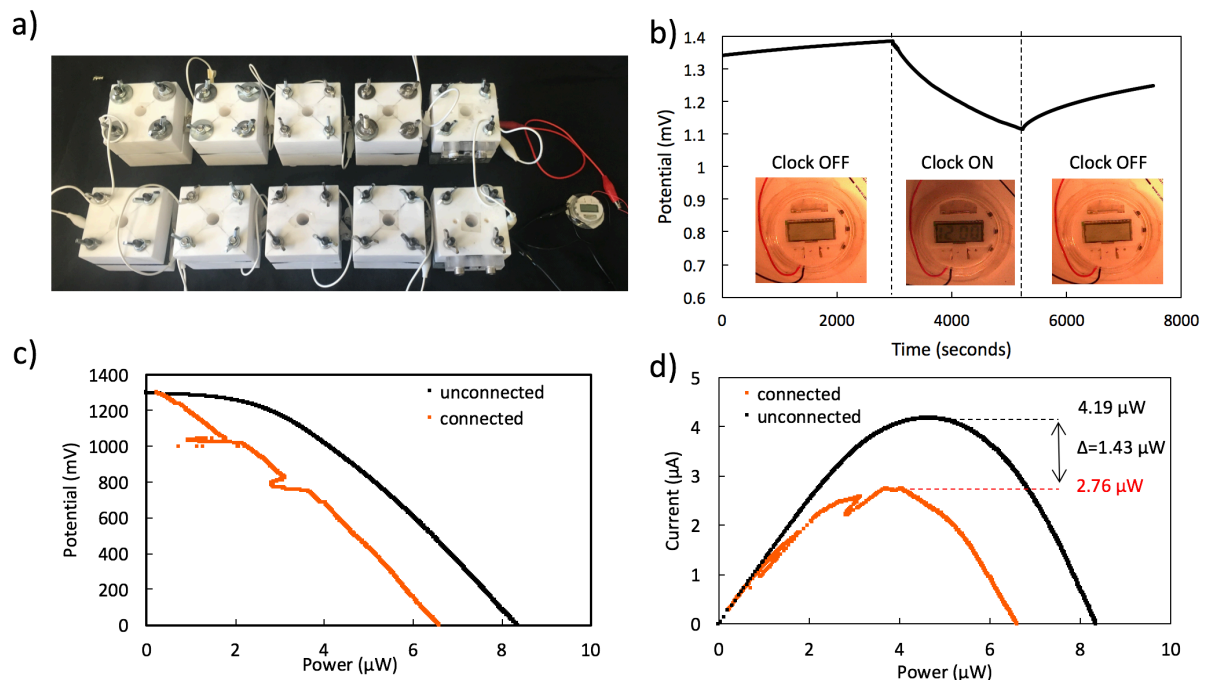


**Fig. 7.14:** a) Photograph of the 10 MFC devices containing *R. palustris* connected to the digital clock, b) chronovoltammetry showing a potential drop when the digital clock was connected

to the MFCs. c) Polarization and d) power curves of the circuit with the digital clock connected and disconnected.

### 7.2.10. Volumetric power scaling in millilitre scale MFCs

Defining a conductive material for MFC anodes may not necessarily mean it's efficiency will scale up to larger volume devices. Limitations in mass transport or cell distribution over the anode material might cause the volumetric power output to decline as volume increases. To test this we measured a smaller volume of carbon fibre (CFi), the same volume as the aerogels, i.e. just 1 mm 'deep' in the anodic chamber. Volumetric power of low volume CFi was  $5.37 \pm 1.16 \text{ W m}^{-2}$ , similar to CFi taking up the whole anodic chamber (4 ml) at  $3.01 \pm 0.302 \text{ W m}^{-2}$  (see Fig. 4.15). This suggests that at smaller scales as used in our MFC block devices, calculations of volumetric power output are not affected by anode volume. Further work to test a greater range of materials and how power output scales with volume would be useful, especially if investigating the feasibility of large scale MFCs using carbon based electrodes.

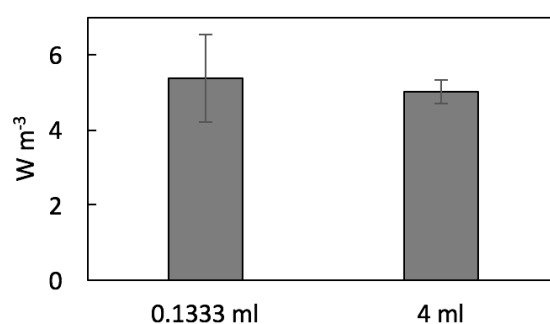


**Fig. 7.15:** Power output from low and medium volume carbon fibre anodes in the same MFC devices with *R. palustris*. Error bars show the standard error and  $n=3$ .

### 7.2.11. Graphene as an MFC cathodic catalyst:

The ability of PD and pristine graphene to function as a cathode was tested. Plain SS with deposited PD and pristine graphene flakes (SS-Gr-PD) was compared to industry standard platinum particle coated carbon paper cathode catalyst in MFC devices containing *R. palustris* (Mustakeem 2015). Carbon fibre was used in the anodic chamber. LSV was used to measure and compare the current density and volumetric power output of devices using each cathode.  $I_D$  and  $P_V$  from SS-Gr-PD increased 500-fold over plain SS, yielding  $0.172 \pm 0.0378 \text{ A m}^{-2}$  ( $I_D$  of SS =  $0.000373 \pm 0.000103 \text{ A m}^{-2}$ ) and  $1.04 \pm 0.252 \text{ W m}^{-3}$  ( $P_V$  of SS =  $0.00228 \pm 0.000552 \text{ W m}^{-3}$ ) (Fig. 4.15a, b). With the conductive carbon paper coated with platinum particles, the values were  $I_D = 0.672 \pm 0.152 \text{ A m}^{-2}$  and  $P_V = 5.01 \pm 0.302 \text{ W m}^{-3}$ . Thus the values with PD and graphene as a cathode were only a few fold lower than those with a carbon paper/platinum cathode.

### 7.2.12. Graphene – graphene catalysed MFC:

Given the possibility of using graphene/PED/OT:PSS to substitute for platinum-coated carbon paper at the cathode, the performance of an all graphene/PEDOT:PSS MFC was tested. An A-CMC-Gr-PD aerogel anode was combined with a SS-Gr-PD cathode, yielding  $I_D$  of  $0.0753 \pm 0.739 \text{ A m}^{-2}$  and  $P_V$  of  $0.390 \text{ W m}^{-3}$  (Fig. 4.15c, d).

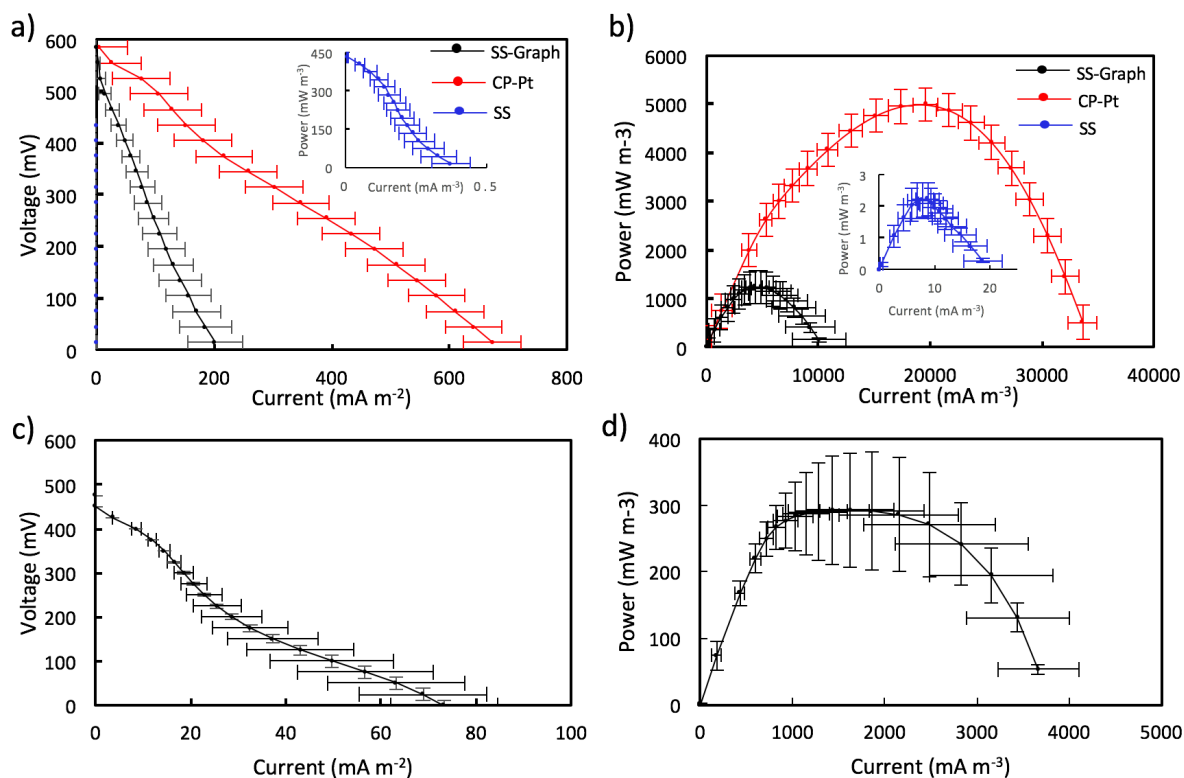


**Fig. 7.16:** a) Polarization and b) power curves from MFC devices containing *R. palustris* with different cathodic catalyst materials stainless steel (SS, blue lines, inset), stainless steel with graphene deposits (SS-Gr, black lines), and carbon paper with platinum catalyst (CP-Pt, red lines). c) Polarization

### 7.3. Discussion:

#### 7.3.1. Effect of graphene flakes inclusion in MFC aerogel anodes on power output:

This project aimed to test graphene's potential as an MFC electrode material. We demonstrated that a surface coating of graphene decreased the charge transfer and surface resistance of carbon foam, leading to a doubling of power output from  $138 \pm 28.2 \text{ mW m}^{-3}$  to  $265 \pm 12.1 \text{ mW m}^{-3}$ , and that high surface area graphene and PEDOT:PSS enhanced aerogels further increase volumetric power output by an order of magnitude. It is likely that the power boosting effect of the graphene coating is due not only to the increased conductivity decreasing the

overall circuit resistance, but also to the facilitation of electron transfer from cells to electrode. While *R. palustris* is intrinsically capable of extracellular electron transfer to reducing carbon foam and other electrode materials, catalytic side groups and impurities present even on pristine graphene flakes may help catalyse more efficient electron transfer (Ambrosi et al. 2014). The magnitude of the changes in overall surface resistance vs charge transfer resistance support this with the  $R_{sur}$  of carbon foam decreasing by a factor of 1.3 with a graphene coating, and 5.6 with the addition of graphene flakes to the CMC aerogel scaffold, compared to  $R_{ct}$  decreasing by a factor of 45 and 2,200 respectively. This difference is also likely due to conductivity barriers between the graphene flakes and the supporting scaffold, be it carbon foam or CMC, and the stainless steel mesh anode connector. The facilitated cell to graphene charge transfer is also indicated by the CV plots of A-CMC and A-CMC-Gr, where the CV plot of A-CMC represents most likely the charge transfer to the steel mesh as CMC is non-conductive. Not only does current flow increase for a given potential of the working electrode, but two distinct peak pairs emerge in the CV plot of A-CMC-Gr, evidence of the redox mechanisms for EET from *R. palustris* to graphene.

### **7.3.2. Effect of PEDOT:PSS inclusion in MFC aerogel anodes on power output:**

PEDOT was an interesting addition to the aerogel composition, when formulating the inks Tian Carey found at least 1% PEDOT:PSS was necessary to disperse the graphene flakes made from liquid phase exfoliation of graphite in the Gr-PD ink for coating the carbon foam. At low concentrations it is unlikely PEDOT:PSS had much of an effect on the electrochemical properties of the coating. Although the aim of this study was to explore uses of graphene in MFC electrodes, the highest volumetric power output came from the CMC-PEDOT:PSS 20% aerogel. An additional 10% PEDOT:PSS increased  $P_V$  from  $1.01 \pm 0.178$  to  $7.12 \pm 0.893$  W m<sup>-3</sup>. Because cells in an MFC are necessarily have negatively charged surfaces, it is likely that

positively charged PEDOT:PSS is able to link cells to a conductive network. This effect is may counteract the electrostatic repulsion from negatively charged graphene flakes. It would be interesting to further investigate cellular interactions with PEDOT:PSS at higher concentrations, however aerogels with higher concentrations of PEDOT:PSS were apparently impractical to assemble.

### **7.3.3. Effect of anode surface area on power output:**

The available surface area of the anode was also a key factor for increasing power output. Stainless steel mesh is a reliable anode material however it's smooth, convex surface and single plane of surface mean cell to surface area contact is limited. The low number of cells remaining attached to the surface in SEM images also suggest low adherence strength. Comparably, the convex pockets of carbon foam are able to retain greater cell densities, and cells appear to adhere more strongly to the rougher surface. The aerogels have a much higher surface area to mass ratio, or specific surface area ( $S_A$ ), which correlated well with  $P_V$  when comparing CF-Gr-PD to A-CMC-Gr. Both  $S_A$  and  $P_V$  increased by a factor of 10 (2.0 to 20.2 m<sup>2</sup> g<sup>-1</sup>, and 0.265 ± 0.0121 to 2.59 ± 0.514 Wm<sup>-3</sup>). Mercury porosimetry of the electrode materials before use in a MFC may be slightly misleading as fragile structure of aerogels may deform under the pressures required to push mercury into the material. However if some of the smallest pores and filamentous structures are deformed and masked the actual specific surface would be much higher, potentially on the order of 50-100 m<sup>2</sup> g<sup>-1</sup>. SEM images suggest the degree of this masking may not be too significant, with average pore sizes around an order of magnitude lower (c. 20-50 μm) in the aerogels compared to the carbon foams (c. 200-500μm). The higher  $S_A$  from A-CMC-Gr compared to the other aerogels may be explained by the SEM images (Fig. 4.4g, h) showing graphene flakes forming structures over the surface of the CMC, with the gaps between stacks of flakes joined end to end likely the source of the the spike in pore size

frequency around 0.1  $\mu\text{m}$  in A-CMC-Gr. Adding PEDOT reduces  $S_A$  by effectively binding the graphene flakes onto the CMC surface as visible in (Fig. 4.4i, j). During MFC loading and operation, graphene flakes detached from the A-CMC-Gr, entering suspension and turning the cell culture black, and the aerogel broke apart during removal from the MFC. With A-CMC-Gr-PD, the cell culture remained *R. palustris* red, and maintained mechanical integrity during removal from the MFC after operation.

While the overall picture remains true when comparing  $S_A$  and apparent pore sizes from pre-MFC SEM images, images taken of the aerogels after bioelectrochemical characterization reveal a more complex interplay between cells and the anode. When loading MFC devices containing aerogels with cell culture, aerogels visibly contract and deform as they rehydrate by capillary action. The deformation upon rehydration of what technically become hydrogels may be due to either the partial solubilisation and insufficient rigidity of the CMC backbone. SEM images of aerogels after use in the MFC reveal the material has significantly altered structure as well as the incorporation of cells not just on the surface but within the material. It is possible that the SEM preparation process may have caused some physical changes - further contraction occurred as macroscale cracks split the aerogel sample during flash freezing in liquid ethane. However, the *R. palustris* cells appear generally well preserved and it is difficult to see how the distribution of cells within the aerogel matrix could be an artefact of flash freezing. The 'cracking' open of the sample had the benefit of providing a cross sectional view inside the sample. Estimating the specific surface area available for cell to anode contact is clearly complicated by way cells are visibly enmeshed in the matrix of aerogel material. However, the rate of cell to aerogel contact is without doubt far higher than to carbon foam. Another effect of rehydration and MFC operation for at least 3 days is the separation of constituent materials. It is difficult to see from SEM whether CMC and PD polymers are separated or not in post MFC

SEM images, but graphene flakes in A-CMC-Gr and A-CMC-Gr-PD have visibly agglomerated into plaques, connected by a network of filaments of CMC, PEDOT:PSS, or CMC-PEDOT:PSS.

#### **7.3.4. Effect of anode material on biofilm formation:**

*R. palustris*, like many electrogenic bacteria, expresses conductive type IV pili, or nanowires, which it uses for extracellular electron transfer to and from its environment (Venkidusamy et al. 2015). These allow it to form conductive biofilms capable of transporting electrons far beyond the confines of the outer cell wall. Nanowire like filaments are clearly visible in the SEM images of stainless steel (Fig. 4.5) and carbon foam anodes (Fig. 4.6) and appear distinct from other non-cellular matter of biological origin including excreted extracellular matrix, it is highly likely that these are conductive type IV pili, as they appear in places to form a network of nanowires visibly connected to the anode surface. The network of nanowires can be seen connecting cells that are not in direct contact with the surface to other cells, or other nanowires, that are directly attached to the surface. On the surface of the stainless steel wires of the mesh anode some pili structures are visible adhered to the surface, where their parent cell has detached during the washing step. It is less clear if nanowires are being expressed by cells embedded in the aerogels. The filamentous network of CMC and PEDOT:PSS polymers may substitute the need for expressing the cells' own conductive network, or it may act as a guide for the growth of bacterial nanowires. Where cells can be seen in contact with regions of graphene flake agglomeration, however, there appear some structures that could be nanowires bridging the gaps. Attempts to see whether altering the bias potential of the anodic substrate would influence nanowire expression did not yield conclusive results, nanowires were visible in all three samples incubated at 600 mV, 0 V, and -600 mV. Further investigation into factors influencing their expression could be interesting for applied MFC research.

### 7.3.5. Potential applications of graphene/PEDOT:PSS aerogel electrodes:

Applied use of microbial fuel cells has proven challenging principally due to power densities not reaching cost effective levels for energy production or other large scale applications. However we demonstrated that only 10 devices can power a simple digital clock, suggesting applications for small, wearable technology, or remote, off-grid applications such as sensors (Amar et al. 2015). The cumulative volume of each aerogel and layered electrode set up amounts to not much more than an AA size battery, our approach using 10 devices may support the idea that connecting multiple small MFCs may be more promising for applications than scaling up individual devices (Ieropoulos et al. 2008). Although the relative increases in power outputs we achieved firmly support our conclusions about material composition and properties, reported power densities from comparable materials (mostly graphene oxide as opposed to pristine graphene) are much higher. MFC design often comes down to a question of geometry, limited mainly by the requirement for protons to travel from the anodic to cathodic chambers whilst preventing an electrical short circuit. For example the figure of  $750 \pm 40 \text{ W m}^{-3}$  reported by Yang *et al.* (2016) was using a two-chamber nitrogen purged anodic chamber containing the highly electrogenic species *Shewanella oneidensis*, and with a high surface area carbon cloth cathode immersed in 0.1 M potassium ferricyanide as a catholyte (Y. Yang et al. 2016), whereas our devices use a single chamber with a 2D planar air cathode. With proper design and consideration for the optimal electrogenic bacteria species and conditions for anode respiration, more energy intensive applications than a simple digital clock will be achievable. We also demonstrate graphene's potential as a cathode material, permitting 'metal-free' MFCs that circumvent the need for expensive catalytic metals such as platinum. Whilst other carbon materials have been used as cathodes in different set-ups, we were able to use graphene flakes

to coat and functionalize another material, stainless steel, to catalyse the cathodic oxygen reduction reaction (Li et al. 2012; Kannan & Gnana kumar 2016).

#### **7.4. Conclusions**

Graphene based aerogels are gaining a lot of attention as effective MFC electrodes, in collaboration with the Graphene Centre we show that increased conductivity, porosity, surface area, and organic/inorganic electrochemical interface are key factors in improving power output. We also show that a pristine graphene coating can enhance power generation from existing materials and catalyse the cathodic reaction. If the price of graphene continues to drop it will be a very attractive material to use for MFC electrodes. Even if large scale MFC still suffer from difficulties in maintaining efficiency when scaling, we have shown a direct application for graphene based aerogels in small, low power consumption electronics. These results also highlight the potential of conductive polymers, with PEDOT:PSS proving the highest performing aerogel anode at higher concentrations in our setup. MFCs may one day be a key technology in waste water treatment and renewable energy, however many challenges remain to be overcome.

## 8. GENERAL DISCUSSION

### 8.1. Achievement of aims:

The aims of this project were to understand and mitigate bottlenecks in energy transduction through BESs using two model bacteria, working towards a system with a commercially viable level of power output. While it is clear that there is a long way to go before these systems generate enough power for commercial interest, there are other applications where energy production is not the primary goal. This project highlighted a number of bioengineering interventions that may be taken to enhance power output, as well as the importance of BES design and electrode materials.

#### 8.1.1. Light absorption and dissipation by *Synechocystis* affect BPV output:

In chapter 3 we tested the idea of reducing light absorption capacity to increase overall productivity, finding that PBS truncation in *Synechocystis* had a positive effect on charge density. The reasons for this are most likely a combination of increasing the path length of light through the biofilm by reducing shading, and a reduction in photoprotective light dissipation. This means the principle could be applied to other systems using photosynthetic microorganisms to generate power or biomass. At around low to medium light intensity the strain with one PC disc on the PBS produced around double the charge density of the wild type. In a scaled up system genetically engineered organisms are often at a disadvantage or are not permissible in certain open air situations, but reduced light absorption is a trait that could be selected for using directed evolution to retain a competitive advantage. Measuring NPQ in the antenna truncated mutants in chapter 4 proved problematic, and further work will be needed to quantify the effect of NPQ on BPV output, however the results do suggest a difference in NPQ

upregulation in the antenna truncated mutants. Testing other NPQ related mutants such as an OCP<sup>O/R</sup> knockout or state transition inhibited mutants would be invaluable, as light dissipation undoubtedly plays an important role in limiting productivity. The relationship between bias potential and fluorescence seems to suggest that a positive potential decreases photosynthetic efficiency. Further work to elucidate the fluorescence mechanisms being affected by an external potential could yield insights as to how they are regulated.

### **8.1.2. Metabolic electron sink knockouts in *Synechocystis* increase BPV output:**

Reducing equivalents either from photosynthetic light capture or metabolism of carbon substrates are used to drive cell metabolism, competing with the EET pathway. In chapter 5 multiple metabolic electron sinks were knocked out in *Synechocystis* with the aim of diverting electrons to EET. In removing up to seven genes we found that reducing competition for electrons had a positive effect on biophotovoltaic charge density. The effect of knocking out electron sink genes *hoxH*, *norB*, *COX*, *cyd*, and *ARTO* was fairly cumulative, however including deletions of *narB* and *nirA*, did not increase the electrical output further. This may have been because EET mechanisms have reached a limit in capacity for *Synechocystis* or that the growth deficits from nitrate assimilation removal negate any positive effect.  $\Delta narB$  and  $\Delta nirA$  by themselves resulted in similar charge density increases to all of the other knockouts combined. However, nitrate assimilation to ammonia is too important to cell metabolism and greatly affected viability, to the extent that a source of ammonia had to be added externally, possibly confounding results.

### **8.1.3. Storage molecule outputs in *R. palustris* did not increase MFC output:**

In chapter 6 the removal of glycogen and PHB in *R. palustris* was expected to result in a clear increase in power output, as they are significant electron sink and similar interventions have

resulted in increased hydrogen (Yang & Lee 2011). No significant effect was observed, however, which may have been due to the limited test environment in our MFC devices not simulating conditions where the production of glycogen and PHB would limit EET. The MFC anodic chambers were designed to optimize for electrode surface area and conductivity, requiring materials that are inherently opaque. Other conditions more likely to elicit a difference in current output would include ensuring an anoxic environment, and providing light for photosynthetic growth, although this would not be biophotovoltaic as *R. palustris* light reactions drive only cyclic electron transfer. Provision of an external source of ferrous iron ( $\text{Fe}^{2+}$ ) could increase the production of NADH for which PHB synthesis would compete. If an optimal set of storage molecule limiting conditions are found then the mutants could be used in applications with similar conditions, and deletion sites would serve as insertion sites for recombinant product synthesis.

#### **8.1.4. EET to materials – interesting findings, surface area and conductivity important.**

Whilst tweaking the physiology and metabolism of electrogenic bacteria did enhance electrical output to some degree, arguably the biggest barrier to overcome is the electrical connection between the cells and the anode itself. In chapter 7 we characterized a set of custom made aerogel anodes incorporating the conductive polymer PEDOT:PSS and pristine graphene flakes. These were found to increase the maximum power output from MFCs containing *R. palustris* over similar structures of carbon foam by increasing the specific surface area and conductivity. Of all the BES interventions in this project, use of tailored, high surface area aerogels is the most directly applicable, they were cheap and easy to fabricate, and their composition could be controlled and varied to optimize for mechanical or electrical properties. The highest power output from graphene/PEDOT:PSS aerogels was in fact reported in chapter 6, due possibly to differences between batches of cells and more measures taken to ensure an

anaerobic environment. At c.  $15 \text{ W m}^{-3}$  for the best performing replicate this is still far from the highest reported values in the literature to date of around  $750 \text{ W m}^{-3}$  from a nitrogen doped graphene aerogel anode (Y. Yang et al. 2016). The use of cheaper, unmodified, pristine graphene makes our solution widely applicable for drop in electrodes; given further resources the mechanical properties could be enhanced to maintain structural integrity over longer time periods, as well as embedding or binding graphene flakes to the aerogel matrix. PEDOT:PSS proved to be very effective, with the 20% PEDOT:PSS outperforming 10% PEDOT:PSS with graphene, however higher quantities not viable due to high costs, so finding a cheaper alternative would be beneficial.

## **8.2. Technical challenges and shortcomings of lab based ‘DIY’ devices:**

### **8.2.1. Importance of developing modular, standardized, and high throughput BES equipment:**

A vital area of development is the development of a defined BES with standardized components and reproducibly variable parameters. Headway is being made in this direction with a multi-well single chamber BES under development by Clayton Rabideau (personal communication) tested for use in this project. Increasing the throughput and reliability of BES experiments may save a lot of time and help overcome one of the inherent difficulties of BPV and MFC experiments, that of reproducibility. Each experiment in this project had to go through multiple iterations to produce reliable results to compare mutant strains with each other. Despite remarkable durability and ease of use of the Teflon® block design, hand crafted components and constant reassembly between runs inevitably introduced high variability. In addition, a poor understanding of conditions leading to the formation of an electrogenic biofilm is likely to have further obscured differences caused by genetic mutations. Comparison of all

of the electron sink knockout strains in *Synechocystis* was only possible by using several years of developed ‘know-how’ to set up the measuring apparatus and light system in accordance and devise a novel protocol with short enough measurements to avoid ‘fouling’ of the electrodes, thereby permitting a simple washing step in between runs and avoiding the pitfall of manual reassembly each time. Even so the error bars were still large, with the runs being set up over 3.5 days at all hours, inviting enquiry into other, less well understood confounding factors such as the effect of circadian rhythms on EET or biofilm formation.

### **8.2.2. Inclusion of a reference electrode proved problematic:**

It is worth noting that in all the experiments presented as part of this project the BES has used a two electrode set up, with a working (anode) and a counter (cathode) electrode. Electrochemical experiments are ideally performed with a third electrode, the reference electrode, to measure the potential of the cell accurately. Reference electrodes were incorporated in early BPV device designs, however an unusable level of noise was also introduced. This was partly mitigated by having just a platinum wire as a pseudo-reference electrode, but no difference was observed when using just the two electrode set up. A two electrode set up is equally valid as we are measuring in effect the potential of the whole cell, including counter electrode and electrolyte, and the current passing through the anode with a bias potential applied by a potentiostat.

### **8.3. Notable phenomena for future study:**

#### **8.3.1. Understanding mechanisms of EET is key to designing more efficient BESs:**

In this project we did not investigate in depth the mechanisms of EET, only considering the importance of pili for mediating EET from *Synechocystis* in chapter 3 and from *R. palustris* in

chapter 7 after observing a high frequency of nanowire like structures under SEM. The mechanisms of EET in both species are poorly understood, although the involvement of type IV pili is increasingly likely. With a proper understanding of EET pathways, interventions in other parts of the cell could be applied with more precision to minimize losses in cell viability and maximize the efficiency of diverting reducing power to the anode. Characterization of outer membrane cytochromes or metal respiring pathways could also reveal conditions in which EET is preferentially expressed, especially given the unusual environment of the BPV or MFC with high light stresses or substrate concentrations, dense biofilms, and bias potentials. CV was used in here as a secondary experimental technique to chronoamperometry and LSV, further development of CV techniques would provide a powerful tool to characterize the cell to anode interaction. CV plots of *Synechocystis* already reveal a prominent feature, a consistent and large spike at 0.2 V that may be the oxidation potential of a membrane cytochrome essential to EET. The underlying mechanism could be revealed by identification and knockout of outer membrane cytochromes in *Synechocystis*, and loss of the CV spike phenotype.

### **8.3.2. Electrogenic activity of *Synechocystis* biofilms emerges only after initial light exposure:**

After many iterations of monitoring BPV devices with *Synechocystis* an initial ‘primer’ light exposure seemed to pre-condition the biofilm for a consistent EET response to light exposure. This step was standardized in later protocols, but a controlled experiment to investigate the relationship with ‘primer’ light exposure length, intensity, and wavelength to EET was not undertaken. This effect may be linked to the expression of pili as a phototaxis response to light, and should be investigated further if only to ensure standardization of physiological conditions for BPV experiments as well as the device itself. In mediator free systems, understanding the

role of the biofilm and how electrogenic behavior emerges from it is central to understanding EET and bioelectricity production from *Synechocystis*.

### **8.3.3. Initial photocurrent fluctuation:**

A striking and recurring feature of BPV chronoamperometry experiments was the initial rapid variation in current or membrane depolarization. This effect varied greatly between BPV runs and did not appear to be affected by any of the genetic knockouts we used. The fact that stimulation of photosynthesis causes rapid fluctuations in membrane potential alludes to a rebalancing of internal metabolic electron flux that has been the basis for noninvasive measurements of photosynthesis (Lee et al. 2014), but has yet to be linked to current production in a BPV device. Zhang et al. (2017) use the analogy of an action potential to describe the initial variation, with ions diffusing across the outer membrane in response to light driven changes in internal pH and redox state. Refining analysis of the light response could be developed into a methodology for probing internal metabolism of photosynthetic microorganisms, or perhaps produce a species specific pattern.

## **8.4. Technical developments:**

### **8.4.1. Multifaceted BPV analysis by combining PAM fluorescence with a BPV device:**

During the course of the project, various techniques and materials were developed to achieve the aims. The combination of a PAM fluorimeter with a biofilm based BPV to measure simultaneous EET and fluorescence is fairly novel, and could be developed into a more refined tool for characterizing photosynthetic physiology. A more holistic view of light use, electron production, metabolic electron use, and EET could be achieved by the inclusion of an oxygen

fluorescence probe and more advanced techniques such as membrane inlet mass spectroscopy (MIMS) (Tolleteer et al. 2017).

#### **8.4.2. Graphene based anodes and cathodes:**

During the characterization of graphene based aerogels we demonstrated the ability of ten coin sized anodes to power a microwatt consuming clock. The total electrode area including the planar platinum coated Nafion® membrane air cathode was the size of a small battery, making it conceivable that graphene based MFC electrodes could find a way onto the market to power low energy technology. The aerogels could be molded into any shape provided the single chamber set up still allowed sufficient proton migration to the cathode. Such a device could contain long lived anaerobic anode respiring bacteria and be ‘fed’ occasionally with organic substrates independent of charging *via* the electrical grid. By setting up a MFC device with a graphene aerogel anode and a graphene coated stainless steel cathode, we demonstrated the first all graphene catalyzed MFC and the first demonstration of pristine graphene catalyzing the ORR in place of platinum and yielding a fifth of the power output. This is significant because the use of expensive platinum cathodes is a limiting factor for scaling up MFC production, and the price of graphene is falling every year. Using pristine graphene over modified versions of graphene is another advantage. The MFC market is projected to grow from an estimated \$9 million to \$18.6 million in 2025 (MicromarketMonitor.com 2016), and graphene based aerogels could play an important role.

### **8.3. Alternative project aims and next steps:**

#### **8.3.1. Engineering *R. palustris* for biofuel production:**

This project focused on improving certain aspects of BPV and MFC devices in terms of electrical performance, however an ulterior aim was to develop a system for the production of recombinant compounds using waste streams as a feedstock in the MFC. A three enzyme pathway was assembled and synthesized for production of *n*-alkanes, ready for insertion into *R. palustris*  $\Delta$ *phaAB* or  $\Delta$ *glgAC* knockout sites. Experiments were also performed with David Lea-Smith proving the efficacy of using crude glycerol and anaerobic digestate as the MFC feedstock. Further development of this area could be very fruitful for MFC applications, where the anode is not used principally to produce electrical power, but to maintain an environment conducive to high yields of product synthesis. In this case the anode may provide protection against production of free radicals and cell inhibition.

#### **8.3.2. Towards a combined waste remediation and bioelectrosynthetic system:**

A recently emerging field in BES technology is bioelectrosynthesis, using cathode oxidizing bacteria to accumulate biomass and produce desired molecules. The cathode can be tuned to provide electrons at the specific potential needed for certain metabolic pathways, with reducing power sourced from an inorganic oxidation reaction or an anode respiring culture (Choi & Sang 2016). Rengasamy et al. (2017) demonstrated increased production of PHB from a biocathode with *Rhodopseudomonas palustris* TIE-1, which also possesses the P<sub>io</sub> pathway for iron oxidation and so is well adapted to receive electrons from an alternative source. Work was done in parallel to this project to set up BESs containing both a bioanode and a biocathode, opening tangential avenues of research into an important area of BES applications. A device with identical cultures of *R. palustris* and identical electrodes (carbon fibre) in both chambers

polarized one way such that one chamber became the anodic chamber and one the cathodic chamber. Analyzing differential gene expression in either side could be informative about the respective routes for electron export and uptake. Another device was set up using with a *Synechocystis* biofilm on the anode and an *R. palustris* biocathode. This device displayed the same BPV chronoamperometry kinetics as with an inorganic cathode and continued to function for several months. Further characterization of this type of system could lead to a BES using photosynthetic electrons from water or electrons from a mixed waste substrate at the anode being consumed by an axenic, engineered strain producing a desired compound in the cathode chamber, thus using zero cost solar energy or consuming waste or pollutants and increasing yields of product synthesis.

#### **8.4. Conclusions:**

The results from this project shed light on key limitations for bioelectricity production from BPV and MFC devices using two model species. Light absorption of individual cells should be taken into consideration when designing BPV reactors and fluorescence could be used as a tool to measure BPV efficiency. BPV current production is significantly increased by deleting metabolic electron sinks, removal of the nitrate assimilation pathway proved too disruptive in addition to the others, but other peripheral electron sinks with a less central role in cell metabolism could be targeted to further increase the output. MFC current production may not be directly increased by removing storage molecules in *R. palustris*, but optimizing the cell to electrode interaction by using high surface area and highly conductive materials had a significant improvement on power output. The gradual improvement in power output from BESs has accelerated over the past decade, making it highly likely BPV and MFC devices will

emerge as a cornerstone technology for bioremediation, bioelectrosynthesis, and renewable electricity production.

## BIBLIOGRAPHY

- Abed, R.M.M., et al. 2009. Applications of cyanobacteria in biotechnology. *Journal of applied microbiology*, 106(1), pp.1–12.
- Abourached, C. et al. 2016. Wastewater treatment by Microbial Fuel Cell (MFC) prior irrigation water reuse. *Journal of Cleaner Production*, 137(August), pp.144–149.
- Acuña, A.M. et al., 2015. Resolving the contribution of the uncoupled phycobilisomes to cyanobacterial pulse-amplitude modulated (PAM) fluorometry signals. *Photosynthesis research*, 127(1), 91-pp102.
- Aelterman, P. et al., 2006. Microbial fuel cells for wastewater treatment. *Water Science & Technology*, 54(8), p.9.
- Al-najjar, M.A.A., 2014. Light Utilization Strategies in Photosynthetic Microbial Mats May Give Hints to Improve Cyanobacterial Biomass Production. *Annals of Marine Biology Research*, 1(1), pp.1-4.
- Al-Najjar, M.A.A. et al., 2012. Light utilization efficiency in photosynthetic microbial mats. *Environmental Microbiology*, 14(4), pp.982–992.
- Allahverdiyeva, Y. et al., 2015. Cyanobacterial Oxygenic Photosynthesis is Protected by Flavodiiron Proteins. *Life*, 5(1), pp.716–743.
- Allahverdiyeva, Y. et al., 2013. Flavodiiron proteins Flv1 and Flv3 enable cyanobacterial growth and photosynthesis under fluctuating light. *Proceedings of the National Academy of Sciences*, 110(10), pp.4111–4116.
- Alves, M.N. et al., 2015. Unraveling the electron transfer processes of a nanowire protein from *Geobacter sulfurreducens*. *Biochimica et Biophysica Acta (BBA) - Bioenergetics*, 1857(1), pp.7–13.
- Alvey, R.M. et al., 2011. Effects of Modified Phycobilin Biosynthesis in the Cyanobacterium *Synechococcus* sp. Strain PCC 7002. *JOURNAL OF BACTERIOLOGY*, 193(7),

pp.1663–1671.

Amar, A. Ben, Kouki, A.B. & Cao, H., 2015. Power approaches for implantable medical devices. *Sensors (Switzerland)*, 15(11), pp.28889–28914.

Ambrosi, A. et al., 2014. Electrochemistry of graphene and related materials. *Chemical Reviews*, 114(14), pp.7150–7188.

Antonyuk, S. et al., 2015. Influence of coating and wetting on the mechanical behaviour of highly porous cylindrical aerogel particles. *Powder Technology*, 285, pp.34–43.

Arteni, A. et al., 2009. Structural organisation of phycobilisomes from *Synechocystis* sp. strain PCC6803 and their interaction with the membrane. *Biochimica et biophysica acta*, 1787(4), pp.272–9.

Arutyunov, V.S. & Lisichkin, G. V, 2017. Energy resources of the 21st century: problems and forecasts. Can renewable energy sources replace fossil fuels? *Russian Chemical Reviews*, 86(8), pp.777–804.

Babauta, J. et al., 2012. Electrochemically active biofilms: facts and fiction. A review. *Biofouling*, 28(8), pp.789–812.

Bajracharya, S. et al., 2016. An overview on emerging bioelectrochemical systems (BESs): Technology for sustainable electricity, waste remediation, resource recovery, chemical production and beyond. *Renewable Energy*, 98, pp.153–170.

Beams, R. et al., 2015. Raman characterization of defects and dopants in graphene. *Journal of Physics: Condensed Matter*, 27, p.83002.

Beckmann, J. et al., 2009. Improvement of light to biomass conversion by de-regulation of light-harvesting protein translation in *Chlamydomonas reinhardtii*. *Journal of Biotechnology*, 142(1), pp.70–77.

Bernát, G., et al., 2009. Towards efficient hydrogen production: the impact of antenna size and external factors on electron transport dynamics in *Synechocystis* PCC 6803.

- Photosynthesis research*, 99(3), pp.205–16.
- Bersanini, L. et al., 2014. Flavodiiron Protein Flv2/Flv4-Related Photoprotective Mechanism Dissipates Excitation Pressure of PSII in Cooperation with Phycobilisomes in Cyanobacteria. *PLANT PHYSIOLOGY*, 164(2), pp805-818.
- Berteotti, S., Ballottari, M. & Bassi, R., 2016. Increased biomass productivity in green algae by tuning non-photochemical quenching. *Scientific reports*, 6(August 2015), p.21339.
- Bhaya, D. et al., 2000. Type IV pilus biogenesis and motility in the cyanobacterium *Synechocystis* sp. PCC6803. *Molecular Microbiology*, 37(4), pp.941–951.
- Bird, L.J., Bonnefoy, V. & Newman, D.K., 2011. Bioenergetic challenges of microbial iron metabolisms. *Trends in Microbiology*, 19(7), pp.330–340.
- Blankenship, R.E. et al., 2011. Comparing photosynthetic and photovoltaic efficiencies and recognizing the potential for improvement. *Science (New York, N.Y.)*, 332(6031), pp.805–9.
- Blokhina, O., Virolainen, E, Fagerstedt K. V. 2003. Antioxidants, Oxidative Damage and Oxygen Deprivation Stress: a Review. *Annals of Botany*, 91(2), pp.179–194.
- Bombelli, P. et al., 2015. A High Power-Density , Mediator-Free , Microfluidic Biophotovoltaic Device for Cyanobacterial Cells. *Adv. Energy Mat.*5, pp.1–6.
- Bombelli, P. et al., 2016. Electrical output of bryophyte microbial fuel cell systems is sufficient to power a radio or an environmental sensor. *Royal Society Open Science*, 3(10).
- Bombelli, P. et al., 2011. Quantitative analysis of the factors limiting solar power transduction by *Synechocystis* sp. PCC 6803 in biological photovoltaic devices. *Energy & Environmental Science*, 4(11), p.4690.
- Bombelli, P. et al., 2012. Surface morphology and surface energy of anode materials influence power outputs in a multi-channel mediatorless bio-photovoltaic (BPV) system.

- Physical Chemistry Chemical Physics*, 14(35), pp.12221–9.
- Bombelli, P. et al., 2012. Surface morphology and surface energy of anode materials influence power outputs in a multi-channel mediatorless bio-photovoltaic (BPV) system. *Physical chemistry chemical physics : PCCP*, 14, pp.12221–12229.
- Bose, A. & Newman, D.K., 2011. Regulation of the phototrophic iron oxidation (pio) genes in *Rhodospseudomonas palustris* TIE-1 is mediated by the global regulator, FixK. *Molecular microbiology*, 79(1), pp.63–75.
- Bose, a et al., 2014. Electron uptake by iron-oxidizing phototrophic bacteria. *Nature communications*, 5, p.3391.
- Bradley, R.W. et al., 2012. Biological photovoltaics: intra- and extra-cellular electron transport by cyanobacteria. *Biochemical Society transactions*, 40(6), pp.1302–7.
- Bradley, R.W. et al., 2013a. Terminal oxidase mutants of the cyanobacterium *Synechocystis* sp. PCC 6803 show increased electrogenic activity in biological photo-voltaic systems. *Physical chemistry chemical physics : PCCP*, 15(32), pp.13611–8.
- Bradley, R.W. et al., 2013b. Terminal oxidase mutants of the cyanobacterium *Synechocystis* sp. PCC 6803 show increased electrogenic activity in biological photo-voltaic systems. *Physical chemistry chemical physics : PCCP*, 15(32), pp.13611–8.
- Brotosudarmo, T.H.P. et al., 2011. The light intensity under which cells are grown controls the type of peripheral light-harvesting complexes that are assembled in a purple photosynthetic bacterium. *The Biochemical journal*, 440(1), pp.51–61.
- Bücking, C. et al., 2012. Outer-membrane cytochrome-independent reduction of extracellular electron acceptors in *Shewanella oneidensis*. *Microbiology (United Kingdom)*, 158(8), pp.2144–2157.
- Büsch, A., et al., 2002. Characterization of the norB Gene, Encoding Nitric Oxide Reductase, in the Nondenitrifying Cyanobacterium *Synechocystis* sp. Strain PCC6803. *Applies and*

*Environmental Microbiology*. 68(2), pp.669-672

- Campbell, D. et al., 1998. Chlorophyll fluorescence analysis of cyanobacterial photosynthesis and acclimation. *Microbiology and molecular biology reviews : MMBR*, 62(3), pp.667–683.
- Cao, X. et al., 2009. A completely anoxic microbial fuel cell using a photo-biocathode for cathodic carbon dioxide reduction. *Energy & Environmental Science*, 2(5), p.498.
- Carlozzi, P. et al., 2006. Growth characteristics of *Rhodospseudomonas palustris* cultured outdoors, in an underwater tubular photobioreactor, and investigation on photosynthetic efficiency. *Applied microbiology and biotechnology*, 73(4), pp.789–95.
- Cereda, A. et al., 2014. A bioelectrochemical approach to characterize extracellular electron transfer by *synechocystis* sp. PCC6803. *PLoS ONE*, 9(3), pp.1–8.
- Chandra, A., Joubert, L.M. & Bhaya, D., 2017. Modulation Of Type IV Pili Phenotypic Plasticity Through A Novel Chaperone-Usher System In *Synechocystis* sp 6803. *bioRxiv*, pp.1–17.
- Chang, J.K. et al., 2015. Graphene Anodes and Cathodes: Tuning the Work Function of Graphene by Nearly 2 eV with an Aqueous Intercalation Process. *ACS Applied Materials and Interfaces*, 7(31), pp.17155–17161.
- Chaturvedi, V. & Verma, P., 2016. Microbial fuel cell: a green approach for the utilization of waste for the generation of bioelectricity. *Bioresources and Bioprocessing*, 3(1), p.38.
- Chen, J. et al., 2013. Manipulation of Microbial Extracellular Electron Transfer by Changing Molecular Structure of Phenazine-Type Redox Mediators.
- Chen, W. et al., 2014. Preparation of a macroporous flexible three dimensional graphene sponge using an ice-template as the anode material for microbial fuel cells. *RSC Advances*, 4(41), p.21619.
- Choi, O. & Sang, B.-I., 2016. Extracellular electron transfer from cathode to microbes:

- application for biofuel production. *Biotechnology for biofuels*, 9(1), p.11.
- Ciesielski, P.N. et al., 2010. Enhanced photocurrent production by Photosystem I multilayer assemblies. *Advanced Functional Materials*, 20(23), pp.4048–4054.
- Ciniciato, G.P.M.K. et al., 2016. Investigating the association between photosynthetic efficiency and generation of biophotocurrent in autotrophic microbial fuel cells. *Nature Publishing Group*, (August), pp.1–10.
- Collins, A.M. et al., 2012. Photosynthetic pigment localization and thylakoid membrane morphology are altered in *Synechocystis* 6803 phycobilisome mutants. *Plant physiology*, 158(4), pp.1600–9.
- Cooley, J.W. & Vermaas, W.I.M.F.J., 2001. Succinate Dehydrogenase and Other Respiratory Pathways in Thylakoid Membranes of *Synechocystis* sp. Strain PCC 6803 : Capacity Comparisons and Physiological Function. , 183(14), pp.4251–4258.
- Das, S. et al., 2013. Rheology and morphology of pristine graphene/polyacrylamide gels. *ACS Applied Materials and Interfaces*, 5(17), pp.8633–8640.
- Dienst, D. et al., 2008. The cyanobacterial homologue of the RNA chaperone Hfq is essential for motility of *Synechocystis* sp. PCC 6803. *Microbiology*, 154(10), pp.3134–3143.
- Dohnalkova, A.C. et al., 2011. Imaging hydrated microbial extracellular polymers: Comparative analysis by electron microscopy. *Applied and Environmental Microbiology*, 77(4), pp.1254–1262.
- Dong, K. et al., 2013. Microbial fuel cell as power supply for implantable medical devices: A novel configuration design for simulating colonic environment. *Biosensors and Bioelectronics*, 41(1), pp.916–919.
- Drake, L.C., 1949. Pore-Size Distribution in Porous Materials. *Industrial & Engineering Chemistry*, 41(4), pp.780–785.
- Dutton, B.Y.P.L. & Evans, W.C., 1969. The Metabolism of Aromatic Compounds by

Rhodopseudomonas palustris.

- Ermakova, M. et al., 2016. Distinguishing the roles of thylakoid respiratory terminal oxidases in the cyanobacterium *Synechocystis* sp. PCC 6803. *Plant Physiology*, 171(June), p.pp.00479.2016.
- Estrada-Arriaga, E.B. et al., 2017. Performance of air-cathode stacked microbial fuel cells systems for wastewater treatment and electricity production. *Water Science and Technology*, p.wst2017253.
- Fabbro, A. et al., 2016. Graphene-Based interfaces do not alter target nerve cells. *ACS Nano*, 10(1), pp.615–623.
- Ferrari, A.C. et al., 2006. Raman spectrum of graphene and graphene layers. *Physical Review Letters*, 97(18).
- Ferrari, A.C. et al., 2014. Science and technology roadmap for graphene, related two-dimensional crystals, and hybrid systems. *Nanoscale*, 7(11), pp.4598–4810.
- Flemming, H.-C. et al., 2016. Biofilms: an emergent form of bacterial life. *Nature Reviews Microbiology*, 14(9), pp.563–575.
- Foyer, C.H., et al., 2017. Viewing oxidative stress through the lens of oxidative signalling rather than damage. *Biochemical Journal*, 474(6), pp.877–883.
- Fraiwan, A. et al., 2013. A paper-based microbial fuel cell: Instant battery for disposable diagnostic devices. *Biosensors and Bioelectronics*, 49, pp.410–414.
- Freguia, S. & Rabaey, K., 2007. Electron and Carbon Balances in Microbial Fuel Cells Reveal Temporary Bacterial Storage Behavior During Electricity Generation. , pp.2915–2921.
- Frías, J.E. & Flores, E., 2015. Induction of the Nitrate Assimilation nirA Operon and Protein-Protein Interactions in the Maturation of Nitrate and Nitrite Reductases in the Cyanobacterium *Anabaena* sp . Strain PCC 7120. *Journal of Bacteriology*, 197(14),

pp.2442–2452.

- Fricke, K., et al., 2008. On the use of cyclic voltammetry for the study of anodic electron transfer in microbial fuel cells. *Energy & Environmental Science*, 1(1), p.144.
- Fu, H.-Y. et al., 2017. Redesigning the QA binding site of Photosystem II allows reduction of exogenous quinones. *Nature Communications*, 8(May), p.15274.
- Gonska, N. et al., 2018. Characterization of the quinol- dependent nitric oxide reductase from the pathogen *Neisseria meningitidis* , an electrogenic enzyme. , 8, p.3637.
- Gorbunov, M.Y. et al., 2011. A kinetic model of non-photochemical quenching in cyanobacteria. *Biochimica et Biophysica Acta - Bioenergetics*, 1807(12), pp.1591–1599.
- Gorby, Y.A. et al., 2009. Electrically conductive bacterial nanowires produced by *Shewanella oneidensis* strain MR-1 and other microorganisms. , 106(23), p.9535.
- Gosse, J.L. et al., 2007. Hydrogen production by photoreactive nanoporous latex coatings of nongrowing *Rhodospseudomonas palustris* CGA009. *Biotechnology Progress*, 23(1), pp.124–130.
- Grotjohann, I. & Fromme, P., 2005. Structure of cyanobacterial Photosystem I. *Photosynthesis Research*, 85(1), pp.51–72.
- Gude, V.G., 2016. Wastewater treatment in microbial fuel cells - An overview. *Journal of Cleaner Production*, 122, pp.287–307.
- Gutekunst, K. et al., 2014. The Bidirectional NiFe-hydrogenase in *Synechocystis* sp . PCC 6803 Is Reduced by Flavodoxin and Ferredoxin and Is Essential under Mixotrophic, Nitrate-limiting Conditions. *The Journal of Biological Chemistry*. 289(4), pp.1930–1937.
- Gutthann, F. et al., 2007. Inhibition of respiration and nitrate assimilation enhances photohydrogen evolution under low oxygen concentrations in *Synechocystis* sp. PCC 6803. *Biochimica et Biophysica Acta - Bioenergetics*, 1767(2), pp.161–169.

- Han, Y., et al., 2010. A microbial fuel cell as power supply for implantable medical devices. *Biosensors and Bioelectronics*, 25(9), pp.2156–2160.
- Hansen, J. et al., 2013. Assessing “dangerous climate change”: required reduction of carbon emissions to protect young people, future generations and nature. *PloS one*, 8(12), p.e81648.
- Harwood, C.S. & Gibson, J., 1988. Anaerobic and Aerobic Metabolism of Diverse Aromatic Compounds by the Photosynthetic Bacterium *Rhodospseudomonas palustris*. , 54(3).
- Heinz, S. et al., 2016. Analysis of photosystem II biogenesis in cyanobacteria. *Biochimica et Biophysica Acta - Bioenergetics*, 1857(3), pp.274–287.
- Hohmann-Marriott, M.F. & Blankenship, R.E., 2011. Evolution of photosynthesis. *Annu. Rev. Plant Biol.*, 62, pp.515–48.
- Hu, S. et al., 2012. Characterization of Crude Glycerol from Biodiesel Plants. *Agricultural and Food Chemistry*. 60, pp5915-5921
- Ieropoulos, I., et al., 2008. Microbial Fuel Cells based on carbon veil electrodes : Stack configuration and scalability. *International Journal of Energy Research*, 32(13), pp.1228–1240.
- Imam, S. et al., 2011. iRsp1095 : A genome-scale reconstruction of the *Rhodobacter sphaeroides* metabolic network iRsp1095 : A genome-scale reconstruction of the *Rhodobacter sphaeroides* metabolic network. *BMC Systems Biology*, 116(5).
- Inglesby, A.E., et al., 2012a. *Rhodospseudomonas palustris* purple bacteria fed *Arthrospira maxima* cyanobacteria: demonstration of application in microbial fuel cells. *RSC Advances*, 2(11), p.4829.
- Inglesby, A.E., Beatty, D. a. & Fisher, A.C., 2012b. *Rhodospseudomonas palustris* purple bacteria fed *Arthrospira maxima* cyanobacteria: demonstration of application in microbial fuel cells. *RSC Advances*, 2(11), p.4829.

- Jittawuttipoka, T. et al., 2013. Multidisciplinary Evidences that Synechocystis PCC6803 Exopolysaccharides Operate in Cell Sedimentation and Protection against Salt and Metal Stresses. *PLOS One*, 8(2).
- Kaneko, T. & Tabata, S., 1997. Complete Genome Structure of the Unicellular Cyanobacterium Synechocystis sp. PCC6803. *Plant Cell Physiol*, 38(11), pp.1171–1176.
- Kang, Y.L., et al., 2015. Synergetic effect of conductive polymer poly(3,4-ethylenedioxythiophene) with different structural configuration of anode for microbial fuel cell application. *Bioresource Technology*, 189, pp.364–369.
- Kannan, M. V. & Gnana kumar, G., 2016. Current status, key challenges and its solutions in the design and development of graphene based ORR catalysts for the microbial fuel cell applications. *Biosensors and Bioelectronics*, 77, pp.1208–1220.
- Kellogg, B. et al., 2017. PASSIVE WI-FI: Bringing Low Power to Wi-Fi Transmissions. *GetMobile: Mobile Computing and Communications*, 20(3), pp.38–41.
- Kernan, C. et al., 2015. Experimental and Computational Investigation of Biofilm Formation by Rhodospseudomonas palustris Growth under Two Metabolic Modes. *Plos One*, 10(6)
- Kim, D. et al., 2012. Scaling-up microbial fuel cells: Configuration and potential drop phenomenon at series connection of unit cells in shared anolyte. *ChemSusChem*, 5(6), pp.1086–1091.
- Kim, E. & Lee, J.K., 2010. Competitive Inhibitions of the Chlorophyll Synthase of Synechocystis sp . Strain PCC 6803 by Bacteriochlorophyllide a and the Bacteriochlorophyll Synthase of Rhodobacter sphaeroides by Chlorophyllide a . *Jounral of Bacteriology*. 192(1), pp.198–207.
- Kirst, H., et al., 2014. Maximizing photosynthetic efficiency and culture productivity in cyanobacteria upon minimizing the phycobilisome light-harvesting antenna size.

- Biochimica et Biophysica Acta (BBA) - Bioenergetics*, 1837(10), pp.1653–1664.
- Kodru, S. et al., 2015. The slow S to M rise of chlorophyll a fluorescence reflects transition from state 2 to state 1 in the green alga *Chlamydomonas reinhardtii*. *BBA*, pp.1–11.
- Kolodny, N.H. et al., 2006. Effect of Nitrogen Source on Cyanophycin Synthesis in *Synechocystis* sp. Strain PCC 6308. *Journal of Bacteriology*, 188(3), pp.934–940.
- Koropatkin, N.M. et al., 2006. Atomic structure of a nitrate-binding protein crucial for photosynthetic productivity. *Proceedings of the National Academy of Sciences of the United States of America*, 103(26), pp.9820–5.
- Kracke, F., Vassilev, I. & Kr??mer, J.O., 2015. Microbial electron transport and energy conservation - The foundation for optimizing bioelectrochemical systems. *Frontiers in Microbiology*, 6(JUN), pp.1–18.
- Kufryk, G.I. et al., 2002. Transformation of the cyanobacterium *Synechocystis* sp . PCC 6803 as a tool for genetic mapping : optimization of efficiency. *FEMS Microbiology Letters*, 206, pp.215–219.
- Kuhne, S. et al., 2013. Characterization of terrestrial cyanobacteria to increase process efficiency in low energy consuming production processes. *Sustainable Chemical Processes*, 1(1), p.6.
- Kwon, J.-H. et al., 2013. Reduced light-harvesting antenna: Consequences on cyanobacterial metabolism and photosynthetic productivity. *Algal Research*, 2(3), pp.188–195.
- Kwong, J., 2012. Microwatt Electronics and Beyond. *PowerMEMS 2012*, 77.
- Laczko-Dobos, H. et al., 2008. Role of phosphatidylglycerol in the function and assembly of Photosystem II reaction center, studied in a *cdsA*-inactivated PAL mutant strain of *Synechocystis* sp. PCC6803 that lacks phycobilisomes. *Biochimica et Biophysica Acta - Bioenergetics*, 1777(9), pp.1184–1194.
- Lamb, J.J. et al., 2014. Functional Role of PilA in Iron Acquisition in the Cyanobacterium

- Synechocystis sp. PCC 6803. *PLoS ONE*, 9(8), p.e105761.
- Larimer, F.W. et al., 2004. Complete genome sequence of the metabolically versatile photosynthetic bacterium *Rhodospseudomonas palustris*. *Nature biotechnology*, 22(1), pp.55–61.
- Lea-Smith, D.J. et al., 2015. Photosynthetic, respiratory and extracellular electron transport pathways in cyanobacteria. *Biochimica et Biophysica Acta (BBA) - Bioenergetics*, 1857(3), pp.1–9.
- Lea-Smith, D.J. et al., 2014. Phycobilisome-Deficient Strains of *Synechocystis* sp. PCC 6803 Have Reduced Size and Require Carbon-Limiting Conditions to Exhibit Enhanced Productivity. *Plant physiology*, 165(2), pp.705–714.
- Lea-Smith, D.J. et al., 2013. Thylakoid terminal oxidases are essential for the cyanobacterium *Synechocystis* sp. PCC 6803 to survive rapidly changing light intensities. *Plant physiology*, 162(1), pp.484–95.
- Lee, C. et al., 2008. Measurement of the Elastic Properties and Intrinsic Strength of Monolayer Graphene. *Science (New York, N.Y.)*, 321(5887), pp.385–388.
- Lee, E.H., Lee, S.W. & Saraf, R.F., 2014. Noninvasive measurement of membrane potential modulation in microorganisms: Photosynthesis in green algae. *ACS Nano*, 8(1), pp.780–786.
- Leofanti, G. et al., 1998. Surface area and pore texture of catalysts. *Catalysis Today*, 41(1–3), pp.207–219.
- Lepage, G. et al., 2012. Characterization of a microbial fuel cell with reticulated carbon foam electrodes. *Bioresource Technology*, 124, pp.199–207.
- Li, Y. et al., 2012. Nitrogen-doped graphene nanosheets as cathode materials with excellent electrocatalytic activity for high capacity lithium-oxygen batteries. *Electrochemistry Communications*, 18(1), pp.12–15.

- Liberton, M. et al., 2017. Phycobilisome truncation causes widespread proteome changes in *Synechocystis* sp. PCC 6803. *PLOS One*, 6803, pp.1–18.
- Liberton, M. et al., 2006. Ultrastructure of the membrane systems in the unicellular cyanobacterium *Synechocystis* sp. strain PCC 6803. *Protoplasma*, 227(2–4), pp.129–138.
- Lin, Y. et al., 2016. Pristine Graphene Aerogels by Room-Temperature Freeze Gelation. *Advanced Materials*, 28(36), pp.7993–8000.
- Liu, J. et al., 2012. Graphene/carbon cloth anode for high-performance mediatorless microbial fuel cells. *Bioresource Technology*, 114, pp.275–280.
- Lockhart, P.J. et al., 2006. Evolution of chlorophyll and bacteriochlorophyll : The problem of invariant sites in sequence analysis. *PNAS*, 93(March 1996), pp.1930–1934.
- Logan, B.E. et al., 2006. Microbial fuel cells: Methodology and technology. *Environmental Science and Technology*, 40(17), pp.5181–5192.
- Lotya, M. et al., 2009. Liquid phase production of graphene by exfoliation of graphite in surfactant/water solutions. *Journal of the American Chemical Society*, 131(10), pp.3611–3620.
- Maksimov, E.G. et al., 2014. The time course of non-photochemical quenching in phycobilisomes of *Synechocystis* sp. PCC6803 as revealed by picosecond time-resolved fluorimetry. *Biochimica et Biophysica Acta - Bioenergetics*, 1837(9), pp.1540–1547.
- Martínez-Gómez, K. et al., 2012. New insights into *Escherichia coli* metabolism: carbon scavenging, acetate metabolism and carbon recycling responses during growth on glycerol. *Microbial Cell Factories*, 11(1), p.46.
- Mattevi, C. et al., 2009. Evolution of Electrical, Chemical, and Structural Properties of Transparent and Conducting Chemically Derived Graphene Thin Films. *Advanced Functional Materials*, 19(16), pp.2577–2583.

- McCormick, A.J. et al., 2013. Hydrogen production through oxygenic photosynthesis using the cyanobacterium *Synechocystis* sp. PCC 6803 in a bio-photoelectrolysis cell (BPE) system. *Energy & Environmental Science*, 6(9), p.2682.
- McCormick, A.J. et al., 2011. Photosynthetic biofilms in pure culture harness solar energy in a mediatorless bio-photovoltaic cell (BPV) system. *Energy & Environmental Science*, 4(11), p.4699. Available at: <http://xlink.rsc.org/?DOI=c1ee01965a> [Accessed November 27, 2013].
- McCormick, A.J. et al., 2015. Biophotovoltaics: oxygenic photosynthetic organisms in the world of bioelectrochemical systems. *Energy & Environmental Science*, 0, pp.1–18.
- McGrath, J.E. & Harfoot, C.G., 1997. Reductive dehalogenation of halocarboxylic acids by the phototrophic genera *Rhodospirillum* and *Rhodopseudomonas*. *Applied and environmental microbiology*, 63(8), pp.3333–5.
- McKinlay, J.B. et al., 2014. Non-growing *Rhodopseudomonas palustris* increases the hydrogen gas yield from acetate by shifting from the glyoxylate shunt to the tricarboxylic acid cycle. *The Journal of biological chemistry*, 289(4), pp.1960–70.
- Mckinlay, J.B. & Harwood, C.S., 2010. Carbon dioxide fixation as a central redox cofactor recycling mechanism in bacteria. *PNAS*, 107(26), pp11669-11675.
- Van De Meene, A.M.L. et al., 2006. The three-dimensional structure of the cyanobacterium *Synechocystis* sp. PCC 6803. *Archives of Microbiology*, 184(5), pp.259–270.
- Mekjinda, N. & Ritchie, R.J., 2015. Breakdown of food waste by anaerobic fermentation and non-oxygen producing photosynthesis using a photosynthetic bacterium. *Waste Management*, 35, pp.199–206.
- Melis, A., 2009. Solar energy conversion efficiencies in photosynthesis: Minimizing the chlorophyll antennae to maximize efficiency. *Plant Science*, 177(4), pp.272–280.
- Mershin, A. et al., 2012. Self-assembled photosystem-I biophotovoltaics on nanostructured

- TiO<sub>2</sub> and ZnO. *Scientific reports*, 2, p.234.
- Mirkovic, T. et al., 2016. Light Absorption and Energy Transfer in the Antenna Complexes of Photosynthetic Organisms. *Chemical Reviews*.
- Morishima, K. et al., 2007. Improving the performance of a direct photosynthetic/metabolic bio-fuel cell (DPBFC) using gene manipulated bacteria. *Journal of Micromechanics and Microengineering*, 17(9), pp.S274–S279.
- Müh, F. et al., 2012. Light-induced quinone reduction in photosystem II. *Biochimica et Biophysica Acta - Bioenergetics*, 1817(1), pp.44–65.
- Mullineaux, C.W. & Allen, J.F., 1990. State 1-State 2 transitions in the cyanobacterium *Synechococcus* 6301 are controlled by the redox state of electron carriers between Photosystems I and II. *Photosynthesis Research*, 23, pp.297–311.
- Murakami, A. & Fujita, Y., 1993. Regulation of Stoichiometry between PSI and PSII in Response to Light Regime for Photosynthesis Observed with *Synechocystis* PCC 6714: Relationship between Redox State of Cyt b<sub>6</sub>-f Complex and Regulation of PSI Formation. *Plant and Cell Physiology*, 34(8), pp.1175–1180.
- Mussgnug, J.H. et al., 2007. Engineering photosynthetic light capture: Impacts on improved solar energy to biomass conversion. *Plant Biotechnology Journal*, 5(6), pp.802–814.
- Mustakeem, 2015. Electrode materials for microbial fuel cells: Nanomaterial approach. *Materials for Renewable and Sustainable Energy*, 4(4), pp.1–11.
- Mustakeem, M., 2015. Electrode materials for microbial fuel cells : nanomaterial approach. *Materials for Renewable and Sustainable Energy*, 4(4), pp.1–11.
- Mustila, H. et al., 2016. The Flavodiiron Protein Flv3 Functions as a Homo-Oligomer During Stress Acclimation and is Distinct from the Flv1 / Flv3 Hetero-Oligomer Specific to the O<sub>2</sub> Photoreduction Pathway. *Plant Cell Physiol.* , 57(7), pp.1468–1483.
- Muthukumaran, S. et al., 2016. On-Line Monitoring of Biofilm Forming *Pseudomonas* Sp on

- Stainless Steel Electrodes by Repetitive Cyclic Voltammetry. *IJBTT*. 19(1), pp.6–9.
- Nagarajan, A. et al., 2014. Consequences of Decreased Light Harvesting Capability on Photosystem II Function in *Synechocystis* sp. PCC 6803. *Life*, 4(4), pp.903–914.
- Nakane, D. & Nishizaka, T., 2017. Asymmetric distribution of type IV pili triggered by directional light in unicellular cyanobacteria. *Proceedings of the National Academy of Sciences*, 114(25), pp.6593–6598.
- Nakao, M. et al., 2009. CyanoBase: The cyanobacteria genome database update 2010. *Nucleic Acids Research*, 38(SUPPL.1), pp.2009–2011.
- Nakasugi, K. et al., 2006. The competence gene, *comF*, from *Synechocystis* sp. strain PCC 6803 is involved in natural transformation, phototactic motility and piliation. *Microbiology*, 152(12), pp.3623–3631.
- Nardecchia, S. et al., 2013. Three dimensional macroporous architectures and aerogels built of carbon nanotubes and/or graphene: synthesis and applications. *Chem. Soc. Rev.*, 42(2), pp.794–830.
- Nelson, N., 2011. Photosystems and global effects of oxygenic photosynthesis. *BBA - Bioenergetics*, 1807(8), pp.856–863.
- Nevin, K.P. et al., 2008. Power output and columbic efficiencies from biofilms of *Geobacter sulfurreducens* comparable to mixed community microbial fuel cells. *Environmental microbiology*, 10(10), pp.2505–14.
- Ng, F.-L. et al., 2014. Evaluation of algal biofilms on indium tin oxide (ITO) for use in biophotovoltaic platforms based on photosynthetic performance. *PloS one*, 9(5), p.e97643.
- Ng, F.L. et al., 2017. Enhancement of Power Output by using Alginate Immobilized Algae in Biophotovoltaic Devices. *Scientific Reports*, 7(1), pp.1–8.
- Novak, R.T. et al., 2004. Phototrophic utilization of taurine by the purple nonsulfur bacteria

- Rhodopseudomonas palustris and Rhodobacter sphaeroides. *Microbiology*, 150(6), pp.1881–91.
- Ochiai, H. et al., 1983. Properties of semiconductor electrodes coated with living films of cyanobacteria. *Applied Biochemistry and Biotechnology*, 8(4), pp.289–303.
- Oda, Y. et al., 2003. Biogeography of the Purple Nonsulfur Bacterium Rhodopseudomonas palustris. *Applied and Environmental Microbiology*, 69(9), pp.5186–5191.
- Oh, S. & Logan, B.E., 2006. Proton exchange membrane and electrode surface areas as factors that affect power generation in microbial fuel cells. *Applied Microbiol Biotechnol*, 70, pp.162–169.
- Oh, S.T. et al., 2010. Sustainable wastewater treatment: how might microbial fuel cells contribute. *Biotechnology advances*, 28(6), pp.871–81.
- Ohashi, Y. et al., 2011. Regulation of nitrate assimilation in cyanobacteria. *Journal of Experimental Botany*, 62(4), pp.1411–1424.
- Okamoto, A. et al., 2014. Flavin redox bifurcation as a mechanism for controlling the direction of electron flow during extracellular electron transfer. *Angewandte Chemie (International ed. in English)*, 53(41), pp.10988–91.
- Ooms, M.D. et al., 2016. Photon management for augmented photosynthesis. *Nature Communications*, 7, p.12699.
- Paton, K.R. et al., 2014. Scalable production of large quantities of defect-free few-layer graphene by shear exfoliation in liquids. *Nature Materials*, 13(6), pp.624–630.
- Pechter, K.B. et al., 2017. Molecular Basis of Bacterial Longevity. *American Society for Microbiology*, 8(6), pp.1–12.
- Peng, L., You, S.J. & Wang, J.Y., 2010. Carbon nanotubes as electrode modifier promoting direct electron transfer from *Shewanella oneidensis*. *Biosensors and Bioelectronics*, 25(5), pp.1248–1251.

- Philippis, R. de et al., 1992. Factors affecting PHB accumulation in cyanobacteria and in purple non-sulfur bacteria.pdf. *FEMS microbiological reviews*, 103, pp.187–194.
- Pisciotta, J.M. et al., 2010. Light-dependent electrogenic activity of cyanobacteria. *PloS one*, 5(5), p.e10821.
- Pisciotta, J.M. et al., 2011. Role of the photosynthetic electron transfer chain in electrogenic activity of cyanobacteria. *Applied microbiology and biotechnology*, 91(2), pp.377–85.
- Porra, R.J., et al., 1989. Determination of accurate extinction coefficients and simultaneous equations for assaying chlorophyll a and b extracted with four different solvents: verification of the concentration of chlorophyll standards by atomic absorption spectroscopy. *Biochimica et Biophysica Acta*, 975, pp.384–394.
- Pott, R.W.M. et al., 2013. Photofermentation of crude glycerol from biodiesel using *Rhodospseudomonas palustris*: comparison with organic acids and the identification of inhibitory compounds. *Bioresource technology*, 130, pp.725–30.
- Pott, R.W.M. et al., 2014. The purification of crude glycerol derived from biodiesel manufacture and its use as a substrate by *Rhodospseudomonas palustris* to produce hydrogen. *Bioresource technology*, 152, pp.464–70.
- Potter, M.C., 1911. Electrical effects accompanying the decomposition of organic compounds. *Proceedings of the Royal Society of London Series B*, 84(571), pp.260–276.
- Prindle, A. et al., 2015. Ion channels enable electrical communication within bacterial communities Arthur. *Nature*, 527(6), pp.59–63.
- Rahimnejad, M. et al., 2014. A review on the effect of proton exchange membranes in microbial fuel cells. *Biofuel Research Journal*, 1, pp.7–15.
- Rasmussen, M. & Minteer, S.D., 2014. Photobioelectrochemistry: Solar Energy Conversion and Biofuel Production with Photosynthetic Catalysts. *Journal of the Electrochemical Society*, 161(10), pp.H647–H655.

- Reguera, G. et al., 2006. Biofilm and nanowire production leads to increased current in *Geobacter sulfurreducens* fuel cells. *Applied and Environmental Microbiology*, 72(11), pp.7345–7348.
- Rengasamy, K. et al., 2017. Improving microbial electrosynthesis of polyhydroxybutyrate (PHB) from CO<sub>2</sub> by *Rhodospseudomonas palustris* TIE-1 using an immobilized iron complex modified cathode.
- Ried, J.L. & Collmer, A., 1987. An nptI-sacB-sacR cartridge for constructing directed, unmarked mutations in Gram-negative bacteria by marker exchange-eviction mutagenesis (*Erwinia chrysanthemi*; pectate lyase; pelC; recombinant DNA). *Gene*, 57(2–3), pp.239–246.
- Ringeisen, B.R. et al., 2006. High power density from a miniature microbial fuel cell using *Shewanella oneidensis* DSP10. *Environmental Science and Technology*, 40(8), pp.2629–2634.
- Ritchie, R.J., 2013. The use of solar radiation by the photosynthetic bacterium, *Rhodospseudomonas palustris*: model simulation of conditions found in a shallow pond or a flatbed reactor. *Photochemistry and photobiology*, 89(5), pp.1143–62.
- Ritchie, R.J. & Larkum, a. W.D., 2012. Modelling photosynthesis in shallow algal production ponds. *Photosynthetica*, 50(4), pp.481–500.
- Salmon, R.C. et al., 2013. The CouPSTU and TarPQM transporters in *Rhodospseudomonas palustris*: redundant, promiscuous uptake systems for lignin-derived aromatic substrates. *PloS one*, 8(3), p.e59844.
- Santoro, C. et al., 2017. Three-dimensional graphene nanosheets as cathode catalysts in standard and supercapacitive microbial fuel cell. *Journal of Power Sources*, 356, pp.371–380.
- Sawa, M. et al., 2017. Electricity generation from digitally printed cyanobacteria. *Nature*

- Communications*, 8(1), pp.1–9.
- Schafer, A. et al., 1994. Small mobilizable multi-purpose cloning vectors derived from the *Escherichia coli* plasmids pK18 and pK19: selection of defined deletions in the chromosome of *Corynebacterium glutamicum*. *Gene*, 145, pp.69–73.
- Scheuring, S. et al., 2006. The photosynthetic apparatus of *Rhodospseudomonas palustris*: structures and organization. *Journal of molecular biology*, 358(1), pp.83–96.
- Schneider, G. et al., 2015. Microbial fuel cell-based diagnostic platform to reveal antibacterial effect of beta-lactam antibiotics. *Enzyme and Microbial Technology*, 73–74, pp.59–64.
- Schneider, K. et al., 2016. An investigation of anode and cathode materials in photomicrobial fuel cells. *Philosophical Transactions A*, 374(February), p.20150080.
- Schuermans, R.M. et al., 2015. Comparison of the photosynthetic yield of cyanobacteria and green algae: Different methods give different answers. *PLoS ONE*, 10(9), pp.1–17.
- Scott, S. et al., 2010. Biodiesel from algae: challenges and prospects. *Current opinion in biotechnology*, 21(3), pp.277–86.
- Seekaew, Y. et al., 2014. Low-cost and flexible printed graphene-PEDOT:PSS gas sensor for ammonia detection. *Organic Electronics: physics, materials, applications*, 15(11), pp.2971–2981.
- Shi, L. et al., 2016. Extracellular electron transfer mechanisms between microorganisms and minerals. *Nat Rev Microbiol*, 14(10), pp.651–662.
- Shin, W.-S. et al., 2016. Truncated light-harvesting chlorophyll antenna size in *Chlorella vulgaris* improves biomass productivity. *Journal of Applied Phycology*. 28(6), pp3193-3202
- Smart, L.B. et al., 1994. Genetic Manipulation of the Cyanobacterium *Synechocystis* sp. PCC 6803 (Development of Strains Lacking Photosystem I for the Analysis of Mutations in

- Photosystem II). *Plant physiology*, 104(2), pp.349–354.
- Soltani-Kordshuli, F. et al., 2016. Graphene-doped PEDOT:PSS nanocomposite thin films fabricated by conventional and substrate vibration-assisted spray coating (SVASC). *Engineering Science and Technology, an International Journal*, 19(3), pp.1216–1223.
- Standards, M.U.S.F. et al., 2012. Advanced Biofuel Market Report
- Stoller, M.D. et al., 2008. Graphene-Based ultracapacitors. *Nano Letters*, 8(10), pp.3498–3502.
- Strik, D. et al., 2011. Microbial solar cells: applying photosynthetic and electrochemically active organisms. *Trends in biotechnology*, 29(1), pp.41–9.
- Sukhova, E. et al., 2017. Influence of the variation potential on photosynthetic flows of light energy and electrons in pea. *Photosynthesis Research*, 136(2), pp.215-228.
- Sun, B. et al., 2012. Graphene nanosheets as cathode catalysts for lithium-air batteries with an enhanced electrochemical performance. *Carbon*, 50(2), pp.727–733.
- Sure, S. et al., 2015. Inquisition of *Microcystis aeruginosa* and *Synechocystis* nanowires: characterization and modelling. *Antonie van Leeuwenhoek, International Journal of General and Molecular Microbiology*, 108(5), pp.1213–1225.
- Sure, S. et al., 2016. Microbial nanowires: an electrifying tale. *Microbiology*, 162(12), pp.2017–2028.
- Tajima, N. et al., 2011. Genomic Structure of the Cyanobacterium *Synechocystis* sp. PCC 6803 Strain GT-S. *DNA Research*, 18(5), pp.393–399.
- Tian, L. et al., 2013. Light harvesting and blue-green light induced non-photochemical quenching in two different C-phycoyanin mutants of *synechocystis* PCC 6803. *Journal of Physical Chemistry B*, 117(38), pp.11000–11006.
- Ting, C.S. et al., 2002. Cyanobacterial photosynthesis in the oceans : the origins and significance of divergent light-harvesting strategies. *Trends in Microbiology*, 10(3),

pp.134–142.

- Tolleter, D. et al., 2017. Measuring CO<sub>2</sub> and HCO<sub>3</sub><sup>-</sup> permeabilities of isolated chloroplasts using a MIMS-18O approach. *Journal of Experimental Botany*, 68(14), pp.3915–3924.
- Touloupakis, E. et al., 2015. A bioenergetic assessment of photosynthetic growth of *Synechocystis* sp. PCC 6803 in continuous cultures. *Biotechnology for biofuels*, 8(1), p.133.
- Tsao, J. et al., 2006. Solar FAQs. *US department of Energy*, pp.1–24.
- Tsujimura, S. et al., 2001. Photosynthetic bioelectrochemical cell utilizing cyanobacteria and water-generating oxidase. *Enzyme and Microbial Technology*, 29(4–5), pp.225–231.
- Ungerer, J. & Pakrasi, H.B., 2016. Cpf1 Is A Versatile Tool for CRISPR Genome Editing Across Diverse Species of Cyanobacteria. *Scientific Reports*, 6(October), pp.1–9.
- Venkidusamy, K. et al., 2015. Electron transport through electrically conductive nanofilaments in *Rhodospseudomonas palustris* strain RP2. *RSC Adv.*, 5(122), pp.100790–100798.
- Vermaas, W., 2001. Photosynthesis and respiration in cyanobacteria. *eLS The Phototrophic Prokaryotes*. pp201-209
- Wagner, R.C. et al., 2010. Optimal Set Anode Potentials Vary in Bioelectrochemical Systems. *Env Sci Technol*, 44(16), pp.6036–6041.
- Wang, B. et al., 2012. Application of synthetic biology in cyanobacteria and algae. *Frontiers in microbiology*, 3, p.344.
- Wang, H. et al., 2013. High power density microbial fuel cell with flexible 3D graphene-nickel foam as anode. *Nanoscale*, 5(21), pp.10283–90.
- Wang, L. et al., 2013. One-dimensional electrical contact to a two-dimensional material. *Science*, 342(November), pp.614–7.
- Wang, L. & Sanchez-Soto, M., 2015. Green bio-based aerogels prepared from recycled

- cellulose fiber suspensions. *RSC Adv.*, 5(40), pp.31384–31391.
- Wang, X. et al., 2015. Formation characteristics of an anoxygenic photosynthetic bacterial biofilm in a photorotating biological contactor for azo dye wastewater treatment. *J Chem Technol Biotechnol*, 90, pp.176–184.
- Wenzel, T. et al., 2018. Porous translucent electrodes enhance current generation from photosynthetic biofilms. *Nature Communications*, 9(1299).
- Westmacott, D. & Primrose, S.B., 1976. Synchronous growth of *Rhodospseudomonas palustris* from the swarmer phase. *Journal of general microbiology*, 94(1), pp.117–125.
- Wilson, A. et al., 2006. A soluble carotenoid protein involved in phycobilisome-related energy dissipation in cyanobacteria. *The Plant cell*, 18(4), pp.992–1007.
- Wilson, W.A. et al., 2011. Regulation of glycogen metabolism in yeast and bacteria. , 34(6), pp.952–985.
- Winter, M. & Brodd, R.J., 2004. What are batteries, fuel cells, and supercapacitors? *Chemical Reviews*, 104(10), pp.4245–4269.
- Wong, W.-T. et al., 2014. Promoting Effects of a Single *Rhodospseudomonas palustris* Inoculant on Plant Growth by *Brassica rapa chinensis* under Low Fertilizer Input. *Microbes Environ. Vol.*, 29(3), pp.303–313.
- Xie, X. et al., 2015. Design and fabrication of bioelectrodes for microbial bioelectrochemical systems. *Energy Environ. Sci.*, 8, pp.3418–3441.
- Xing, D. et al., 2008. Electricity generation by *Rhodospseudomonas palustris* DX-1. *Environmental science & technology*, 42(11), pp.4146–51.
- Xu, Q.Q. et al., 2014. Growth performance and meat quality of broiler chickens supplemented with *Rhodospseudomonas palustris* in drinking water. *Br Poult Sci*, 1668, pp.4–11.
- Yang, C.-F. & Lee, C.-M., 2011. Enhancement of photohydrogen production using phbC

- deficient mutant *Rhodospseudomonas palustris* strain M23. *Bioresource technology*, 102(9), pp.5418–24.
- Yang, H. et al., 2015. Microbial fuel cells for biosensor applications. *Biotechnology Letters*, 37(12), pp.2357–2364.
- Yang, X. et al., 2016. Eighteen-month assessment of 3D graphene oxide aerogel-modified 3D graphite fiber brush electrode as a high-performance microbial fuel cell anode. *Electrochimica Acta*, 210, pp.846–853.
- Yang, Y. et al., 2016. Boosting Power Density of Microbial Fuel Cells with 3D Nitrogen-Doped Graphene Aerogel Electrode. *Advanced Science*.
- Yanisch-perron, C. et al., 1985. Improved M13 phage cloning vectors and host strains : nucleotide sequences of the M13mp18 and pUC19 vectors. *Gene*, 33, pp.103–119.
- Yilmaz, L.S. et al., 2010. Electron Partitioning During Light- and Nutrient-Powered Hydrogen Production by *Rhodobacter sphaeroides*. *BioEnergy Research*, 3(1), pp.55–66.
- Yong, Y.-C. et al., 2014. Highly Active Bidirectional Electron Transfer by a Self-Assembled Electroactive Reduced- Graphene-Oxide-Hybridized Biofilm. *Angewandte Chemie International Edition*, (53), pp.4480–4483.
- Yoshihara, S. et al., 2001. Mutational Analysis of Genes Involved in Pilus Structure, Motility and Transformation Competency in the Unicellular Motile Cyanobacterium *Synechocystis* sp. PCC 6803. *Plant and Cell Physiology*, 42(1), pp.63–73.
- Yu, F. et al., 2016. Applications of Graphene-Modified Electrodes in Microbial Fuel Cells. *Materials*, 9(10), p.807.
- Zerulla, K. et al., 2016. The ploidy level of *synechocystis* sp. PCC 6803 is highly variable and is influenced by growth phase and by chemical and physical external parameters. *Microbiology (United Kingdom)*, 162(5), pp.730–739.

- Zevenhuizen, L.P.T.M. & Ebbink, A.G., 1974. Interrelations between glycogen, poly-beta-hydroxybutyric acid and lipids during accumulation and subsequent utilization in a *Pseudomonas*. *Antonie van Leeuwenhoek*, 40(1), pp.103–120.
- Zhang, J.Z. et al., 2017. Photoelectrochemistry of photosystem II in vitro vs . in vivo. *JACS*.140(1), pp6-9
- Zhang, P. et al., 2012. Operon flv4-flv2 Provides Cyanobacterial Photosystem II with Flexibility of Electron Transfer. *The Plant Cell*, 24(5), pp.1952–1971.
- Zhang, Y. et al., 2011. A graphene modified anode to improve the performance of microbial fuel cells. *Journal of Power Sources*, 196(13), pp.5402–5407.
- Zhang, Y.Z. et al., 2011. A graphene modified anode to improve the performance of microbial fuel cells. *Journal of Power Sources*, 196(13), pp.5402–5407.
- Zhao, F. et al., 2009. Techniques for the study and development of microbial fuel cells: an electrochemical perspective. *Chemical Society Reviews*, 38(7), p.1926.
- Zhao, F. et al., 2009. Techniques for the study and development of microbial fuel cells: an electrochemical perspective. *Chemical Society reviews*, 38(7), pp.1926–1939.
- Zhao, H.-B. et al., 2016. Biomass-Based Mechanically Strong and Electrically Conductive Polymer Aerogels and Their Application for Supercapacitors. *ACS Applied Materials & Interfaces*, p.acsami.6b00510.